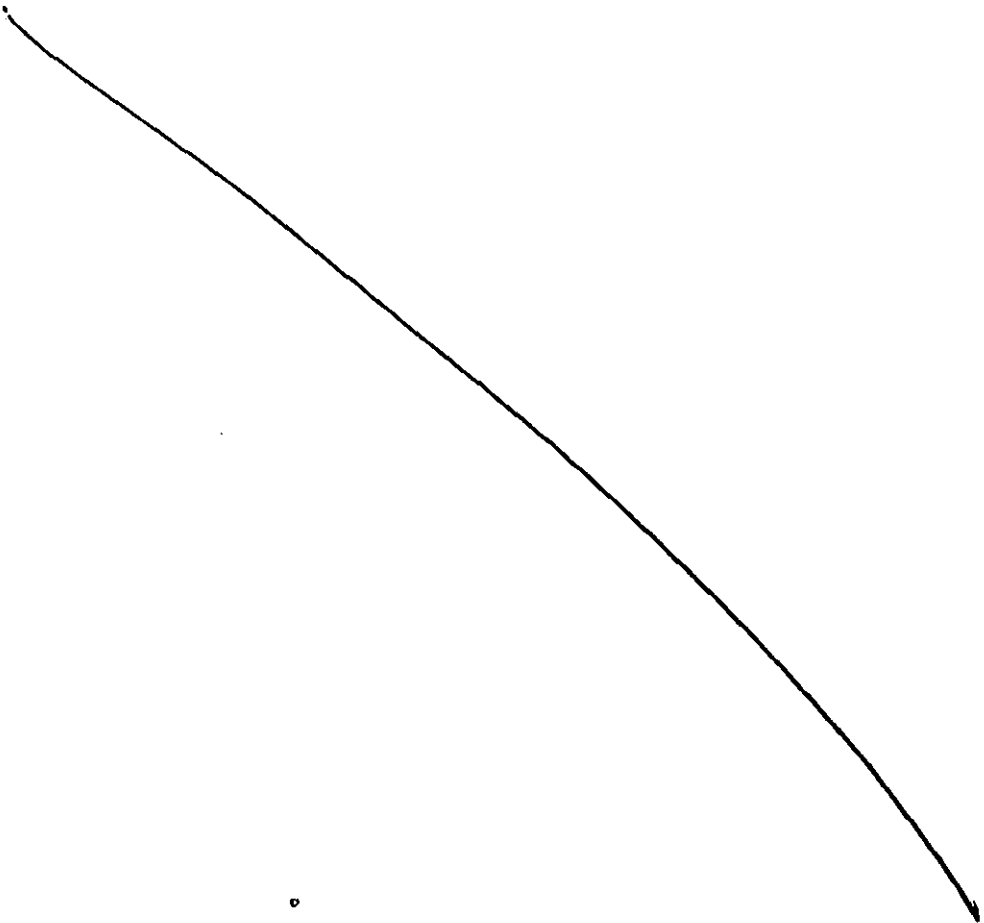
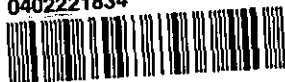


BLDSC no:- DX 213097



0402221834





**INVESTIGATION OF FLAT CAPACITOR  
DISCHARGE ELECTROMAGNETIC  
LAUNCHERS**

by

**Alastair Richard Hoyle, BEng(Hons)**

A Doctoral Thesis  
Submitted in partial fulfilment of the requirements  
for the award of  
Doctor of Philosophy of the Loughborough University


July 1999

**LOUGHBOROUGH UNIVERSITY**  
Department of Electronic and Electrical Engineering

© by Alastair Richard Hoyle 1999





 Loughborough University File Library
Date <i>July 00</i>
Class
Acc No. <i>040222183</i>

*M0001982LB*

In this thesis, studies of flat or pancake type electromagnetic launcher systems are described. The studies involved the development of several numerical models, and are supported throughout by experimental investigation. The models were based on a coaxial filamentary division technique, and the results they provided were compared with those from a commercial electromagnetic finite element modelling package. They were used to investigate some of the many possible launcher structures and power supply arrangements, as part of a wide-ranging parametric study. The aim of this thesis was to gain an insight into the factors that affect the performance of the launchers. Several different techniques were implemented to reduce the computation time.

Practical experimentation provided a clear demonstration of the launcher technology, and supplied valuable model validation data. To aid the experimental work new projectile speed and yaw measurement systems were developed, and these were supported by results from a high-speed camera. A novel dual projectile launcher was tested, and was shown to improve the launch efficiency and to operate at higher energies, due to the reduction in drive coil recoil. Projectile deformation was investigated in both solid discs and flat annular projectiles.

---

## ACKNOWLEDGEMENTS

---

I am indebted to the Department of Electronic and Electrical Engineering of Loughborough University for the award of a research studentship. I would like to express my gratitude to my Director of Research, Prof. Ivor R. Smith for nominating me for the studentship and his leadership of the Pulse Power Research group. Thanks must also go to my Supervisor, Dr Keith Gregory for his suggestions and guidance in the writing of this thesis and his endless enthusiasm for the subject.

I would like to thank Mr George Mayo and Mr Jerry Albrow for their help and advice in the workshop, along with their humour and joviality. Thanks must also go to my colleagues who helped make my stay enjoyable in particular Paul, Bob, Rob, Peter, Rod and Lynn.

I am also grateful to my mum, Jean and dad Richard, who helped me in the early years of my education. Especially I would like to thank my fiancé Clare, for her patience, support, and unending motivation.

---

## TABLE OF CONTENTS

---

	Page
Synopsis .....	I
Certificate of Originality .....	II
Acknowledgements.....	III
Table of Contents.....	IV
List of Principal Symbols.....	IX
<b>1. Introduction .....</b>	<b>1</b>
<b>2. Electromagnetic Launchers .....</b>	<b>3</b>
2.1. Introduction To Electromagnetic Launchers.....	3
2.2. Early History .....	4
2.3. Recent Electromagnetic Launcher History.....	4
2.4. Railguns .....	7
2.5. Coilgun Launchers .....	10
2.5.1. Synchronous Induction Launchers.....	11
2.5.2. Travelling Wave Induction Launchers .....	13
2.5.3. Pulsed Induction Launchers .....	15
2.5.4. Flat Coil Launchers .....	18
2.5.5. Other Novel Launchers .....	20
2.6. Power Supplies .....	20
2.6.1. Capacitor Discharge Supplies.....	21
2.6.2. Homopolar Generators.....	21
2.6.3. Compulsators .....	22
2.6.4. Flux Compressors .....	22
2.6.5. MHD Generators.....	23
2.7. Figures.....	24
<b>3. Modelling Techniques .....</b>	<b>31</b>
3.1. Finite Difference Analysis.....	31

3.2.	Finite Element Analysis .....	32
3.2.1.	Modelling Software .....	33
3.3.	Filamentary Analysis.....	34
3.4.	Conclusions .....	35
<b>4.</b>	<b>Analysis Of Filamentary Networks .....</b>	<b>37</b>
4.1.	Equivalent Circuit Analysis.....	37
4.2.	Matrix Notation .....	37
4.3.	All Mesh Networks .....	39
4.3.1.	Branch Network Equations .....	40
4.4.	Conclusions .....	43
4.5.	Figures .....	44
<b>5.</b>	<b>Numerical Techniques .....</b>	<b>47</b>
5.1.	Solution of Differential Equations .....	47
5.2.	Runge-Kutta Method.....	48
5.2.1.	Local Error Estimation in the Runge-Kutta Method.....	49
5.2.2.	Runge-Kutta-Fehlberg Method .....	50
5.2.3.	Runge-Kutta-Merson Method .....	51
5.3.	Predictor-Corrector Methods.....	52
5.3.1.	Local Error Estimation in the Predictor-Corrector Method...	54
5.4.	Methods of Matrix Factorisation.....	55
5.4.1.	Gauss-Jordan Method .....	55
5.4.2.	Implicit Factorisation Method.....	56
5.4.3.	Triangular Decomposition Method.....	58
5.5.	Conclusions .....	59
<b>6.</b>	<b>Implementation of Filamentary Model.....</b>	<b>61</b>
6.1.	Analysis of Launcher Parameters.....	61
6.1.1.	Method of Filamentary Division.....	61
6.1.2.	Electrical Equations .....	63
6.1.2.1.	Inductance Calculations .....	63
6.1.2.2.	Resistance and Thermal Calculations .....	66
6.1.3.	Mechanical Equations.....	67

6.1.4. Aerodynamic Drag.....	68
6.2. Solution of Filamentary Model .....	69
6.3. Sparsity.....	72
6.3.1. Indexed Matrix Sparsity.....	72
6.3.2. Matrix Partitioning.....	74
6.4. Discontinuities .....	75
6.5. Initial Model Validation.....	76
6.6. Conclusions .....	77
6.7. Figures.....	78
<b>7. Development of Filamentary Model.....</b>	<b>86</b>
7.1. Programme Speed Improvements .....	86
7.2. Pre-calculated Inductances.....	88
7.2.1. Cubic Spline Interpolation .....	89
7.3. Variable Time Stepping Model .....	90
7.4. Instant Crowbar Turn On .....	92
7.5. Sinusoidal Approximation.....	93
7.6. Reduced Parameters .....	96
7.7. Constrained Branch Solution .....	99
7.8. Mesh Generation .....	102
7.9. Projectile Deformation .....	105
7.10. Conclusion.....	109
7.11. Figures.....	111
<b>8. Design Study .....</b>	<b>124</b>
8.1. Projectile Mass .....	124
8.2. Projectile Radii.....	124
8.3. Optimum Number of Drive Coil Turns.....	126
8.3.1. Sinusoidal Model Investigation .....	126
8.3.2. Re-investigation of Optimum Drive Coil Turns .....	127
8.4. Dual Projectile Studies .....	129
8.5. Launcher Radii .....	130
8.6. Drive Coil Thickness.....	131

8.7. Initial Projectile Displacement .....	131
8.8. Re-investigation of Projectile Mass .....	132
8.9. Unusual Launcher Arrangements .....	133
8.10. Conclusions .....	134
8.11. Figures .....	137
<b>9. Experimental Equipment .....</b>	<b>152</b>
9.1. The Test Rig .....	152
9.2. Voltage Measurement .....	153
9.3. Current Measurement .....	154
9.4. Speed Measurement .....	155
9.5. Measurement of Projectile Yaw .....	158
9.6. Power Supply .....	160
9.7. Determination of Power Supply Parameters .....	160
9.8. Conclusion .....	161
9.9. Figures .....	162
<b>10. Experimental Work .....</b>	<b>172</b>
10.1. Launcher Construction .....	172
10.2. Initial Experiments .....	173
10.3. Conclusions .....	176
10.4. Figures .....	177
<b>11. Results .....</b>	<b>182</b>
11.1. Model Validation .....	182
11.1.1. Rectangular Wire Model .....	182
11.1.2. Round Wire Model .....	184
11.1.3. Dual Projectile Model Validation .....	185
11.2. Study of Projectile Yaw .....	186
11.3. Study of Projectile Rifling .....	186
11.4. Study of the Effects of Re-using a Projectile .....	186
11.5. Projectile Deformation .....	187
11.6. Conclusions .....	189
11.7. Figures .....	191

<b>12. Conclusion and Further Work .....</b>	<b>209</b>
12.1. Conclusions .....	209
12.2. Further Work .....	212
<b>13. References .....</b>	<b>214</b>
<b>A. Calculation of Complete Elliptic Integrals .....</b>	<b>224</b>
A.1. References .....	225
<b>B. Material Characteristics.....</b>	<b>226</b>
B.1. Copper .....	226
B.2. Aluminium .....	226
B.3. Tungsten .....	227
B.4. Titanium .....	227
B.5. Figures .....	227
B.6. References .....	231
<b>C. Launcher Dimensional Data .....</b>	<b>232</b>
C.1. Figure.....	234



---

## LIST OF PRINCIPAL SYMBOLS

---

$\mu$	Permeability	H/m
$\pi$	Pi	
$\phi$	Temperature	°C
$\zeta$	Electrical Conductivity	1/ $\Omega$ m
$\rho$	Resistivity	$\Omega$ m
$\lambda$	Flux linkage	Wb
$\tau$	Shear stress	
$\gamma$	Shear strain	
$\nu$	Poisson's ratio	
$\mu_0$	Permeability of air	H/m
$\sigma_0$	Density of air	kg/m <sup>3</sup>
$\nu_0$	Viscosity of air	kg/ms
<b>A</b>	Magnetic vector potential	
<b>A</b>	Area	m <sup>2</sup>
<b>a</b>	Acceleration	m/s <sup>2</sup>
<b>B</b>	Magnetic flux density	T
<b>c</b>	Specific heat capacity	J/Kkg
<b>C<sub>m</sub><sup>b</sup></b>	Branch / mesh transformation tensor	
<b>C<sub>m</sub><sup>.b</sup></b>	Mesh / branch transformation tensor	
<b>d</b>	Drag coefficient	
<b>D</b>	Flux density	A/m <sup>3</sup>
<b>D<sub>bb</sub></b>	Incremental branch inductance matrix	H/s
<b>D<sub>mm</sub></b>	Incremental mesh inductance matrix	H/s
<b>E</b>	Modulus of elasticity	
<b>e</b>	Back EMF	V
<b>E</b>	EMF vector	V
<b>E<sub>b</sub></b>	Branch EMF vector	V

$f$	Force	N
$G$	Shear modulus of elasticity	
$h$	Time step size	s
$H$	Magnetic field strength vector	A/m
$i$	Current	A
$I$	Current vector	A
$\mathbf{I}^b$	Branch current vector	A
$\mathbf{I}^m$	Mesh current vector	A
$J$	Current density	A/m <sup>3</sup>
$\mathbf{K}_{bb}$	Branch stiffness matrix	Ns/m
$\mathbf{L}_{bb}$	Branch inductance matrix	H
$\mathbf{L}_{mm}$	Mesh inductance matrix	H
$L_n$	Self inductance of element n	H
$m$	Mass	kg
$M_{mn}$	Mutual inductance between element m and n	H
$r$	Distance in the radial direction	m
$R$	Resistance	$\Omega$
$\mathbf{R}_{bb}$	Branch resistance matrix	$\Omega$
$Re$	Reynolds number	
$\mathbf{R}_{mm}$	Mesh resistance matrix	$\Omega$
$t$	time	s
$u$	Velocity	m/s
$v$	Voltage	V
$\mathbf{V}_b$	Branch voltage vector	V
$\mathbf{V}_m$	Mesh voltage vector	V
$W_e$	Electrical energy	J
$W_f$	Magnetic stored energy	J
$W_m$	Mechanical energy	J
$x$	Thickness in radial direction	m

$Z$	Impedance matrix	$\Omega$
$z$	Distance in the axial direction	$m$
$Z_{mm}$	Mesh impedance matrix	$\Omega$

All symbols are as above unless they are defined locally. Additional symbols are defined as they appear.

# 1. INTRODUCTION

Although conventional guns, missiles, and rockets have been in use for hundreds of years, they have been continually developed, modified and improved. The development of the conventional gun is now nearing its optimum. In a conventional chemical gun, the muzzle velocity is limited to the speed of sound in the driving gas behind the projectile. Missiles and rockets do not suffer from this limitation, but their payloads are usually around only 1% of their total ground weight. In addition, any chemically propelled projectile requires the movement and storage of hazardous and explosive chemicals. Electromagnetic launchers have the potential to increase the muzzle velocity and range, while removing the need for hazardous chemicals. With a theoretical velocity limit of the speed of light, the use of electromagnetic launchers opens a whole new range of possibilities.

However, the use of current electromagnetic launchers is severely limited by their low energy transfer efficiencies and large pulse power supply requirements. Although electrical energy is easily generated, it is much more difficult to generate the very high energies in the short pulsed bursts required by electromagnetic launchers. There are many different types of electromagnetic launchers, but this thesis considers a little studied type known as flat induction launcher or pancake coil launcher.

To enable a wide range of theoretical studies to be undertaken, without the time and expense of practical experimentation, several computer models were used. Possible launcher arrangements were studied using both finite element and filamentary models. Since the topological nature of the launchers lends itself to a filamentary / circuit analysis approach, a dedicated filamentary modelling package was developed. By dividing the conducting regions into small filaments, it was possible to use classic circuit analysis methods, with the developments by Kron, Happ and others, to formulate an electrical equivalent circuit model.

During the development of the filamentary models, several numerical techniques were employed. These fall into two areas, the solution of differential equations and that of

large sets of simultaneous equations. Both single-step and multi-step techniques were used to solve the differential equations. While the multi-step methods were fast, they required knowledge of the previous time steps. A single-step method was therefore used to generate the required data history, before the program switched to using a multi-step method. While several Gaussian methods for solving simultaneous equations were implemented, the triangular decomposition method was proven to be the most efficient. To reduce the amount of computer storage that was required by the filamentary model, two sparse matrix techniques were adopted.

Analysing the utilisation of computer time led to a significant reduction in the time taken. In addition, the filamentary model was reformulated several times in an attempt to reduce further the solution time. The model contained both electrical and mechanical components of the system in an integrated manner, and allowed the speed of the launched projectiles to be accurately predicted. Also developed was a structural model of the projectile, which could be used to predict its deformation. In addition, a flexible method of modelling the power supply components was developed, to allow a variety of power supply arrangements to be studied.

Optimum launcher arrangements were studied using the filamentary model. From these, it was shown that there was an optimum supply voltage for a given projectile mass. The effects of several parameters on the optimum launcher conditions were studied, including the projectile mass, relative projectile size, number of drive coil turns, supply voltage, inter-turn insulation, drive coil thickness and initial projectile displacement. In addition, several novel launcher structures were investigated, including two-layer drive coils and dual projectile launchers.

The results from a series of practical experiments clearly validated the modelled results. From the practical work a new method of determining projectile yaw was developed. In addition, the effects of projectile deformation were investigated.

## **2. ELECTROMAGNETIC LAUNCHERS**

*This chapter provides a historical overview of the main areas and subjects involved in electromagnetic launchers. Although launcher developments have been presented in many different journals, much of the development work, especially that in the US, has been presented at eight international symposia over the last 19 years. This chapter reviews the work presented at these symposia, together with other published work.*

### **2.1. INTRODUCTION TO ELECTROMAGNETIC LAUNCHERS**

The area of electromagnetic launchers covers a wide range of very different machines, but they all attempt to accelerate projectiles to very high velocities by using electrical energy. As the name implies, the projectile is accelerated by the interaction between magnetic fields and current carrying conductors.

Possible forms of electromagnetic launchers were conceived some time ago, but only in the last twenty years or so, have they been the focus of a major research effort. As related technologies advanced, the development of more useful and practical launchers with many different applications has become possible. Most of the research has been directed towards military applications, such as a replacement for the conventional artillery gun. However, other possible uses include the acceleration of hydrogen fuel pellets for fusion reactors, launching unmanned spacecraft, surface treatments by accelerated plasma pulses, magnetic levitation trains, pile drivers and many others.

Many different types and groups of launchers have been developed. Unfortunately, due to the rapid development of launcher technology, there is some confusion over their description and naming. This means that many launcher names have evolved along with the research, which has led to different terminology being used by different authors for very similar devices. The two most distinctly different types are railguns and coilguns. However, hybrid launchers have been invented which blur even this distinction. This distinction between the various types of coilgun is even more vague,

with some terms being used almost interchangeably. The launchers investigated in this thesis are all the pancake or flat coil type and will be generally called “launchers”.

## **2.2. EARLY HISTORY**

Linear electric motors have existed for almost as long as their rotary counterparts. The first such motor was a reluctance machine built by Charles Wheatstone in 1845. In 1889, Tesla and Ferraris published a description of a method of generating polyphase currents, and Tesla exhibited a crude type of three-phase induction motor at the Frankfurt Exhibition in 1891. This was soon followed by a patent for the first linear induction motor, submitted by the Mayor of Pittsburgh in 1895. A patent was granted to Jacquard, Weaver & Electric Shuttle Company in 1895 for a linear motor designed to propel a weaving shuttle at 50 ft/sec. In 1914, Bachelet demonstrated a true flying shuttle, which was both propelled and levitated electromagnetically. Although there was no lack of innovation in textile applications, the relatively high cost of the electrical apparatus required prevented its wide-spread use.

The first electromagnetic launcher was the Birkeland Cannon of 1918 [1]. This was a reluctance type machine with a tubular construction and a row of DC coils energised in sequence. In 1920, Fauchon Villeplée published a book on the subject of electromagnetic launchers, called “Cannons Electrique”. Many attempts at developing useful linear motors and launchers soon followed, and by the Second World War 45 patents had been issued [2]. After the war (1946) Westinghouse built a full size aircraft launcher called the “Electropult”, which was fundamentally an induction motor with a moving primary.

## **2.3. RECENT ELECTROMAGNETIC LAUNCHER HISTORY**

Although much research had been done, it had been performed in an individual and disjointed manner. The possible development of an electromagnetic launcher was producing some interest in the 1970s, because of independent developments in support technologies, such as high energy density storage devices and improvements

in high current moving contacts. In 1978, the US Department of Defence set-up an advisory panel to focus the efforts of researchers. At a workshop held at the US Naval Academy in December 1978, sixty scientists and engineers discussed recent developments in the supporting technologies. From this workshop, it was evident that there were many practical possibilities for electromagnetic launcher technology.

A US Department of Defence working group proposed the following list of six possible experiments [2].

- Railgun to launch 0.3 kg mass up to 3km/s using a 15MJ homopolar generator.
- Design and construction of a small (26in diameter, 11in height) 5MJ 1100kg homopolar generator.
- Gram size railgun with 10km/s launch speed using an explosive flux compressor supply.
- Railgun with a metal penetrator projectile.
- Design and testing of high efficiency (> 50%) accelerator concepts.
- Construction of a plasma pinch accelerator.

This research effectively formed a new technical community with the aim of developing electromagnetic launchers for a wide variety of uses.

In 1980, a symposium was held at San Diego to present the results of the initial experiments and to focus future research efforts [3]. The increase in interest from the US military had, directly and indirectly, helped to initiate many projects throughout the world. It was clear from the outset that there were many different types of launchers, supplies and other support devices to be studied. However, most of the initial research work was directed at the development of the railgun type launchers, as these were relatively simple and could be scaled up to launch useful sized projectiles. A second symposium was held at Boston in 1983 [4], at which it was decided that successive symposia would be held biannually. In 1983 the president of the USA (Ronald Reagan) announced the launch of the Star Wars project. This allowed the electromagnetic launcher area to be widened, to provide both tactical and strategic weapons. Electromagnetic launchers able to launch guidable exo-atmospheric



projectiles with very high velocities (10 to 20 km/s) were now required [5], and this led to the need for larger power supplies. To further the development of a tactical weapon, there was also a need to develop a small mobile launcher, capable of launching a projectile with 15MJ of kinetic energy.

With disarmament talks between the US and Russia in the late 1980s, and the ever increasing costs of the Star Wars projects, the need for such weapons was being questioned. As the recently expanded US development program started to feel the effects of peace, by means of funding constraints, the research programs in other countries such as the UK, Japan, Netherlands, Germany and France were just starting. Many of these new programs presented their results from initial project proposals and feasibility studies at the fourth symposium in 1988 [6]. Over the next few years research continued at a steady pace, but by the end of the Cold War further reductions in military funding were looking increasingly inevitable.

By the fifth symposium, the change in direction of the studies into electromagnetic launchers was becoming apparent [7], with a shift in emphasis from large scale demonstration launchers to programs focused on gaining a greater understanding of concepts and technologies. As the military funding was withdrawn or reduced, the focus of the research moved towards less military applications. Research into alternative uses, such as the acceleration of hydrogen fuel pellets to re-supply fusion reactors and the treatment of surfaces using accelerated plasma pulses, gave rise to an increasing source of funds. The US Army however, was still very keen to develop the idea of a “wholly electric ground combat vehicle” [8].

The philosophy of the UK was to concentrate on the development and demonstration of the potential of electromagnetic gun technology, before producing a compact power supply. The development of an electrothermal gun in the UK initially started in the early 1980s as a small scale pilot study [9], but by the early 1990s the level of funding had increased. The main aim of the initial research was to develop an understanding of the subject. With research spread across several locations and organisations, DERA (Defence Evaluation and Research Agency), Royal Ordnance, and

Universities, the work was not directed towards one particular gun system, and many different methods were investigated [10]. Recent work in the UK has concentrated on the development of electromagnetic launchers for use as the main armament on a future battle tank [11], and this has centred on the development of 90mm and 40mm railgun launchers. Two main facilities were constructed, the first at Kirkcudbright in south Scotland [12], and the second at Fort Halstead in Kent. The Kirkcudbright site was developed to carry out all the free-flight testing, whereas the Fort Halstead site uses sand butts to stop projectiles, and focuses its attention on materials testing. Firings at the 2000m range at the Kirkcudbright facility have allowed the unexpected benefit of the recovery of intact armatures from high energy tests.

## 2.4. RAILGUNS

The railgun is the simplest of the electromagnetic launchers initially studied. In its basic form it comprises two conducting rails mounted in parallel, with the projectile forming a circuit between them, as shown in Figure 2.1. When a supply is discharged into the railgun, current flows out along one rail, through the armature of the projectile and returns through the other rail. The projectile is driven by the Lorentz force generated by the interaction of the current flowing in the projectile with the magnetic fields generated by the currents flowing in the two rails. The initial work on railguns was undertaken at the Australian National University, where they had the world's largest homopolar generator, and unique experience in high current moving contacts. They were able to build successfully and to demonstrate a railgun to accelerate a 3gm projectile to 5.9km/s [2].

Due to their simple arrangement, railguns became the main focus of attention for electromagnetic launcher development. In early experiments, it was shown that the solid armatures could be replaced by plasma armatures [13]. Unfortunately, plasma armatures are much more complex and difficult to model. The Westinghouse Research and Development Centre produced a 2D steady-state model, to predict the current and magnetic field distributions in a railgun [14]. A distributed energy store railgun was proposed by the Centre of Electromechanics at The University of Texas at

Austin (CEMUT). This used multiple power supplies to feed a single pair of launcher rails, and it was hoped that the multiple supply would effectively maintain the maximum current flow through the projectile armature for longer periods. It was concluded from simulations that a significant improvement in the overall performance of the railgun could be achieved [15].

The great interest in railguns can be seen in the increase in the number of papers presented at the second symposium [4]. These typically describe the use of different computer models, and the installation of test railgun launchers. The interest was widening, and included studies on structural and electromagnetic modelling, rail erosion and armature design. New areas were opened up with the development of several different launchers, such as the augmented railgun, shown in Figure 2.2. It was suggested by Rockwell International [16], that the use of augmenting rails would increase the magnetic field, which would generate an increased force on the projectile without increasing the rail / armature current. The conclusion was that the use of augmenting rails did produce an increased force for the same maximum current. However, it was also found that the increases in heating losses and system inductance reduced the overall efficiency of the launcher. With the increasing realisations of the limit of railguns, different types of hybrid launchers were proposed, which included chemical pre-launchers [17] and plasma injectors [18].

With an increase in the available supply energy, the forces and currents developed in railgun launchers became increasingly important. One of the main areas of interest was the erosion of the railgun rails and contacts, since with the increase in power the copper rails that were widely used were being so badly damaged by a single shot that they had to be replaced. In addition, the forces generated during a launch acted to blow the rails apart. Although there were no reports of railguns exploding, the structures required to hold them together were becoming increasingly complex. These two problems led to a study into how many different materials reacted under extreme conditions. To tackle the problem of rail erosion, a chemical vapour deposition coating was developed by a partnership between Ultramet and CEMUT [19].

By the fourth symposium, improvements in armature design and understanding had lead to an increase in performance by a factor of two [6]. In addition, the developments achieved in railgun launchers were generating other possible uses for electromagnetic launcher technology, such as earth to space satellite launchers [20] and the possible generation of power from impact fusion reactors [21]. Modelling work at CEMUT investigated the use of multiple rail railguns; as shown in Figure 2.3, these were not augmented railguns, but instead had additional rails to reduce the rail current and hence the current per contact. Unfortunately, simulations showed a 40% reduction in the force on the projectile when the number of rails was increased from two to four [22]. In contrast, later work appeared to show an improvement in the performance of a four rail launcher over a two rail launcher [23]. Several papers presented at the fourth symposium described the construction and testing of high powered demonstration railgun launchers, while a number of studies outlined work on the study of armatures, plasmas and rail erosion. Others described the development of novel railgun launcher adaptations, such as the development of an exploding foil pre-launch injector [24]. Two papers published by the Los Alamos National Laboratory showed that there were significant problems with plasma armatures, one of which was plasma restrike [25]. This is an effect in which a secondary arc is formed some way behind the main plasma armature, which dissipates energy without providing any useful work. To prevent plasma restrike, the team at Los Alamos segmented one of the rails and connected it to the supply via individual fuses. These isolated each section of the launcher after the projectile had passed through it, thereby increasing the armature front velocity by 30% [26].

The direction of research began to change by the fifth symposium [7], and the construction of even bigger power supplies and higher energy launchers was replaced by more detailed studies of the complex interrelated systems that make up an electromagnetic launcher. There was a continued effort to study different railguns and their associated systems, and an increase in the number of papers describing different armature / plasma monitoring techniques. As the available computing power increased, so to did the complexity of the models used, with the introduction of 3D

modelling programs such as 3D MEGA developed at Bath University [27]. The replacement of experiments by accurate models was becoming increasingly feasible.

Railguns continued to dominate other launcher types at the sixth symposium held in 1992 [28]. As many railguns had been built and tested, work on their application became more prevalent. Launcher packages including sabots and other projectile components were studied. In addition, there was an increase in the number of projects studying hybrid launchers. The majority of these used a conventional gun to launch the projectile, before it was further accelerated by the railgun section. In addition, a novel multiphase railgun design was proposed by CEMUT [29].

With the increasing cost of experimental work and the falling cost of computing power, computer models were becoming increasingly relied on. By the eighth symposium, the use of 3D models to model railguns was becoming wide-spread [30]. Most notably, several papers compared different computer models, in an attempt to unify the development of future models [31], [32], [33]. Many others described studies into the effects of rail erosion, but due to the shape of railguns this could not easily be measured or investigated. In a paper by IAP Research Inc., the building and testing of a rail erosion test rig was described [34]. This used the edge of a rotating disc to mimic the surface of railgun rails, and made it possible to study the effects of both single and repetitive firings.

## **2.5. COILGUN LAUNCHERS**

The efficiency of electromagnetic launchers can be of great importance. If a launcher is too inefficient, it will require a much larger power supply, which limits its usefulness and can increase its cost. Although coilgun launchers are theoretically much more efficient than railguns, they are also more complex. Due to this additional complexity most of the early research work was concentrated on railguns, however many research projects have studied coilgun launchers over the last twenty years. Coilgun launchers cover a wide diversity of arrangements, but they can be split into the two main types: synchronous and induction. Induction launchers can be split into

two further sub-types, travelling wave, and pulse segmented coil launchers. Both produce a travelling wave, with the distinction lying in the manner the travelling wave is produced.

### 2.5.1. SYNCHRONOUS INDUCTION LAUNCHERS

A synchronous launcher works in a very similar manner to a conventional synchronous machine. The armature current is usually maintained by either connecting rails or by a flyaway lead, although some launchers have used superconducting armatures with an impressed current. The travelling magnetic wave in the stator can be generated in many ways, as in an induction launcher, but it is synchronised to the location of the armature.

An arc commutated launcher was proposed by the Massachusetts Institute of Technology (MIT) [35]. The projectile formed part of the stator circuit by means of arc contacts on the projectile, and the stator coils were hence automatically synchronised to the projectile. Several arrangements were suggested but no overall conclusions were drawn. Also developed at MIT was a helical rail launcher [36]. By using two brushes to connect the outer armature circuit to the helical stator coil, correct synchronisation between the armature and stator coils was assured. A hybrid launcher, proposed by Case Western Reserve University [37], had an armature fed by rails but a stator made from separate coils energised in sequence, in a manner similar to that of a pulsed induction launcher.

At the second symposium, Electromagnetic Launch Research Inc. Cambridge MA presented their work on tubular multistage synchronous accelerators [38]. They proposed a helical brush commutated launcher, in which the inside of a helical drive coil was exposed, to allow contact with brushes on the armature. This provided a simple means of synchronising the fields of the drive and projectile coils, and from the analysis of the various inductively coupled systems they concluded that efficiencies of greater than 50% would be possible.

Researchers at the Polytechnic University Brooklyn (PUB) suggested that, with the correct launcher section parameters, it would be possible to produce an inductive commutated launcher [39]. An extension to the brush commutated launcher was proposed by researchers at the Jet Propulsion Laboratories (JPL) [40]. By producing the rising and falling of barrel currents by external voltages, it was suggested that higher magnetic fields could be generated for a given armature current. The work at Electromagnetic Launch Research Inc. continued with the publication of a set of design criteria for brush commutated launchers [41].

In a system suggested by Nalty and Driga of CEMUT, an induction launcher was supplied by a super-synchronous induction generator, with the launcher acting as a synchronous motor [42]. They proposed either to impress a current in the projectile before injecting it into the launcher, or to use sliding contacts to feed the required current into the projectile. An initial feasibility study was undertaken which did not model the transient operation of the launcher, and relied heavily on phasor analysis. Further work suggested included the development of a transient filamentary model of the launcher and a winding method that would produce well balanced bearing loads in the generator.

A theoretical study of inductively commutated launchers was undertaken at CEMUT. The development of a model and results of initial simulation work were presented at the sixth symposium [43]. In a second paper, they described the development of another launcher, in which the stator coils are “charged” in series [44], by the discharge of a capacitor bank. At maximum current the individual flywheel thyristors of each stator coil are fired simultaneously, and the stator current flows around each of the individual stator flywheel circuits. This effectively trapped the current in the individual stator coils. The armature supply was then fired, with the armature connected to the supply by flyaway leads.

### 2.5.2. TRAVELLING WAVE INDUCTION LAUNCHERS

A travelling wave induction launcher is a special form of linear induction motor, in which the magnetic field travels along the motor instead of rotating in it, as in a rotary machine. Like their rotary counterparts, travelling wave launchers are inherently constant speed machines. In some applications, such as magnetically levitated trains, this can be an advantage, but it poses problems when designing an electromagnetic launcher. However, a polyphase induction machine can be used as a launcher, if the effective supply frequency is increased as the projectile accelerates. The required change in effective frequency can be achieved either by using a controlled variable frequency supply or by varying the pole pitch of the stator. The stator pole pitch can be varied in two ways, either by graded slotting or by graded winding. Graded slotting allows conventional winding techniques to be used, but the slotting is more complex, as shown in Figure 2.4. A graded winding uses evenly spaced slots, with each coil split into groups so that a coil may occupy portions of several slots, as shown in Figure 2.5. Although the graded slotting method is simpler to construct and easy to analyse, it is not necessarily cheaper.

The possibility of developing a travelling wave induction launcher was presented as far back as 1971 [45], and again in 1984 [46]. However the difficulty in producing a variable frequency supply of the type needed by a travelling wave induction launcher, led to very few research projects focusing on this particular type of launcher. With the invention of a rising frequency generator at CEMUT, it was hoped that a practical polyphase induction launcher would be possible. CEMUT described several possible structures at the third symposium [47]. A paper at the same symposium by Williamson and Leonard described the development and validation of a filamentary model of a travelling wave induction launcher [48]. The test launcher built for the model validation was supplied by a 3 phase 50Hz supply, but no details of the coil connections were given. It was later proposed by CEMUT that a distributed energy store could be used to supply a travelling wave induction launcher, by splitting the launcher into several different sections and supplying each of these from a separate rising frequency generator [49]. A paper presented by JPL at the fourth symposium,



described the analysis of a travelling wave induction launcher [50]. Whilst showing that a travelling wave launcher is feasible and efficient, it also pointed to the lack of any efficient supply to provide the required power for such a launcher.

In a method developed at PUB, a series of capacitors were discharged in sequence to generate a transient three-phase supply [51]. This allowed the frequency of the power supply to be controlled by altering the discharge timing of the capacitors. With a segmented launcher, the effective frequency could be raised, by supplying the sequential sections at increasing frequencies. To model the launcher, they produced a lumped parameter model of the system [52]. This was developed in several papers at the fifth symposium, which described a current sheet model and its comparison with experimental work [53], [54], [55]. CEMUT presented a parametric study at the fifth symposium, using a filamentary model [56], and in a later paper they suggested that although a travelling wave induction launcher could launch fast, small projectiles, it would be better suited to launching larger and slower projectiles, such as artillery shells [57].

The model validation of a capacitor driven travelling wave induction launcher was presented jointly by Seoul National University and Kangwon National University, both from Korea [58]. A study of the in-bore dynamics of tubular induction launchers was undertaken at PUB. From their analysis, the authors predicted that if the gap between the stator and armature was too large, the projectile might touch the barrel wall. However, if this gap was reduced, no signs of contact were evident [59], [60]. Also studied at PUB was the effect of the transition between launcher sections. They concluded that, although the time of firing of each section effected a launch, the launcher was relative insensitive to this and the launcher sections operated relatively independently [61].

In an expansion to the initial single-stage launcher developed in Korea, a sequential design method led to the development of a three stage launcher [62]. Using a capacitor supply system, researchers at PUB launched a 137g projectile at a velocity of 476m/s with a 60cm barrel [63]. It was also predicted that 2km/s could be achieved

with an eight section launcher. A generator driven supply was also developed and modelled, and it was concluded that, although this would be more complex to control, it would be less bulky and heavy, especially as the power requirements of the launchers increased.

### 2.5.3. PULSED INDUCTION LAUNCHERS

Pulsed induction launchers are similar to the travelling wave induction launchers described in the previous section, with the main difference being the way in which the required travelling magnetic wave is generated. Pulsed launchers use a row of individually energised coils, with each coil fed by an individual supply or all the coils switched from a single supply. The coils are energised in sequence to provide the travelling wave, and they are often triggered by a projectile position sensing system. Figure 2.6 shows a typical five-stage pulsed induction launcher with individual supplies.

One of the first pulsed induction launchers was a superconductively levitated train called “Magneplane”, initially conceived at the Brookhaven National Laboratory but successfully demonstrated at MIT [2]. By the first symposium, a coaxial launcher was under construction at MIT to demonstrate the possibility of a lunar launcher [2]. Sandia National Laboratories presented their initial work on the theta gun (a pulsed induction launcher), including a finite difference model and some low power validation [64]. It was clear from very early work that the synchronisation of the projectile position and the firing of the corresponding stator coils would be difficult. A research team from Princeton University produced an experimental launcher and an energy transfer model, and using a superconducting projectile developed at MIT and a nominal design acceleration of  $5000\text{m/s}^2$  they hoped to achieve a final velocity of  $112\text{m/s}$ . Most notably, they also proposed a system to slow the projectile, using an identical launcher in reverse to recharge the capacitor supply [65].

At the second symposium, Sandia National Laboratories presented their study of multistage induction launchers, which included a magnetohydrodynamic model [66].

By the second symposium, the construction of a multistage demonstration induction launcher at MIT was almost complete, and results from successful early experiments of both single and dual stage launchers were presented [67]. From initial low voltage single-stage tests, speeds of 150m/s were achieved. However, from calculations they predicted that, at full voltage, projectiles would be able to achieve a speed of 325m/s.

In a paper presented at the third symposium, plans for a 'Reconnection Gun' were discussed [68]. This was a pulsed induction launcher, but instead of the stator coils being wound around a central tube each stator segment had two rectangular coils, spaced by a small gap, through which a flat plate projectile was accelerated edge on. This unique arrangement was investigated experimentally with B dot and Rogowski search coils due to the complexity of the system. It was hoped that this unusual launcher would produce a greater axial force than a comparable tubular launcher.

A design study of linear induction launchers was undertaken at CEMUT [69]. They use an iterative parametric approach to optimise the launcher design over a limited parameter space. The optimiser used a filamentary model to filter the possible solutions. However, this led to long run times, even when using a CRAY XMP-24 computer. By using standard linear optimisation techniques, an optimum design was produced, which showed that the best results were obtained when the drive coil and projectile were approximately the same length and the gap between the two coils was minimised. Also, but not so obvious, the optimisation also suggested that the projectile and drive coils should have a long thin shape.

The development of the reconnection launcher at Sandia National Laboratories was outlined at the fifth symposium [70]. The development of a 14 stage flat projectile launcher was described, together with the ensuing development of 6 and 10 stage tubular launchers [71]. The development of a filamentary model, and its comparison to test results, were also presented, [72]. A 10g projectile was successfully launched by the 10 staged launcher, with a final velocity of 317m/s and an energy transfer efficiency of 9%. This low efficiency was achieved during a low energy test, and

similar low energy tests were used to provide model validation and component testing data.

To reduce the concentration of current in the outside rear edge of the projectile, a wound projectile was developed at CEMUT [73]. Using a combination of filamentary and finite elements models, a projectile was successfully developed. Simulations established that multi-turn armatures have significant advantages over solid single turn projectiles, with an increase in efficiency from 15% to over 40%. The use of a reluctance accelerator was also proposed [74], but although this has the advantages of no projectile coil it is significantly more complex to study. In addition, it can only pull the projectile whereas other launchers can provide both push and pull, by choosing the relative polarity of the stator and armature windings.

Using the knowledge gained from constructing several different types of launcher, CEMUT suggested that a near optimum design could be achieved by balancing the different practical limitations of a pulsed induction launcher [75]. The construction and initial testing of a demonstration launcher, built at the Sandia National Laboratories, was described at the sixth symposium [76]. During a half energy test, it was able to launch a 340g projectile to 406m/s. A study of synchronisation timing errors was undertaken at Cambridge University using a filamentary model [77]. From this study they concluded that the timing errors affected the performance of a launcher, and suggested that a worst case studies could be used as a design tool. A qualitative study of induction launcher operation was undertaken at Sandia National Laboratories, which led to a set of algebraic expressions to determine approximately the performance [78]. Although the expressions were somewhat crude, they were used to gain an initial insight into the size and type of launchers that would be required by different applications. A dynamic and transient finite element model of a pulsed coaxial launcher system developed at Bath University was presented at the sixth symposium [79].

Models were widely used to help in the design of pulsed induction launchers. However, most of the launchers were developed on a trail and error basis, and it was

suggested that general optimisation routines could be applied to electromagnetic launchers. To avoid the problem of local optima, it was further suggested that a global optimisation routine should be used [69]. However, the use of most such routines would require a vast number of trial simulations but, by using a method called "very fast simulated re-annealing", it was hoped that good results would be obtained without too many simulations [80].

The results of an initial model validation carried out at Loughborough University were also presented at the seventh symposium [81]. The test launcher was of a single-stage tubular form, supplied by an ignitron / capacitor supply. Also proposed at the seventh symposium was the use of a "flux concentrator", as used in an experimental launcher at the French-German Research Institute of Saint Louis to improve the mechanical strength of a multi-turn stator coil [82]. In a later paper, the use of flux concentrators was investigated by means of 3D finite element modelling [83]. Although flux concentrators proved to be an attractive way of reducing the stressing in multi-turn stator coils, their efficiency is rather poor. From the investigation, it was concluded that both 2D and 3D models were accurate to within a few percent and suggested that a filamentary model may also be possible.

#### 2.5.4. FLAT COIL LAUNCHERS

Flat coil launchers work on the same principles as tubular induction launchers. They use a disc shaped drive coil and projectile, with the projectile initially placed close to one side of the drive coil, as shown in Figure 2.7. Flat coil launchers are also known as pancake launchers or coilguns, and although they have been around for some years they have only been occasionally studied. It is this type of launcher that forms the topic of this thesis. Although many single segment induction launchers have been considered, most of these have been forerunners to multi-segmented launchers, and have been similar to tubular type launchers, with the projectile inside the stator coil, as shown in Figure 2.8.

One of the first examples of a flat coil launcher was the "jumping ring" experiment [84]. Although the aim was to produce levitation by using an AC excited stator coil,

and not to launch the ring, it nevertheless provided a simple demonstration of the principles of electromagnetism. However, the transient nature of this simple experiment made it extremely difficult to analyse. The first use of a flat coil launcher was in a study of the effects of shock on different materials [85]. The launcher was mounted face down in a box of sawdust, with the projectile held against the drive coil by a light vacuum. The launcher coil was connected to a 120 $\mu$ F 20kV capacitor discharge supply, which was switched and crowbarred by two ignitrons. By varying the capacitor voltage, the magnitude of the impulse force applied to the sample was controlled, and the resulting acceleration was measured using an accelerometer. One of the first studies into flat coil launchers was carried out by Bondaletov and Goncharenko in 1971 [86], and a validated set of approximate relations for the velocity of their projectiles was proposed. Velocities of more than 1km/s were obtained experimentally for 10g projectiles, with an overall electrostatic to kinetic energy efficiency of 43%. An alternative use of a flat coil launcher was proposed by Schmidt Harms in 1985 [87], who developed a high-speed linear actuator to draw a clean arc between two contacts, which could be used as a source for spectroscopic analysis equipment. A connecting rod passed through the drive coil to the centre of the projectile as shown in Figure 2.9. With two electrodes connected to the rod, a current was passed through the isolated part of the rod. When the launcher was fired, the rod moved between the electrodes, producing a gap across which an arc was drawn, as shown in Figure 2.10.

A flat coil launcher was developed at the Astronautical Institute of the Technical University Munich [88]. By varying the initial voltage of the supply capacitor, they demonstrated that the final velocity of the projectile could be controlled to within 1%. They also showed that a solid projectile curled up and away from the launcher if sufficient energy was provided. Further developments of this launcher were presented at the third symposium in 1986 [89], where the launching of both solid and ring shaped “driver plates” (projectiles) were described from a launcher developed for the calibration of space experiments. The driver plate was launched with the test material placed on it. The driver plate hit a retaining plate, and a hole in the retaining plate

allowing the test material to be projected further downrange. A paper by Thornton and Seddon of British Aerospace reported the development of a single-turn flat coil launcher [90]. By means of break wires and witness plates they were able to show that a velocity of 4km/s was achieved at an efficiency of 39%, for a 0.75g projectile. The results from a parametric study of flat coil launchers were published by Sadedin in 1991 [91]. This determined the effects of projectile mass, initial coil separation, and coil aspect ratios on the variation of the “characteristic resistances”.

### 2.5.5. OTHER NOVEL LAUNCHERS

The plasma pinch accelerator called MAID developed at GT Devices (Virginia) consisted of several plasma rings, which imploded onto a common axis. The projectile was initially launched into the accelerator by conventional means, with the plasma rings fired in sequence so that they pinched the rear end of the projectile, accelerating it as shown in Figure 2.11. Both conical and spherical projectiles were tested successfully [92]. This launcher was developed as an initiator for an impact fusion reactor [93].

## 2.6. POWER SUPPLIES

Whatever the launcher technology, a power supply is inevitably required. Capacitors provide a simple and easy method of delivering the required sharp pulses of electrical energy required in many types of electromagnetic launchers, although their size can be prohibitive. Initially the most widely used supply technology was the homopolar generator, but other supplies such as compulsators, flux compressors, and other even more novel forms have been developed and used in recent years. Nevertheless, the capacitor supply has found many uses, due to its simplicity and flexibility. There have been numerous developments in supply and switch technology over recent years, which have resulted in a new and almost independent field of research. Although the development of supply technology has had an impact on the development of electromagnetic launchers, it is beyond the scope of this thesis to include a detailed

review that would do justice to the depth of this subject, so only a brief overview follows.

### 2.6.1. CAPACITOR DISCHARGE SUPPLIES

Capacitors are one of the oldest methods of electrical energy storage. Since the invention of the Leyden jar in about 1750, they have been developed for many particular applications. Although many different geometries are used for the conducting plates, the main variation between different types is in the dielectric materials that are used. Capacitors are available in voltages up to 100kV, but it is the modular nature of a capacitor supply that makes it very versatile, and a popular choice for pulsed power experiments. A bank of capacitors can be connected in series to provide a very high voltage, in the order of megavolts. However, a bank of similar capacitors could be connected in parallel to provide a supply able to deliver tens of megamps of current at a more moderate voltage.

### 2.6.2. HOMOPOLAR GENERATORS

Homopolar generators are similar to conventionally commutated DC rotating machines, although they are simpler and usually have a much lower impedance. Invented by Michael Faraday as long ago as 1831, they have been developed specifically for pulsed power applications during recent years.

One of the main limiting factors of conventional DC generators is the brush / commutator system, which has to reverse the direction of current in a rotor winding as it passes from one pole to the next. The commutator limits the voltage that can be generated, because of the required tracking distances between adjacent conductors that operate at high voltages and in the presence of ionised air and carbon dust. The homopolar generator is the only DC rotating machine without a commutator. In the simplest form the rotor is a monolithic disc that rotates in an axial magnetic field, with the voltage generated between the shaft and the outer radius of the disc. Although homopolar generators do not have a commutator, they still require high-speed, high current moving contacts, which presents one of the main limiting factors in their



design. Homopolar generators with discharge times longer than around 50 ms usually have a steel rotor surrounded by a ferromagnetic stator to help reduce the magnetic reluctance.

Homopolar generators have found particularly favour with railgun research groups, as they provide good high current / low voltage supplies. However they generate a relatively long output pulse, and to make the homopolar generator more suitable for pulse power applications an intermediate inductive energy store is often used, as shown in Figure 2.12. The homopolar generator charges the inductor via switch 1. When the current reaches its maximum switch 2 is opened, diverting the current to the launcher. The high rate of change of current produced by opening switch 2, causes a high voltage pulse to be applied to the launcher.

### 2.6.3. COMPULSATORS

Compensated pulsed alternators (compulsators) have been used in many experiments, but they are particularly suited to rapid repetitive launchers. In their simplest form, compulsators are single-phase alternators with a low impedance and a high current capability. They combine an inertial energy store with voltage generation and power conditioning in one machine, with the idea for a compulsator being developed from conception to prototype testing at CEMUT during the late 1970s [94]. The first machines included an active compensation system, but in later compulsators this was replaced by a passive form of compensation by attaching a highly conductive shield to the outside surface of the rotor. Housing the armature windings in the stator removed the need for high current moving contacts, and in addition the rotor did not need to be laminated, which enabled much higher operating speeds. To enable the construction of machines able to withstand a very high load torque several new construction techniques had to be developed [95].

### 2.6.4. FLUX COMPRESSORS

Flux compression generators have been used as the power source for many different experiments, but they found particular favour with the researchers conducting the

early railgun experiments. There are two main types of flux compressor, the strip generator and the helical generator. Flux compressors are explosively driven single shot devices, in which a magnetic flux is generated in a space between two conductors. As the explosives are detonated, the two conductors are forced together, working against the flux and converting the magnetic energy stored in the magnetic field into electrical energy. The obvious major disadvantages of flux compressors are the need for explosives and the single shot nature of their operation, but nonetheless they provide a compact high energy pulsed power supply which can be modified to match to requirements of individual experiments.

The typical strip generator shown in Figure 2.13 consists of two parallel copper conductors, one of which has a backing of explosive. A small capacitor bank is connected to the input terminals to provide the initial magnetic flux. As the capacitor discharge current reaches its maximum, the explosives are triggered, shorting the input terminal and trapping the flux within the compressor. The detonation travels down the flux compressor pushing the flux into the load.

The helical type generator usually consists of a tubular conductor (the armature) surrounded by an insulated helical winding (the stator), as shown in Figure 2.14. The explosives are packed into the armature, and they are detonated from the input end in a similar manner to the strip flux compressor. Once the capacitor supply has been triggered, and the magnetic field has reached its maximum, the explosives are detonated and the armature is forced to expand conically, shorting the input terminals and trapping the flux in the compressor. The detonation travels down the explosive, until the entire armature has been expanded and is in contact with the stator. The inductance of a helical flux compressor is much greater than a strip type compressor, and they generally have a higher gain.

#### 2.6.5. MHD GENERATORS

Explosively driven magnetohydrodynamic (MHD) generators use the movement of a conductive plasma in a magnetic field to generate a pulse of electrical energy [135]. MHD

generators have been used in a variety of applications, in both research and commercial environments, but they have only found limited use in electromagnetic launcher experiments. The magnetic field in the generator is usually provided by the discharge of a capacitor bank, in a similar manner to that used in a flux compressor. A tubular block of explosive is used to generate the fast moving plasma. When the explosive is detonated, the tube is sealed at one end, as the detonation travels down the explosive, the air trapped in the centre of the tube is compressed and heated. This compressed air forms a conductive plasma, which is then fired into the generator. The motion of the plasma in the magnetic field induces a voltage that can be used to supply a load.

## 2.7. FIGURES

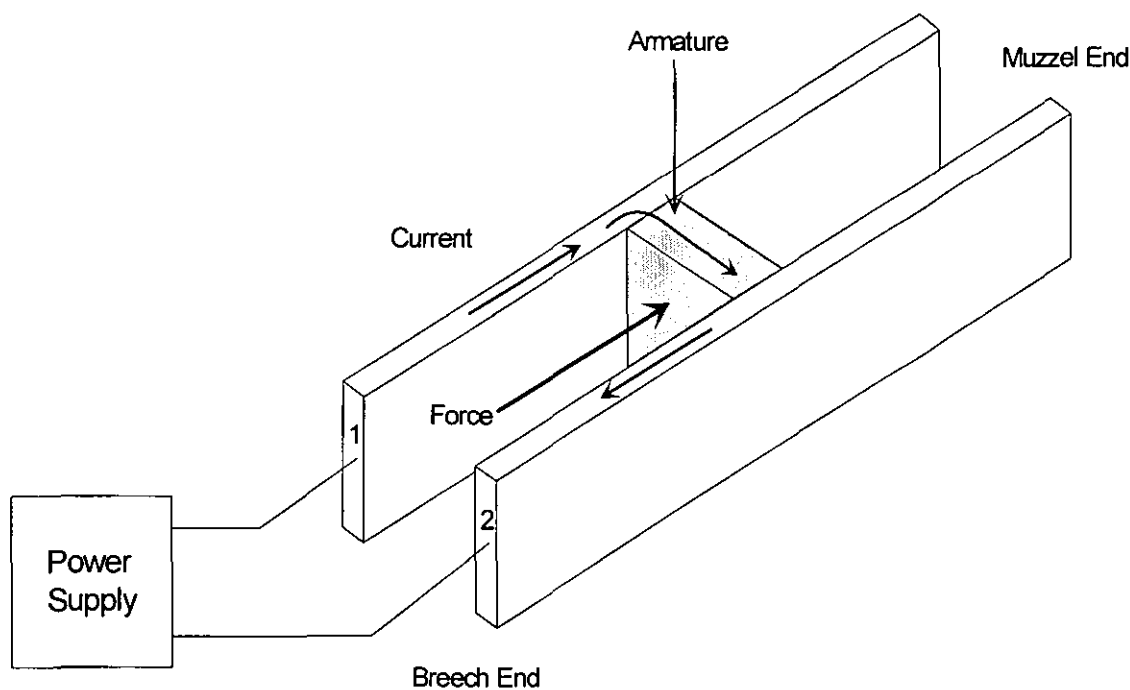


Figure 2.1 Standard railgun

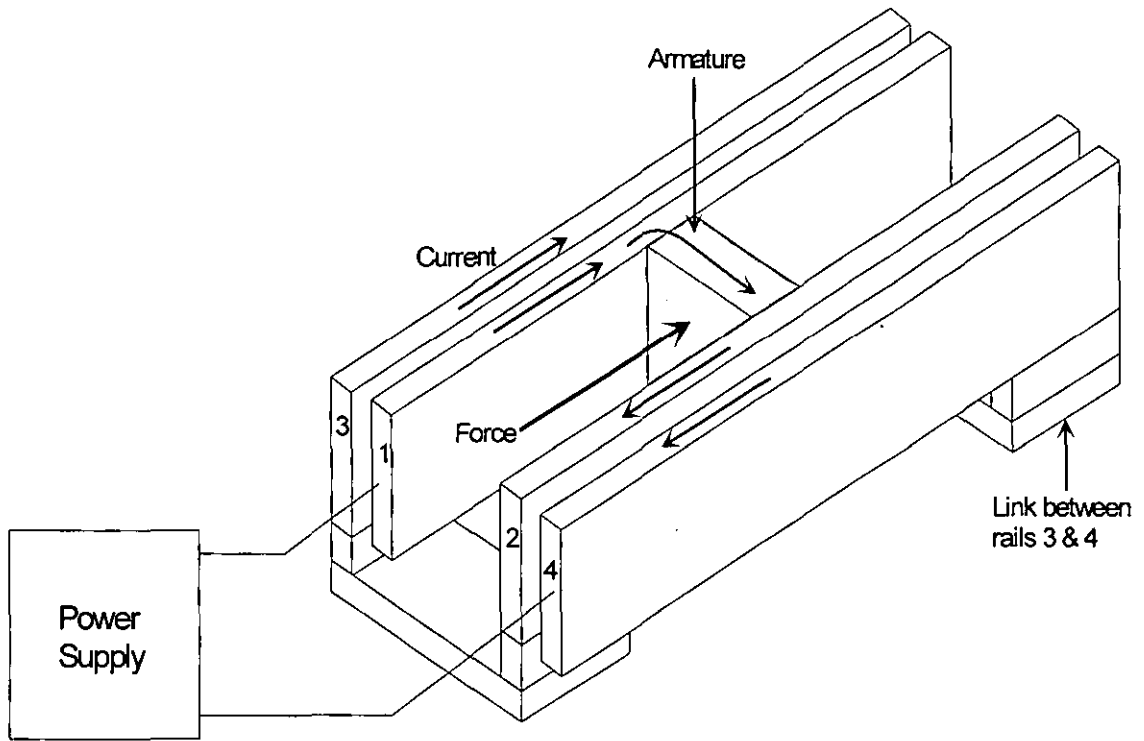


Figure 2.2 Augmented railgun

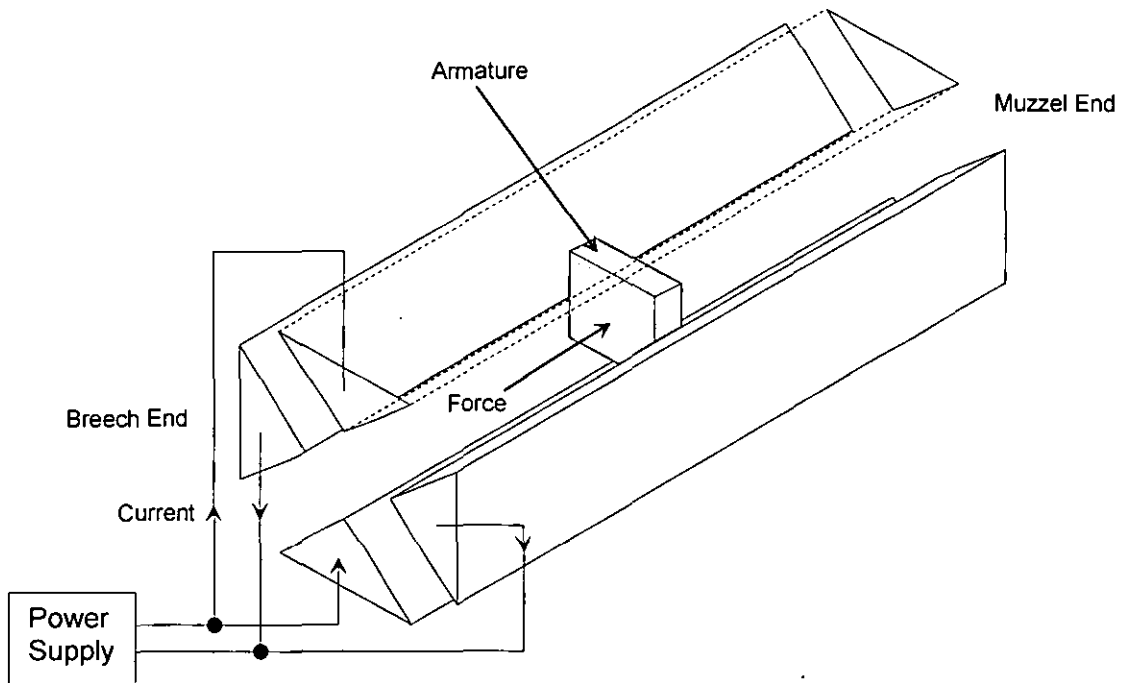


Figure 2.3 Multi-rail railgun

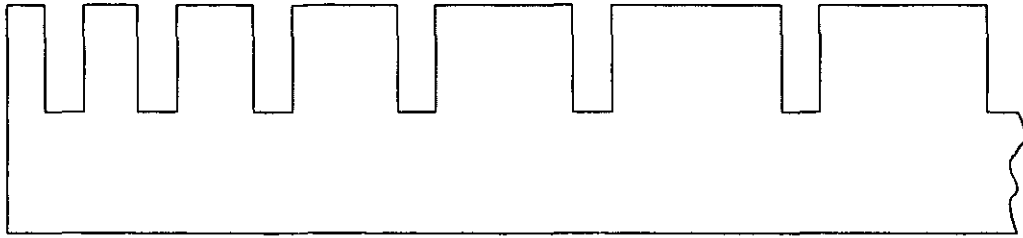


Figure 2.4 Graduated slotting

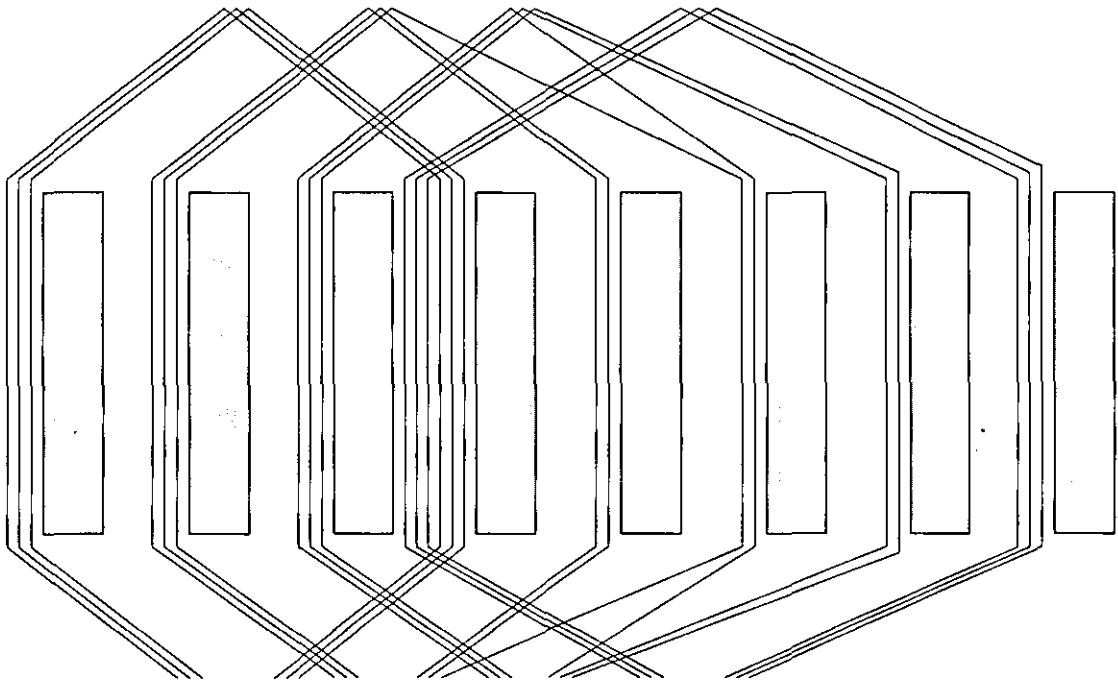


Figure 2.5 Graduated winding

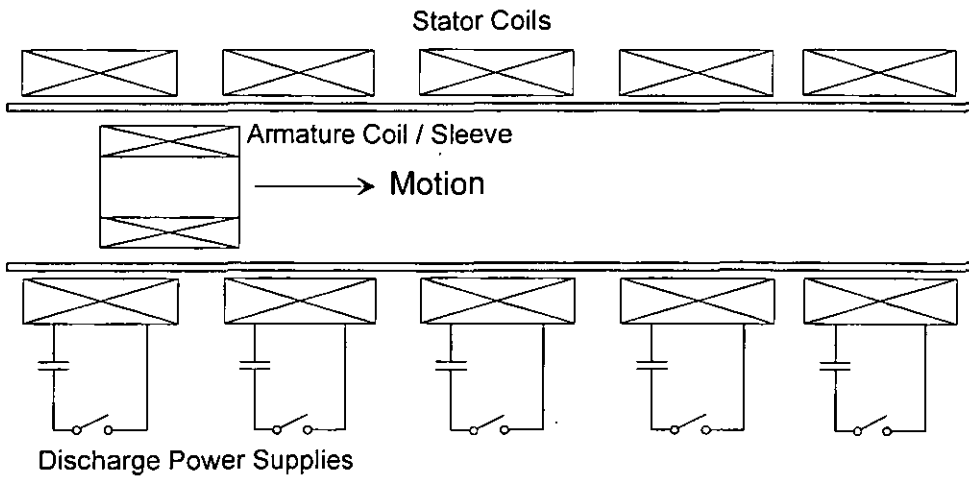


Figure 2.6 Typical five-stage pulsed induction launcher

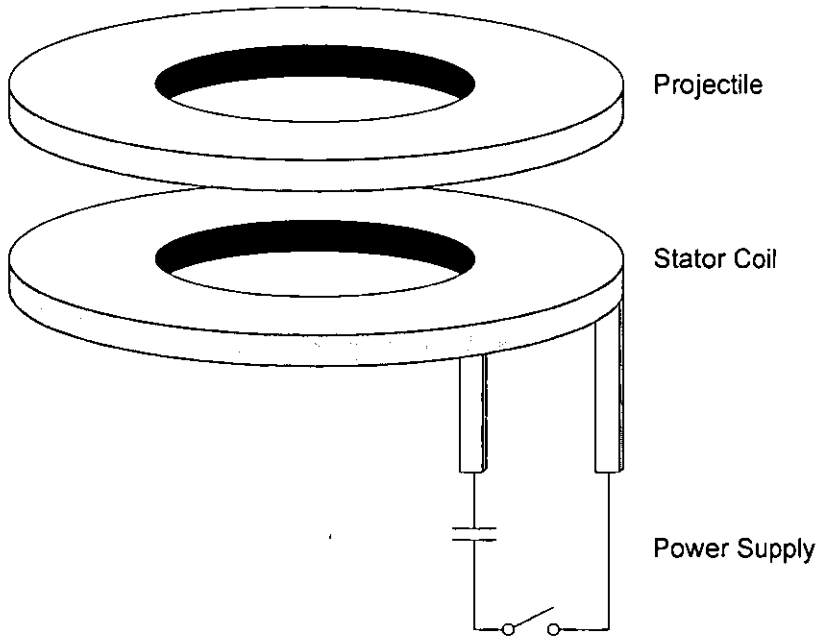


Figure 2.7 Single-stage flat coil launcher

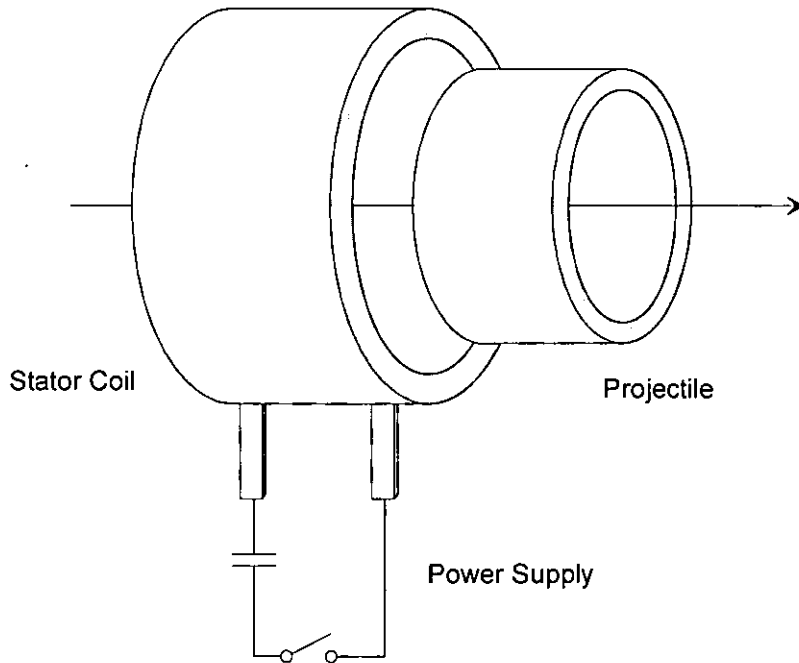


Figure 2.8 Single-stage tubular launcher

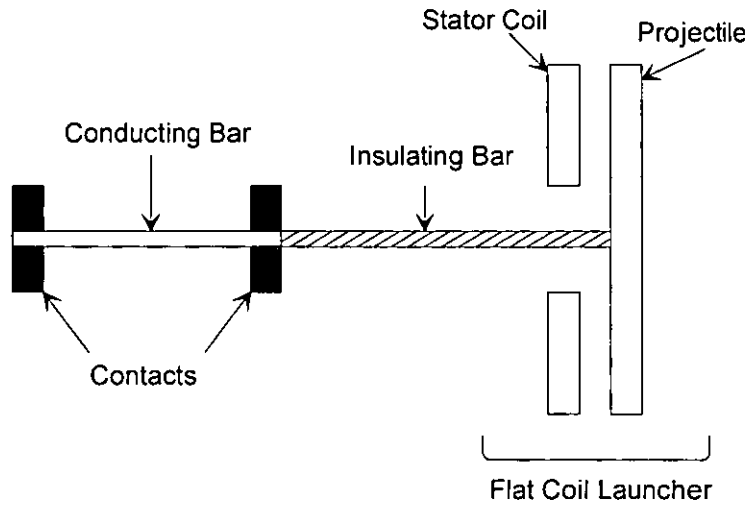


Figure 2.9 High-speed linear actuator

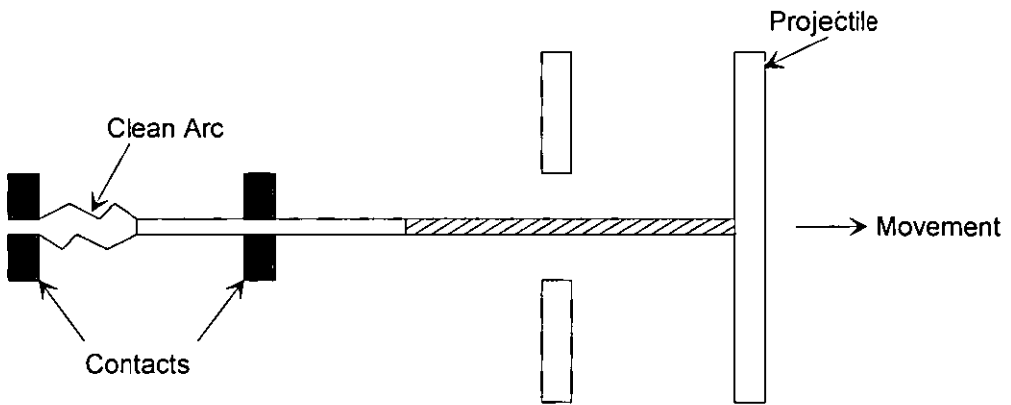


Figure 2.10 Actuator after firing

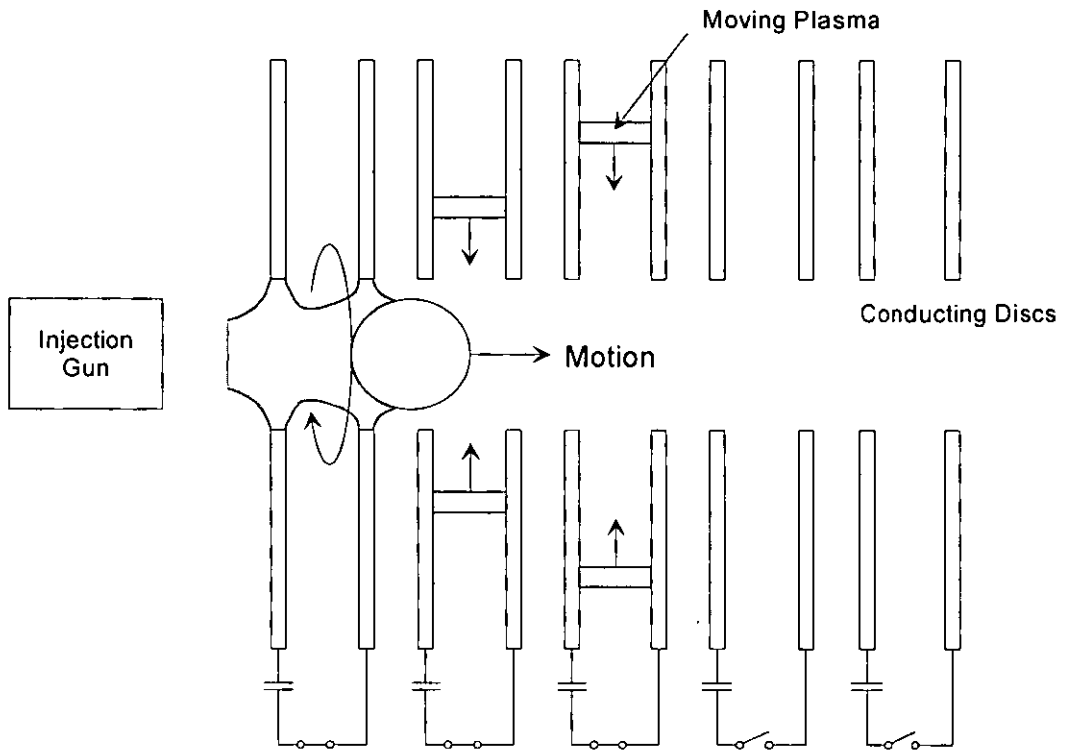


Figure 2.11 Five-stage plasma pinch launcher

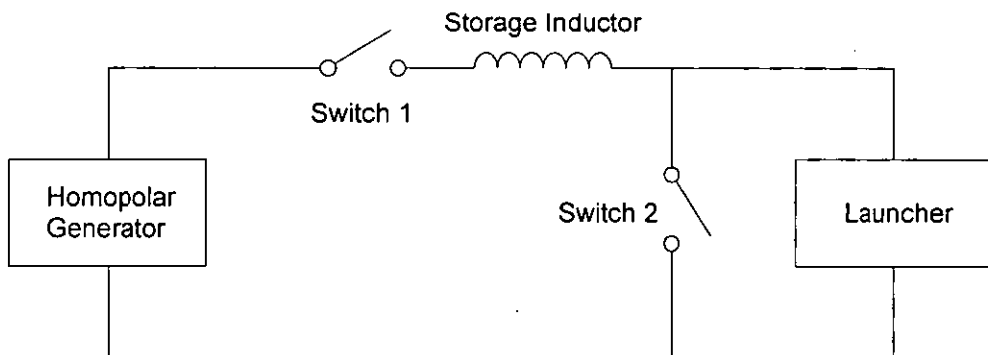


Figure 2.12 Typical homopolar generator and inductor circuit

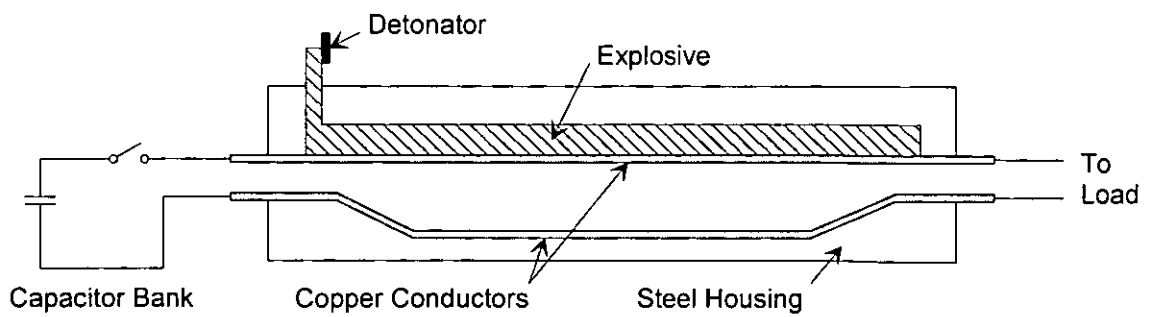


Figure 2.13 Strip flux compression generator



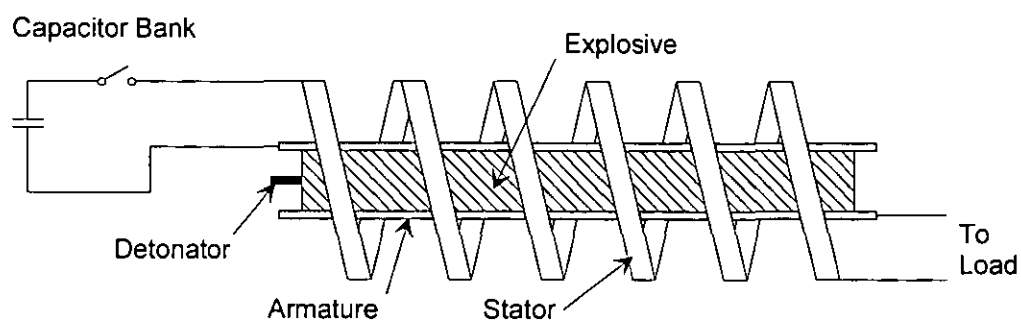


Figure 2.14 Helical flux compression generator

## 3. MODELLING TECHNIQUES

*As computing power increased, the use of numerical techniques for solving non-linear problems became possible, with the complexity of computer models growing in tandem with computer power. Over the last few years, some of the worlds largest computers such as the Cray XMP-24 have been used to model electromagnetic launchers [69]. This chapter describes the origins and uses of the most commonly used modelling techniques.*

### 3.1. FINITE DIFFERENCE ANALYSIS

The finite difference approach was one of the first main methods used in the solution of non-linear problems. Although it was developed in the 1940s, it did not find widespread use until the early 1960s, when computers became more widely available.

Often, differential equations can be used to represent a physical system. Although simple differential equations can be solved analytically, equations modelling a physical system are often non-linear. To solve a non-linear problem, using the finite difference method, the area of the problem must be divided into equal sub-regions with the vertices of these regions being termed nodes. At each node, the derivatives in the differential equations are replaced by appropriate difference quotients. The order of the difference quotients are chosen to maintain a certain level of truncation error. Expanding the derivatives in the form of a Taylor polynomial, and using the intermediate value theorem [96], leads to a set of formulae that can be solved.

Although the method leads to a simple system of equations, it does have some serious limitations. The main one of these is the fixed geometry which requires the region of interest to be divided up into equal squares and makes the modelling of circular and irregular shapes very difficult. The inclusion of varying sources and boundary conditions is also difficult. Any modelling of movement assumes that this is in discrete pixelated steps, of the same size as the sub-regions.

Although finite difference analysis has been used to model magnetic systems, this has been done using custom written software [97]. Any changes to the structure or boundary conditions of the model usually requires the modelling software to be rewritten, which is both time-consuming and error prone.

### 3.2. FINITE ELEMENT ANALYSIS

Finite element analysis has been applied to many types of problem ranging from electromagnetics to building design. Initially, the use of the finite element models was limited to those institutions with the largest computers, but as computer power has increased finite element analysis has become a standard engineering tool. Over recent years it has been used to solve 2D and 3D models involving complex structures and non-linear materials, with the more advanced packages being able to model the movement of conductors and even transient events.

Finite element analysis was born out of structural analysis during the mid 1950s. The technique is based on the concept of dividing a continuous material or surface into small finite components, termed elements. These elements are connected by their edges, with nodes at the vertices. The first attempts at determining the properties of the finite element method were carried out by Hrenikoff [98] and McHenry [99], who replaced a continuous system by an equivalent system of bars. The first true finite elements, of arbitrary shapes, were studied in the mid 1950s by Turner *et al.* [100]. Much of this early work was somewhat intuitive and guided by common sense. As new applications and more complex forms were being studied this approach failed, which produced the need for a more formal method to be developed.

The principles of virtual work provided a powerful tool in the development of structural analysis. From classic structural theory, it can be shown that, if a set of stresses are in equilibrium at all points with a set of external forces, then the sum of the internal and external work done during any displacements must be zero. It was later recognised that the virtual work approach to the finite element method could also be represented as the minimisation of an equation (such as the potential energy of a

system). This led to recognition of the boundary nature of the solution [101], and to the extension of the method to other possible formulations. The variational approach was initially discovered by Pian [102], and later verified as being an application of the Hellinger-Reissner principle. This did not just extend the methodology to different possible solutions of elastic problems, but also expanded it into many other mathematical and physical problems. The variational approach allowed any problem, whose solution could be defined by the stationary value of a function, to be solved by a finite element approximation.

Finite element analysis was first used in electrical engineering in 1967 [103], when first-order triangular elements were used to solve a comparatively simple waveguide problem. Since then, many different types and orders of shape functions have been derived, but the triangular and rectangular remain the most commonly used. The functions must produce a surface over the whole region of interest, that is continuous after integration and in the first and second derivative. Linear polynomials are usually chosen for triangular elements and bilinear polynomials for rectangular elements.

When using finite element analysis the problem must be divided into elements. These are usually triangular but, unlike the finite difference method, they do not have to be of the same size or shape. The use of non-uniform elements allows much more complex and irregular shapes to be modelled than is possible using the finite difference method. In addition, the boundary conditions involving derivatives are incorporated as integrals in the function to be minimised, and hence the basic equations of a problem are independent of the particular boundary conditions of the problem.

### 3.2.1. MODELLING SOFTWARE

The finite element modelling in this thesis used a commercial modelling package called MEGA. MEGA was developed by Bath University Electrical Engineering Department in collaboration with the DERA at Fort Halstead. It was initially developed as a static 2D model to determine railgun current distributions. Later

versions of MEGA have included moving conductors and the ability to model 3D problems. In further collaborations with the DERA, link code was written that enabled the results from MEGA to be passed to a structural finite element package (DYAN3D) [104]. However, the results from the structural model are not yet used to change the location or shape of the conductors in the electromagnetic model. MEGA has been used to model successfully both rotary and linear machines, as well as transformers and other electromagnetic systems.

MEGA can be used to solve several different formulations or problem types, but only one formulation was used in this thesis. Due to the highly axi-symmetrical form of the launcher coils, only the 2D axi-symmetric formulation was needed. Using this formulation, MEGA assumes that the current flow is in the circumferential direction only and that the flux density has no  $B_0$  component. MEGA allowed the inclusion of the power supply components, by the definition of external circuit element (branches) and connecting ports (circuit nodes). Using these facilities, the power supply components were modelled simultaneously with the electromagnetic finite element model. The available version of MEGA only modelled static conductors and used a low frequency subset of Maxwell's equations, which limited its usefulness when modelling transient and dynamic systems. Nevertheless, it provided information not easily obtained from a filamentary model.

### 3.3. FILAMENTARY ANALYSIS

Filamentary analysis is based on an equivalent circuit approach, which in recent years has become increasingly popular in the study of coilguns. The filamentary method only models the conducting regions in a system, and splits these into circular filaments. The equivalent circuit is constructed from the individual equivalent circuit parameters of each filament, and the power supply circuit elements. Using general circuit theory methods, it is possible to determine the current flow in each of the filaments, and in addition other quantities such as temperature and force can be determined.

One of the first models of a launcher to use an equivalent circuit method was presented by Burgess et al [64]. The drive coil was assumed to be an  $N$  turn solenoid with a uniform longitudinal current distribution. However, since the projectile was a single-turn tube, it was modelled by slitting it longitudinally into ten regions to enable the current distribution to be adequately represented.

One of the first examples of the filamentary approach being used to model a launcher was presented by Williamson and Leonard in 1986 [48], when they described the development of a model and compared the results of simulations to those from a demonstration launcher. The filament inductances were calculated by a combination of Grover's [105] and Silvester's [106] methods.

David Elliot of JPL presented a paper on a mesh matrix analysis method for launcher modelling at the fourth symposium in 1989 [107]. By sub-dividing the conductors into filaments, and using functions to determine the flux linkage between filaments and the magnetic field at each filament, he was able to model a coilgun launcher.

Wu and Sun of CEMUT developed Elliot's model, but calculated the inductance of the loop conductors using Grover's equations, and used this model to study the current distributions in homopolar generators [108]. Since then many other models using filamentary analysis have been developed.

### 3.4. CONCLUSIONS

Historically, many different analyses and modelling techniques have been used to model electromagnetic launchers. In the early days, finite difference methods were often used but with the emergence of commercial finite element packages this began to fade. The complex and non-rectangular shapes often encountered severely limited the use of finite difference methods, and the most commonly used techniques are now based on either finite element or filamentary analysis. Whereas finite element analysis leads to much more general and flexible models, these are usually slower than filamentary models when implemented on the same computer [109]. Although finite element packages are commercially available, they tend to be expensive and not easily

modified to suite a particular application. The 2D axi-symmetric formulation is most appropriate to model a flat coil induction launcher of the type studied in this thesis, and the MEGA software package was used for this purpose.

## 4. ANALYSIS OF FILAMENTARY NETWORKS

*This chapter develops the methods of analysis used in the filamentary model. Although the calculation of circuit parameters is highly dependent on the nature of the system being modelled, the methods of analysis are completely general.*

### 4.1. EQUIVALENT CIRCUIT ANALYSIS

The analysis of the equivalent circuit of a launcher is based on Kirchhoff's first and second laws [110]. Implementing these leads to a system of equations in which there are as many equations as there are branches, and hence unknown currents, and which can be solved using standard matrix techniques [111]. However, a system proposed and developed by Maxwell reduced the number of equations to the number of branches that must be removed from a circuit to ensure that no closed paths remain in the circuit [112]. This node and mesh method was developed to form the modern closed circuit analysis widely used today, and it has been further refined by Kron and Happ to include open mesh as well as closed mesh methods [113], [114], [115].

Closed mesh currents are limited to loops that are wholly contained within the network being analysed. Open mesh currents may flow between any two different node points, with the current defined by a source external to the network being analysed. The orthogonal networks developed by Happ are completely general and include both open and closed meshes. However, networks that contain only open and closed meshes were called all mesh networks by Kron and were subsequently re-named augmented all mesh networks by Happ [116].

### 4.2. MATRIX NOTATION

The matrix notation employed in this thesis was originally developed by Happ [114], but has been slightly modified over recent years [117]. In this notation, the indices are used to indicate the reference frames associated with a matrix. The position dots are used to indicate which reference frame is associated with the primary index, or



columns in a normal two-dimensional matrix. Hence  $A_{\bullet b}^c$  is the transpose of  $A_b^{\bullet c}$  and can be shown in matrix form as

$$A_b^{\bullet c} = {}_b \begin{matrix} c \\ [A] \end{matrix} \quad \text{and} \quad A_{\bullet b}^c = {}_c \begin{matrix} b \\ [A] \end{matrix} \quad \{4.1\}$$

This notation also preserves the Einstein summation convention and the transposition rule [113]. In addition, the position of the indices, i.e. whether they are subscript or superscript, indicates whether the associated reference frame is covariant or contra-variant. This allows a simple index balance to be used to check the structure of an equation.

Although determining the variant nature of an index may seem unnecessary and confusing, it does indicate the nature or behaviour of a vector. By convention, variables with contra-variant indices are used to represent flows or velocities, such as currents or speeds.

If it is assumed that the current vector  $I^a$  can be transformed into the reference frame 'b' by pre-multiplying it by the transformation matrix  $C_{\bullet a}^b$  then

$$I^b = C_{\bullet a}^b I^a \quad \{4.2\}$$

Since the power in a system must be independent of any reference frame used to represent that system, the voltage vectors  $E^a$  and  $E^b$  in the a and b reference frames can be related by

$$E_b I^b = E_a I^a \quad \{4.3\}$$

from which it can be shown that

$$E_a = C_a^{\bullet b} E_b \quad \{4.4\}$$

Hence,

$$\mathbf{E}_b = \mathbf{C}_b^{\bullet a} \mathbf{E}_a \quad \{4.5\}$$

In other words, although the current vector is transformed from reference frame 'a' to 'b' by pre-multiplying by a transformation matrix  $\mathbf{C}$ , the voltage vector must be pre-multiplied by the inverse of the transpose of this matrix. Hence, the very different manner in which covariant and contra-variant variables are transformed between two different reference frames can clearly be seen.

### 4.3. ALL MESH NETWORKS

The following analysis of mesh networks is based on that developed by Gregory [117] and is best described by an example. In the following section, a simple network is analysed but the methods described can be expanded to any definable electrical network. The direction of the branch currents and voltages are completely arbitrary, and are accounted for by the relative polarities of the results. Figure 4.1 shows the example network to be analysed. The structure of the network is independent of the individual branch characteristics, and it can be represented by the line diagram or directed graph shown in Figure 4.2. Although any directed graph can be analysed in a variety of ways, the total number of independent closed and open paths in any system will equal the number of branches in that system. The numbers of equations determines the number of independent closed and open meshes.

$$\text{Number of closed meshes} = B - N + S \quad \{4.6\}$$

$$\text{Number of open meshes} = N - S \quad \{4.7\}$$

where  $B$  is the number of branches,  $N$  is the number of nodes, and  $S$  is the number of independent sub-networks. It should be noted that inductively coupled circuits, e.g. transformers, must be considered as independent sub-networks. Hence, for the example system there are three closed meshes and three open meshes.

Figure 4.3 shows one possible configuration of the meshes and branches in the example circuit. By using the mesh definition in Figure 4.3 and Kirchoff's voltage law, the required equations can be determined. Equating the sum of all the branch voltages around each mesh to zero, leads to the set of equations

$$\begin{bmatrix} V_{b1} \\ 0 \\ 0 \\ V_{o4} \\ V_{o5} \\ V_{o6} \end{bmatrix} = \begin{bmatrix} Z_{b1} + Z_{b2} & -Z_{b2} & 0 & 0 & 0 & 0 \\ -Z_{b2} & Z_{b2} + Z_{b3} + Z_{b4} + Z_{b5} & -Z_{b5} & Z_{b3} & Z_{b5} & Z_{b4} \\ 0 & -Z_{b5} & Z_{b5} + Z_{b6} & 0 & -Z_{b5} & 0 \\ 0 & Z_{b3} & 0 & Z_{b3} & 0 & 0 \\ 0 & -Z_{b5} & Z_{b5} & 0 & -Z_{b5} & 0 \\ 0 & Z_{b4} & 0 & 0 & 0 & Z_{b4} \end{bmatrix} \begin{bmatrix} i^{c1} \\ i^{c2} \\ i^{c3} \\ i^{o4} \\ i^{o5} \\ i^{o6} \end{bmatrix} \quad \{4.8\}$$

Although the use of open mesh networks is not as wide-spread as that of their closed mesh cousins, they are often used implicitly when determining the voltages between nodes. If an open mesh impresses a current on a network, it can be considered as being closed externally by an ideal current source. If an open mesh impresses no current on a network, it can be considered as closed by an infinite impedance. The voltage present across the terminals of the infinite impedance is that measured by an ideal voltmeter. Hence the concept of a zero current open mesh can be used to determine the voltage between two nodes of a circuit.

#### 4.3.1. BRANCH NETWORK EQUATIONS

The mesh equation, shown in equation 4.8 can be expressed wholly in branch terms when the following argument is considered. If a branch is closed on itself via a hypothetical voltage source, and is replaced in the network by an identical voltage source, then the modified network will perform in the same manner as the original network. Applying this argument to the whole network enables it to be represented as a set of isolated meshes, as shown in Figure 4.4. Analysing the network of Figure 4.4 in the same manner as the network of Figure 4.3 leads to

$$\begin{bmatrix} V_{b1} \\ \\ \\ \\ \\ \end{bmatrix} + \begin{bmatrix} e_{b1} \\ e_{b2} \\ e_{b3} \\ e_{b4} \\ e_{b5} \\ e_{b6} \end{bmatrix} = \begin{bmatrix} Z_{b1} & & & & & \\ & Z_{b2} & & & & \\ & & Z_{b3} & & & \\ & & & Z_{b4} & & \\ & & & & Z_{b5} & \\ & & & & & Z_{b6} \end{bmatrix} \begin{bmatrix} i^{b1} \\ i^{b2} \\ i^{b3} \\ i^{b4} \\ i^{b5} \\ i^{b6} \end{bmatrix} \quad \{4.9\}$$

Although equation 4.9 can easily be determined, even for large and complex networks, it cannot be solved because the  $\mathbf{E}_b$  vector is unknown. Since both equations 4.8 and 4.9 are determined from the same original network, it is possible to consider both the formulations as one equation expressed in two reference frames. In the example system developed here, equation 4.8 has three degrees of freedom, whereas equation 4.9 has six degrees of freedom.

By considering the constraining network of hypothetical voltage sources, produced while transforming the original network into that expressed by equation 4.9, as shown by Figure 4.5, it is possible to define the  $\mathbf{E}_m$  vector in terms of the  $\mathbf{E}_b$  vector as

$$\begin{bmatrix} e_{m1} \\ e_{m2} \\ e_{m3} \\ e_{m4} \\ e_{m5} \\ e_{m6} \end{bmatrix} = \begin{bmatrix} 1 & & & & & \\ & -1 & 1 & 1 & & \\ & & & & -1 & 1 \\ \text{-----} & & & & & \\ & 1 & & & & \\ & & & 1 & & \\ & & & & & 1 \end{bmatrix} \begin{bmatrix} e_{b1} \\ e_{b2} \\ e_{b3} \\ e_{b4} \\ e_{b5} \\ e_{b6} \end{bmatrix} \quad \{4.10\}$$

Also, by studying the network of Figure 4.5 it is possible to determine  $\mathbf{I}^b$  in terms of  $\mathbf{I}^m$  as

$$\begin{bmatrix} i^{b1} \\ i^{b2} \\ i^{b3} \\ i^{b4} \\ i^{b5} \\ i^{b6} \end{bmatrix} = \begin{bmatrix} 1 & & & & & \\ i & -1 & & & & 1 \\ & 1 & & & & \\ & 1 & & & & \\ & 1 & -1 & & & \\ & & & 1 & & \end{bmatrix} \begin{bmatrix} i^{m1} \\ i^{m2} \\ i^{m3} \\ i^{m4} \\ i^{m5} \\ i^{m6} \end{bmatrix} \quad \{4.11\}$$

By observation, it is clear that the coefficient matrix in equation 4.11 is the transpose of that in equation 4.10. This matrix is purely defined by the manner in which the branches are connected to form the network being analysed, and hence it is commonly termed the connection matrix. However, it can also be considered to transform a branch vector into the mesh reference frame, and hence is sometimes known as a transformation matrix. Using this matrix and the index notation described earlier, enables equations 4.8 to 4.11 to be expressed as

$$\mathbf{V}_m = \mathbf{Z}_{mm} \mathbf{I}^m \quad \{4.12\}$$

$$\mathbf{V}_b + \mathbf{E}_b = \mathbf{Z}_{bb} \mathbf{I}^b \quad \{4.13\}$$

$$\mathbf{E}_m = \mathbf{C}_m^{\bullet b} \mathbf{E}_b \quad \{4.14\}$$

$$\mathbf{I}^b = \mathbf{C}_{\bullet m}^b \mathbf{I}^m \quad \{4.15\}$$

If equation 4.13 is rearranged and substituted into equation 4.14,  $\mathbf{E}_m$  this becomes

$$\mathbf{E}_m = \mathbf{C}_m^{\bullet b} \mathbf{Z}_{bb} \mathbf{I}^b - \mathbf{C}_m^{\bullet b} \mathbf{V}_b \quad \{4.16\}$$

Substituting  $\mathbf{I}^b$  from equation 4.15 gives

$$\mathbf{E}_m = \mathbf{C}_m^{\bullet b} \mathbf{Z}_{bb} \mathbf{C}_{\bullet m}^b \mathbf{I}^m - \mathbf{C}_m^{\bullet b} \mathbf{V}_b \quad \{4.17\}$$

If equation 4.17 is rearranged as shown in equation 4.18, a direct comparison of terms leads to the complete form of the mesh equation expressed by equation 4.19.

$$\mathbf{C}_m^{\bullet b} \mathbf{V}_b + \mathbf{E}_m = \mathbf{C}_m^{\bullet b} \mathbf{Z}_{bb} \mathbf{C}_{\bullet m}^b \mathbf{I}^m \quad \{4.18\}$$

$$\mathbf{V}_m + \mathbf{E}_m = \mathbf{Z}_{mm} \mathbf{I}^m \quad \{4.19\}$$

where

$$\mathbf{V}_m = \mathbf{C}_m^{\bullet b} \mathbf{V}_b \quad \{4.20\}$$

and

$$\mathbf{Z}_{mm} = \mathbf{C}_m^{\bullet b} \mathbf{Z}_{bb} \mathbf{C}_{\bullet m}^b \quad \{4.21\}$$

Equation 4.21 is the impedance transformation defined by Kron [113], and allows a mesh reference frame network to be defined from a branch network.

#### 4.4. CONCLUSIONS

The techniques described in this chapter form the basis for many methods of circuit analysis. While the close mesh technique can be used in almost all circuit analysis, the use of open mesh networks is much more limited. However, open mesh networks are often used without being explicitly termed as such. The most common use of open mesh analysis is to determine the voltage between two nodes in a circuit, and it is used later in this thesis to determine the voltages present across switches when these are non-conducting. While the notation developed by Happ is very formal, it does allow a quick balance of the equations components to be used as a validation check.

4.5. FIGURES

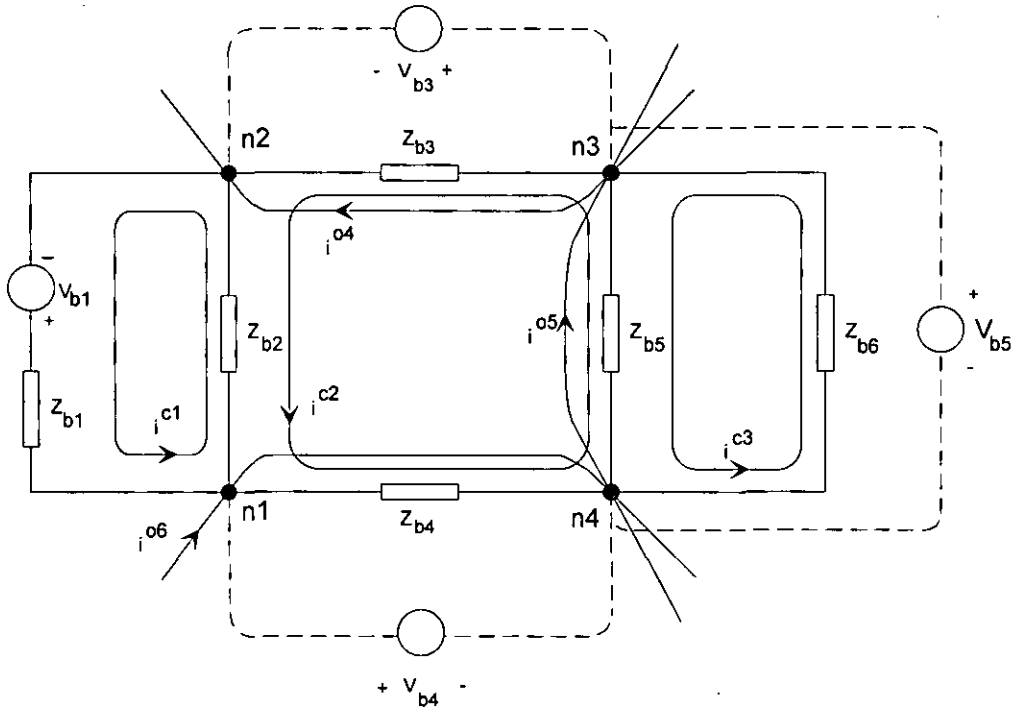


Figure 4.1 Example Circuit

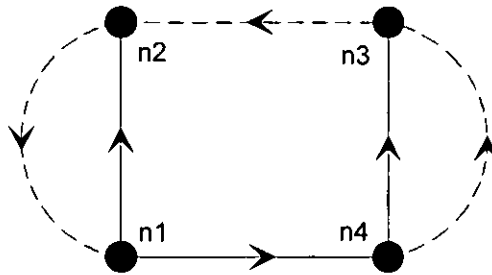


Figure 4.2 Directed graph of example circuit

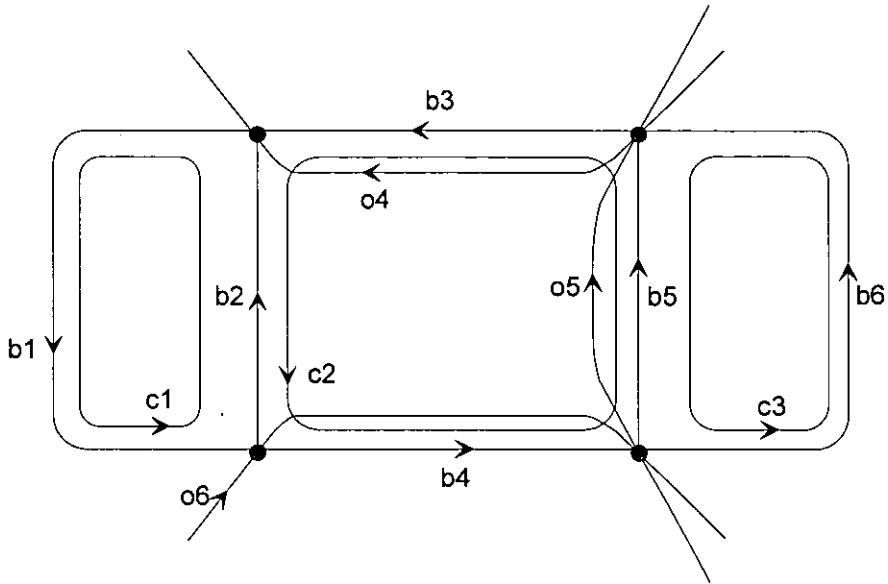


Figure 4.3 Meshes and branches of example circuit

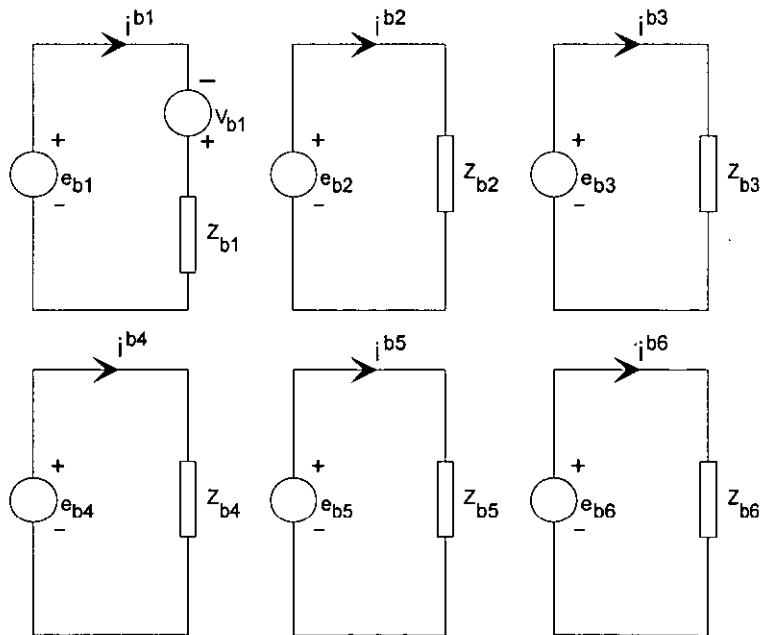


Figure 4.4 Branch network for example circuit



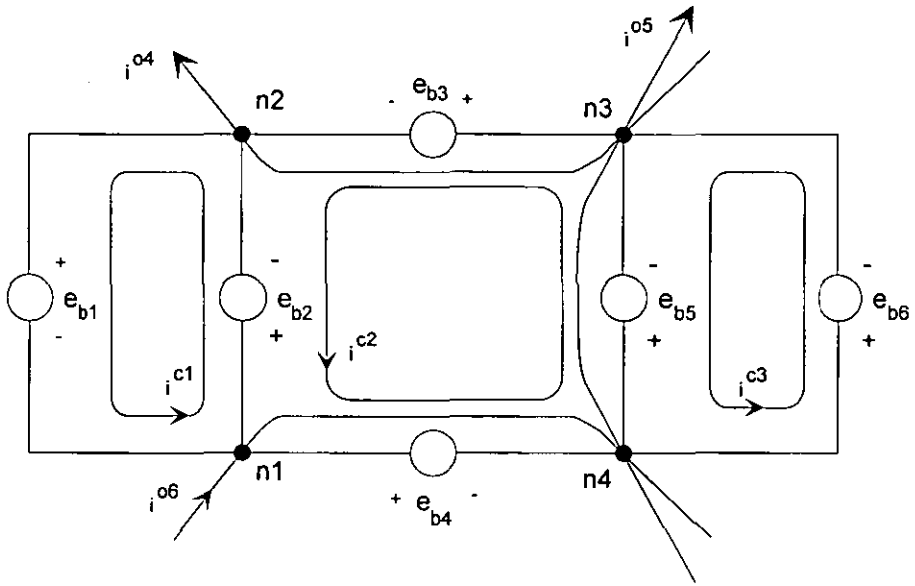


Figure 4.5 Hypothetical voltage source network

# 5. NUMERICAL TECHNIQUES

*Analysing a launcher using filamentary analysis and applying mesh networking techniques leads to a large set of differential equations that must be solved. By considering the solution of a single initial value problem, numerical techniques can be developed, that are suitable for solving such equations. The first part of this chapter develops the numerical techniques to solve differential equations and the second part introduces the techniques used in the solution of large sets of simultaneous equations that are present in the filamentary model.*

## 5.1. SOLUTION OF DIFFERENTIAL EQUATIONS

Often, in science and engineering, models are used to determine some variable with respect to another, and such models may require the solution of initial value differential equations. Ideally, the solution of a differential equation would be in an exact analytical form, but real life problems are normally much too complex and they must be solved by approximate numerical methods. Numerical techniques do not provide a continuous approximation to the real situation, but instead provide approximate solutions at a series of points, which are often evenly spaced. In this thesis, this series consists of sequential points in time, with the gap between two consecutive points being called a time step.

The differential equations used in the filamentary model can be expressed in the form of the initial value problem

$$\frac{dy}{dt} = f(t, y) \quad a \leq t \leq b \quad y(a) = \alpha \quad \{5.1\}$$

where  $f$  is a continuous function that can be evaluated between times  $a$  and  $b$ , and  $\alpha$  is the initial value of  $y$ , at time  $a$ .

If the possibility of errors is included in the problem, the original statement of equation 5.1 is said to be transformed into the perturbed form of equation 5.2, where  $\epsilon_0$  is the error in the initial condition and  $\delta(t)$  is the additional error at time  $t$ .

$$\frac{dz}{dt} = f(t, z) + \delta(t) \quad a \leq t \leq b \quad z(a) = \alpha + \varepsilon_0 \quad \{5.2\}$$

When using numerical methods to solve a problem, the problem must be considered in the perturbed form due to the errors inherent in any numerical technique.

When each point is evaluated an error is introduced into the approximation, which is called the local error. The global or final error of any time stepping technique is the sum of the initial error and all the local errors, but since these are not necessarily of the same sign, the global error is not simply their accumulated sum. Although the global error is usually the more important it cannot be calculated, and to ensure that it is minimised the local errors are usually minimised. However, in this thesis, the transient response of the launcher is one of the most important factors in its performance, and the local error is therefore considered to be more important than the global error.

The different numerical methods for solving ordinary differential equations use either single-step or multi-step techniques. Single-step methods only require the value of the current variable to be known, while multi-step methods require information on the system over several previous time steps. However, multi-step methods usually have the advantage of requiring less computation than that of an equivalently accurate single-step method.

## 5.2. RUNGE-KUTTA METHODS

Runge-Kutta methods are widely used to solve ordinary differential equations for a broad spectrum of applications. Although simpler methods, such as Euler or Taylor methods do exist, their accuracy is somewhat limited and they are seldom used in practice. Although Runge-Kutta methods are clearly distinct from the other two methods, there remains a close link, since Runge-Kutta methods are based on a Taylor expansion, and the Euler formula can be expressed as a special form of the Runge-Kutta methods.

The classic Taylor series expansion of a function requires the derivatives of the function to be found, and if the function has two or more variables evaluation of the derivatives can become very complicated. Runge first proposed a method that removed the need to determine the derivatives while still maintaining the accuracy, by determining the values of the function at a series of intermediate points. The method was subsequently developed and formalised by Kutta, and became the Runge-Kutta method.

The Runge-Kutta formulation used in this thesis is the fourth-order method shown in equation 5.3. Although there are many other possible fourth-order formulations, the one chosen here is widely used and frequently described [96], [118].

$$y_{n+1} = y_n + \frac{h}{6} [g_1 + 2g_2 + 2g_3 + g_4] \quad \{5.3\}$$

where

$$\begin{aligned} g_1 &= f(x_n, y_n) \\ g_2 &= f\left(x_n + \frac{h}{2}, y_n + \frac{h}{2}g_1\right) \\ g_3 &= f\left(x_n + \frac{h}{2}, y_n + \frac{h}{2}g_2\right) \\ g_4 &= f(x_n + h, y_n + hg_3) \end{aligned} \quad \{5.4\}$$

Although the Runge-Kutta method is often used in an incremental form, it was used in the gradient form shown above, since this slightly improves the performance of the program. Since the solution of the filamentary model requires the solution of a large number of differential equations over the same time step, the fractions of the step-length were pre-calculated to further improve the program performance.

### 5.2.1. LOCAL ERROR ESTIMATION IN THE RUNGE-KUTTA METHOD

Although the Runge-Kutta method provides a relatively simple and accurate method of finding the solution of ordinary differential equations, evaluation of its associated local truncation error is far from simple. However, to enable the development of the

variable time step model implemented in Chapter 7, it was necessary to find a suitable method of determining the local truncation error.

The Runge-Kutta method requires additional approximations to enable the local error to be predicted. The difficulty in explicitly estimating the local truncations in a Runge-Kutta formulation is the greatest weakness of this approach. However, the widespread use of these methods has led to the development of several methods of approximately determining the local truncation error, and two of these are considered here.

### 5.2.2. RUNGE-KUTTA-FEHLBERG METHOD

One method of assessing the accuracy of the computation at the end of a single-step is to compare it to the value that is obtained when the step-length is halved. If the difference in the results is too great, then the time step should be halved and the function re-evaluated. Although this method is simple to implement it greatly increases the computational time, with the fourth-order algorithm described above requiring eleven function evaluations as opposed to the original four. Alternatively, the results from two Runge-Kutta algorithms of different orders could be compared. If these are of fourth and fifth orders, four evaluations are required for the fourth-order method and a further six for the fifth-order method. However, a very popular method called the Runge-Kutta-Fehlberg method combines the calculation of both the fourth and fifth approximations, and yet requires only six evaluations. This technique uses the fourth and fifth-order approximations, as shown in equations 5.5 and 5.6, and calculates the local truncation error  $E$  by comparing them, which when simplified leads to equation 5.7.

$$y_{n+1}^{(5)} = y_n + \left( \frac{16}{135}g_1 + \frac{6656}{12825}g_3 + \frac{28561}{56430}g_4 - \frac{9}{50}g_5 + \frac{2}{55}g_6 \right)h \quad \{5.5\}$$

$$y_{n+1}^{(4)} = y_n + \left( \frac{25}{216}g_1 + \frac{1408}{2565}g_3 + \frac{2197}{4104}g_4 - \frac{1}{5}g_5 \right)h \quad \{5.6\}$$

$$E = \left( \frac{1}{360}g_1 - \frac{128}{4275}g_3 - \frac{2197}{75240}g_4 + \frac{1}{50}g_5 + \frac{2}{55}g_6 \right)h \quad \{5.7\}$$

where

$$\begin{aligned} g_1 &= f(x_n, y_n) \\ g_2 &= f\left(x_n + \frac{h}{4}, y_n + \frac{h}{4}g_1\right) \\ g_3 &= f\left(x_n + \frac{3h}{8}, y_n + \frac{3h}{32}g_1 + \frac{9h}{32}g_2\right) \\ g_4 &= f\left(x_n + \frac{12h}{13}, y_n + \frac{1932h}{2197}g_1 - \frac{7200h}{2197}g_2 + \frac{7296h}{2197}g_3\right) \\ g_5 &= f\left(x_n + h, y_n + \frac{439h}{216}g_1 - 8hg_2 + \frac{3680h}{513}g_3 - \frac{845h}{4104}g_4\right) \\ g_6 &= f\left(x_n + \frac{h}{2}, y_n - \frac{8h}{27}g_1 + 2hg_2 - \frac{3544h}{2565}g_3 + \frac{1859h}{4104}g_4 - \frac{11h}{40}g_5\right) \end{aligned} \quad \{5.8\}$$

### 5.2.3. RUNGE-KUTTA-MERSON METHOD

The Runge-Kutta-Merson method is based on a fourth-order Runge-Kutta method, but requires an additional evaluation that provides an additional degree of freedom. By using this extra degree of freedom, it is possible to derive two formulations of the method as given in equations 5.9 and 5.10.

$$y_{n+1} = y_n + \left( \frac{1}{6}g_1 + \frac{2}{3}g_4 + \frac{1}{6}g_5 \right)h \quad \{5.9\}$$

$$\bar{y}_{n+1} = y_n + \left( \frac{1}{2}g_1 - \frac{3}{2}g_3 + g_4 \right)h \quad \{5.10\}$$

where

$$\begin{aligned}
 g_1 &= f(x_n, y_n) \\
 g_2 &= f\left(x_n + \frac{h}{3}, y_n + \frac{h}{3}g_1\right) \\
 g_3 &= f\left(x_n + \frac{h}{3}, y_n + \frac{h}{6}g_2 + \frac{h}{6}g_3\right) \\
 g_4 &= f\left(x_n + \frac{h}{2}, y_n + \frac{h}{8}g_1 + \frac{3h}{8}g_3\right) \\
 g_5 &= f\left(x_n + h, y_n + \frac{h}{2}g_1 - \frac{3h}{2}g_3 + 2hg_4\right)
 \end{aligned} \tag{5.11}$$

Although only the first approximation (equation 5.9) is commonly used to estimate  $y_{n+1}$ , the second estimation allows the local truncation error to also be predicted. Merson showed that if  $f(x, y)$  is approximately linear at  $(x_n, y_n)$ , or  $h$  is sufficiently small, a good estimate of the error in  $y_{n+1}$  can be found from equation 5.12.

$$E = \frac{h}{30}(2g_1 - 9g_3 + 8g_4 - g_5) \tag{5.12}$$

Although equation 5.12 should only be applied when  $f(x, y)$  is linear, it can be used to provide a conservative estimation of the local truncation error, even when  $f(x, y)$  is non-linear.

### 5.3. PREDICTOR-CORRECTOR METHODS

While predictor-corrector methods have the advantage of requiring fewer function evaluations than equivalent Runge-Kutta methods, they require knowledge of previous values and sometimes previous gradient values. Predictor-corrector methods are based in general on equation 5.13. A predictor function is used to provide in initial prediction of  $y_{n+1}$ , but it has no known value of  $y'_{n+1}$  and hence  $\beta_0 = 0$ . The initial prediction is then used by the corrector, in which  $\beta_0 \neq 0$ , to refine the estimation of  $y_{n+1}$ , and so improve its accuracy.

$$y_{n+1} = \alpha_1 y_n + \alpha_2 y_{n-1} + K + h(\beta_0 y'_{n+1} + \beta_1 y'_n + \beta_2 y'_{n-1} + K) \quad \{5.13\}$$

where  $\alpha_n$  and  $\beta_n$  are the coefficients of the method being implemented.

Although the step-length  $h$  does not have to remain constant, allowing it to change requires the coefficients  $\alpha_j$  and  $\beta_j$  to change as functions of the current and previous step-lengths. Due to the additional complexity involved in implementing variable step-length predictor-corrector methods they are rarely used, although there are published methods for producing the required variable coefficients [119]. Often a hybrid combination of predictor-corrector and single-step methods is used to implement a variable time step algorithm, as described in Chapter 7.

There are many different possible formulations, but one of the most common is a combination of an Adams-Bashforth predictor and an Adams-Moulton corrector. Both of these are based on the integration of ordinary differential equations and both use the extrapolation and interpolation forms of Newton's backward formula. The Adams-Bashforth and Adams-Moulton formulae are expressed as

$$y^p_{n+1} = y_n + \frac{1}{24} h(55y'_n - 59y'_{n-1} + 37y'_{n-2} - 9y'_{n-3}) \quad \{5.14\}$$

and

$$y^c_{n+1} = y_n + \frac{1}{24} h(9y'_{n+1} + 19y'_n - 5y'_{n-1} + y'_{n-2}) \quad \{5.15\}$$

respectively, where the superscripts  $p$  and  $c$  represent the predictor and corrector respectively.

The ordinary differential equation is solved by first using the Adams-Bashforth equation 5.14 to predict  $y_{n+1}$ , which is then evaluated to produce the required  $y'_{n+1}$  term. The Adams-Moulton corrector (equation 5.15) is then used to improve the accuracy of the first estimation, before the function  $f(x, y)$  is finally re-evaluated. This method is able to produce results with the same order of accuracy as the Runge-



Kutta method, but it requires only two function evaluations. The predictor-corrector method developed here has the additional advantage that this formulation lends itself elegantly to local error calculations.

### 5.3.1. LOCAL ERROR ESTIMATION IN THE PREDICTOR-CORRECTOR METHOD

All Runge-Kutta methods rely upon a comparison between two different methods of approximating  $y_{n+1}$ , which involve addition function evaluations. However, since the predictor-corrector approach is based on two such approximations, an estimation of the error can be found without the cost of addition evaluations. By assuming that all previous values of  $y_i$  (where  $i \leq n$ ) are exact, the local errors can be expressed as

$$E^P = \frac{y_{n+1} - y_{n+1}^P}{h} = \frac{251}{720} h^4 y'''' \quad \{5.16\}$$

$$E^C = \frac{y_{n+1} - y_{n+1}^C}{h} = -\frac{19}{720} h^4 y'''' \quad \{5.17\}$$

Assuming that, for small values of  $h$ , the approximations of  $y''''$  are the same, subtracting equation 5.16 from 5.17, gives

$$y'''' = \frac{8}{3} \frac{y_{n+1}^C - y_{n+1}^P}{h^5} \quad \{5.18\}$$

Hence, the corrector error can be expressed as

$$E = \frac{19}{270h} |y_{n+1}^C - y_{n+1}^P| \quad \{5.19\}$$

Equation 5.19 provides a good approximation to the local truncation error, and it is not limited to locally linear functions  $f(x, y)$ , as in the case of the Runge-Kutta-Merson method.

## 5.4. METHODS OF MATRIX FACTORISATION

The analysis of any launcher system using the equations in Chapter 4 leads to a set of simultaneous equations having the form

$$\frac{d}{dt} \mathbf{I}^m = \mathbf{L}_{mm}^{-1} \left[ \mathbf{V}_m + \mathbf{E}_m - (\mathbf{R}_{mm} + \mathbf{D}_{mm} \mathbf{u}) \mathbf{I}^m \right] \quad \{5.20\}$$

Before the methods of solution described above can be implemented the required derivative of  $f(x, y)$  must be evaluated, which involves the solution of a large system of simultaneous equations. Equation 5.20 can be simplified to the form shown in equation 5.22, by the substitution of equation 5.21. Equation 5.21 forms the basis for all the matrix factorisation methods described here.

$$\mathbf{Ax} = \mathbf{b} \quad \{5.21\}$$

$$\mathbf{x} = \mathbf{A}^{-1} \mathbf{b} \quad \{5.22\}$$

Many different methods can be used to solve sets of simultaneous equations. However, in general, it is possible to split the different methods into two groups, iterative and direct. Iterative methods use successive approximation until the result has been found to an adequate accuracy, but while requiring less computer memory than the equivalent direct methods they can become unstable and suffer from problems of convergence. Direct methods rely upon direct manipulation of the equations being solved, and while they may require more computer memory to implement, they are much simpler to formulate and are stable. The three direct methods examined below are all based on the Gaussian elimination method, but require significantly different amounts of computer resources.

### 5.4.1. GAUSS-JORDAN METHOD

The Gauss-Jordan method is the simplest of the three methods to be described, and it is a direct adaptation of Gaussian elimination [120]. It is also known as the explicit method, since the inverse matrix is found directly. The method is based on the elimination of each unknown until only one remains, when the last equation can

simply be solved and the result is inserted into the previous equation, which then can be solved. The use of each result in a previous equation is called back substitution, and allows all the results to be found. In the Gauss-Jordan method, all the elements above and below the leading diagonal are set to zero and those on the diagonal are set to one. Although the method finds the solution to a set of equation, it is often more useful to find the inverse of  $\mathbf{A}$ . By augmenting  $\mathbf{A}$  with a unit matrix of the same size and applying the above technique, the resultant matrix will contain the unit matrix, now on the left-hand side, and the inverse of  $\mathbf{A}$  on the right-hand side, as shown below.

$$\left[ \begin{array}{cc|cc} a_{11} & a_{12} & 1 & 0 \\ a_{21} & a_{22} & 0 & 1 \end{array} \right] \Rightarrow \left[ \begin{array}{cc|cc} 1 & 0 & a'_{11} & a'_{12} \\ 0 & 1 & a'_{21} & a'_{22} \end{array} \right] \quad \{5.23\}$$

#### 5.4.2. IMPLICIT FACTORISATION METHOD

This is another formalised method based on Gaussian elimination. The product form of the inverse of  $\mathbf{A}$  is also known as the implicit form [118], due to the result matrix only containing an implied inverse. The implied inverse produces the same result as the full inverse matrix, when multiplied correctly by another matrix or a vector.

As with the other methods described, the solution to equation 5.21 is found by considering the equation in the form of equation 5.22. However, the matrix  $\mathbf{A}^{-1}$  is not calculated explicitly but rather expressed as a product of a series of matrices

$$\mathbf{A}^{-1} = \mathbf{T}_n \mathbf{K} \mathbf{T}_3 \mathbf{T}_2 \mathbf{T}_1 \quad \{5.24\}$$

In Gaussian elimination, the first row of matrix  $\mathbf{A}$  is divided by its diagonal element ( $a_{11}$ ) and all the other rows then have appropriate multiples of the first row subtracted from them. However, it is possible to perform the same series of operations by pre-multiplying the matrix  $\mathbf{A}$  by a transformation matrix  $\mathbf{T}_1$ , where  $\mathbf{T}_1$  is defined by

$$\mathbf{T}_1 = \begin{bmatrix} 1 & 0 & 0 \\ a_{11} & 1 & 0 \\ -\frac{a_{21}}{a_{11}} & 0 & 1 \\ -\frac{a_{31}}{a_{11}} & 0 & 1 \end{bmatrix} \quad \{5.25\}$$

Applying  $\mathbf{T}_1$  to  $\mathbf{A}$  leads to the new matrix  $\mathbf{A}'$ , where

$$\mathbf{A}' = \begin{bmatrix} 1 & a'_{12} & a'_{13} \\ 0 & a'_{22} & a'_{23} \\ 0 & a'_{32} & a'_{33} \end{bmatrix} \quad \{5.26\}$$

in which  $a'_{ij}$  are the same coefficients that would be obtained after the first step of an ordinary Gauss-Jordan elimination. Hence equation 5.21 can be expressed as

$$\mathbf{A}'\mathbf{x} = \mathbf{T}_1\mathbf{A}\mathbf{x} = \mathbf{T}_1\mathbf{b} \quad \{5.27\}$$

This transformation process can be expanded to an  $n^{\text{th}}$  order operation, leading to

$$\mathbf{A}^{(n)}\mathbf{x} = \mathbf{T}_n\mathbf{K} \mathbf{T}_2\mathbf{T}_1\mathbf{A}\mathbf{x} = \mathbf{T}_n\mathbf{K} \mathbf{T}_2\mathbf{T}_1\mathbf{b} \quad \{5.28\}$$

If the process is continued until  $n = i$ , where  $i \times i$  is the size of the original matrix  $\mathbf{A}$ , then  $\mathbf{A}^{(n)}$  will have been reduced to a unit matrix, while the product of  $\mathbf{T}_n$  to  $\mathbf{T}_1$  will be the inverse of  $\mathbf{A}$ . Although this inverse is now expressed as a set of  $i \times i$  matrices, it can be shown that only the  $n^{\text{th}}$  column of each transformation matrix is needed. The rest of the matrix is the same as a unit matrix, and can be included implicitly. If the original matrix  $\mathbf{A}$  is not required after factorisation then the unit matrix created in  $\mathbf{A}$  can also be implied, and the storage space can be used to store each subsequent column from the corresponding transformation matrix.

Implicit factorisation does not produce the actual inverse of  $\mathbf{A}$ . The use of modified pre- or post-multiplication routines allows equations, such as equation 5.21, to be solved with much less computational effect than is required by a corresponding Gauss-Jordan program. It should be noted that the inverse of  $\mathbf{A}$  can be found by

multiplying together all the  $\mathbf{T}$  matrices. However, the inverse of  $\mathbf{A}$  is rarely needed on its own, and it is more commonly multiplied by another matrix or vector.

### 5.4.3. TRIANGULAR DECOMPOSITION METHOD

Triangular decomposition is widely used for solving large sets of simultaneous equations. It is often also termed LU factorisation, and the technique is again based on Gaussian elimination. Although there are several LU factorisation methods, the one considered here is the Crout and Cholesky method [118]. Triangular decomposition is based on the concept that the original matrix  $\mathbf{A}$  can be expressed as the product of two matrices

$$\mathbf{A} = \mathbf{LU} \quad \{5.29\}$$

where the lower triangular matrix  $\mathbf{L}$  has all zero elements above the leading diagonal, and the upper triangular matrix  $\mathbf{U}$  has a unit leading diagonal and all the elements below the diagonal are zero. If it is possible to factorise  $\mathbf{A}$  in this manner, equation 5.21 can be expressed as

$$\mathbf{LUx} = \mathbf{b} \quad \{5.30\}$$

where

$$\mathbf{L} = \begin{bmatrix} l_{11} & 0 & 0 \\ l_{21} & l_{22} & 0 \\ l_{31} & l_{32} & l_{33} \end{bmatrix} \quad \mathbf{U} = \begin{bmatrix} 1 & u_{12} & u_{13} \\ 0 & 1 & u_{23} \\ 0 & 0 & 1 \end{bmatrix} \quad \{5.31\}$$

If an addition vector  $\hat{\mathbf{b}}$  is defined, the solution of equation 5.21 can be considered as the two-part problem

$$\mathbf{Ux} = \hat{\mathbf{b}} \quad \{5.32\}$$

and

$$\mathbf{L}\hat{\mathbf{b}} = \mathbf{b} \quad \{5.33\}$$

Since all the elements above the leading diagonal in the  $L$  matrix are zero,  $\hat{\mathbf{b}}$  can be found by a direct forward substitution. Once  $\hat{\mathbf{b}}$  has been determined,  $\mathbf{b}$  can be found by backward substitution into the upper triangular matrix. Before any system can be solved using this method, the coefficients in both the  $L$  and  $U$  matrices must be found.

It can be shown that Gaussian elimination applied to equation 5.21, and before the back substitution process, produces a set of equations in the form of equation 5.32. To find  $L$ , the step involved in transforming  $\mathbf{b}$  into  $\hat{\mathbf{b}}$  must be reconstructed, as  $L$  can be considered as a transformation matrix that transform  $\hat{\mathbf{b}}$  into  $\mathbf{b}$  as shown in equation 5.33. By considering a (3x3) set of equations,  $L$  can be expressed as

$$L = \begin{bmatrix} a_{11} & 0 & 0 \\ a_{21} & a^{(1)}_{22} & 0 \\ a_{31} & a^{(1)}_{32} & a^{(2)}_{33} \end{bmatrix} \quad \{5.34\}$$

where  $a^{(n)}_{ij}$  is the element at location  $(i, j)$  in the  $A$  matrix after the  $n^{\text{th}}$  step of a Gaussian elimination. By modifying the Gaussian elimination process, it is possible to transform the matrix  $A$  into the matrix  $U$ , by replacing the elements after each step. With a slight modification to the backward substitution phase, it is possible to reduce the amount of computer storage required. If the leading unit diagonal and the zeroes in the  $L$  and  $U$  matrices are implied, both matrices can be stored in the original  $A$  matrix, which has the added benefit that both matrices can be calculated at the same time.

## 5.5. CONCLUSIONS

Although only one method of matrix factorisation and one method of solving ordinary differential equations are required at each time step, all the above methods have been implemented and tested during the development of the filamentary model. The development and testing of the different methods is discussed in chapter seven.

All the methods of matrix factorisation considered here are based on Gaussian elimination, each has its own particular properties. The Gauss-Jordan method is the

simplest to use but it also the most computationally expensive. The implicit factorisation method is faster than the Gauss-Jordan method, but it requires special routines to perform either pre- or post-multiplication. The LU factorisation method is computationally the fastest, but it is only possible to perform an adapted post-multiplication of the resultant matrix.

# 6. IMPLEMENTATION OF FILAMENTARY MODEL

*The first part of this chapter describes how the parameters of each filament are calculated in the branch reference frame. Later parts discuss how the mathematical methods developed in the previous two chapters were used, together with the branch parameters, to produce a working model. This model is compared with a finite element model at the end of the chapter. Although some of the methods developed in this chapter help to reduce the run time of a simulation, further development of the original model was undertaken, as detailed in chapter seven.*

## 6.1. ANALYSIS OF LAUNCHER PARAMETERS

A filamentary model is based on the division of the launcher conductors into sufficiently small parts, to ensure that an equivalent circuit approach will produce sufficiently accurate results. It provides an elegant and direct method of modelling what would otherwise be a difficult electromagnetic field problem. By assuming that only circumferential currents flow in the launcher conductors, these can be represented by a series of independent circular elements. If the current flowing in each element is assumed to be concentrated at its centre, then the element can be thought of as an infinitely thin conductive filament. The launcher is then represented by a large collection of such filaments, the parameters of which can be determined individually. Once these are known, sets of electrical and mechanical equations can be assembled and solved using the procedures outlined in the previous chapters.

### 6.1.1. METHOD OF FILAMENTARY DIVISION

Both round and rectangular cross-sectional conductors are considered in this thesis. Each layer and turn of a coil can be considered to be made up from many strands of conductor. In turn, each strand will be made up from many filaments, as shown in Figure 6.1 and Figure 6.2. The filaments in each strand are modelled as electrically insulated loop conductors, connected in parallel at the end of each turn or layer. The



turns and layers are then connected in series. The strands are considered as individual conductors wound together and connected in parallel at the coil terminals. The use of infinitely thin conducting filaments to model parts of a conductor inherently excludes the concept of a filament having any cross-sectional shape. However, some thought must be given as to how a conductor is divided into filaments.

Rectangular cross-section conductors can easily be divided both horizontally and vertically, to produce approximately square filaments. The required dimensions for each filament can then be calculated.

The division of a circular conductor can be achieved in various ways, and Figure 6.3 shows three of these. The simplest is to divide the cross-sectional area segments, but this can lead to very tall and thin filaments. Since the theoretical filament would be located at the centre of each segment, this method of division would lead to a circle of elements at approximately half the radius of the original conductor. This distribution of filaments would hide any skin effect within the conductors, and could produce a misleading current distribution.

Another method is to approximate the required circle from small square filaments, although if the conductor is already small this will lead to very small filaments. This will of course improve the accuracy of the model, but it will greatly increase the number of filaments required to model a system. This in turn can produce long solution times, and even a problem too big for the available computers to solve.

The method used in this thesis for round conductors is a combination of the previous two methods. The conductors are divided into a number of shells, each containing a different number of filaments, and the filaments are connected in the same manner as for a rectangular conductor, as shown in Figure 6.4. The location of each conductor is calculated from dimensional data. The number and location of the filaments within the conductors is determined from the maximum allowable effective filament cross-sectional area.

### 6.1.2. ELECTRICAL EQUATIONS

The equations described below were used to determine the equivalent circuit parameters of the filaments being modelled. Due to the close link that exists between the resistance of a filament and its temperature, their calculation is considered together.

#### 6.1.2.1. INDUCTANCE CALCULATIONS

By considering the vector potential and the magnetic field energy caused by currents flowing in two loop conductors of infinitely thin wire, it is possible to determine the mutual inductance between the loops. Assuming that the lower of the loop conductor shown in Figure 6.5 lies in the plane  $z=0$  and that the current  $i$  is circumferential, the vector potential at the point P some distance from the loop is given by

$$\mathbf{A} = \frac{\mu_0}{4\pi} \oint \mathbf{i} \frac{\cos\theta}{s} dl \quad \{6.1\}$$

where

$$s = \sqrt{z^2 + r_1^2 + r_2^2 - 2r_1r_2 \cos\theta} \quad \{6.2\}$$

and  $z$ ,  $r_1$ ,  $r_2$  and  $\theta$  are defined in Figure 6.6. Equation 6.1 can be rearranged as

$$\mathbf{A} = \frac{\mu_0 i}{4\pi} r_2 \int_0^{2\pi} \frac{\cos\theta d\theta}{\sqrt{z^2 + r_1^2 + r_2^2 - 2r_1r_2 \cos\theta}} \quad \{6.3\}$$

Unfortunately equation 6.3 cannot be solved directly, but it can usefully be rearranged using the substitutions

$$k = \sqrt{\frac{4r_1r_2}{z^2 + (r_1 + r_2)^2}} \quad \theta = \pi - 2\varphi \quad \{6.4\}$$

and

$$\cos(\theta) = -1 + 2 \sin(\varphi)^2 \quad \{6.5\}$$

to give

$$\mathbf{A} = \frac{\mu_0 i}{2\pi} \sqrt{\frac{r_2}{r_1}} \left( \frac{2-k^2}{k} \right) \mathbf{K}(k) - \frac{\mu_0 i}{k\pi} \sqrt{\frac{r_2}{r_1}} \mathbf{E}(k) \quad \{6.6\}$$

where the functions  $\mathbf{K}(k)$  and  $\mathbf{E}(k)$  are elliptical integrals of the first and second kind respectively. Although these still cannot be solved analytically, numerical solutions exist in both tabular and functional forms [Appendix A].

If the loop is divided up into current elements  $i \, d\mathbf{l}$ , the energy stored in the magnetic field of a set of  $N$  fine loop conductors can be found from [106]

$$W_f = \frac{1}{2} \sum_{m=1}^N \oint_{\mathbf{l}_m} \mathbf{A} \cdot d\mathbf{l}_m i_m \quad \{6.7\}$$

and since each loop contributes to the magnetic vector potential at any point, the total energy may be expressed by

$$W_f = \sum_{m=1}^N \sum_{n=1}^N \frac{\mu_0}{8\pi} i_m i_n \oint \oint \frac{d\mathbf{l}_m \cdot d\mathbf{l}_n}{r} \quad \{6.8\}$$

It can be seen from equation 6.8 that the total energy stored is a combination of a sum of the loop currents and a geometrical expression defined as mutual inductance by Neumann's formula

$$M_{mn} = \frac{\mu_0}{4\pi} \oint \oint \frac{d\mathbf{l}_m \cdot d\mathbf{l}_n}{r} \quad \{6.9\}$$

Use of equation 6.9 for the two loop conductors shown in Figure 6.6 leads to

$$M_{mn} = \frac{\mu_0}{4\pi} \int_0^{2\pi} r_m \int_0^{2\pi} r_n \frac{\cos(\theta_n - \theta_m)}{\sqrt{z^2 + r_m^2 + r_n^2 - 2r_m r_n \cos(\theta_n - \theta_m)}} d\theta_m d\theta_n \quad \{6.10\}$$

and using the substitutions of equations 6.4 and 6.5 enables the mutual inductance to be expressed as

$$M_{mn} = \mu_0 \sqrt{r_m r_n} \left[ \left( \frac{2}{k} - k \right) K(k) - \frac{2}{k} E(k) \right] \quad \{6.11\}$$

To determine the self inductance of an infinitely thin loop conductor using the above method requires both the contours of integration to be the same. However if this is attempted  $k=1$  and hence the resultant self inductance is infinite. To avoid this absurdity, the flux inside each filament is neglected, and the first contour of integration is taken as the centre of the filament and the second at its inner radius. Using these approximations the self inductance of the loop can be determined from

$$L_n = \mu_0 r_n \left[ \left( \frac{2}{k_s} - k_s \right) K(k_s) - \frac{2}{k_s} E(k_s) \right] \quad \{6.12\}$$

where  $y_n$  is the radius of the wire of the  $n^{\text{th}}$  conductor, and  $k_s$  is defined by

$$k_s = 1 - \left( \frac{y_n^2}{8r_n^2} \right) \quad \{6.13\}$$

Alternatively, the self inductance of a loop conductor can be found by using an approximation proposed by Silvester [106] such that

$$L_n = \mu_0 r_n \left( \ln \left( \frac{8r_n}{y_n} \right) - 2 \right) \quad \{6.14\}$$

A comparison of calculations made by these the two methods, over a practical range of loop sizes, is shown in Figure 6.7. A theoretical examination of the methods of calculating the self inductance of a wire was undertaken by Graneau [121], who investigated the difficulties involved in calculating the self inductance of an infinitely thin conductor and concluded that there was no better methods of finding the required self inductance than those described above.

The derivatives of equation 6.11 with respect to  $z$  and  $r$  were given by Garrett [122], and can be rearranged into the forms

$$\frac{\partial M_{mn}}{\partial z} = \frac{\mu_0 k z_{mn}}{4(1-k^2)\sqrt{r_m r_n}} \left[ 2(1-k^2)K(k) - (2-k^2)E(k) \right] \quad \{6.15\}$$

$$\frac{\partial M_{mn}}{\partial r_n} = \frac{\mu_0 r_m}{\sqrt{z^2 + (r_m + r_n)^2}} \left[ K(k) - E(k) + \frac{2r_n(r_n - r_m)}{(r_n - r_m)^2 + z^2} E(k) \right] \quad \{6.16\}$$

The derivative of the self inductance of a loop conductor with respect to the loop radius was derived from equation 6.14 as

$$\frac{\partial L_n}{\partial r_n} = \mu_0 \left( \ln \left( \frac{8r_n}{y_n} \right) - 1 \right) \quad \{6.17\}$$

### 6.1.2.2. RESISTANCE AND THERMAL CALCULATIONS

The filamentary resistance is considered, together with the filamentary temperature, since they are closely related. The resistance of each filament was determined from

$$R_n = \frac{2\pi\rho_n(\phi)r_n}{x_n z_n} \quad \{6.18\}$$

where

- $R_n$  = resistance of filament n
- $\rho_n(\phi)$  = resistivity of filament n material at temperature  $\phi$
- $r_n$  = mean radius of filament n
- $x_n$  = thickness of filament n in the radial direction
- $z_n$  = thickness of filament n in the axial direction

The thermal equations assume that the heating of each filament is due to the power dissipated in that filament by the current flowing through it. Since the time period considered in a simulation was so short, it was also assumed that there is no thermal conduction or radiation into either adjacent filaments or the surroundings. Hence the rate of change of temperature of each filament can be determined from

$$R_n i_n^2 = c_n(\phi) m_n \frac{d\phi_n}{dt} \quad \{6.19\}$$

where  $i_n$  = current in filament n  
 $c(\phi)_n$  = specific heat capacity of the material of filament n at temperature  $\phi$   
 $\phi_n$  = temperature of filament n  
 $m_n$  = mass of filament n

Since both the specific heat capacity and the material resistivity are dependent on the filament temperature, their values must be calculated for each filament at each time step. To prove a simple and fast calculation of these parameters, approximate functions were used. The development of these functions is described in Appendix B.

### 6.1.3. MECHANICAL EQUATIONS

Before any mechanical equations can be developed, the force acting on each filament must be determined. The force component of most interest is that due to the interaction between the current carried in a filament and field that surrounds it. Applying the conservation of energy principle, and assuming that the current in the filament remains constant throughout each time step, the electromagnetic force acting per circumferential meter on filament n in the radial direction is given by

$$f_r = \frac{\sum_{n=1}^N \frac{1}{2} i_n i_m \frac{\partial M_{nm}}{\partial r_n} + \sum_{m=1}^N \frac{1}{2} i_n i_m \frac{\partial M_{nm}}{\partial r_m} + \frac{1}{2} i_n^2 \frac{\partial L_n}{\partial r_n}}{2\pi r_n} \quad \{6.20\}$$

and the force in the z direction on filamentary n is

$$f_z = \sum_{m=1}^N \frac{1}{2} i_m i_n \frac{\partial M_{nm}}{\partial z} \quad \{6.21\}$$

If it is assumed that the retarding force on the projectile can be modelled by the sum of a constant force and a force proportional to its velocity, then the motion of the projectile can be found from a force balance equation, if the projectile is considered as a whole. Thus

$$\sum_{m=1}^N \sum_{n=1}^N \frac{1}{2} i_m i_n \frac{\partial M_{nm}}{\partial z} = f_c + f_v u + m \frac{du}{dt} \quad \{6.22\}$$

where  $f_c$  = constant retarding force  
 $f_v$  = retarding force velocity coefficient

Equation 6.22 can be expanded to include aerodynamic drag and gravitational acceleration. Gravitational effect can be modelled by a constant retarding force, if the projectile is launched vertically. The inclusion of aerodynamic drag is discussed in the following section.

#### 6.1.4. AERODYNAMIC DRAG

The effect of aerodynamic drag depends on the ratio of the projectile speed to that of sound waves in the medium of flight (i.e. air). The speed of the projectile is usually broken down into three regions; subsonic, transonic and supersonic. Since it was expected that the initial practical work would not produce transonic or supersonic speeds, the study of drag was limited to the subsonic region.

At subsonic speeds the force due to aerodynamic drag can be calculated from

$$f_d = d \times A \times \frac{1}{2} \sigma_0 u^2 \quad \{6.23\}$$

where  $d$  = drag coefficient  
 $A$  = projectile surface area =  $\pi(r_o^2 - r_i^2)$   
 $\sigma_0$  = density of air = 1.204 kg/m<sup>3</sup> [123]

The effect of the angle of attack of a square plate and a disc are shown in Figure 6.8, where the angle is measured from the direction of motion [124]. Figure 6.9 shows how the drag coefficient of a disc is affected by a hole at its centre [124]. The diameter ratio 0 represents a solid disc and the ratio 1 represents an extremely fine

disc. The sharp increase in the drag coefficient is due to the flow around the projectile changing from a three to a two dimensional pattern.

Although some projectile yaw was expected, due to irregularities in the coil construction, this is unlikely to be more than  $45^\circ$  over the region of interest. Hence, it was assumed that the drag coefficient did not depend on the angle of attack. The effect of aerodynamic drag was modelled by the inclusion of a retarding force, which was proportional to the square of the velocity, so that the mechanical equation became

$$\sum_{m=1}^N \sum_{n=1}^N \frac{1}{2} i_m i_n \frac{\partial M_{nm}}{\partial z} = f_c + f_d u^2 + m \frac{du}{dt} \quad \{6.24\}$$

where  $f_d$  was calculated from equation 6.23 and where the drag coefficient  $d$  was found from Figure 6.9.

## 6.2. SOLUTION OF FILAMENTARY MODEL

Once the filamentary parameters have been determined, by using the equations developed in the previous section, they must be combined into a system of equations before being solved. Using standard coupled circuit theory and assuming the launcher to be magnetically linear, a system of simultaneous ordinary differential equations can be formed. The launcher circuit parameters can be expressed in the branch reference frame by equation 6.25, in which  $\mathbf{L}_{bb}$  is a function of the projectile position and  $\mathbf{R}_{bb}$  is a function of temperature.

$$\mathbf{V}_b + \mathbf{E}_b = \mathbf{R}_{bb} \mathbf{I}^b + \frac{d}{dt} (\mathbf{L}_{bb} \mathbf{I}^b) \quad \{6.25\}$$

The derivative term in equation 6.25 can be split into the translational and transformer components shown in equation 6.26.

$$\mathbf{V}_b + \mathbf{E}_b = \mathbf{R}_{bb} \mathbf{I}^b + \mathbf{D}_{bb} u \mathbf{I}^b + \mathbf{L}_{bb} \frac{d}{dt} \mathbf{I}^b \quad \{6.26\}$$



where  $\mathbf{D}_{bb}$  is the derivative of the inductances  $\mathbf{L}_{bb}$  with respect to the displacement in the direction of motion. The impressed voltage vector  $\mathbf{V}_b$  is zero, except for the supply capacitor voltage and the forward voltage drop across the conducting switch branches. Although the elements of equation 6.26 are relatively easy to determine, the equation cannot be solved directly, since the contents of the vector  $\mathbf{E}_b$  are unknown. By implementing the network analysis techniques described in Chapter 4, it is possible to transform equation 6.26 from the branch reference frame into the mesh reference frame to give

$$\mathbf{V}_m + \mathbf{E}_m = (\mathbf{R}_{mm} + \mathbf{D}_{mm} \mathbf{u}) \mathbf{I}^m + \mathbf{L}_{mm} \frac{d}{dt} \mathbf{I}^m \quad \{6.27\}$$

Although the parameters in equation 6.27 are not easily defined, it can be solved since  $\mathbf{E}_m$  must be zero in accordance with Kirchhoff's voltage law. Since the inductance and the rate of change of inductance terms are both functions of projectile displacement, and  $\mathbf{R}_{mm}$  is a function of temperature, they must be determined each time equation 6.27 is evaluated.

Although the inductances cannot be defined easily in the mesh reference frame, they can be defined in the branch reference frame and transformed into the mesh reference frame before being used in equation 6.27. In addition, the resistance matrix  $\mathbf{R}_{mm}$  is a function of the filament temperatures and it cannot be easily defined in the mesh reference frame. Hence  $\mathbf{R}_{mm}$  was found by calculating  $\mathbf{R}_{bb}$  and then transforming it into the mesh reference frame. All three transformations can be expressed in the form shown by equation 6.28, where the required branch matrix is substituted for  $\mathbf{Z}_{bb}$ , and the required mesh matrix is represented by  $\mathbf{Z}_{mm}$ .

$$\mathbf{Z}_{mm} = \mathbf{C}_m^{*b} \mathbf{Z}_{bb} \mathbf{C}_{*m}^b \quad \{6.28\}$$

Since the launcher equations are non-linear and time varying, they must be solved using the numerical techniques developed in Chapter 5. The electrical and mechanical equations were solved simultaneously, using a combination of single-step and multi-step methods. The basic model used a standard fourth-order Runge-Kutta algorithm to start a simulation. Once sufficient data have been generated, the model would switch

to using the more efficient Adams-Moulton and Adams-Bashforth, predictor-corrector combination. However, other numerical techniques were tested as described in Chapter 7.

The thermal time constants of the launchers were much longer than their associated electrical and mechanical time constants, and experience showed that acceptable results could be obtained when a forward Euler method was used to solve the thermal equations. Since these equations are easily defined in the branch reference frame, they were solved in this frame.

The capacitor and main switch are represented by a series combination of an ideal capacitor, resistor and inductor. The supply branches are considered to be electrically, but not magnetically, connected to the launcher. The capacitor voltage is found from equation 6.29, which is solved simultaneously with the electrical mesh equations, but in the branch reference frame,

$$v_c = \frac{1}{C} \int i_c dt \quad \{6.29\}$$

where the value of  $i_c$  is the value of the capacitor branch element in the  $\mathbf{I}^b$  vector, which is found by transforming the  $\mathbf{I}^m$  vector from the mesh reference frame. The capacitor voltage is included in the model by substituting the value  $v_c$  into the  $\mathbf{V}_b$  vector, before transforming into the mesh reference frame vector  $\mathbf{V}_m$ .

By considering equation 6.24 in matrix form, the total force on a projectile can be found from

$$\frac{1}{2} \mathbf{I}^{*b} \mathbf{D}_{bb} \mathbf{I}^b = f_c + f_d u^2 + m \frac{du}{dt} \quad \{6.30\}$$

Transforming equation 6.30 into the mesh reference frame enables the left-hand side to be expressed as

$$\frac{1}{2} \mathbf{C}_m^{*b} \mathbf{I}^{*m} \mathbf{C}_{*b}^m \mathbf{D}_{mm} \mathbf{C}_b^{*m} \mathbf{C}_{*m}^b \mathbf{I}^m \quad \{6.31\}$$

so that

$$\frac{1}{2} \mathbf{I}^m \mathbf{D}_{mm} \mathbf{I}^m = f_c + f_d u^2 + m \frac{du}{dt} \quad \{6.32\}$$

### 6.3. SPARSITY

Often problems involving the analysis of a physical system lead to a set of equations that are sparse, that is they have a large number of zero elements. Although such problems can be solved using conventional techniques, these are slow and are often limited by the size and speed of the available computers. However, it is possible to exploit the sparse nature of the matrices to greatly reduce the required computational power, without reducing the effectiveness of the model. Sparsity also has the added benefit of reducing the amount of computer storage required to hold a matrix, which in turn can also reduce the computation time required by a program.

During the implementation of the filamentary model two different sparse techniques were used. The first of these is based on an indexed matrix representation, and the second on matrix partitioning.

#### 6.3.1. INDEXED MATRIX SPARSITY

By storing only a representation of a matrix, and not the original matrix, it is possible to reduce the amount of computer memory required. One of the simplest methods of storing a sparse matrix is to use a co-ordinate system [125], in which the value and the row / column location of each of the non-zero elements are stored as three lists. Thus the example matrix  $\mathbf{A}$ , in equation 6.33 can be stored in the three lists given in Table 6.1.

$$\mathbf{A} = \begin{bmatrix} 3 & 0 & 0 & 0 & 0 \\ 0 & 2 & 0 & 0 & 0 \\ -1 & 0 & 2 & 0 & 0 \\ 0 & 0 & 0 & -1 & 0 \\ 0 & 0 & 5 & 0 & 0 \end{bmatrix} \quad \{6.33\}$$

Value	3	2	-1	2	-1	5
Row	1	2	3	3	4	5
Column	1	2	1	1	4	3

Table 6.1 Simple sparse form of A

It will be seen from this table that the amount of data storage space required decreases from 25 to 18 elements. When this method is applied to much larger and more sparsely populated matrices, the reduction in the computer storage space required clearly outweighs the slight additional complexity of the necessary computer code.

All the elements in the network connection matrices used in this thesis only need to contain one of three possible values, -1, 0, and 1. If the locations of the positive and negative elements are stored separately, there is no need to store their values only their locations are required [117]. The example in equation 6.34 can be represented by the four lists shown in Table 6.2.

$$A = \begin{bmatrix} 1 & & & & & & & & & & \\ & -1 & & & & & & & & & \\ & & & & & & & & & & \\ & & & 1 & 1 & -1 & & & & & \\ & & & 1 & & & 1 & 1 & & & \\ & & & & & & & & & & -1 \end{bmatrix} \quad \{6.34\}$$

Positive	Row	1	3	3	2	4	5
	Column	1	2	3	4	4	4
Negative	Row	1	2	3	5		
	Column	3	1	4	5		

Table 6.2 Sparse form of A

Although this method requires four lists to be stored, it provides a significant improvement in speed when considering matrix multiplication. Multiplication of other matrices by the connection matrix and its transpose are required each time a quantity is transformed from one reference frame to another, which must be completed several times during each time step. By using the connection matrix in the form described above, these large matrix multiplications can be replaced by a series of additions and subtractions of individual elements, much improving the speed of the program.

### 6.3.2. MATRIX PARTITIONING

Matrix partitioning can reduce the computation time and the data storage required when handling large matrices, even when they are full. By splitting a matrix into separate sub-matrices, it is possible to take advantage of inherent symmetries and redundancies within the original matrix. If the block of ones in the middle of the matrix  $\mathbf{A}$  in equation 6.35, and the diagonal symmetries in the sub-matrices  $\mathbf{a}$  and  $\mathbf{b}$  can be implied, then only 12 elements need to be stored, as opposed to the original 48 elements.

$$\mathbf{A} = \begin{bmatrix} 24 & -4 & 6 & 1 & 1 & -3 & 2 & 8 \\ -4 & 15 & 7 & 1 & 1 & 2 & 6 & -10 \\ 6 & 7 & 36 & 1 & 1 & 8 & -10 & 7 \\ -3 & 2 & 8 & 1 & 1 & 24 & -4 & 6 \\ 2 & 6 & -10 & 1 & 1 & -4 & 15 & 7 \\ 8 & -10 & 7 & 1 & 1 & 6 & 7 & 36 \end{bmatrix} = \begin{bmatrix} \mathbf{a} & 1 & \mathbf{b} \\ \mathbf{b} & 1 & \mathbf{a} \end{bmatrix} \quad \{6.35\}$$

Matrix partitioning was used in the filamentary model to reduce the computation required when calculating both the inductance and the rate of change of inductance matrices. The branch elements were collected into three groups; drive coil branches, projectile branches, and power supply branches, which leads to the branch matrices being sub-divided into the nine sections shown in equation 6.36. By taking advantage of the inherent symmetry in the  $\mathbf{L}_{bb}$  and  $\mathbf{D}_{bb}$  matrices, only half the calculations that would be needed for a full matrix are actually required. In addition, the large number of zero elements in the  $\mathbf{D}_{bb}$  matrix allows it to be reduced, as shown in equation 6.37. If the connection matrix is correctly sub-divided into nine sections, in a manner similar to that used for the branch matrices, some of the matrix partitioning can be maintained when  $\mathbf{D}_{bb}$  is transformed into  $\mathbf{D}_{mm}$  using equation 6.28, as shown in equations 6.38 to 6.40.

$$\mathbf{Z}_{bb} = \begin{bmatrix} Z_d & Z_{pd} & Z_{sd} \\ Z_{dp} & Z_p & Z_{sp} \\ Z_{ds} & Z_{ps} & Z_s \end{bmatrix} \quad \{6.36\}$$

$$\mathbf{D}_{bb} = \begin{bmatrix} 0 & \mathbf{D} & 0 \\ \mathbf{D}^T & 0 & 0 \\ 0 & 0 & 0 \end{bmatrix} \quad \{6.37\}$$

$$\mathbf{D}_{mm} = \begin{bmatrix} \mathbf{C}_d^T & & \\ & \mathbf{C}_p^T & \\ \mathbf{C}_{ds}^T & & \mathbf{C}_s^T \end{bmatrix} \begin{bmatrix} \mathbf{D}^T & \mathbf{D} \\ & \end{bmatrix} \begin{bmatrix} \mathbf{C}_d & \mathbf{C}_{ds} \\ & \mathbf{C}_p & \mathbf{C}_s \end{bmatrix} \quad \{6.38\}$$

$$\mathbf{D}_{mm} = \begin{bmatrix} \mathbf{C}_d^T & & \\ & \mathbf{C}_p^T & \\ \mathbf{C}_{ds}^T & & \mathbf{C}_s^T \end{bmatrix} \begin{bmatrix} \mathbf{D}^T \mathbf{C}_d & \mathbf{D} \mathbf{C}_p \\ & \mathbf{D}^T \mathbf{C}_{ds} \end{bmatrix} \quad \{6.39\}$$

$$\mathbf{D}_{mm} = \begin{bmatrix} & \mathbf{C}_d^T \mathbf{D} \mathbf{C}_p & \\ \mathbf{C}_p^T \mathbf{D}^T \mathbf{C}_d & & \mathbf{C}_p^T \mathbf{D}^T \mathbf{C}_{ds} \\ & \mathbf{C}_{ds}^T \mathbf{D} \mathbf{C}_p & \end{bmatrix} \quad \{6.40\}$$

Using this partitioned form of  $\mathbf{D}_{mm}$  can also reduce the amount of calculation required to determine the force acting on a projectile. Since  $\mathbf{D}_{mm}$  is post-multiplied by  $\mathbf{I}^m$  and pre-multiplied by the transpose of  $\mathbf{I}^m$ , the required factor of a half can be implemented by ignoring the non-zero elements below the leading diagonal in  $\mathbf{D}_{mm}$ , when equation 6.32 can be rearranged as

$$\mathbf{I}^m \begin{bmatrix} 0 & \mathbf{C}_d^T \mathbf{D} \mathbf{C}_p & 0 \\ 0 & 0 & \mathbf{C}_p^T \mathbf{D}^T \mathbf{C}_{ds} \\ 0 & 0 & 0 \end{bmatrix} \mathbf{I}^m = f_c + f_d u^2 + m \frac{du}{dt} \quad \{6.41\}$$

#### 6.4. DISCONTINUITIES

To allow the action of the power supply switches to be modelled, it is necessary to ensure that the model is able to deal with discontinuities. The actions of both the main and crowbar switches were implemented by the addition and removal of appropriate meshes from the equations. The diode switches turn on when the voltage applied

across them in the forward bias direction is greater than the switch forward conducting voltage drop. The triggered switches only start conducting when triggered, which is usually at the beginning of a simulation. All the switches turn off when the current flowing through them either drops to zero or attempts to reverse.

After each time step, the model checks to see if one or more of the switches has changed state during that step. Due to the nature of the equations that are being solved, the location of any discontinuity must be found reasonably accurately. If it not determined correctly the simulation may become unstable and the switch operation may become oscillatory. The linear interpolation routine used to estimate the location of a discontinuity is based on a single-stage of an iterative location technique developed for power system analysis [117]. Figure 6.10 shows an example of a switch turning off, as the current flowing through it attempts to reverse. The program integrates normally between A and B, and then again between B and C; however when the program reaches point C the discontinuity routine flags the fact that the switch state should have changed. Using linear interpolation between the values at the start and the end of the step, the time at which the switch should have stopped conducting is calculated. Once the point of discontinuity D has been determined, the model re-integrates between the last time step B and the discontinuity, by using a single-step method. The switch mesh affected is then removed from the connection matrix, and the derivatives recalculated at point D. Due to the different conditions that can apply after a discontinuity, the step size is usually adjusted to maintain the required accuracy. Once the step size has been adjusted the simulation is restarted, by using a single-step method, until sufficient data has been acquired to allow the model to switch to a multi-step method of integration.

## 6.5. INITIAL MODEL VALIDATION

To check the validity of the filamentary model, results from a static model were compared with those from a finite element model. Using MEGA a finite element test model was constructed, and a filamentary model was developed for the same launcher arrangement [Appendix C]. Figure 6.11 and Figure 6.12 compare the drive coil currents and capacitor voltages respectively, and the two sets of results can be seen to

have the same general characteristics. MEGA also provided two methods of force calculation, and results from these are compared with the force calculated from the filamentary model in Figure 6.13. Figure 6.14 and Figure 6.15 show the current density and filamentary current respectively, over a series of time steps. From the above comparisons it was concluded that the filamentary modelling program worked as expected and that the equations used in this model produced similar results to those from the finite element model.

## 6.6. CONCLUSIONS

Using a filamentary approach it is possible to develop an equivalent circuit method of modelling what would otherwise be a complex electromagnetic field problem. Methods of dividing the conductors into filaments were developed for both rectangular and round conductors. Equations for the individual filament inductances were described. In addition, the rates of change of filament inductances were formulated, some of which have not previously been used in this application. Mechanical equations of motion were based on a simple force balance equation, which included the effect of aerodynamic drag on the projectile. While all the filamentary parameters were defined in a branch reference frame, the system was transformed into a mesh reference frame, to enable a solution to be obtained. To improve the computation speed of the model, and to reduce the amount of storage required, two sparse techniques were used. An indexed matrix method was developed that allowed the connection matrix to be stored, by storing only the location of the positive and negative elements. This allowed matrix additions and subtractions to be used to replace large matrix multiplications. The second sparse technique used matrix partitioning to reduce the computer storage and processing that the model required. A discontinuity system was developed to allow the model to simulate the switching action of the power supply switches. The equations developed and described form the basis of the filamentary model used in this thesis. By comparison with a finite element model it was shown that the filamentary model provided a fast and accurate method of simulating a launcher.



6.7. FIGURES

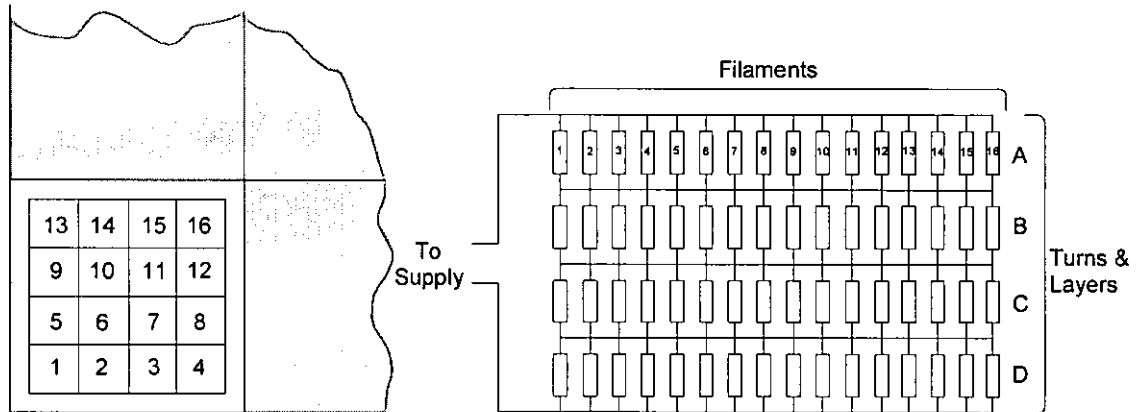


Figure 6.1 Rectangular conductor definition

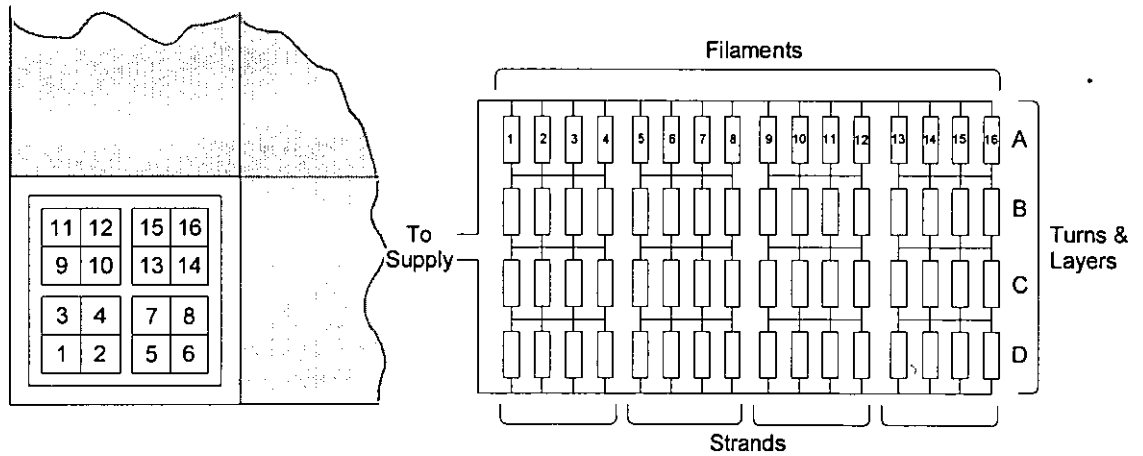


Figure 6.2 Stranded conductor definition

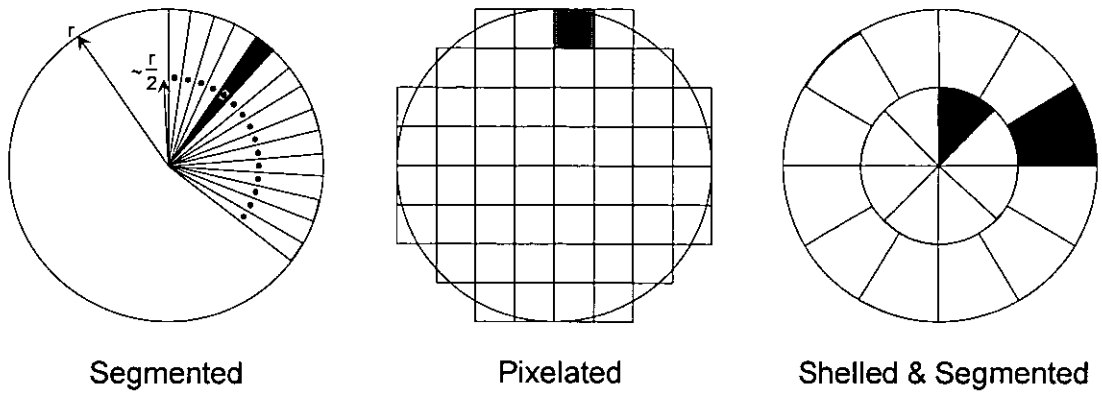


Figure 6.3 Different possible methods of dividing up a circular conductor

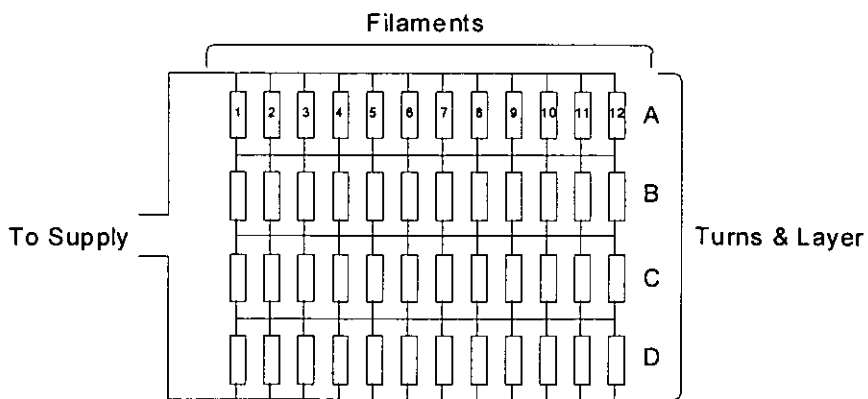
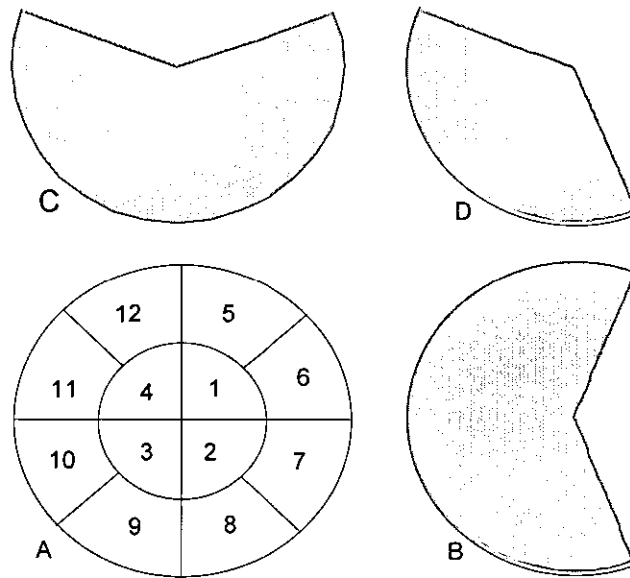


Figure 6.4 Circular conductor definition

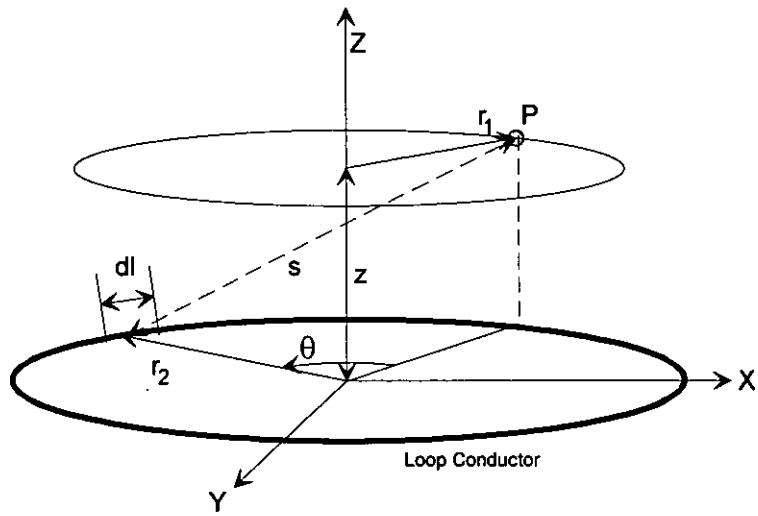


Figure 6.5 Location of point P

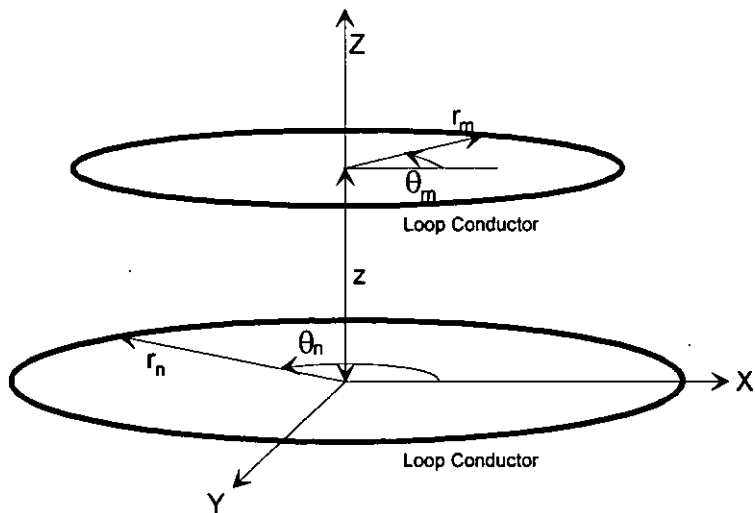


Figure 6.6 Location of two loop conductors

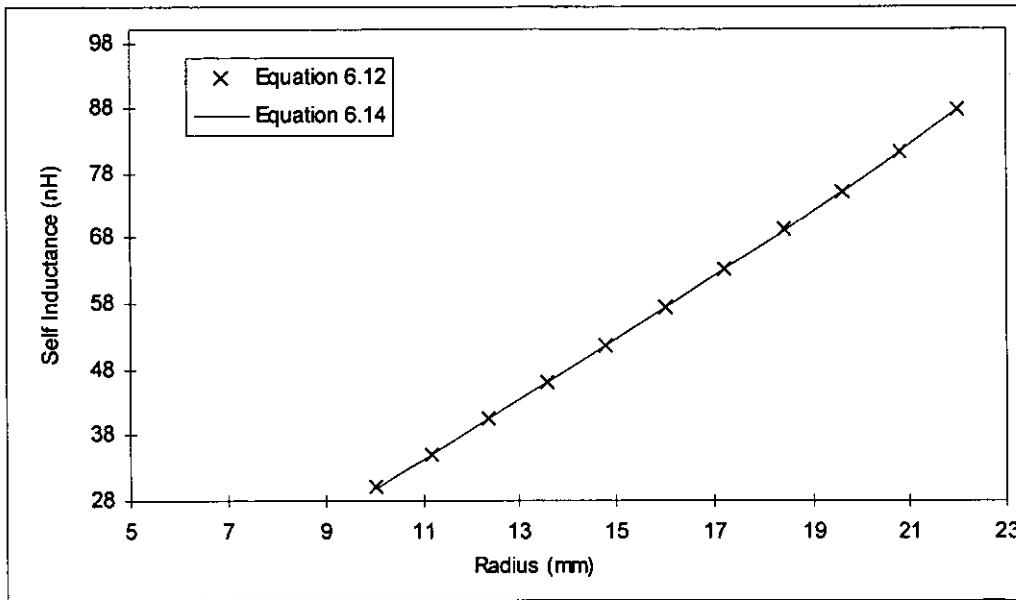


Figure 6.7 Comparison between methods of self inductance calculation

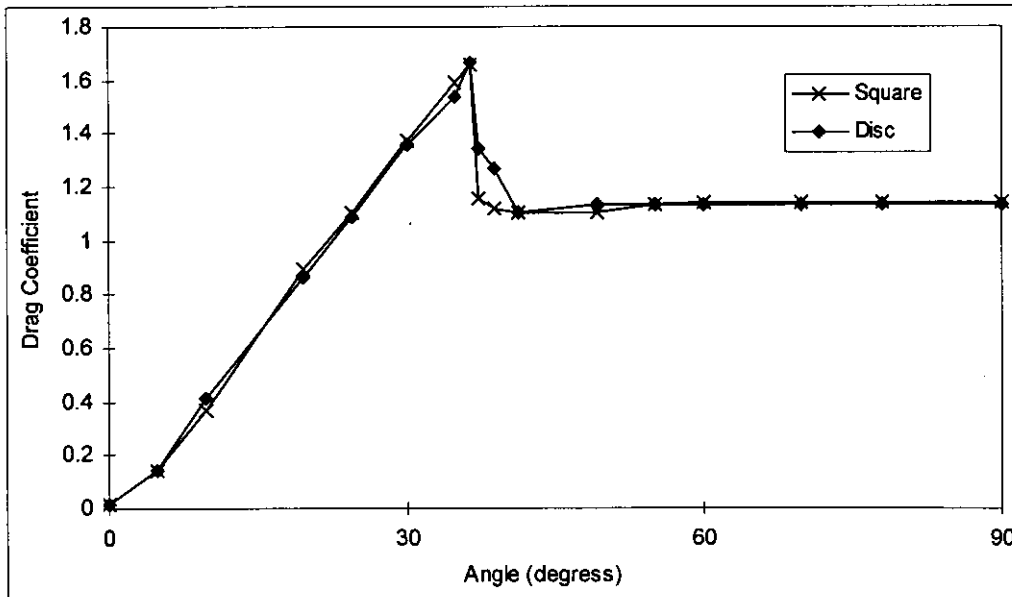


Figure 6.8 Effects of angle of flight for square and round plates

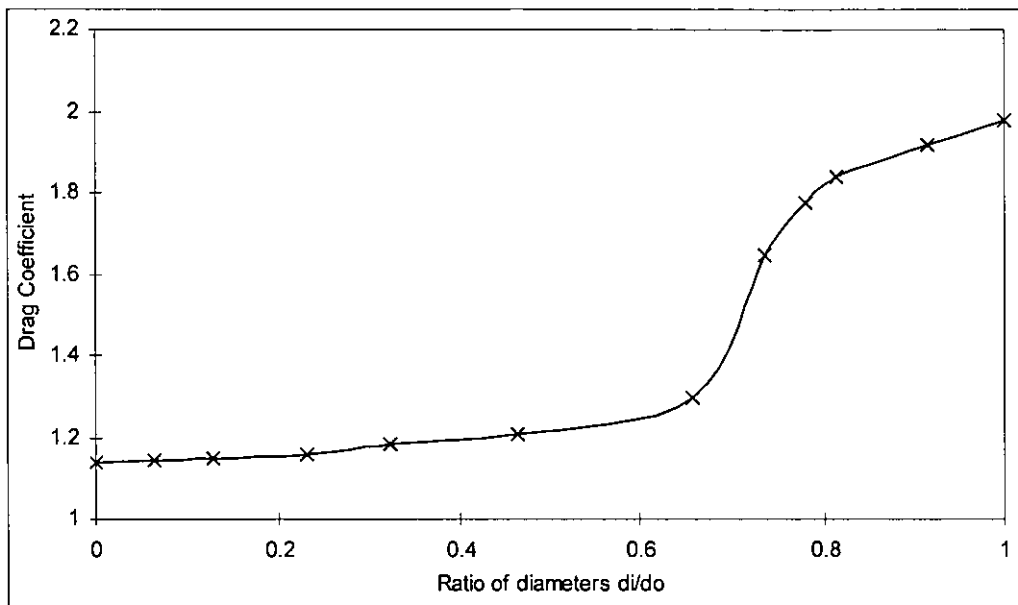


Figure 6.9 Effects of a hole in the centre of a disc

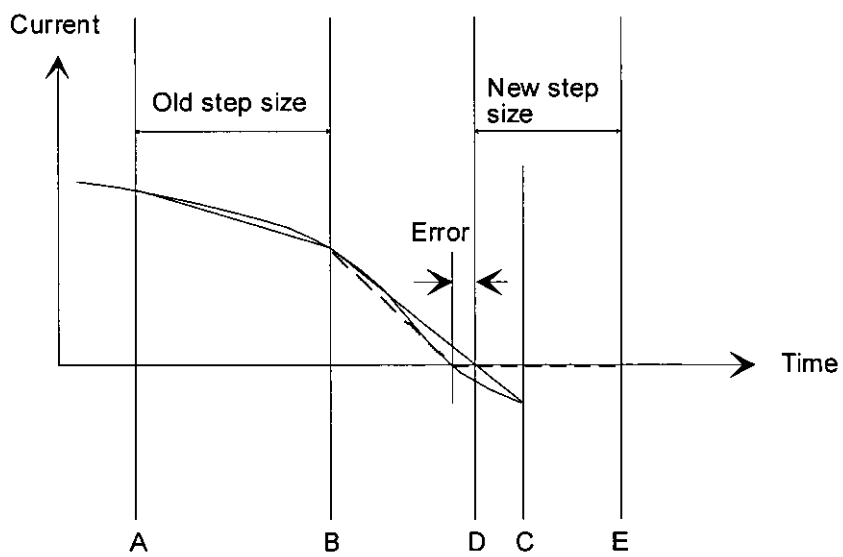


Figure 6.10 Example of a switch turn off discontinuity

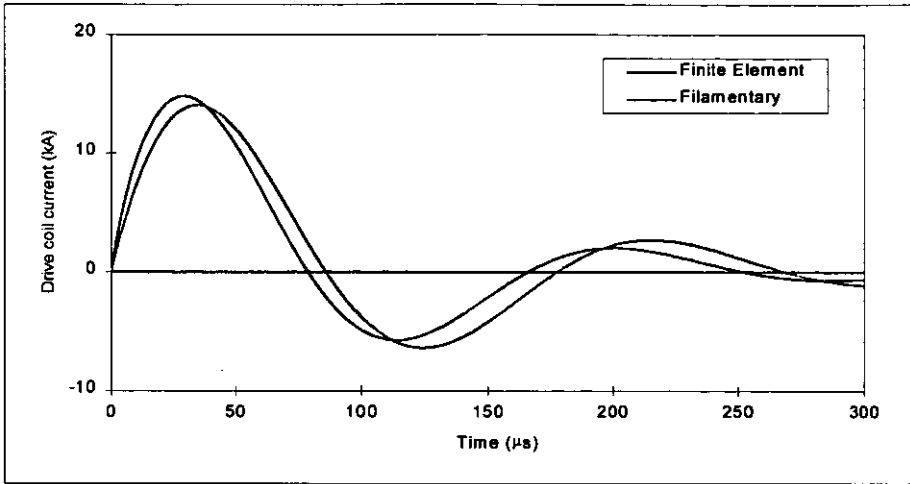


Figure 6.11 Comparison of predicted drive coil currents

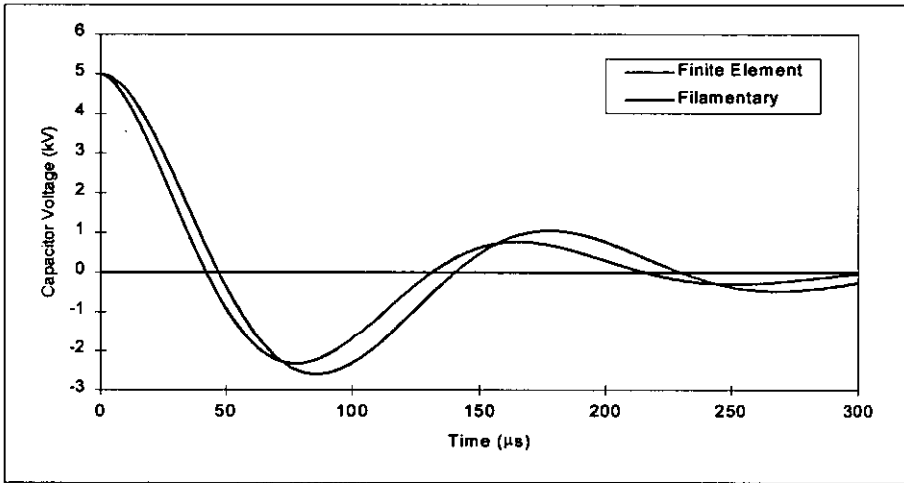


Figure 6.12 Comparison of predicted capacitor voltages

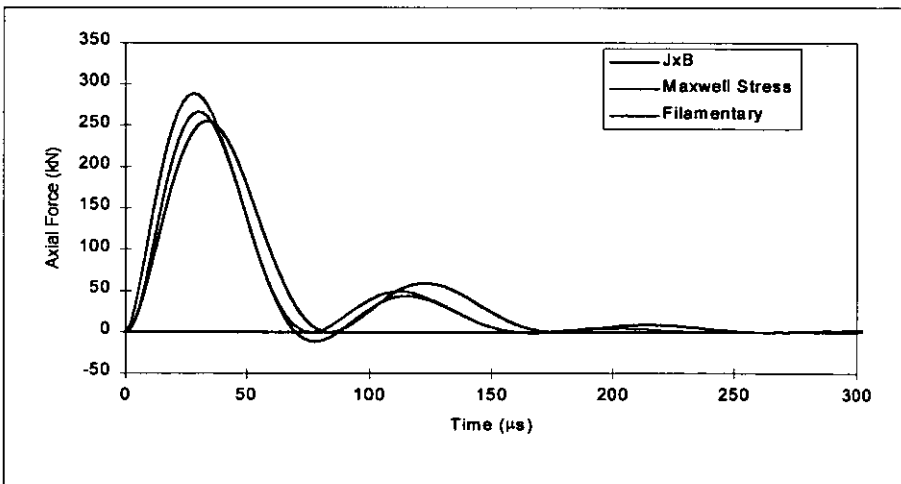


Figure 6.13 Comparison of predicted axial forces

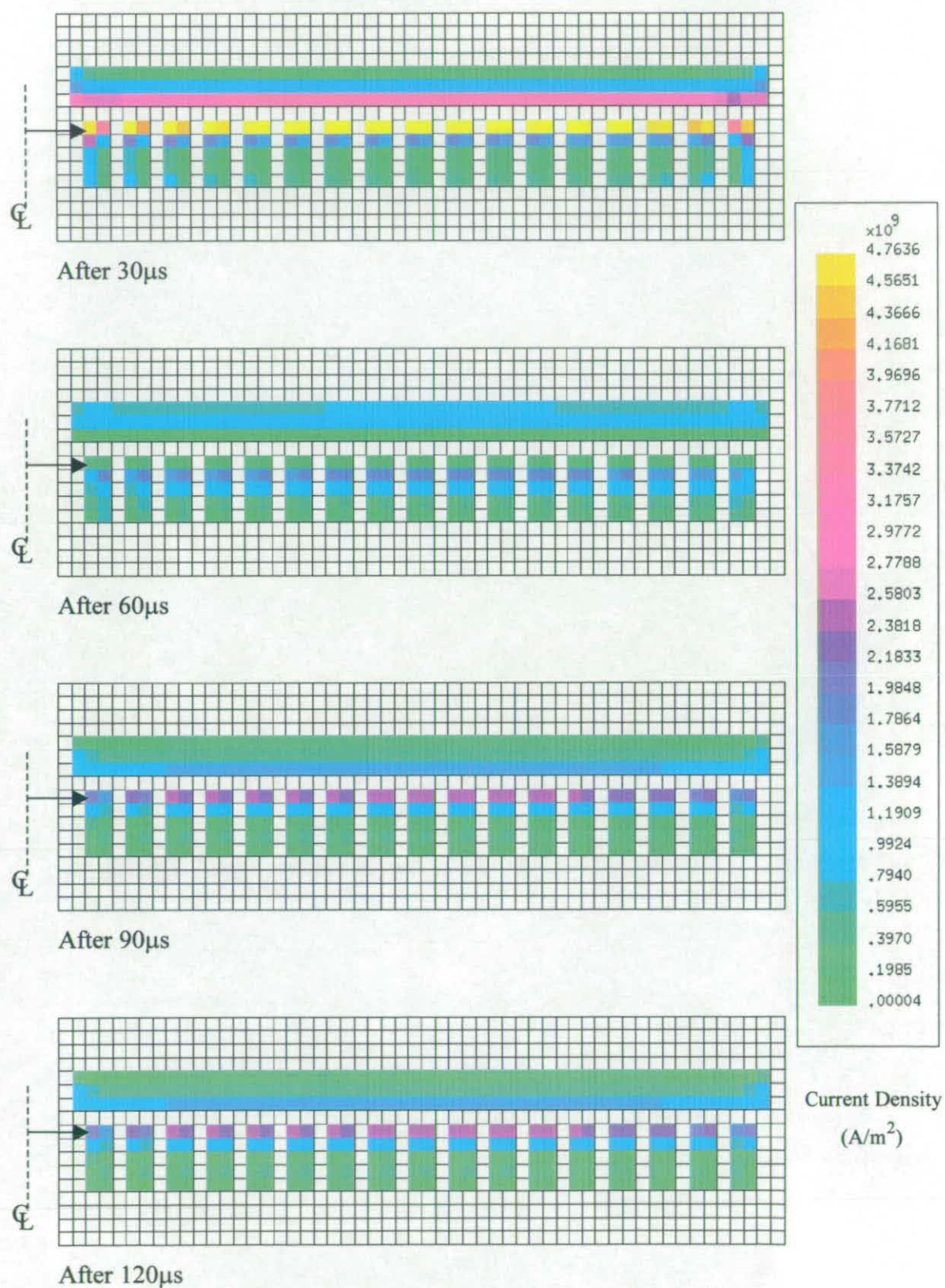


Figure 6.14 Current at densities predicted by the finite element model



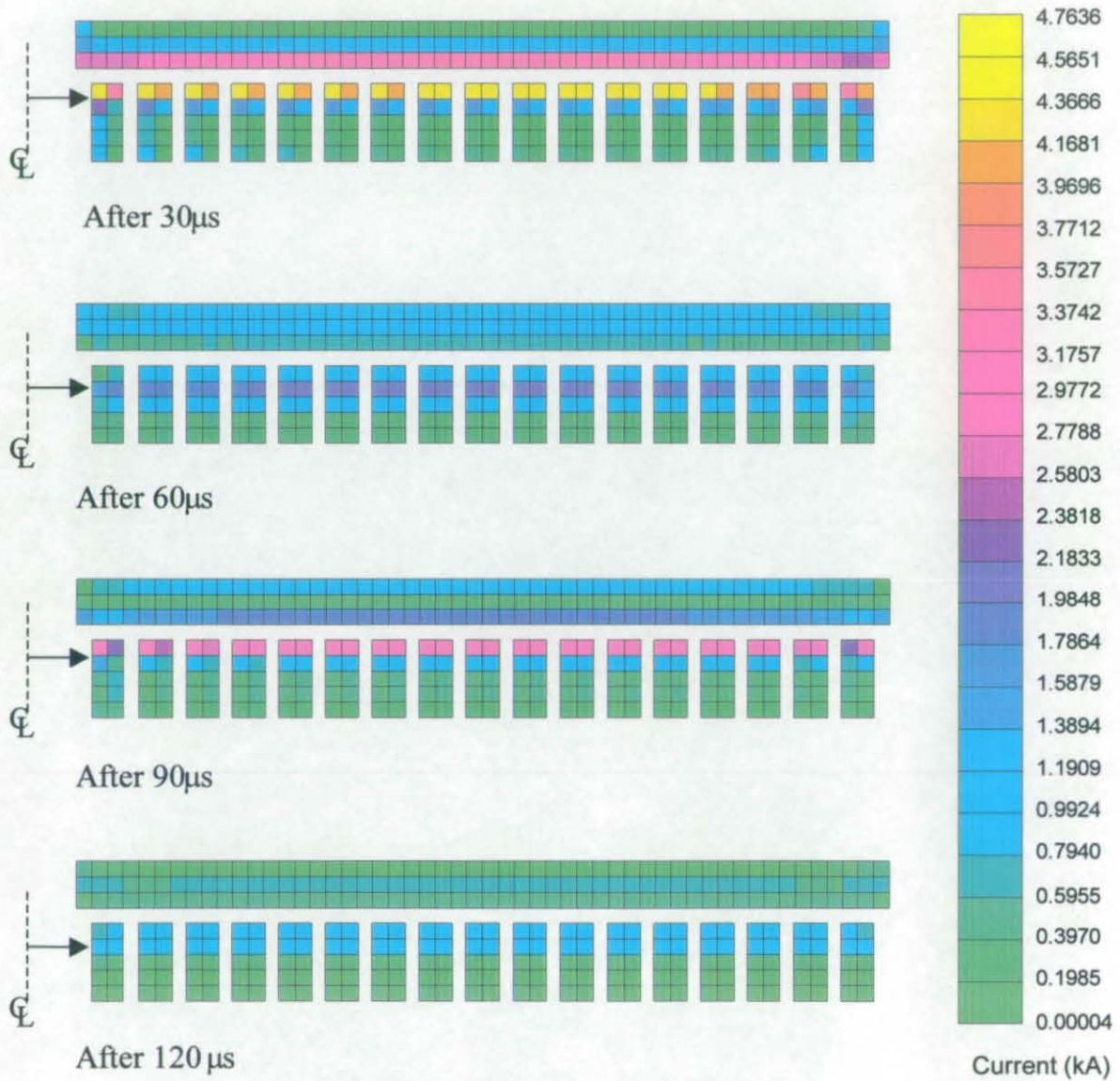


Figure 6.15 Predicted filamentary currents



## 7. DEVELOPMENT OF FILAMENTARY MODEL

*The first part of this chapter describes several different techniques and methods developed to reduce the time required to solve the filamentary model equations. The second section describes the expansion of the filamentary model to include the mechanical deformation of the projectile, and to provide greater power supply flexibility.*

### 7.1. PROGRAM SPEED IMPROVEMENTS

Before any attempt was made to improve the performance of the program, a study was undertaken to determine which areas of the program were the least efficient. The results of this showed a large proportion of the computer time was taken up by just a few subroutines, with the processor time distribution indicated in Figure 7.1. However, since the program was run on a multi-user computer the time to run a model was heavily dependent on the other tasks running at the same time. To allow useful comparisons to be made, each simulation was run ten times and the average results were used. Since the computer loads varied widely with the time of day, each of the ten simulations were run at different times during the day to produce a real average. Details of the test simulation used in these and later timing tests is shown in Appendix C.

From Figure 7.1, it can be seen clearly that the explicit matrix inversion routine requires the greatest proportion of the processor time, and although some attempt was made to improve the performance of this routine, no significant improvement resulted. To reduce the time for the matrix inversions, other methods of matrix factorisation were tested, and the use of an implicit matrix inversion method reduced the processor time by 37%. Despite this reduction the factorisation routine still dominated the total processor time. Using LU matrix factorisation reduced the processor time by a further 23%. After some minor adjustments, it was decided that no further improvement in the matrix factorisation routine was possible. Attention

was then focused on the second transformation routine, used to transform the filament inductances from the branch to the mesh reference frame. Changes in the order of some operations and other minor changes lead to an improvement in the computer run time of 16%. Focused then moved to the system call routines, which in total were the third largest consumers of the computer time. The majority of these calls were to `$$fill` routines. It was found that they were caused by the use of the `“$init on”` directive, which instructs the compiler to fill all new matrices with zeros. Although it was necessary to blank some of the new matrices before they were used to store data, it was possible to achieve the same results with the addition of a few extra loops. Removing the need for the `$$fill` subroutine reduced the overall processor time by a further 12%.

It appeared possible that calculating the branch inductances before the start of a simulation, instead of during each time step, would greatly improve the performance of the modelling program. The self inductance of a filament only changes if the filament size or shape is changed, hence the self inductances of all the filaments remained constant, as the coils were assumed to be rigid. The mutual inductance between two filaments changes if the filaments move with respect with each other, and with the coils assumed to be rigid there is only relative movement between the drive and projectile coils. Hence, the mutual inductance between two filaments in the same coil also remains unchanged. Calculating the fixed inductances before the start of a simulation reduced the time required for a simulation by about 7%.

Although the elliptic integral functions, `E` and `K` required very little processor effort, the fact that they were called almost 19,000,000 times during the test simulation caused them to use a significant amount of processor time. However, the routines were very simple, and no speed improvement could be made. Fortunately, the introduction of some temporary variables into the inductance calculation routines reduced the number of calls to the functions to 9,500,000 and produced a 4% reduction in the overall processor time. Figure 7.2 shows how the improvements described above effected the average run time for the test simulation.

## 7.2. PRE-CALCULATED INDUCTANCE

The self and mutual inductance of filaments in the same coil were calculated and stored in the branch reference frame, before the start of a simulation. It was proposed that if the mutual inductances between the moving filaments were also calculated before the start of a simulation, this would lead to an improvement in the performance.

However, since the mutual inductance between relatively moving filaments changes with displacement, it was proposed that an interpolation function could be used to determine the required variations from a range of pre-calculated inductances. Although the radius of every filament was considered as fixed, it was not possible to produce a system in which only the relative displacements were interpolated, since this would require a different interpolation for each pair of filaments. A general interpolation function for all filaments, had to include both the filament radii and their relative displacements, and therefore a four dimensional interpolation was required.

The first method of interpolation tested was a linear interpolation function, in which the mutual inductance was calculated over a range of steps in both radii and displacement before the start of a simulation. During the simulation, the interpolation function selected the values closest to the point of interest and interpolated between them, to calculate the required mutual inductance. A linear interpolation method was successfully implemented, but due to the limited stability of the model any small errors in the mutual inductance calculation led to the program becoming unstable, before most simulations ended. Increasing the number of points at which the mutual inductance was pre-calculated improved the stability of the program, but slowed it down greatly.

The linear interpolation method showed that the desired speed improvements could be obtained if the accuracy of the interpolation routine was improved. It was thought that a cubic spline method might provide the required accuracy without too much computation.

### 7.2.1. CUBIC SPLINE INTERPOLATION

The cubic spline method fits a smooth curve to a set of data points. Although it is based on polynomials, it does not require a polynomial to be fitted over the whole region of interest, but rather it fits successive polynomials over small sub-regions. The simplest form of a spline interpolation is a single order polynomial, which is a linear interpolation, but this has the disadvantages that it is inaccurate and discontinuous at each data point. Spline curves with more than one degree of freedom have however a continuous slope. Since the mutual inductance between two coils is a smooth function, it was hoped that use of a smooth interpolation routine would improve the accuracy of the program. The most common piece-wise polynomial interpolation method is the cubic spline method, which uses cubic polynomial approximations between successive pairs of data points. A general cubic polynomial is defined by four coefficients to ensure that the interpolant is continuous in both the first and second derivative and that it passes through all the original data points. The equation for a cubic spline in the  $i^{\text{th}}$  interval, that is between the data points  $(x_i, y_i)$  and  $(x_{i+1}, y_{i+1})$ , can be expressed by

$$g_i(x) = a_i(x - x_i)^3 + b_i(x - x_i)^2 + c_i(x - x_i) + d_i \quad \{7.1\}$$

where  $a$ ,  $b$ ,  $c$  and  $d$  are the four coefficients of the  $i^{\text{th}}$  interval, and  $g$  is the resultant approximate function.

While the above equation defines the cubic spline for internal points, there are several methods of defining the boundary conditions. The one used here is the free or natural boundary condition, in which the second derivative of the cubic spline is set to zero at its end, as shown below.

$$g_0''(x_0) = g_n''(x_n) = 0 \quad \{7.2\}$$

The natural boundary condition was chosen, as this was the simplest to implement. With the original data points correctly chosen, the first and last approximations will never be needed and the boundary conditions will not affect the accuracy of the model.

A four dimensional cubic spline method was developed, using several standard cubic splines [96] combined to calculate the required mutual inductance. The spline coefficients were calculated from the pre-calculated mutual inductance data as required while the model was running. Direct comparison of some example mutual inductances shown that the cubic spline method was more accurate than the linear interpolation method, which meant that the model did not fail so often. Although the cubic spline method worked, it actually took longer than with the original model. It was decided therefore that pre-calculating the variable mutual inductances was unlikely to produce any improvement in the solution time.

### **7.3. VARIABLE TIME STEPPING PROGRAM**

A variable time stepping program was written to reduce the computation time, and to improve the reliability of the program, with originally two possible step-lengths being used to prevent the program crashing during commutation of the main and crowbar switches. Although the step-lengths were set individually for each simulation, it was found from experience that values of  $1\mu\text{s}$  and  $0.1\mu\text{s}$  were adequate for most situations. Although it is a simple matter to reduce the step-length and to re-run a simulation should the solution become unstable, this can become time-consuming if a simulation has to be restarted several times.

It was hoped that the use of a variable time step would allow more stable simulations to be achieved in a reduced number of steps, and thus reduce the need to re-run the more unstable simulations. To enable any time step varying model to operate, it is necessary to know the accuracy of the model. It is obviously impossible to compare a numerical model to an exact solution, in all but the simplest situations, to provide an indication of the global error in a simulation, most methods evaluate the local error at each time step. As previously mentioned, the original program used a combination of a fourth-order Runge-Kutta and a fourth-order Adams-Moulton / Adams-Bashforth predictor-corrector methods, while the local error of the Runge-Kutta method was found by using the Runge-Kutta-Fehlberg and Runge-Kutta-Merson methods as described in Chapter 5. These two methods were implemented to determine which of these required the least computational effort. After testing both methods on the test

simulation it was found that the Runge-Kutta-Merson approach was significantly faster. The local error of the predictor-corrector method was found directly from the original method, as described in Chapter 5. Although three different methods of estimating the local truncation error were implemented these were all used to vary the time step-length in the same manner. Since the coefficients of all three methods are dependent on the step-length  $h$ , then the local truncation error  $E$  for any of these methods can be approximated to equation 7.3 for a  $n^{\text{th}}$  order system,

$$E(h) = O(h^n) \quad \{7.3\}$$

where  $O(x)$  represents a number of the order  $x$ .

Assuming that equation 7.3 can be re-written to given equation 7.4, and that the new step-length is defined by  $qh$ , then the new error can be expressed by equation 7.5.

$$E(h) \approx Kh^n \quad \{7.4\}$$

$$E(qh) \approx K(qh)^n = q^n (Kh^n) \approx q^n E(h) \quad \{7.5\}$$

Since the aim of a variable step-length algorithm is to ensure that the error remains within a given tolerance, the error must be bounded by a given error limit  $\epsilon$ .

$$\therefore E(qh) \leq \epsilon \quad \{7.6\}$$

hence

$$q^n \leq \frac{\epsilon}{E(h)} \quad \{7.7\}$$

Since all the methods used in this thesis are fourth-order,  $q$  can be found from

$$q = \left( \frac{\epsilon}{E(h)} \right)^{1/4} \quad \{7.8\}$$

To prevent the results of a singular time step changing the step-length to an unsustainable value,  $q$  is usually limited as shown below.

$$0.1 \leq q \leq 4$$

{7.9}

Although the variable step-length can easily be calculated by the above method, care must be given to its implementation. When the program uses a single-step method it can simply change the step-length and continue with the next time step. If however the program uses a multi-step method, after each step-length change the program must switch to the more time-consuming single-step method. Only when the step-length has remained sufficiently constant to collect the required history data, could the program revert to using a multi-step method. Although many programs have been developed that use a variable time step approach, the filamentary model developed here has the added complication that the system being modelled changes due to the switching discontinuities.

Figure 7.3 shows how the variable time step approach was integrated with the discontinuity routines to ensure the simulation remained stable. Since the accuracy of the time step after a discontinuity cannot be predicted, the time step was arbitrarily divided by ten, to prevent the program crashing after the discontinuity. Although the rate at which the step-length increases is limited by enforcing the inequality in equation 7.9, the step-length could still grow to an unreasonable size. To prevent the step-length becoming too large a maximum step-length was imposed, which greatly improved the reliability of the program.

When the variable time step-length algorithm was implemented, it reduced the number of steps required to solve the test model from 493 to 265, and was able to solve simulations that repeatedly crashed when using the original model. Although the model worked in most situations, it was occasional possible that a simulation would cause the time step-length to change almost every step in an oscillatory manner.

#### **7.4. INSTANT CROWBAR TURN ON**

When a discontinuity occurs, the size of the time step is often changed to ensure that the program remains stable. When both switches are conducting, the step-length is reduced to prevent the increased rates of change of current in the power supply circuit

making the program unstable. To achieve this, the step-length must often be reduced by more than an order of magnitude, but the use of very small time steps slows down the simulation dramatically. It was considered that if the main and crowbar switches were assumed to commute instantaneously there would be no need for the smaller step-lengths. By implementing an instantaneous crowbar turn on, the number of steps required for the test simulation was in fact reduced from 493 to 400. It can be seen from Figure 7.4 that this instantaneous action leads the model to predict a slightly higher crowbar current. From Figure 7.5, it can also be seen that the capacitor voltage does not drop below the forward voltage drop of the crowbar switch, when the switches commute instantly. There is no significant negative voltage build up on the capacitor bank, since the main switch ceases conduction as soon as the crowbar switch starts to conduct. This idealised situation is obviously more efficient, since no significant energy is returned to the capacitor, as is the case in the more realistic model. Although a slight improvement in the maximum velocity can be seen in Figure 7.6, it is apparent from Figure 7.7 to Figure 7.9 that the instantaneous crowbar turn on does not greatly affect the mechanical results.

Although modelling a system with an instantaneous crowbar turn on reduces the accuracy, it provides a much faster solution. The faster program could be used to find an area of interest during an investigation, before using the original program to investigate the area in more detail.

## 7.5. SINUSOIDAL APPROXIMATION

After adopting the program speed improvements described above, it was thought unlikely that any further improvements to the original program could be made. It was therefore decided that an alternative approach to the solution of the model equations was required, and the first approach investigated was the sinusoidal approximation method.

It was observed that the majority of the projectile acceleration occurred before the main switch ceased conduction. A method for producing a quick comparison between simulations seemed possible, if it was assumed that the crowbar current had only a



limited effect. Under this assumption, there would be no difference in the performance of a system if it were allowed to oscillate. The main switch current in an oscillatory system can then be represented by

$$i(t) = B e^{-\alpha t} \sin(\omega t) \quad \{7.10\}$$

where  $B$ ,  $\alpha$  and  $\omega$  are constants.

By simplifying the system a step further, the main current can be considered to be part of a simple sine wave function. Figure 7.10 shows a comparison between the main switch current predicted by the original filamentary model, an exponentially decaying sine wave, and a sine wave. Although the exponential function provides a very close fit to the current predicted by a full filamentary model, the use of this function did not lead to the required simplification in the problem. The simple sine wave system was therefore investigated, and it was hoped that a fast approximate solution would be possible. When a finite element model was tested using the sinusoidal steady-state solver built into MEGA, the encouraging initial results led to the development of a filamentary sinusoidal model. Using the complex notation that is part of the Fortran language, the filament inductances and resistances were calculated in the branch reference frame. The complex branch parameters were transformed and combined to produce the complex mesh impedance matrix  $\mathbf{Z}_{mm}$ . The solutions of the electrical equations were found by solving

$$\mathbf{I}^m = \mathbf{Z}_{mm}^{-1} \mathbf{V}_m \quad \{7.11\}$$

If the supply is considered to be an ideal voltage source, the coefficient values in  $\mathbf{V}_m$  require setting. If however the power supply is considered as an ideal current source, the electrical system of equations can be re-written as

$$\mathbf{V}_m = \mathbf{Z}_{mm} \mathbf{I}^m \quad \{7.12\}$$

Unfortunately, using equation 7.12 requires the whole model to be re-formulated. To enable the formation shown in equation 7.11 to be used, and to allow both ideal current and voltage sources to be modelled in the same simulation, the ideal current

sources were first transformed into equivalent ideal voltage sources, by applying equation 7.12 to only the meshes that included the ideal currents. The resultant voltages were subsequently added to the ideal voltage sources, before solving equation 7.11. Once the electrical equations had been solved, the force on the projectile was found from

$$f = \frac{1}{2} \mathbf{I}^{\bullet m} \mathbf{D}_{mm} \mathbf{I}^m \quad \{7.13\}$$

where  $\mathbf{D}_{mm}$  is the rate of change of mutual inductances when they have been transformed into the mesh reference frame, in a manner similar to  $\mathbf{Z}_{mm}$ . Since the sinusoidal approximation model was not solved transiently, it had to be assumed that the projectile remained static. Since the force is the product of two out of phase sine waves, it can be expressed as the sum of a continuous and a double frequency sinusoidal component. Thus if the force is considered as the product of the two sinusoidal components  $a$  and  $b$

$$a = |A| e^{j\alpha} \quad \text{and} \quad b = |B| e^{j\beta} \quad \{7.14\}$$

then

$$f(t) = |A||B|(\cos(\omega t + \alpha) - \cos(\omega t + \beta)) \quad \{7.15\}$$

$$f(t) = \frac{|A||B|}{2} \cos(\alpha - \beta) + \frac{|A||B|}{2} \cos(2\omega t + \alpha + \beta) \quad \{7.16\}$$

where  $A$ ,  $B$ ,  $\alpha$ ,  $\beta$  and  $\omega$  are constants.

The first term in equation 7.16 is independent of time and is the continuous component that provides the average force. The sinusoidal approximation model was implemented with a limited amount of success, due to the various assumptions that were made during its development. The results from this model are presented and discussed in Chapter 8.

## 7.6. REDUCED PARAMETERS

A lumped parameter model was considered as an approximation to a particular launcher arrangement, but although lumped parameter models can easily be solved, their parameters must be carefully chosen. It was decided that the values for the lumped parameter model could be obtained by a matrix reduction of the filamentary parameters calculated in a full filamentary model.

A similar matrix reduction to that developed by Kron [113] that was used to reduce the number of equations in an oscillatory system defined by equation 7.17, was proposed.

$$\mathbf{V} = \mathbf{Z}\mathbf{I} \quad \{7.17\}$$

After rearranging the original system of equations into groups, depending on whether or not they have any impressed voltages, the system can be expressed in the compound matrix form

$$\begin{bmatrix} \mathbf{V}_1 \\ 0 \end{bmatrix} = \begin{bmatrix} \mathbf{Z}_1 & \mathbf{Z}_2 \\ \mathbf{Z}_3 & \mathbf{Z}_4 \end{bmatrix} \cdot \begin{bmatrix} \mathbf{I}_1 \\ \mathbf{I}_2 \end{bmatrix} \quad \{7.18\}$$

Separating the equations in this way allows them to be considered as two independent sets. The sub-vector  $\mathbf{I}_2$  can then be defined in terms of the sub-vector  $\mathbf{I}_1$  from

$$\mathbf{Z}_4 \cdot \mathbf{I}_2 = -\mathbf{Z}_3 \cdot \mathbf{I}_1 \quad \{7.19\}$$

hence

$$\mathbf{I}_2 = -\mathbf{Z}_4^{-1} \cdot \mathbf{Z}_3 \cdot \mathbf{I}_1 \quad \{7.20\}$$

Substituting the first set of equations into equation 7.18 gives

$$\mathbf{V}_1 = \mathbf{Z}_1 \cdot \mathbf{I}_1 - \mathbf{Z}_2 \cdot \mathbf{Z}_4^{-1} \cdot \mathbf{Z}_3 \cdot \mathbf{I}_1 \quad \{7.21\}$$

which can be simplified to

$$\mathbf{V}_1 = \mathbf{Z}_1' \cdot \mathbf{I}_1 \quad \{7.22\}$$

where  $\mathbf{Z}_1'$  is the reduced impedance matrix, defined as

$$\mathbf{Z}_1' = \mathbf{Z}_1 - \mathbf{Z}_2 \cdot \mathbf{Z}_4^{-1} \cdot \mathbf{Z}_3 \quad \{7.23\}$$

A similar reduction technique was attempted for use with the filamentary model. By using reductions similar to those in equation 7.23, it was anticipated that the actual number of the equations to be solved could be reduced to three. Since the full matrix problem was reduced before it was solved, the projectile was considered to be static. Although there was no difficulty in reducing both the required inductance and resistance matrices, reducing the rate of change of inductance matrix  $\mathbf{D}$  proved to be more complicated. If  $\mathbf{D}$  is reduced in the same manner as the resistance and inductance matrices, then

$$\mathbf{D}_1' = \mathbf{D}_1 - \mathbf{D}_2 \cdot \mathbf{D}_4^{-1} \cdot \mathbf{D}_3 \quad \{7.24\}$$

but, since  $\mathbf{D}$  has a zero leading diagonal, it is impossible to define  $\mathbf{D}_4^{-1}$ . An alternative method of determining  $\mathbf{D}'$  is therefore required. By considering the matrix  $\mathbf{D}$  in the same partitioned form as the other reducible matrices, the  $\mathbf{D}$  matrix can be expressed by equation 7.25. By also considering, the current vector in it partitioned form, as shown in equation 7.18, the force can be found from equation 7.26.

$$\mathbf{D} = \begin{bmatrix} \mathbf{D}_1 & \mathbf{D}_2 \\ \mathbf{D}_3 & \mathbf{D}_4 \end{bmatrix} \quad \{7.25\}$$

$$2f = \begin{bmatrix} \mathbf{I}_1^T & \mathbf{I}_2^T \end{bmatrix} \begin{bmatrix} \mathbf{D}_1 & \mathbf{D}_2 \\ \mathbf{D}_3 & \mathbf{D}_4 \end{bmatrix} \begin{bmatrix} \mathbf{I}_1 \\ \mathbf{I}_2 \end{bmatrix} \quad \{7.26\}$$

$$2f = (\mathbf{I}_1^T \mathbf{D}_1 + \mathbf{I}_2^T \mathbf{D}_3) \mathbf{I}_1 + (\mathbf{I}_1^T \mathbf{D}_2 + \mathbf{I}_2^T \mathbf{D}_4) \mathbf{I}_2 \quad \{7.27\}$$

Since  $\mathbf{I}_2$  can be defined in terms of  $\mathbf{I}_1$ , as shown in equation 7.20,  $\mathbf{I}_2^T$  can be defined as

$$\mathbf{I}_2^T = -\mathbf{I}_1^T \mathbf{Z}_3^T (\mathbf{Z}_4^T)^{-1} \quad \{7.28\}$$

By substituting equations 7.20 and 7.28 into equation 7.27, and collecting like terms, the force on the projectile can be expressed as

$$2f = \left( \mathbf{I}_1^T (\mathbf{D}_1 - \mathbf{D}_2 \mathbf{Z}_4^{-1} \mathbf{Z}_3) + \mathbf{I}_2^T (\mathbf{D}_3 - \mathbf{D}_4 \mathbf{Z}_4^{-1} \mathbf{Z}_3) \right) \mathbf{I}_1 \quad \{7.29\}$$

Since  $\mathbf{Z}_4$  is symmetrical  $\mathbf{Z}_4^{-1} = (\mathbf{Z}_4^T)^{-1}$  and equation 7.29 can be re-written as

$$2f = \mathbf{I}_1^T \left( (\mathbf{D}_1 - \mathbf{D}_2 \mathbf{Z}_4^{-1} \mathbf{Z}_3) - \mathbf{Z}_3^T \mathbf{Z}_4^{-1} (\mathbf{D}_3 - \mathbf{D}_4 \mathbf{Z}_4^{-1} \mathbf{Z}_3) \right) \mathbf{I}_1 \quad \{7.30\}$$

If the force is defined in the form shown below, and  $\mathbf{Z}_4^{-1} \mathbf{Z}_3$  is replaced by  $\mathbf{Z}_5$ , reduction of matrix  $\mathbf{D}$  leads to  $\mathbf{D}'$  as expressed in equation 7.32.

$$f = \frac{1}{2} \mathbf{I}_1^T \mathbf{D}' \mathbf{I}_1 \quad \{7.31\}$$

$$\mathbf{D}' = \mathbf{D}_1 - \mathbf{D}_2 \mathbf{Z}_5 - \mathbf{Z}_5^T \mathbf{D}_3 - \mathbf{Z}_5^T \mathbf{D}_4 \mathbf{Z}_5 \quad \{7.32\}$$

Since  $\mathbf{D}$  is also symmetrical,  $\mathbf{D}'$  can be written as

$$\mathbf{D}' = \mathbf{D}_1 - \mathbf{D}_2 \mathbf{Z}_5 - (\mathbf{D}_2 \mathbf{Z}_5)^T - \mathbf{Z}_5^T \mathbf{D}_4 \mathbf{Z}_5 \quad \{7.33\}$$

Before writing a reduced parameter modelling program, the concept was tested on a small model using the commercial mathematical package MathCad. The test model simulated the system shown in Figure 7.11, and there was no noticeable difference in the results from the reduced and full models. A second test simulation was run, which modelled the system shown in Figure 7.12. As shown in Figure 7.13, there was again no noticeable difference between the sets of results. After these limited test simulations, a reduced parameter modelling program was written. Figure 7.14 presents a comparison between results from a full model, a full model with a static projectile and results from the reduced model. It can be seen that, as expected, there is a noticeable difference between the full model and the static model results. However, there is also a marked difference between the static model results and those from the reduced model. After checking the program code, and re-assessing the

mathematics of the reduced model, it was found that the difference between the static and reduced model results was due to a flaw in the mathematics of the reduced model. Although the Kron's reduced model was based on equation 7.18, the reduced model was based only on a similar reduction of equation 7.24. This in turn leads to

$$\begin{bmatrix} V \\ 0 \end{bmatrix} = \begin{bmatrix} R_{11} & R_{12} \\ R_{21} & R_{22} \end{bmatrix} \begin{bmatrix} I^1 \\ I^2 \end{bmatrix} + \begin{bmatrix} L_{11} & L_{12} \\ L_{21} & L_{22} \end{bmatrix} \begin{bmatrix} \frac{d}{dt} I^1 \\ \frac{d}{dt} I^2 \end{bmatrix} \quad \{7.34\}$$

Since  $I^2$  was defined in terms of  $I^1$  by equation 7.20, this implied that equation 7.35 must be valid for this definition to be true.

$$0 = L_{21} \frac{d}{dt} I^1 + L_{22} \frac{d}{dt} I^2 \quad \{7.35\}$$

However, it can easily be shown that equation 7.35 cannot be assumed, and hence the reduced model does not work.

## 7.7. CONSTRAINED BRANCH SOLUTION

After the failure of the reduced parameter model to improve the speed of the program, it was hoped that improvements would be obtained by applying Kirchhoff's second law directly to the launcher equations in the branch reference frame. Using the branch parameters developed in the first part of chapter six, the electrical system of equations can be expressed as

$$V_b + E_b = R_{bb} I^b + \frac{d}{dz} L_{bb} I^b + L_{bb} \frac{d}{dt} I^b \quad \{7.36\}$$

As previously mentioned, equation 7.36 cannot be solved immediately, since the vector  $E_b$  is unknown. In the original model, this problem was overcome by transforming the whole problem into the mesh reference frame, to give

$$V_m + E_m = (R_{mm} + D_{mm} u) I^m + L_{mm} \frac{d}{dt} I^m \quad \{7.37\}$$

effectively constraining the problem to comply with Kirchhoff's second law. This constraint can be expressed by

$$\mathbf{C}_m^{\bullet b} \mathbf{E}_b = \mathbf{E}_m = 0 \quad \{7.38\}$$

Applying this constraint to equation 7.36 and re-arranging leads to

$$\mathbf{E}_b = (\mathbf{R}_{bb} + \mathbf{D}_{bb}u) \mathbf{I}^b + \mathbf{L}_{bb} \frac{d}{dt} \mathbf{I}^b - \mathbf{V}_b \quad \{7.39\}$$

$$\mathbf{C}_m^{\bullet b} \left\{ (\mathbf{R}_{bb} + \mathbf{D}_{bb}u) \mathbf{I}^b + \mathbf{L}_{bb} \frac{d}{dt} \mathbf{I}^b - \mathbf{V}_b \right\} = 0 \quad \{7.40\}$$

$$\mathbf{C}_m^{\bullet b} \mathbf{L}_{bb} \frac{d}{dt} \mathbf{I}^b = \mathbf{C}_m^{\bullet b} \mathbf{V}_b - \mathbf{C}_m^{\bullet b} (\mathbf{R}_{bb} + \mathbf{D}_{bb}u) \mathbf{I}^b \quad \{7.41\}$$

Since  $\mathbf{C}_m^{\bullet b} \mathbf{L}_{bb}$  is not square it cannot be inverted. However, if the rate of change of current is transformed into the mesh reference frame, equation 7.41 can be re-written as

$$\mathbf{C}_m^{\bullet b} \mathbf{L}_{bb} \mathbf{C}_m^b \frac{d}{dt} \mathbf{I}^m = \mathbf{C}_m^{\bullet b} \mathbf{V}_b - \mathbf{C}_m^{\bullet b} (\mathbf{R}_{bb} + \mathbf{D}_{bb}u) \mathbf{I}^b \quad \{7.42\}$$

The inductance product is now a square matrix and can be inverted, enabling the rate of change of current to be found in the mesh reference frame, from

$$\frac{d}{dt} \mathbf{I}^m = \left[ \mathbf{C}_m^{\bullet b} \mathbf{L}_{bb} \mathbf{C}_m^b \right]^{-1} \mathbf{C}_m^{\bullet b} \left( \mathbf{V}_b - (\mathbf{R}_{bb} + \mathbf{D}_{bb}u) \mathbf{I}^b \right) \quad \{7.43\}$$

By transforming this expression into the branch reference frame, the rate of change of current can be found from

$$\frac{d}{dt} \mathbf{I}^b = \mathbf{C}_m^b \left[ \mathbf{C}_m^{\bullet b} \mathbf{L}_{bb} \mathbf{C}_m^b \right]^{-1} \mathbf{C}_m^{\bullet b} \left( \mathbf{V}_b - (\mathbf{R}_{bb} + \mathbf{D}_{bb}u) \mathbf{I}^b \right) \quad \{7.44\}$$

Where  $C_{\bullet m}^b \left[ C_m^{\bullet b} L_{bb} C_{\bullet m}^b \right]^{-1} C_m^{\bullet b}$  can be considered as the inverse of the constrained branch inductance matrix, and assembled in the following sequence.

$$C_m^{\bullet b} L_{bb} C_{\bullet m}^b \Rightarrow L_{mm} \Rightarrow L^{mm} \Rightarrow C_{\bullet m}^b L^{mm} C_m^{\bullet b} \Rightarrow L^{bb}$$

It was expected that the constrained branch solution would improve the speed of the program, without introducing any additional assumptions, and therefore without any loss in accuracy. The constrained branch model was compared with the mesh reference frame model and there was no discernible difference between results from the two models, even when comparing large dynamic simulations. However, the constrained solution was slower than the original model when it was implemented using an explicit inversion method. This was later replaced by the triangular decomposition method described in Chapter 5, which significantly improved the performance of the model, but it remained slower than the original model. However, by considering the part of equation 7.44 shown below, it was found that the number of multiplications and additions required could be reduced.

$$(R_{bb} + D_{bb}u)I^b \quad \{7.45\}$$

The initial approach multiplied the  $R_{bb}$  and  $I^b$  terms, before simultaneously multiplying the  $D_{bb}$ ,  $u$  and  $I^b$  terms and adding the results. The second method took advantage of the partitioned nature of the matrices, by multiplying  $D_{bb}$  by  $I^b$  to produce a vector, before multiplying the results by  $u$ . The  $R_{bb}$  and  $I^b$  terms were then multiplied and added to the previous results, as shown below.

$$\begin{bmatrix} & D \\ D^T & \end{bmatrix} \begin{bmatrix} I^1 \\ I^2 \\ I^3 \end{bmatrix} \Rightarrow \begin{bmatrix} DI^2 \\ D^T I^1 \\ 0 \end{bmatrix} \times u \Rightarrow \begin{bmatrix} R_1 & & \\ & R_2 & \\ & & R_3 \end{bmatrix} \begin{bmatrix} I^1 \\ I^2 \\ I^3 \end{bmatrix} + \begin{bmatrix} DI^2 u \\ D^T I^1 u \\ 0 \end{bmatrix}$$

If  $D$  is a  $(m \times m)$  matrix, and there are  $n$  branches in total, the first method requires  $2n^2+n$  multiplications and  $n^2+n$  additions, but the second requires only  $(2m^2+2m+n)$  multiplications and  $(2m^2+2m)$  additions. Table 7.1 shows that method two requires



less than a quarter of the multiplications, and less than half the additions of method one.

m	n	Method 1		Method 2	
		multiplications	additions	multiplications	additions
10	23	1081	552	243	220
100	203	82621	41412	20403	20200
1000	2003	8026021	4014012	2004003	2002000

Table 7.1 Comparison of processing effort required by both methods

After implementing method two and the earlier improvements, the constrained branch model was almost as fast as the original model. Nevertheless much greater speed improvements were possible if the branch inductances were considered to be fixed. Since all the matrix transformations are associated with branch inductance calculations, the model speed was improved by 94% when the projectile was considered to be static and the inductance matrix was only recalculated whenever a discontinuity occurred. This improvement in the branch model was much greater than would have been achieved if the same assumptions had been applied to the original program. A further 54% improvement was achieved by assuming that the rates of change of inductances were also fixed. Figure 7.15 to Figure 7.20 present a comparison between results from the dynamic branch model and those from a fixed inductance model, with both fixed inductance and  $D_{bb}$  terms. Although it can be seen that the results are significantly affected, the large reduction in the time taken to model a system might justify the use of this method as an initial design tool.

## 7.8. MESH GENERATION

Although much time was spent trying to reduce the run time for a simulation, other developments were also considered. The first planned expansion of the original model was to increase the flexibility and complexity of the supply circuits that could be modelled. The original model developed used a rigid meshing technique. The meshes that were wholly internal to the drive coil were generated first; this was

followed in turn by the meshes that were internal to the first and second projectiles. The main and crowbar circuit meshes were added as necessary, depending on the state of the switches. Although the power supply meshes were added last, this is not a requirement to enable the removal and addition of the switching meshes, as the connection matrix is stored in a sparse form. Figure 7.21 shows how the internal coil meshes generated by a simple counting algorithm are defined. A set of nested loops is used to count through the filaments and connect them to the appropriate meshes. The meshes between strands are added next by a second set of nested loops. The terminal mesh (number nine in this example) is calculated last. This partial mesh could be closed on itself, by not adding any further branches to the mesh, as would the case for a projectile coil. On the other hand, this mesh could include some or all of the power supply branches, as would the case of a drive coil.

Although the rigid method of defining the meshes worked well, it limited the possible launcher and supply arrangements that could be studied. Since other power supply and launcher topologies might improve the efficiency, or provide increased insight into its operation, a more flexible mesh generation technique was required to widen the possible configuration that could be studied. Since the underlining equations of the original filamentary model do not depend on the supply circuit, any change to this only required changes to the connection matrix and some modification of the switch discontinuity routines. The automatic mesh generation routine developed here does not require the branches to be in any particular order, or to be consecutively numbered. However, each branch must have defined start and end nodes, and the circuit that is constructed must be realistic. Due to the way in which switch discontinuities are processed, each mesh can only contain a maximum of one switch. This is to allow a particular mesh to be added or removed from the problem when its associated switch either starts or stops conducting.

The routine generates each mesh by “walking” through the circuit. The routine is based on three lists; the current mesh branch list, the deleted branch list and the node list. The best way to describe how the routine works is by considering the example circuit shown in Figure 7.22. The routine starts at the lowest available branch number (b1). The current node is set as the end node of the first branch, and both start and

end nodes of the first branch are added to the node list. The program then tries to find the lowest branch at the current node (n2), and although 'b1' is the lowest branch found it is also the last branch, so that branch 'b2' is selected as the current branch. After checking that 'b2' is valid, it is added to the branch list and node (n6) is set as the current node, and added to the node list. The routine continues to "walk" around the circuit, until branch b9 is added and node n6 is selected as the current node again. At this point, the three lists contain the data shown in Table 7.2.

Current mesh branch list	b1	b2	b5	b6	b9	
Node list	n1	n2	n6	n7	n3	n6
Deleted branch list						

Table 7.2 Connection lists when error is flagged

Since all the branches at the node n6 have been added to the current mesh, and n6 was not the start node, an error is flagged and the routine "walks" backwards until an alternative path is found. If the routine walks all the way back to the start, it assumes that the start branch is shorted on itself. Table 7.3 shows the state of the three lists after the first mesh has been completed.

Current mesh branch list	b1	b2	b5	b6	b9	-b7	
Node list	n1	n2	n6	n7	n3	n6	n1
Deleted branch list	b9	b6					

Table 7.3 Connection lists after completion of first mesh

The negative sign for branch b7 indicates that the branch has been connected into the mesh in the opposite direction to its definition. The mesh generation routine is described in more detail by the flowchart shown in Figure 7.23. Table 7.4 shows the completed mesh / branch table for the example circuit.

Mesh 1	Mesh 2	Mesh 3
b1	b3	b5
b2	-b4	b6
b5	-b8	b9
-b7		

Table 7.4 Completed mesh branch table

### 7.9. PROJECTILE DEFORMATION

It is assumed that the direction of flight is perpendicular to the drive coil, and that the projectile will remain parallel to the drive coil. To calculate the general motion of the projectile, only the total force in the expected direction of motion is required, if the projectile is assumed to be rigid. However, if this is not assumed the force distributions in both the axial and radial directions are required. Although not implemented, a set of equations for the internal stresses and strains within a projectile have been developed.

A paper by Clifton and Mongeau [126], proposed a structural model of a set of pulsed coaxial coils using lumped parameter analysis and formulated equation 7.46 to define the motion of a finite number of sub-elements. The sub-elements that they describe have a great similarity to the filaments used in this thesis. Thus

$$\mathbf{m}_{bb}\mathbf{a}^b - \mathbf{K}_{bb}\mathbf{u}^b = \mathbf{f}_b \quad \{7.46\}$$

where  $\mathbf{m}_{bb}$  is the diagonal mass matrix,  $\mathbf{u}^b$  is the branch displacement vector,  $\mathbf{a}^b$  is the branch acceleration vector,  $\mathbf{K}_{bb}$  is the stiffness coefficient matrix, and  $\mathbf{f}_b$  is the branch force vector, in one direction. By resolving the branch forces and displacements in two directions and solving equation 7.46 simultaneously for both directions, the full motion of the filaments can be predicted. The force in both the radial and axial directions to be found from equations 6.20 and 6.21 respectively.

To determine the values of the required stiffness coefficients, only radial movement was initially considered, as shown in Figure 7.24. The stiffness matrix for the four filaments shown in Figure 7.24 can be defined as

$$\mathbf{K}_{bb} = \begin{bmatrix} K_{h1} + K_{n13} + K_{p12} & -K_{p12} & -K_{n13} & 0 \\ -K_{p12} & K_{h2} + K_{n24} + K_{p12} & 0 & -K_{n24} \\ -K_{n13} & 0 & K_{h3} + K_{n13} + K_{p34} & -K_{p34} \\ 0 & -K_{n24} & -K_{p34} & K_{h4} + K_{n24} + K_{p34} \end{bmatrix} \quad \{7.47\}$$

where  $K_h$  is the hoop stiffness of a filament, and  $K_n$  and  $K_p$  are the normal and parallel stiffnesses. All the stiffness coefficients can be considered to be defined by

$$f = K\delta \quad \{7.48\}$$

where  $f$  is the force required to move an element a small distance  $\delta$  from its location if the projectile was assumed to be rigid. The first coefficient considered is the hoop stiffness, based on the hoop stress calculation for thin walled pressure vessels, and use of the dimensions given in Figure 7.25 and the equation of hoop stress [127], enables it to be expressed as

$$K_h = \frac{2\pi E x}{zr} \quad \{7.49\}$$

where  $E$  is the modulus of elasticity of the projectile material. The normal stiffness component is developed by considering Figure 7.26. The shear stress in the shaded region is given by

$$\tau = G\gamma \quad \{7.50\}$$

where  $G$  is the shear modulus of elasticity and is defined by

$$G = \frac{E}{2(1 + \nu)} \quad \{7.51\}$$

in which  $\nu$  is Poisson's ratio and  $E$  is the modulus of elasticity. If the bottom filament is considered to be stationary, the shear stress  $\tau$  can be found from

$$\tau = \frac{f}{A} \quad \{7.52\}$$

where the force  $f$  is the force that must be applied to the top element to cause it to be displaced by  $\delta$ , and  $A$  is the interface area between the two elements. Assuming the displacement  $\delta$  is small, the shear strain  $\gamma$  can be found from

$$\delta = a \tan \gamma \approx a\gamma \quad \{7.53\}$$

where  $a$  is the displacement between the filament centres as shown in Figure 7.26.

Combining equations 7.50, 7.52 and 7.53 leads to equation 7.54, which when rearranged as equation 7.55 gives  $K_n$ .

$$f = \pi 2rxG \frac{\delta}{a} \quad \{7.54\}$$

$$K_n = \frac{2\pi rxG}{a} \quad \{7.55\}$$

The parallel stiffness can be found by considering the two elements shown in Figure 7.27. There are however two formulations for the parallel stiffness, depending on which element the force is considered to be acting. Both formulations are based on the calculation of stresses in thick walled cylinders, when either internal or external loads are applied. In the first, the inner filament is considered to be fixed, and the force to be acting on the outer filament. By regarding the shaded area as a thick walled pressure vessel, the force can be assumed to be an external force, and  $\Delta a$  can be expressed by equation 7.56 [128].

$$\Delta a = \frac{qr_2}{E} \left( \frac{r_2^2 + r_1^2}{r_2^2 - r_1^2} - \nu \right) \quad \{7.56\}$$

where  $q$  is the outward external force per unit area. Rearrange equation 7.56 leads to

$$K_{te} = \frac{2\pi zE}{\left( \frac{r_2^2 + r_1^2}{r_2^2 - r_1^2} - \nu \right)} \quad \{7.57\}$$

The second formulation considers the outer filament to be fixed and the shaded area to be a thick walled pressure vessel. The force on the pressure vessel is assumed to an outward internal force, and the second stiffness coefficient  $K_{ti}$  can be found from

$$K_{ti} = 2\pi zE \frac{(r_2^2 - r_1^2)}{2r_1 r_2} \quad \{7.58\}$$

When all the stiffness coefficients in the radial direction have been formulated, the coefficients in the axial direction must be considered. Although the stiffness matrix in the axial direction can also be spilt into parallel and normal components, these are not the same components that were developed above and are defined in Figure 7.28. Since the projectile is free to move in the axial direction, there is no equivalent hoop stiffness. The displacements in the  $u$  vector are those relative to the locations of the filaments within the projectile, and are not relative to the displacement of the projectile from the drive coil.

The parallel components  $K_p$  can be derived from the calculation of the change in height of a thin walled cylinder when a uniform axial load is applied [128]. If the shaded region in Figure 7.29 is regarded as a thin walled cylinder,  $K_p$  can be found from equation 7.59, where the dimension are taken from Figure 7.29.

$$K_p = \frac{2\pi r E x}{a} \quad \{7.59\}$$

The normal component in the  $z$  direction  $K_n$  can be found by considering the shaded area shown in Figure 7.30. If the inner filament is fixed the force on the outer filament, which is required to produce the displacement  $\delta$  can be found from

$$f = G\delta \frac{1}{(r_2 - r_1)} \pi z (r_2 + r_1) \quad \{7.60\}$$

where equation 7.60 is derived by considering equations 7.50, 7.52 and 7.53 in terms of the dimensions shown in Figure 7.30. The normal stiffness coefficient can be found by rearranging equation 7.60 as

$$K_n = G\pi z \frac{(r_2 + r_1)}{(r_2 - r_1)} \quad \{7.63\}$$

## 7.10. CONCLUSIONS

The study into the usage of computer processor time indicated that a few routines dominated the use of the processor. Using different methods of matrix inversion led to a major reduction in the time taken to solve a test simulation, while changing the order of operation of some algorithms also improved the program performance. A further improvement was achieved by removal of some unneeded system calls. Pre-calculating the inductance of the self and fixed mutual inductances improved the program performance even further. However, the use of interpolation routines to enable the pre-calculation of variable mutual inductances did not offer any advantages. A variable time stepping program was written to reduce the number of steps required to solve a simulation, and during its development two single-step methods were implemented. By a direct comparison, it was shown that the Runge-Kutta-Merson method was the faster. While a variable time stepping program improved the performance of the program for some simulations, it also made it worse for others. However, the variable time stepping program enabled previously unstable simulations to be completed.

While the instant crowbar model does not represent the launcher with the same accuracy as the normal model, it provides a good approximation and significant reduction in processing effort. To further improve the speed of the program a sinusoidal approximation was developed, in which the drive coil current was approximated by part of a sine wave. Although a sinusoidal approximation model was successfully implemented, it proved to be too inaccurate to provide a usable analysis tool.

After showing that approximate methods were unlikely to provide accurate results, it was thought that reformulating the model would improve the program speed. The first attempt at this was based on a matrix reduction of the original model but, although initial tests suggested that this method would provide an accurate and fast



approach, it was later shown to be flawed. A second reformulation based on applying Kirchhoff's second law in the branch reference frame was successfully implemented, but this was no faster than the original model when simulating dynamic systems. However, when the constrained branch solution was used to model static systems, this was significantly faster than the original program when modelling the same system.

In addition to the developments that reduced the processing time, other development expanded the scope of the original model. To allow more flexible power supply and launcher topologies to be studied a flexible mesh generation routine was developed. Although the new mesh generation routine allowed any combination of launcher coils and power supply components to be simulated, the mesh generation routines were not fully integrated into the program.

Another expansion to the original model was the development of a detailed structural model of the launcher based on the same filamentary division as the electrical model. Equations were developed for the stress and strains in both the axial and radial directions, and were formulated to produce a set of differential equations that could be solved simultaneously with the electrical equations. The inclusion of the structural model within the simulation program would allow the examination of the effects of coil deformation in a coherent manner. Although the structural equations are based on published pressure vessel equations, their application to magnetic launchers is thought to be new.

7.11. FIGURES

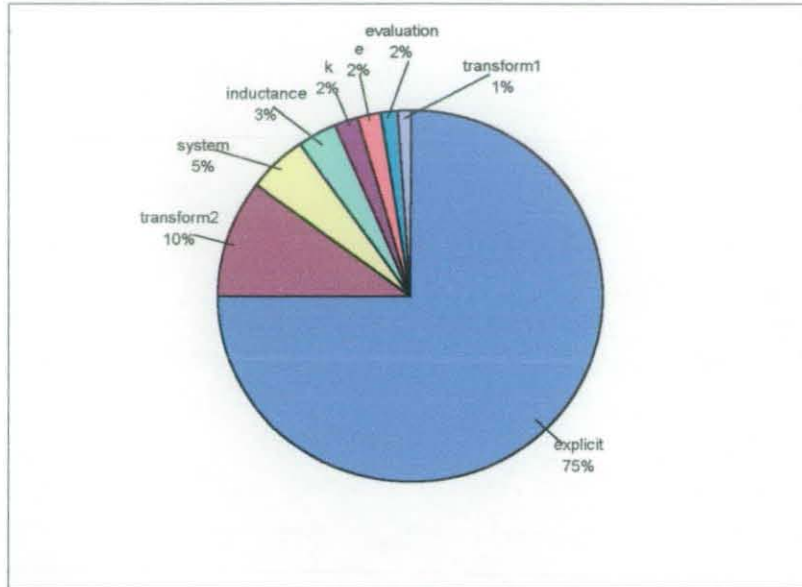


Figure 7.1 Typical computer processor activity distribution

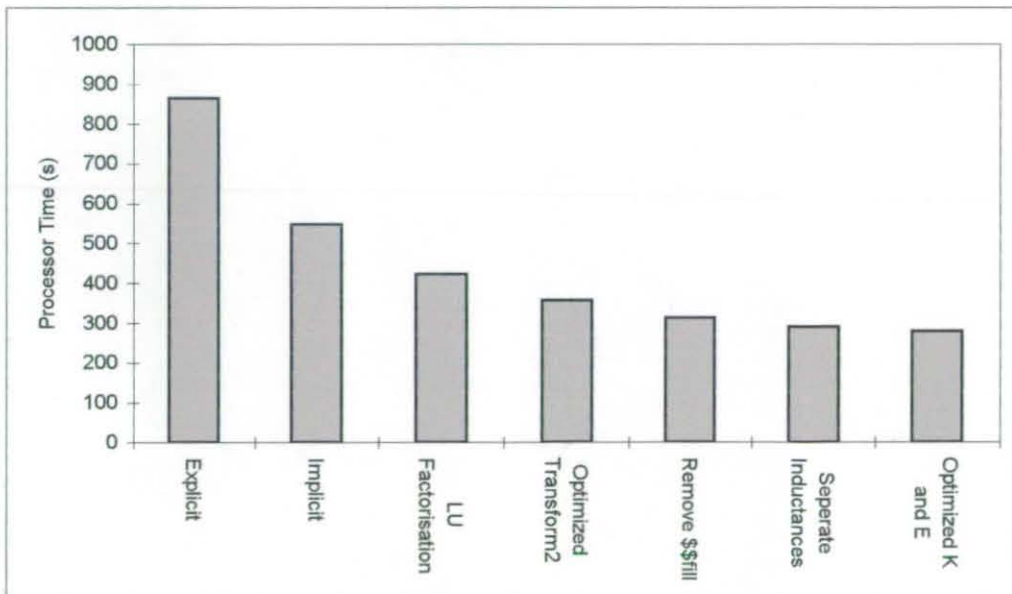


Figure 7.2 Improvements in average processor time

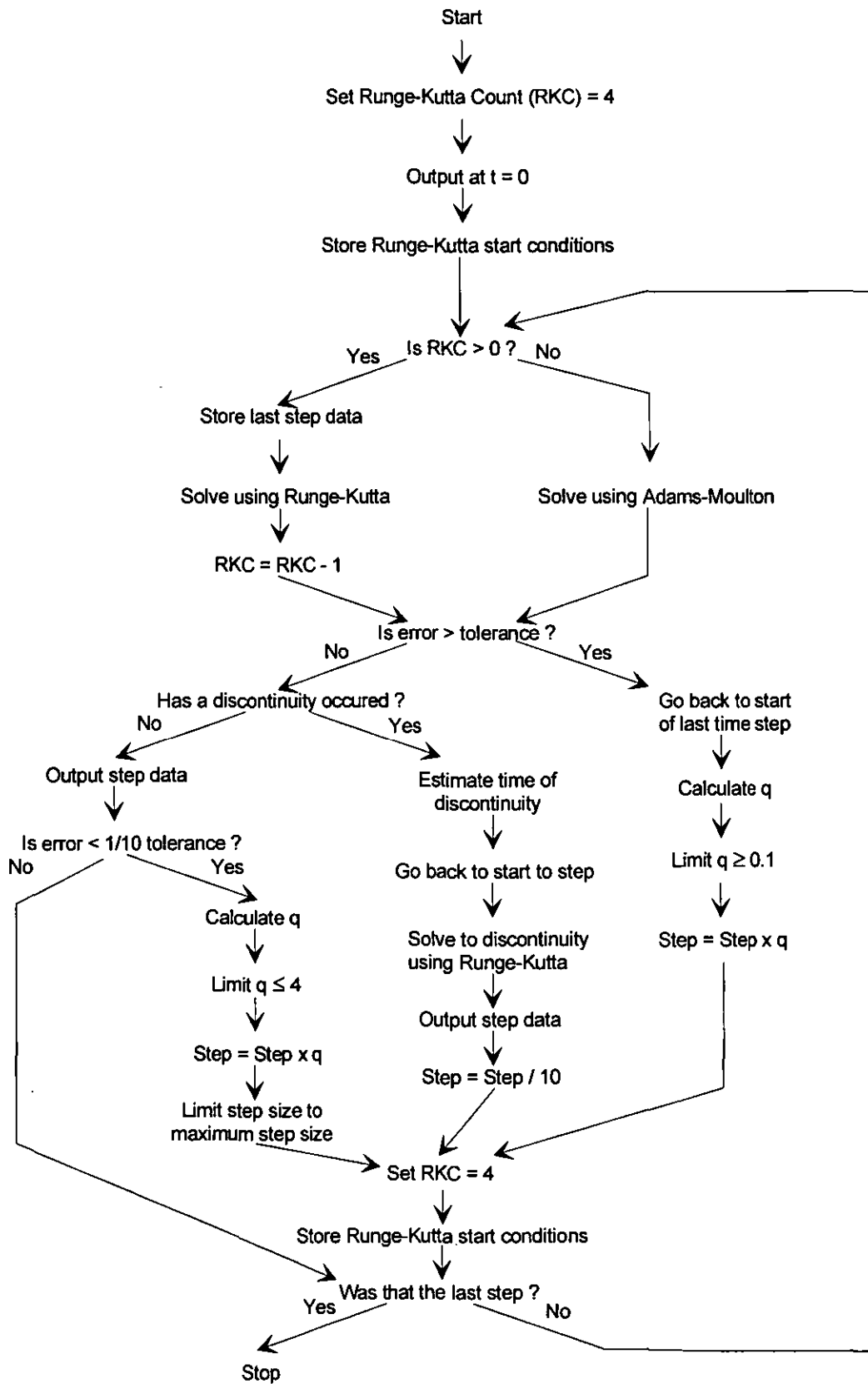


Figure 7.3 Variable time stepping program flow chart

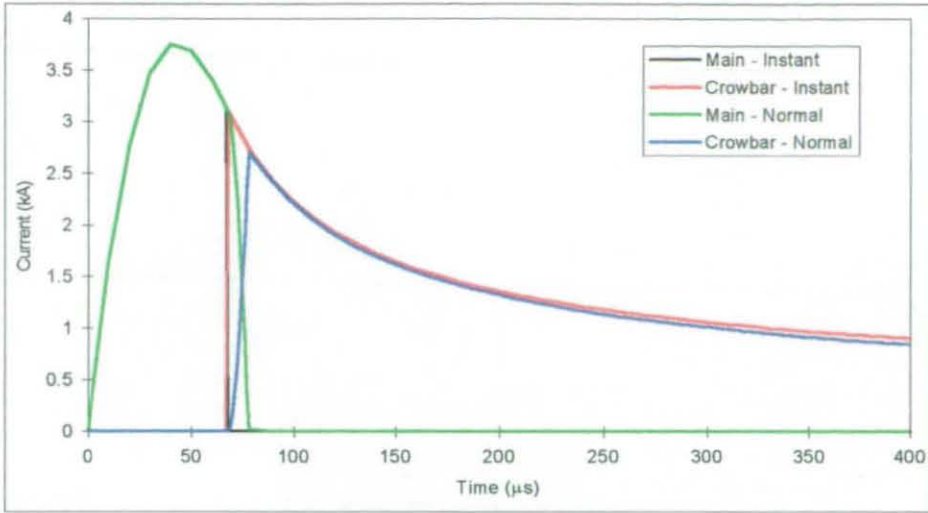


Figure 7.4 Comparison of supply currents

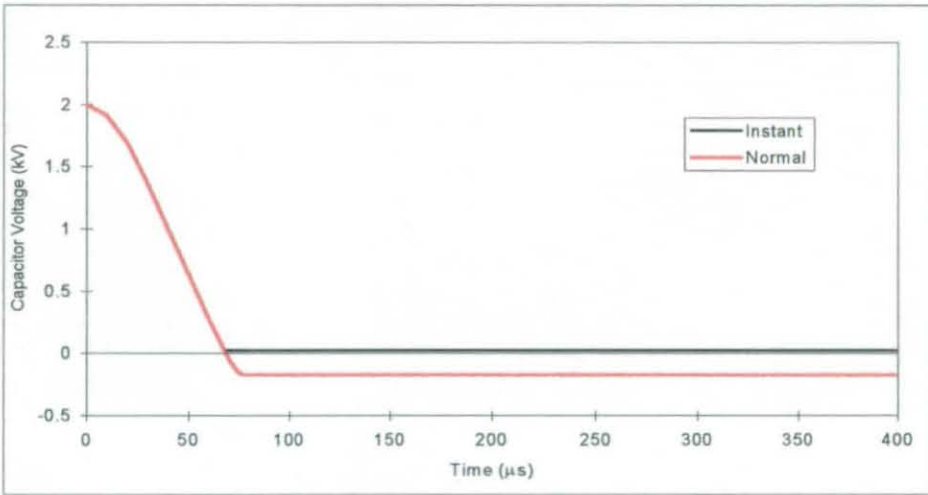


Figure 7.5 Comparison of capacitor voltages

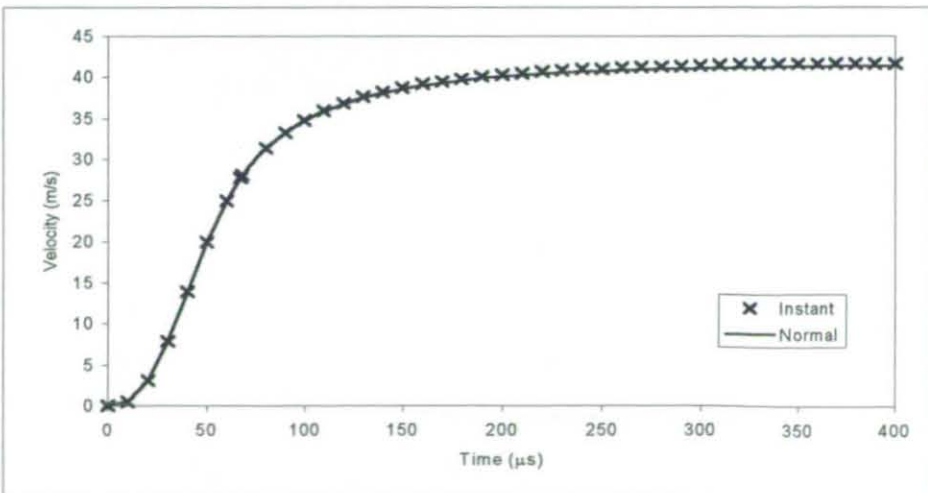


Figure 7.6 Comparison of projectile velocities

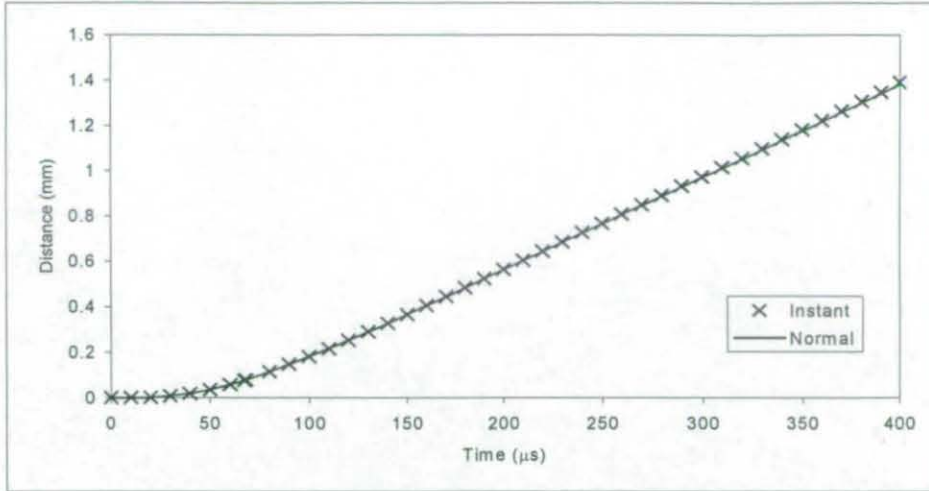


Figure 7.7 Comparison of projectile displacements

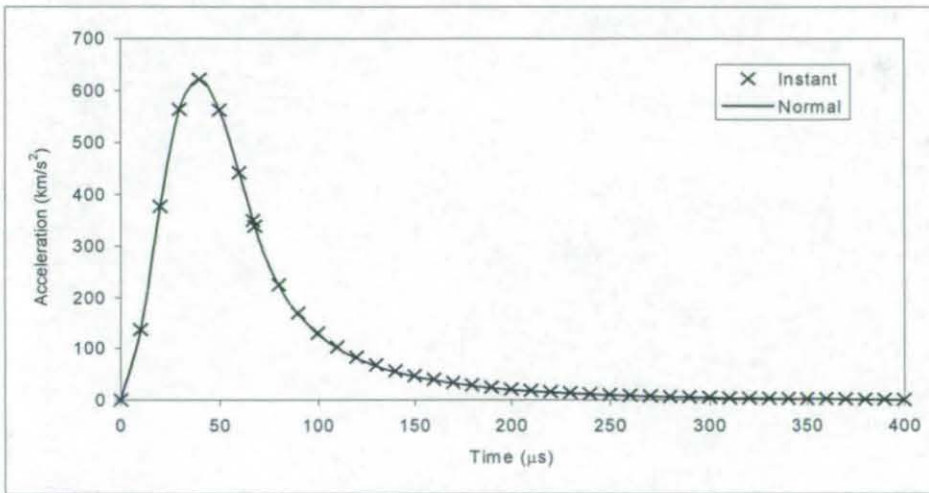


Figure 7.8 Comparison of projectile accelerations

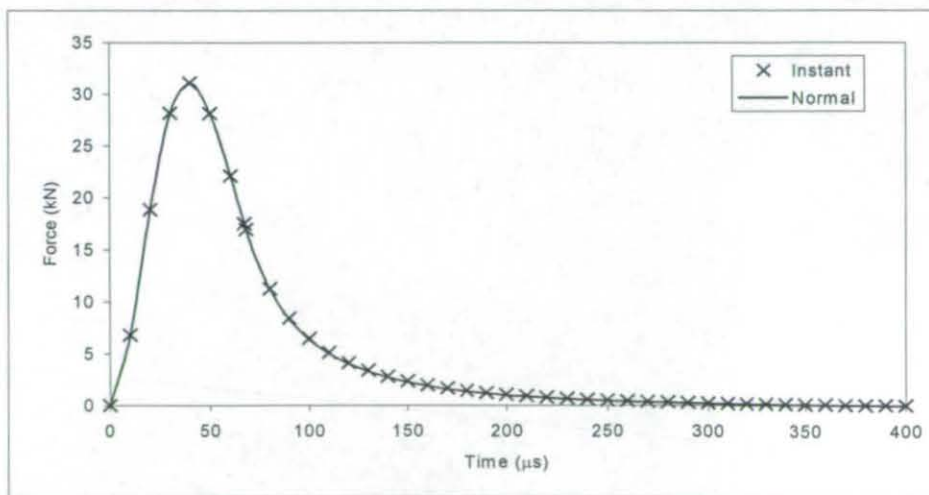


Figure 7.9 Comparison of the total forces applied to the projectiles

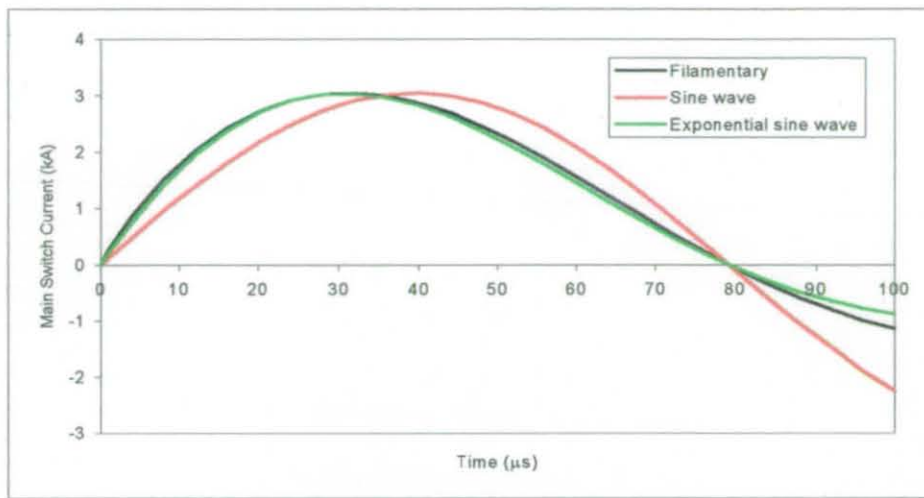


Figure 7.10 Comparison between main switch currents for the original, sine wave, and reduced models

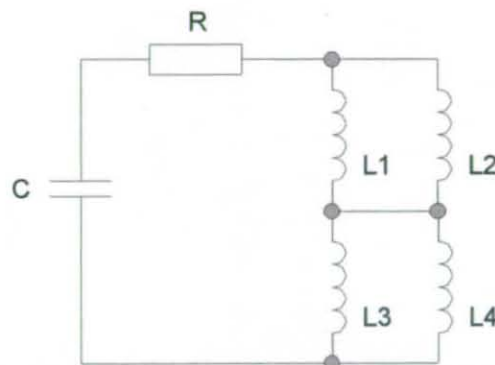


Figure 7.11 First reduced model test circuit

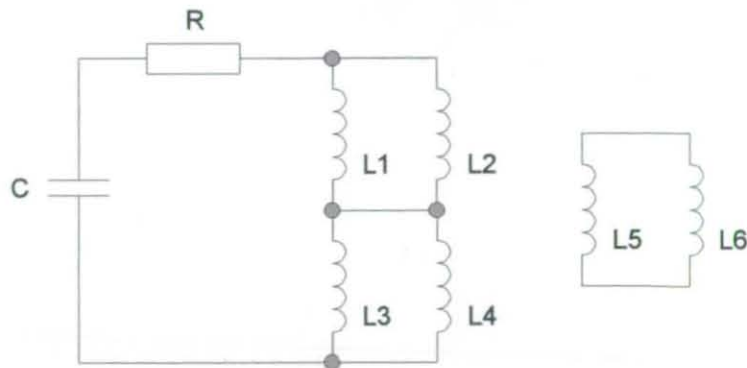


Figure 7.12 Second reduced model test circuit

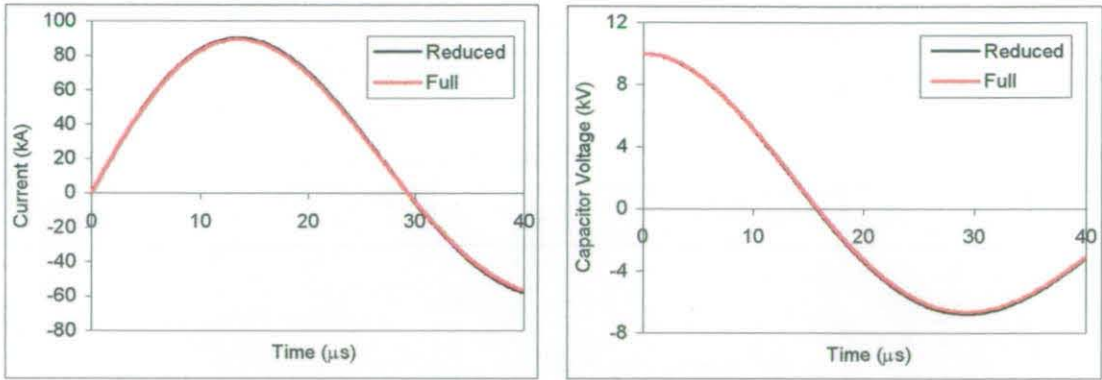


Figure 7.13 Results from second reduced model test

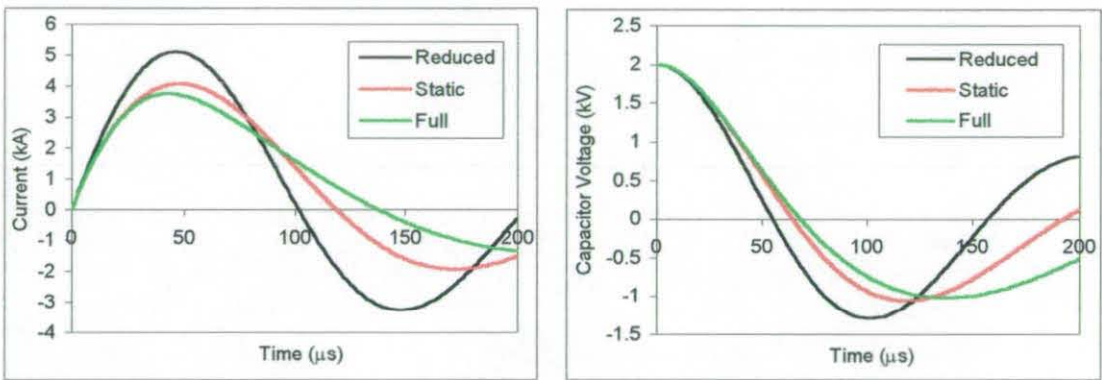


Figure 7.14 Comparison between the results from full, static and reduced models

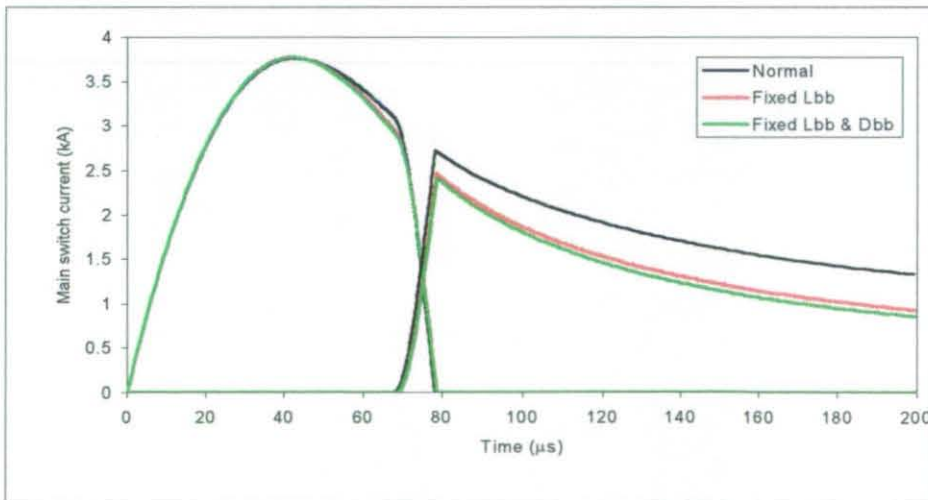


Figure 7.15 Comparison of supply currents



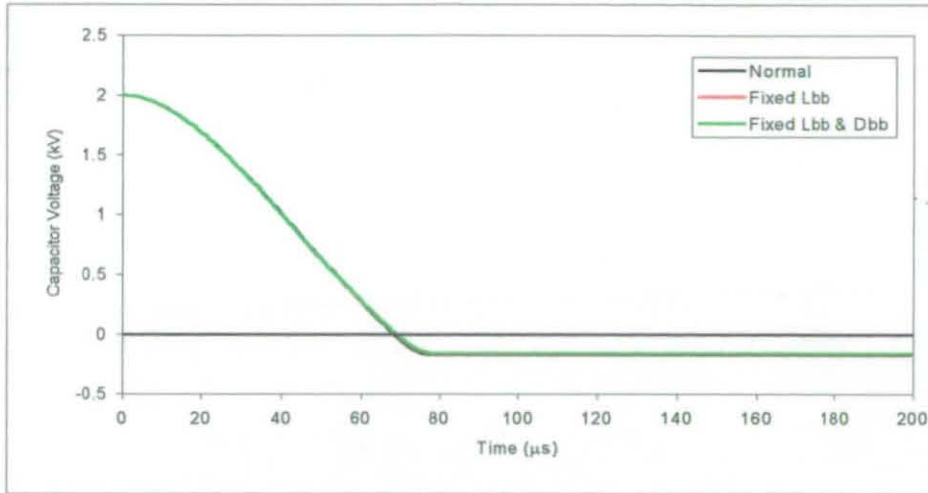


Figure 7.16 Comparison of capacitor voltages

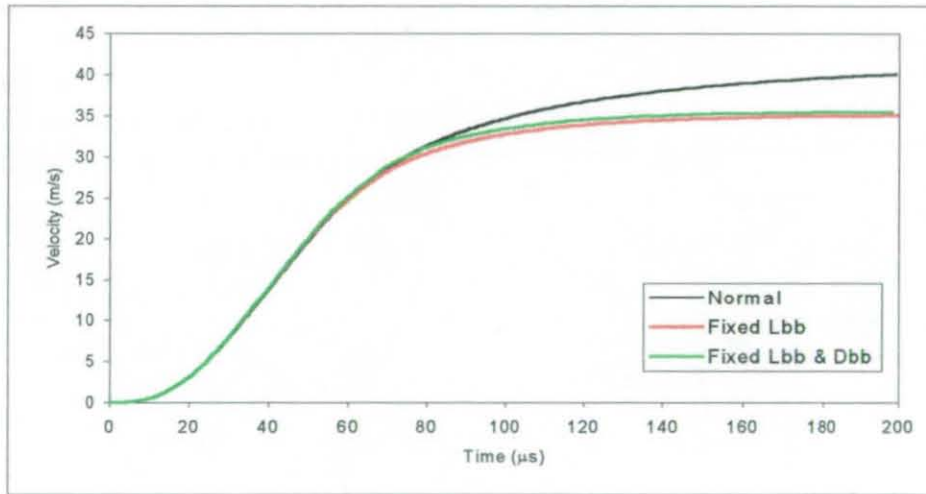


Figure 7.17 Comparison of projectile velocities

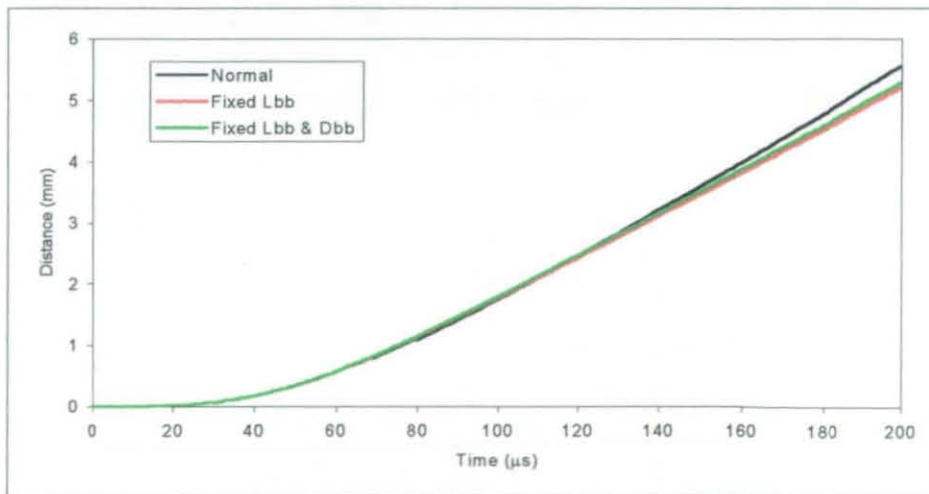


Figure 7.18 Comparison of projectile displacements



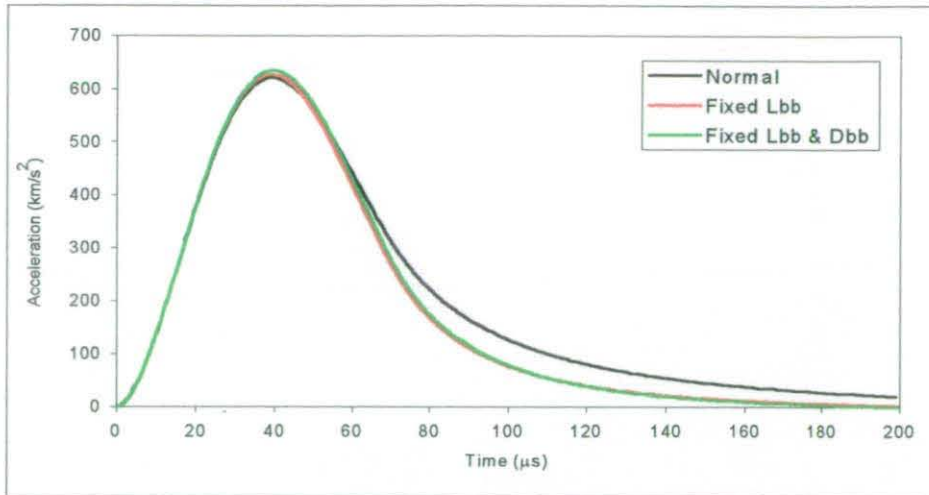


Figure 7.19 Comparison of projectile accelerations

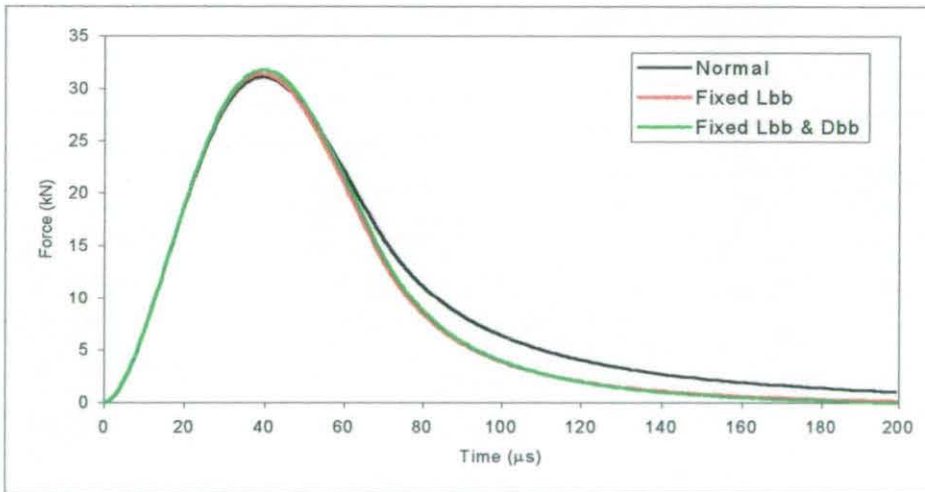


Figure 7.20 Comparison of the total forces applied to the projectiles

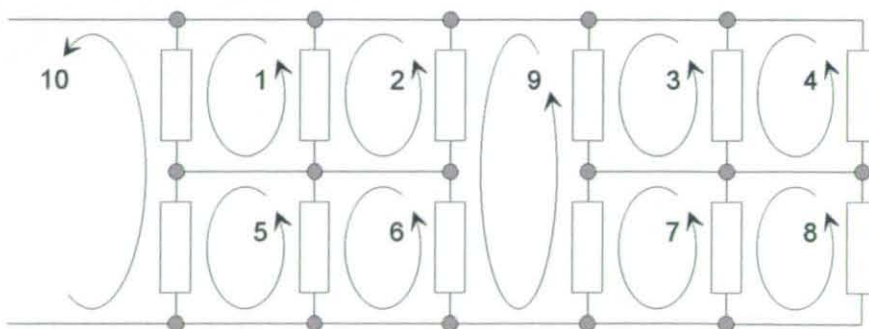


Figure 7.21 Internal coil mesh definition example

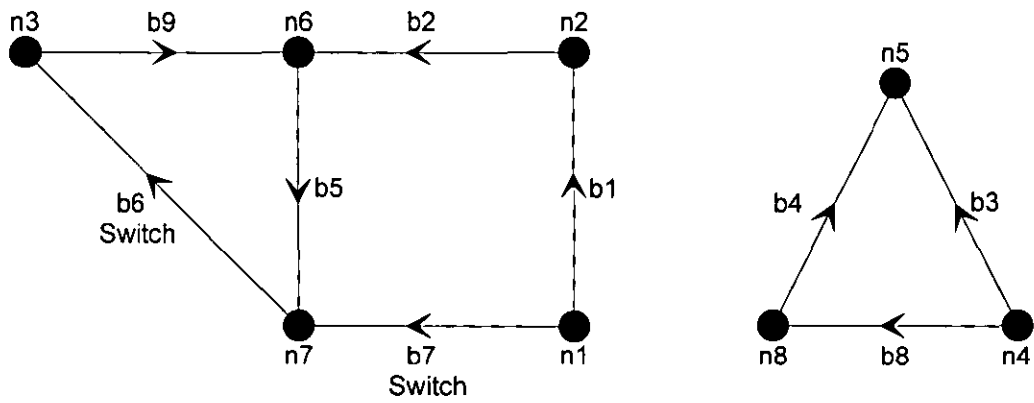


Figure 7.22 Mesh generation example circuit

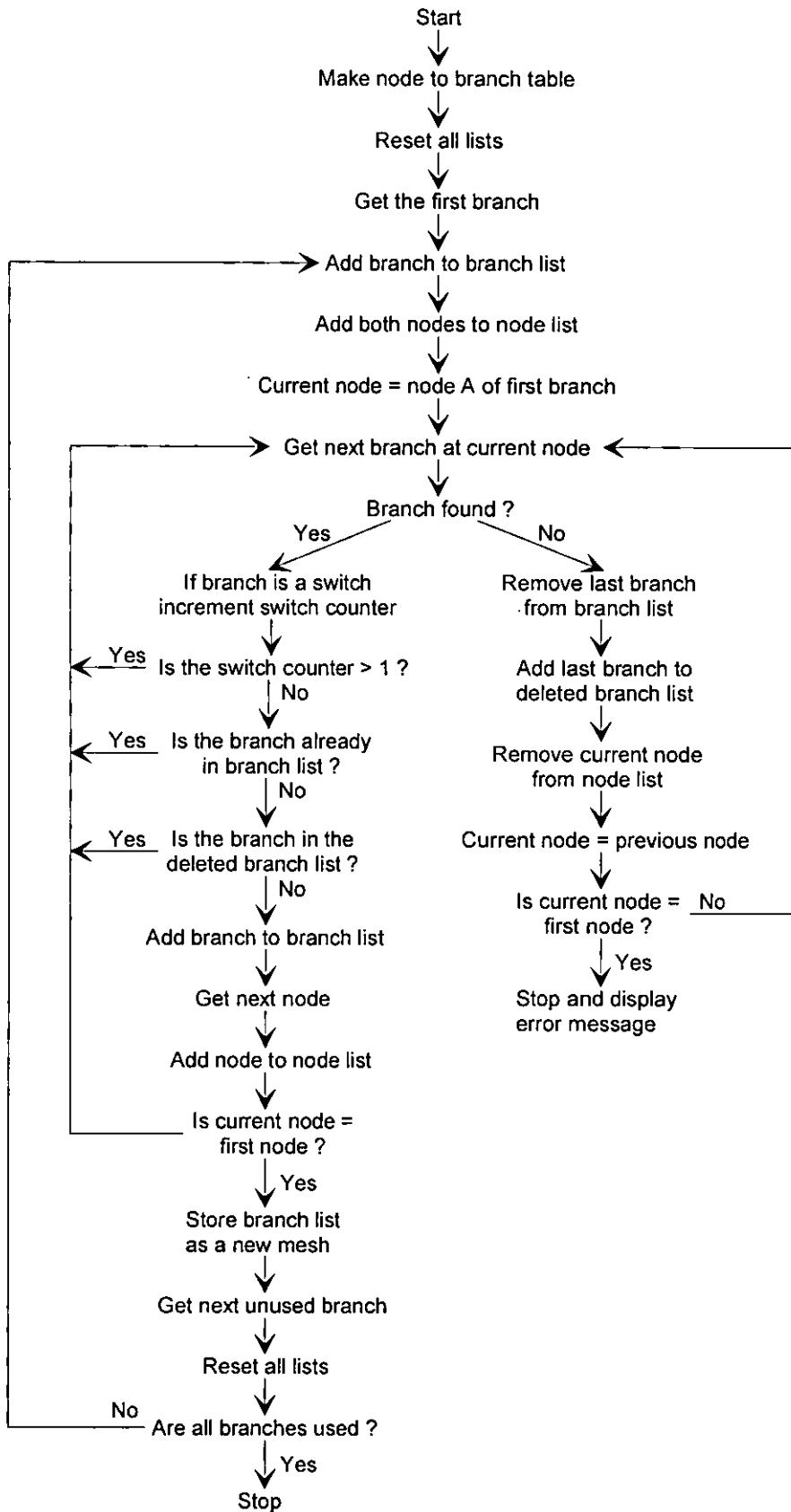


Figure 7.23 Mesh generation flowchart

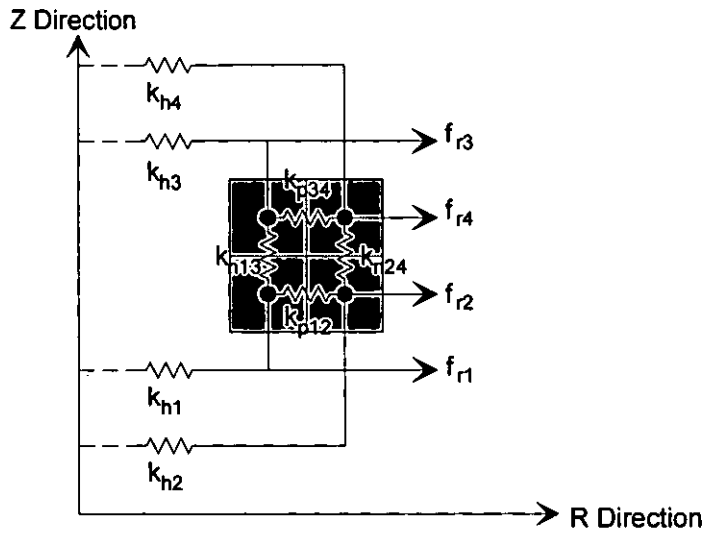


Figure 7.24 Definition of radial stiffness coefficients

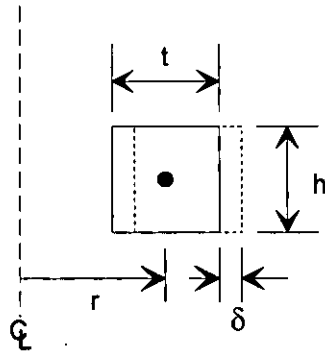


Figure 7.25 Hoop stiffness

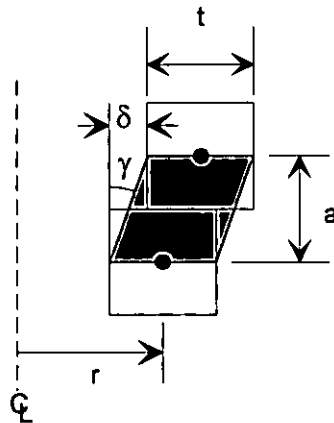


Figure 7.26 Normal radial stiffness

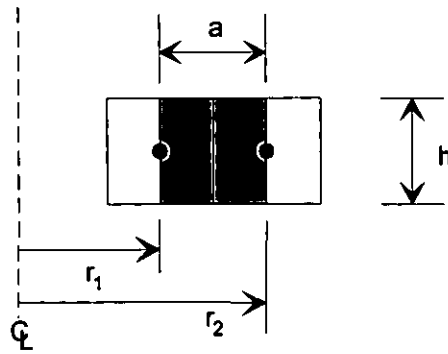


Figure 7.27 Tangential radial stiffness

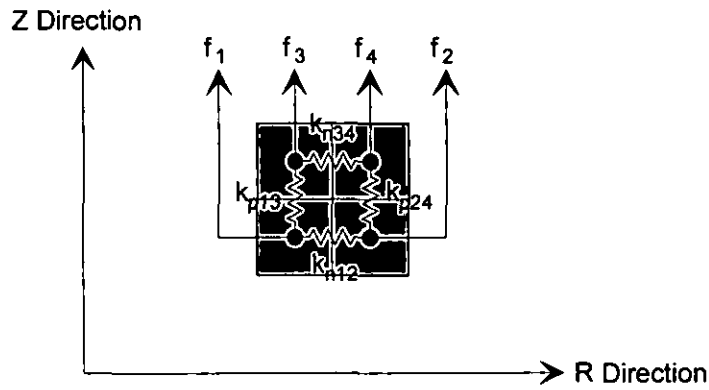


Figure 7.28 Definition of axial stiffness coefficients

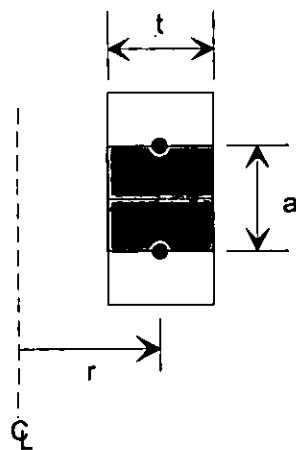


Figure 7.29 Tangential axial stiffness

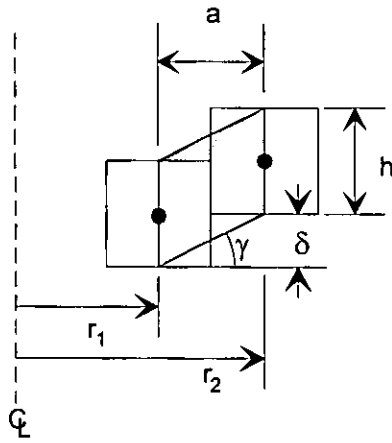


Figure 7.30 Normal axial stiffness

# 8. DESIGN STUDIES

*Using the modelling programs developed earlier, a series of simulated experiments were conducted. The aim was to design an optimal launcher within given parameters, and to gain a more general understanding of how a launcher works.*

## 8.1. PROJECTILE MASS

The first design study undertaken was to determine the affect of projectile mass on the operation of the launcher [Appendix C], when the mass was varied within practical limits. Figure 8.1 shows how the maximum velocity is effected by the change in projectile mass. The launcher efficiency is defined as the percentage of the initial electrical energy stored in the capacitor bank that is converted into the kinetic energy of the projectile. Figure 8.2 shows that the efficiency is affected by the projectile mass in a non-linear manner. Results indicate that reducing the mass of the projectile increases both the maximum velocity and efficiency of the launcher; however, if this is extrapolated too far it leads to the absurd situation of an optimal launcher having no mass. Clearly since, the end application of any launcher is to launch a given payload, reducing the projectile mass might also reduce its effectiveness.

## 8.2. PROJECTILE RADII

Previous studies into tubular induction launchers suggested that the difference between the radii of the projectile and drive coil would greatly effect the launcher performance [80]. To investigate this, the outside radius of the projectile was varied while all other factors remained constant. This was repeated with three different drive coil radii. The inside radius of the projectile was then varied, while the inside radius of the drive coil was set at three different values. The results from these tests are shown in Figure 8.3, and the dimensions of the three drive coils are shown below.

	Inside radius	Outside radius
Drive coil 1	15 mm	40 mm
Drive coil 2	25 mm	50 mm
Drive coil 3	35 mm	60 mm

Table 8.1 Dimensions of the three drive coils

The maximum velocities from the above study were normalised with respect to the maximum achieved in each set of tests and were plotted against the differences between the radii. A positive difference indicates that the projectile is larger than the drive coil. It can be from Figure 8.4 that, although the maximum velocity rapidly reduces when the projectile is undersize, it does not significantly increase when the projectile is oversize. It was thought that the reduction in the maximum velocity could be due to an increase in radial crushing forces, as well as the reduction in the projectile volume. Three example launchers were therefore studied using the finite element model. Magnetic vector potential contours and force vectors plots for oversized, normal and undersized projectiles, are shown in Figure 8.5, Figure 8.6, and Figure 8.7 and the total axial and radial forces in Figure 8.8 and Figure 8.9 respectively. Figure 8.8 shows that there is only a very slight improvement in the maximum axial force between the normal and oversized projectile. Whereas there is a marked reduction in the force applied to the under sized projectile, confirming the results from the filamentary study. While the axial forces on the normal and oversized coils are similar, the radial forces are significantly different. Although the reduction in radial force applied to the oversized projectile does not improve the performance of the launcher, it might help to prevent the unwanted deformation of soft projectiles. However, it should be noted that in these studies the mass of the projectile remained constant, whereas in reality the additional mass of the oversized projectile would reduce its maximum velocity and might off-set the structural advantages. Although the oversized projectile arrangement was very slightly faster than the normal projectile, it was decided that the normal projectile would be used in future studies, due to its simplicity.



It can be seen in Figure 8.3 that the maximum velocity achieved increases with the mean launcher radius. To see if this was a general pattern, a further three launchers with different mean radii were modelled. Figure 8.10 shows how the maximum velocity varied with launcher mean radius and while the increase in launcher performance diminishes with increased radii, the improvement seems to be continuous.

### 8.3. OPTIMUM NUMBER OF DRIVE COIL TURNS

Another factor often investigated during studies into other types of electromagnetic launchers, is the number of stator or drive coil turns [129]. Although most recently published papers on launchers involve single-turn drive coils [90], some earlier launcher systems were based on multi-turn drive coils [89] and therefore a study of these coils was undertaken. To prevent the amount of copper in the drive coil varying, the inter-turn insulation was assumed to be infinitely thin during this study, with the width of each turn calculated to ensure that the overall coil dimensions remained constant. From Figure 8.11 it can be seen that the maximum velocity increased with the number of turns. Other studies have often optimised the number of drive coil turns [62], but no optima appears to be present in the previous results. To see if an optimum launcher could be found, the investigations described below were therefore undertaken.

#### 8.3.1. SINUSOIDAL MODEL INVESTIGATION

The sinusoidal approximation model was used to determine if there was an optimum supply discharge frequency. An initial study was undertaken using a finite element model, with a fixed magnitude sinusoidal current, which was implemented using MEGA. The force components are plotted individually in Figure 8.12, because it was noticed that the quadrature component approached zero as the resultant force reached its maximum and this could be used to find the maximum force much more quickly. A similar study undertaken using a fixed magnitude voltage source gave the results shown in Figure 8.13. Since the sinusoidal approximation could be solved much

faster than the transient model, a filamentary sinusoidal model was written. Figure 8.14 and Figure 8.15 show results provided by this model. The study was repeated for several projectile thicknesses and a number of drive coil turns, with the results obtained being shown below.

Turns	Thickness (mm)	Maximum force (N)	Optimum frequency (Hz)
12	3	1889	27000
12	1.5	1926	26000
12	1	1933	14000
17	3	2342	25000
17	1.5	2344	25000
17	1	2360	13000
24	3	5008	18000
24	1.5	5014	18000
24	1	5031	10000

Table 8.2 Effects of drive coil turns and projectile thickness on the optimum supply frequency and maximum force.

The sinusoidal model showed that increasing the number of turns, or reducing the projectile thickness improved the launcher performance. The improvement in performance due to the reduction of the projectile thickness was caused by the current being concentrated closer to the drive coil.

### 8.3.2. RE-INVESTIGATION OF OPTIMUM DRIVE COIL TURNS

Although an optimum supply frequency had been found, there was still no indication of any optimum number of drive coil turns. The voltage used in the initial studies had been limited to the maximum achievable with the supply and auxiliary systems available (as described in Chapter 9). However, earlier launcher studies investigated systems that worked at much higher voltages [90]. To investigate this a series of high voltage simulation were undertaken, and from the results shown in Figure 8.16 it can be seen that an optimum number of turns was found. While the optimum number

can clearly be seen at higher voltages, it is not as obvious at low voltages. Although the 5kV results seem to be a straight line, an optimum was found at 26 turns and hence no other simulations were required. The optimum number can be approximated by the trend line shown in Figure 8.17.

At 2kV no optimum was found below 45 turns and unfortunately the very large number of filaments required to model a drive coil having over 45 turns, made simulation very difficult. However, it was concluded from the trend line in Figure 8.17 that the optimum number of turns at 2kV was approximately 48.

In addition, it was noticed that the maximum velocity achieved with the optimum number of turns varied almost linearly with supply voltage, as shown in Figure 8.18. Plotting the efficiencies of the optimal launchers, as shown in Figure 8.19, indicated that a maximum efficiency occurs at a supply voltage of 10kV with a 18 turn drive coil.

During the above study, the inter-turn insulation was assumed to be infinitely thin. To investigate the effects of this assumption the study was repeated with the inter-turn insulation fixed at 0.05mm and 0.5mm, while the overall dimensions of the coil were kept constant. Figure 8.20 shows that the introduction of 0.05mm thick insulation had little effect on the optimum numbers of turns. It was also seen that the introduction of 0.5mm thick insulation has little effect at high voltages, but the difference is obvious at lower voltages. The increasing effect of the insulation is not directly attributable to the decrease in voltage, since the increase in the resistance of the drive coil might have been the limiting factor. Despite the effects of the insulation thickness and the increase in resistance, Figure 8.21 shows that the maximum velocities achieved were only slightly reduced.

One way of achieving the optimum number of turns, even at low voltages, might be by dividing the drive coil into two layers. Undertaking a similar study to the previous investigation, the optimum number of turns for a two-layer drive coil was determined at several voltages. Figure 8.22 shows there was a slight increase in the optimum number of turns, and although the optimum number of turns at 2kV is only just

practical an optimum can nevertheless be found for low voltage launchers. From the comparison of the maximum velocities shown in Figure 8.23, it can be seen that the two-layer drive coil does not affect the launcher performance at low voltages, and only slightly reduces its performance at high voltages.

#### **8.4. DUAL PROJECTILE STUDIES**

A novel dual projectile launcher was also studied, with a second projectile, identical to the first, placed close to the “back” of the drive coil. The second projectile was driven in the same way as the first, but in the opposite direction. The main reason for investigating this structure was as an aid to later experimental work. During previous experimental work [81] some problems were experienced in obtaining clear results from high-energy experiments, it was thought that some of the problems were caused by the recoil of the launcher. It was hoped that using a second projectile would reduce these effects and provide clearer results.

To investigate the effects of a second projectile, a series of studies similar to those in the previous section were undertaken. A single layer drive coil was investigated initially, and although the difficulty of constructing a single layer dual projectile launcher was recognised, it was nevertheless considered a to be good starting point. From these initial tests the optimum number of drive coil turns were determined for a range of supply voltages. The comparison shows in Figure 8.24 between the optimum number of drive coil turns for both dual and single projectile launchers shows that the optimum number of turns is increased for the dual projectile arrangement. It was proposed that the addition of the second projectile reduces the effective inductance of the launcher, which is then restored to its optimum by the addition of extra turns.

It can be seen in Figure 8.25 that the maximum velocities of the dual projectile launcher are lower than the single projectile launcher. However, since twice the mass is being accelerated the dual projectile system is more efficient, as shown by Figure 8.26. However, it can also be seen that the efficiency declines much more rapidly at low voltage. The theoretical maximum efficiency is the subject of some discussion,

with some believing that the theoretical limit is 50%, and by others, including researchers at Loughborough, that the limit is 100% [130]. For the dual projectile launcher, calculations from simulated results gave an optimum efficiency of 51.4% at an initial voltage of 10kV.

The consequences of multiple coil layers were predicted to affect the dual projectile launcher in a similar manner to the single projectile launcher. To test this proposition, a study of a dual projectile launcher with a two-layer drive coil was undertaken. The results obtained are compared with results from the previous study in Figure 8.27, and it can be seen that the two-layer drive coil only slightly increases the optimum number of turns.

### **8.5. LAUNCHER RADII**

Although it was shown in previous studies that the optimum number of drive coil turns was affected by several factors, the projectile and drive coil radii remained constant throughout these studies. In addition, it was shown in the first study that the launcher is near an optimum when the drive coil and projectile radii are the same. A study was undertaken to investigate the effect of varying both the projectile and drive coil radii simultaneously on the optimum number of drive coil turn. To determine to effect of increasing the outside radii they were varied between 40 and 90mm, while the inside radii were maintained at 25mm. It can be seen from Figure 8.28 that the maximum velocity appears to increase monotonically as the outside radii increases. The inside radii were then varied between 30mm and 5mm, with the outside radii set at 50mm. From Figure 8.29, it can be seen that the maximum velocity reaches a limited maximum before falling, as the inside radius is reduced. Both Figure 8.30 and Figure 8.31 show that the optimum number of turns varies in an almost linear manner. The slight deviation that can be seen in both figures is caused by the integer nature of the number of turns.

Since the optimum number of turns varies almost linearly with the launcher radii, it might allow an approximate optimum number of turns to be determined for a launcher

of any size, if other factors remain constant. Since the optimum number of turns only increases slowly with launcher size, this study could be used to find a coil size at which it is practical to wind a coil with the optimum number of turns.

### **8.6. DRIVE COIL THICKNESS**

During all the above studies, it was assumed that the drive coil was 5mm thick, as this is a readily available size of copper strip. Since the coil thickness was arbitrarily chosen, and other factors had been optimised, the possibility exists that there might be an optimum drive coil thickness. It was thought that reducing the thickness of the drive coil would increase its resistance, and hence reduce its performance. However, it was also thought that reducing the thickness of the drive coil would force the current to be concentrated closer to the projectile, and hence would improve its performance. Although the optimum shown in Figure 8.32 seems to be clear, it should be noted that all the results are within 98% of the maximum. The results from this study confirm that concentrating the drive coil current closer to the projectile does improve the effective coupling, but the increased resistance has a limiting effect.

### **8.7. INITIAL PROJECTILE DISPLACEMENT**

Intuitively it seemed obvious that reducing the initial distance between the projectile and drive coil will improve the magnetic coupling, and hence improve the performance. A previous study by Bondaletov and Gonchareko found that both the maximum velocity and efficiency both fell rapidly as the minimum initial displacement was increased [86]. With the initial displacement defined as the distance between the drive coil and the projectile, an optimum arrangement would have a zero initial displacement. However practical limitations prevent the initial displacement from being reduced to zero, and a study was undertaken to quantify the effects of this limitation.

In this study, the initial displacement was varied between 0 and 2mm, with the supply voltage set at various levels and the number of drive coil turns kept at 18. However,

some unexpected results were obtained, as shown in Figure 8.33. The 2kV and 10kV results intersect at a displacement of 1.25mm, and the predicted optimum displacements for the 20kV and 40kV experiments were not zero. It was thought that this might be caused by the fixed number of drive coil turns and the 40kV test was re-run with its optimum number of drive coil turns (8). Figure 8.33 shows that the optimum initial distance for the second 40kV test was zero, as initially expected. However, when the results from this study are compared with those obtained by Bondaletov and Gonchareko, further differences are found. They predicted that the rate at which the launcher performance declined would be highest at the minimum displacement, and would reduce as the displacement increased. However, Figure 8.33 shows that the minimum gradient occurs at the minimum displacement, and that the gradient increases with displacement.

The results from both studies show that the performance of a launcher decreases as the initial projectile displacement is increased. The optimum initial displacement is affected by the number of drive coil turns and the supply voltage, demonstrating the existence of some relationship between the turns / voltage optima and the initial displacement optimum. Although the nature of the relationship is unclear, the optimum initial displacement is zero when the other launcher parameters are close to their optima.

## 8.8. RE-INVESTIGATION OF PROJECTILE MASS

During the first investigation of the effect of projectile mass, it was found that the efficiency of the launcher increased as the projectile mass was reduced. This was in contrast to the work of Bondaletov and Gonchareko [86] who found that the launcher efficiency peaked and then reduced, as the projectile mass was reduced. An important difference between the two studies was the range of projectile masses studied.

To provide a better comparison between the two studies, a series of simulations were undertaken with the projectile mass varied over a wider range than previously studied. Figure 8.34 shows that the maximum velocity increases in a similar manner to that

shown in Figure 8.1 over the extended range of masses, but Figure 8.35 shows that the efficiency falls-off in the manner described by Bondaletov and Gonchareko.

While the results of the study into the effects of projectile mass produced the expected results, the drive coil current waveforms were not as expected. Figure 8.36 shows the presence of a second hump in the drive coil current waveform that is initially undetectable, but becomes the dominant feature as the projectile mass is reduced. Comparison of Figure 8.35 and Figure 8.36 shows that the maximum launcher efficiency occurs when the second hump becomes noticeable. The second hump could be caused by the translational voltage components of the launcher equations, since a lightweight projectile can gain a very high velocity almost instantaneously. In effect, the high speeds possible with a light-weight projectile may mean that the translational EMF induced in the drive coil is sufficient to affect the discharge of the supply capacitor. This EMF effectively delays the discharge of the supply until the projectile has moved away from the drive coil, making the launcher much less efficient. In previous launchers, with single turn drive coils and thin projectiles, this second hump might have completely hidden the first, and could in turn have led to incorrect calculation of the power supply parameters.

## **8.9. UNUSUAL LAUNCHER ARRANGEMENTS**

Since, in its most basic form, an induction launcher can be considered as two opposing electromagnets, the performance might be improved if the projectile is “magnetised” prior to the discharge of the supply. The simplest method of achieving this would be to make the projectile from a permanent magnet, but this would of course be depolarised by the very high magnetic fields present in the launchers [46]. Alternatively, if a current was circulating in on the projectile prior to its launch, the magnetic field generated might improve the launcher performance.

An initial projectile current could be obtained by connecting it to the main or an auxiliary supply. Unfortunately, these both require the projectile to be open circuit prior to launch, and to instantly close when the launch coil is energised. It was shown



by a static finite element model, that the maximum axial force on the projectile increased by 11% when it was connected in series with the drive coil. Although this improvement might seem significant, it would be almost impossible to reproduce in practice. Supplying the projectile from a second 1kV DC source improved the performance by 31%, this again could not be made in practice.

It was decided that the use of an additional pre-exciter coil was the only practical method of producing a current in the projectile prior to the discharge of the main supply, and two possible locations considered. Locating the exciter coil behind the drive coil would cause a significant voltage to be induced in the drive coil and only a small current flow in the projectile. Placing the exciter coil in front of the projectile would increase the mass of the projectile, but is the most likely modification to succeed. The exciter coil would be a low voltage coil supplied by a continuous AC supply. This exciter coil would have many turns of thin wire, to produce large currents in the main projectile, which would act as a shorted single-turn transformer secondary. The exciter would be connected to its supply by thin break wire leads and the main supply would be discharged at the point on the exciter supply waveform that maximised its effect. To determine what improvements in performance could be achieved, an exciter coil was designed to maximise the current flow in the projectile. Figure 8.37 shows that a 200Hz exciter supply produces the maximum total current in the projectile for a given exciter current and Figure 8.38 shows the current distribution through the exciter coil and launcher, prior to the main supply discharge. Although Figure 8.39 clearly shows that the maximum axial force on the projectile increases with exciter current, the increase in launcher performance is only moderate.

## 8.10. CONCLUSIONS

The initial study of projectile mass suggested that both the velocity and efficiency tended to increase as the projectile mass was reduced, but a later study showed that the efficiency began to decrease once the mass was below 100gm. This helps reconcile the idea that a projectile of zero mass will have zero kinetic energy, and hence the efficiency must fall to zero as the mass is reduced.

The study into the effects of projectile radius relative to the drive coil radius showed a slight improvement in the performance was obtained when the projectile overhung the drive coil. However, this was so small that it was ignored, and the projectile and drive coil radii were maintained the same in all other testes.

The initial study of drive coil turns showed that performance improvements were possible, but the expected optimum did not materialise. While the sinusoidal approximation demonstrated that optimum launcher conditions existed, the conclusions that could be drawn from the results were limited. It later become apparent that the lack of an optimum condition in the first study was due to the supply voltage range considered. A second study showed that the optimum number of drive coil turns was dependent on the power supply voltage. The maximum velocity increased almost linearly with the supply voltage, and the optimum efficiency occurred at 10kV.

The study of drive coil turns was expanded to investigate the effects of insulation thickness and of winding the drive coil in two layers. The use of a two-layer drive coil meant that an optimum number became practical, for even moderate supply voltages.

A similar series of studies performed on a dual projectile launcher showed that the optimum number of drive coil turns was increased. This was probably due to the second projectile reducing the effective inductance of the launcher. It was also shown that while the velocities were lower, the overall efficiency was higher than that of a single projectile arrangement. Simulated results showed that a dual projectile launcher could have an efficiency exceeding 50%.

The study of launcher radii showed that the launcher performance improved as the launcher outside radii were increased, suggesting that the outside radii should be maximised within practical limitations. It was also shown that the inside radii could be optimised for a particular outside radius, and that the optimum number of drive coil turns increased only slowly with launcher size. This suggests that scaling the launcher

size could allow a practical low voltage launcher to be made with their optimum number of drive coil turns.

The study of drive coil thickness showed that the effective coupling of the drive coil and projectile could be improved by forcing the drive coil current to flow nearer to the projectile. However, this study also showed that reducing the drive coil thickness increased the resistance and hence reduced the launcher performance. While some unexpected results were produced at the start of the study into the effects of initial projectile displacement, it was clear that the optimum launcher performance occurs with the minimum initial displacement.

The second study of projectile mass confirmed the results found by Bondaletov and Gonchareko, and in addition established that the projectile mass affected the shape of the current discharge waveform. Light projectiles accelerate so quickly that the motion of the projectile induces large EMFs in the drive coil, which act to limit the peak discharge current and hence the launcher performance.

Several unusual launcher arrangements were investigated, to see if pre-exciting the launcher would improve its performance. While significant theoretical improvements were achieved these, they would be very difficult to reproduce in practice. A practical system used a second wound coil to produce a current in the projectile prior to its launch, but the improvements in performance were offset by the additional complexity.

## 8.11. FIGURES

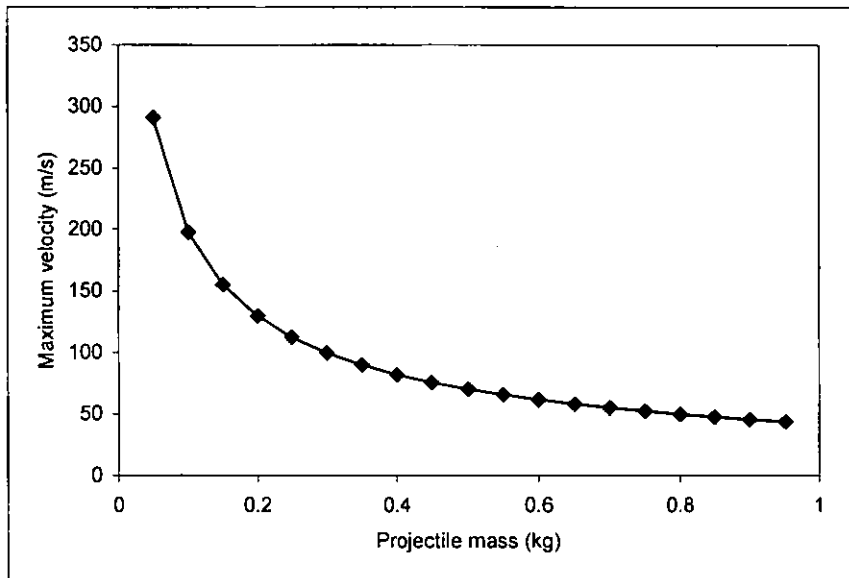


Figure 8.1 Effect of projectile mass on maximum velocity

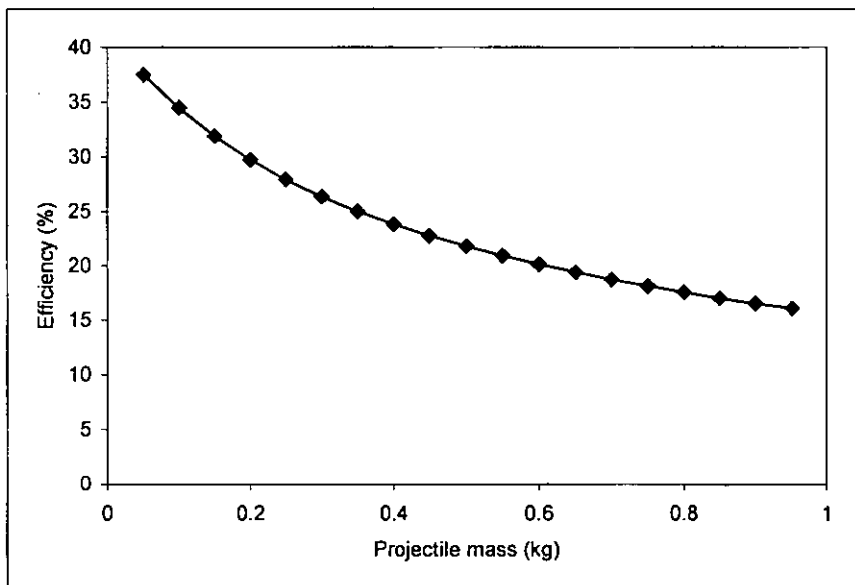


Figure 8.2 Effect of projectile mass on launcher efficiency

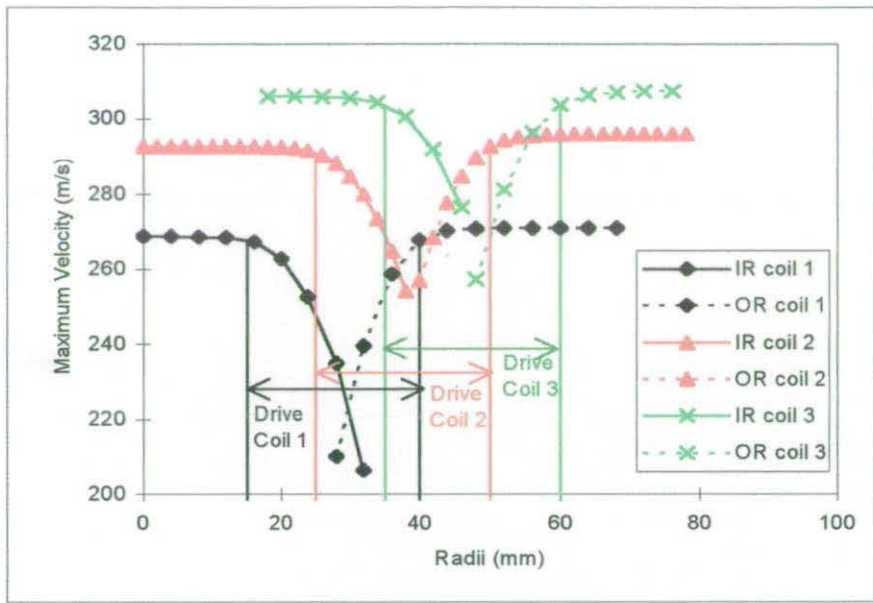


Figure 8.3 Effect of radii on maximum velocity

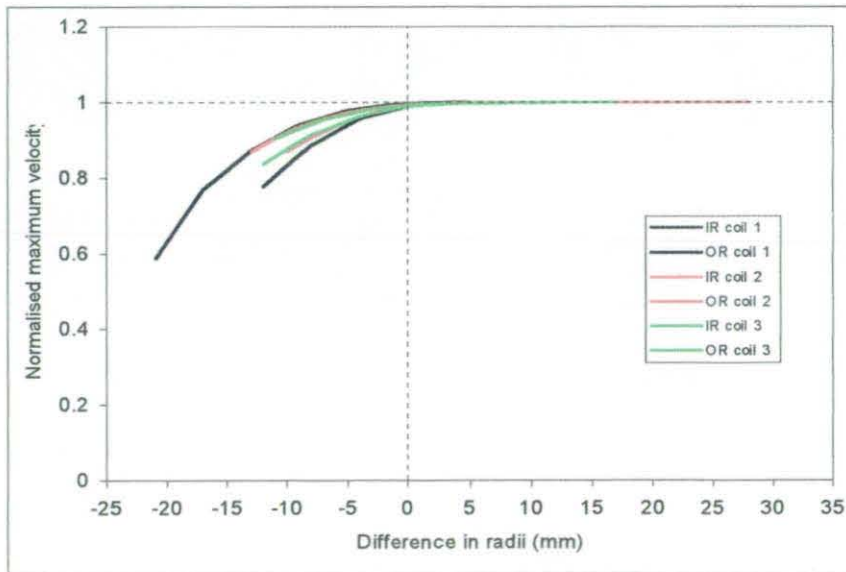


Figure 8.4 Effect of normalised radii on normalised maximum velocity

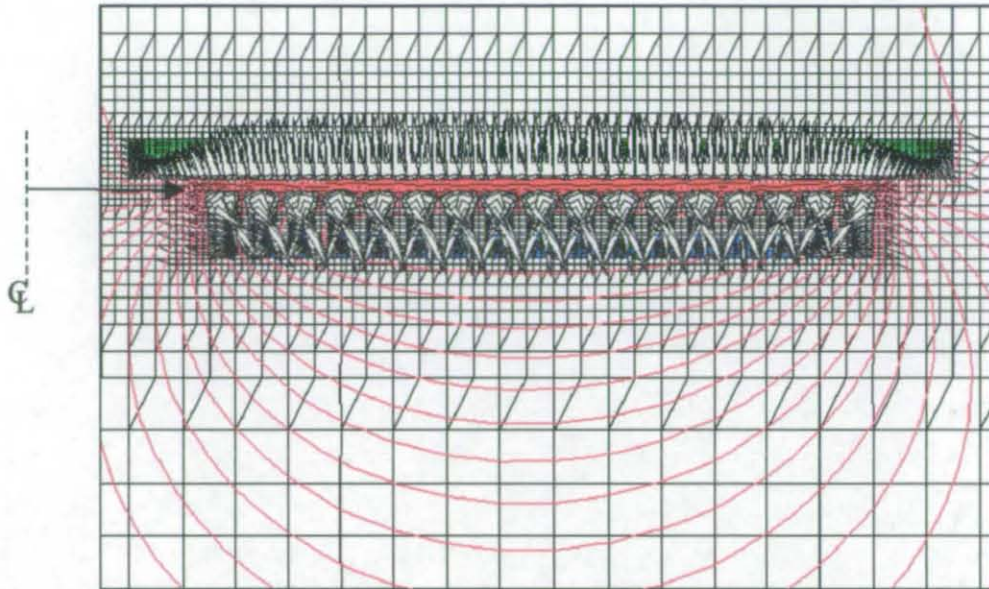


Figure 8.5 Force vector and field contour plot for an over sized projectile

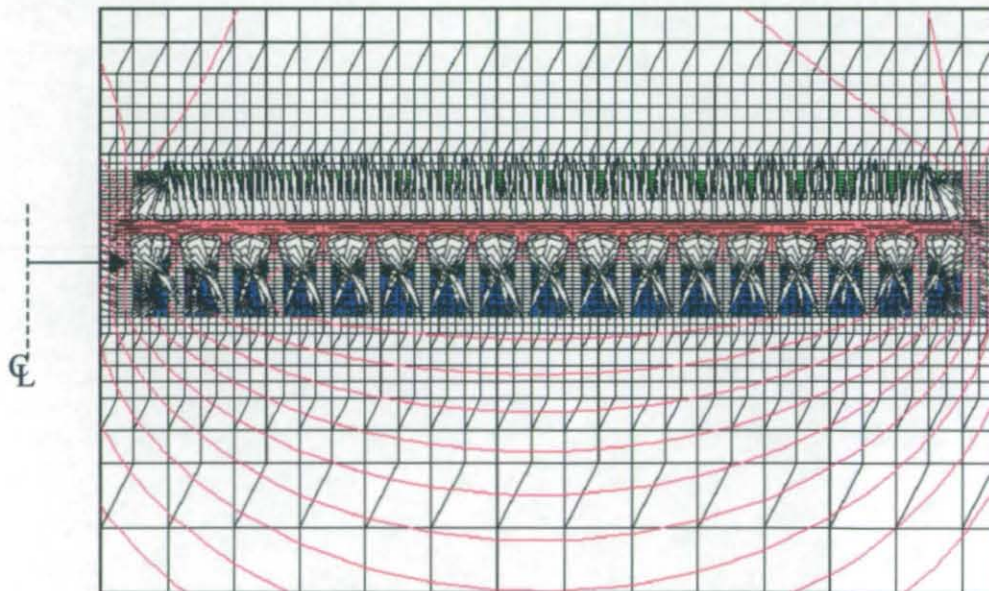


Figure 8.6 Force vector and field contour plot for a normal projectile



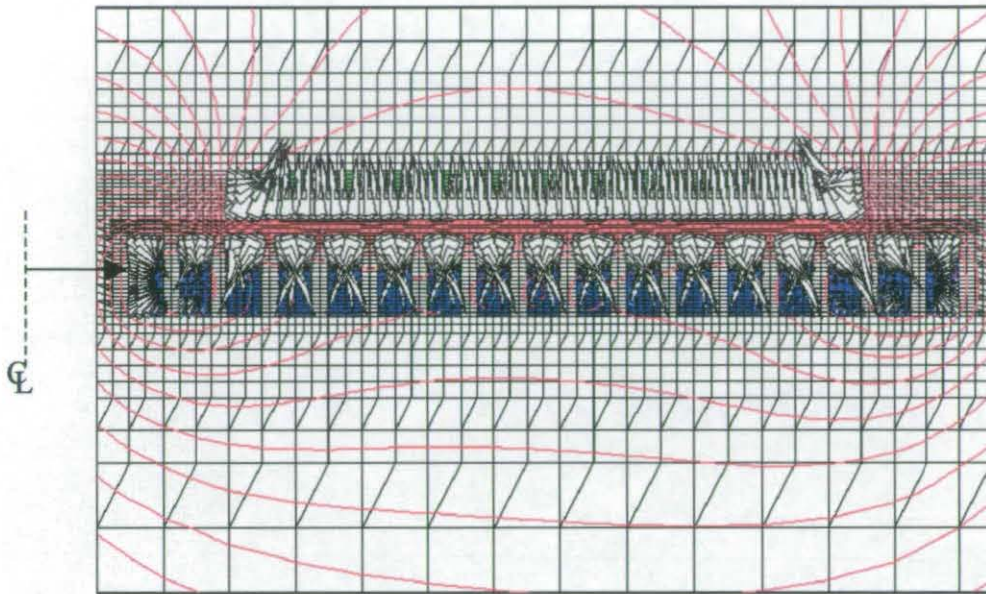


Figure 8.7 Force vector and field contour plot for an under sized projectile

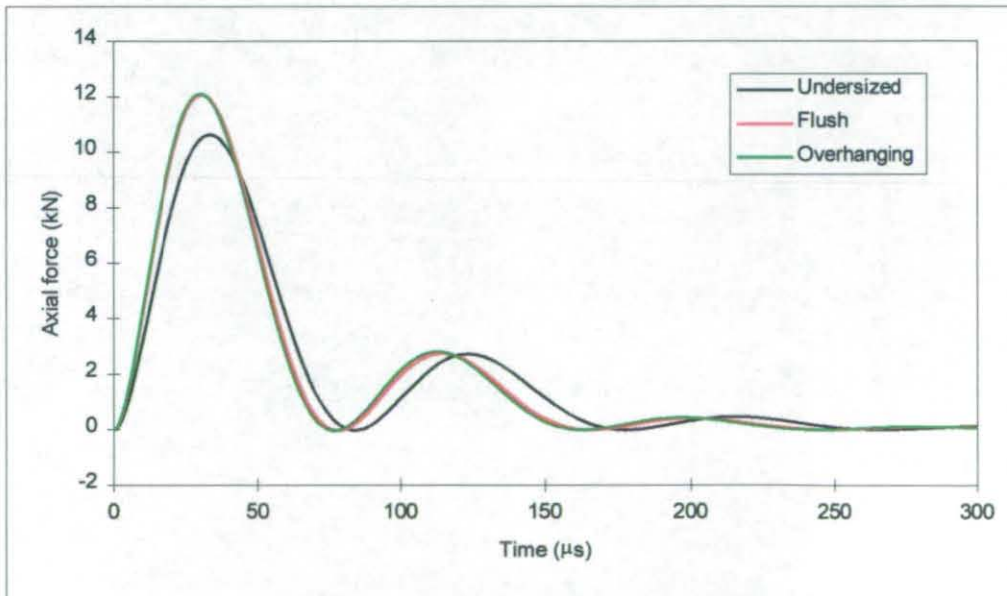


Figure 8.8 Effects of projectile size on total axial force

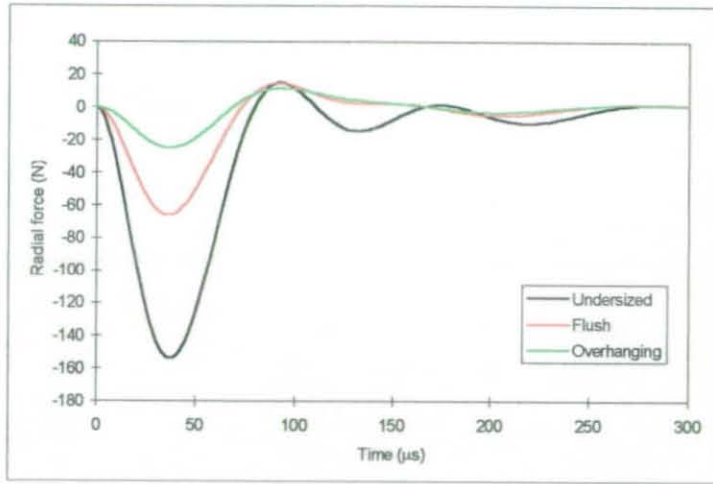


Figure 8.9 Effects of projectile size on total radial force

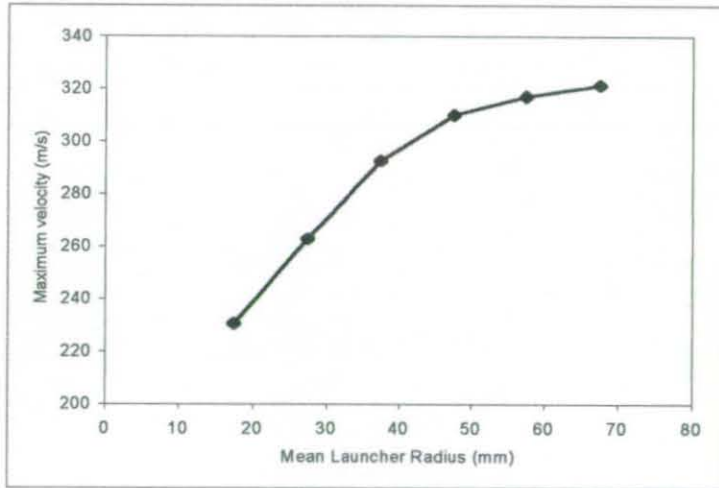


Figure 8.10 Effect of the mean launcher radius on maximum velocity

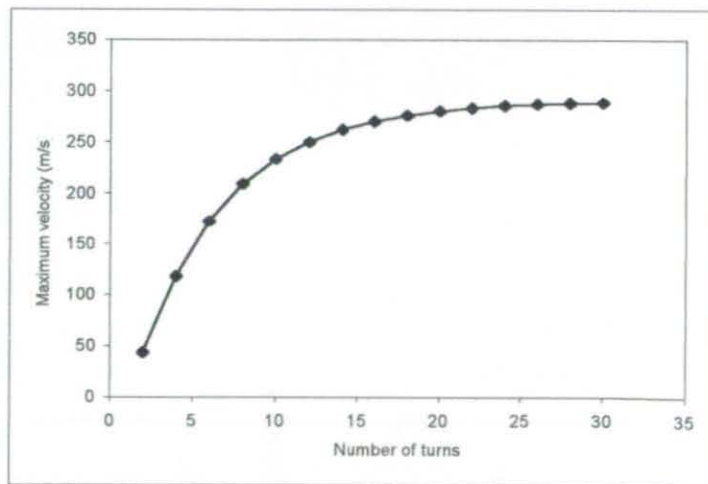


Figure 8.11 Effect of number of turns on maximum velocity



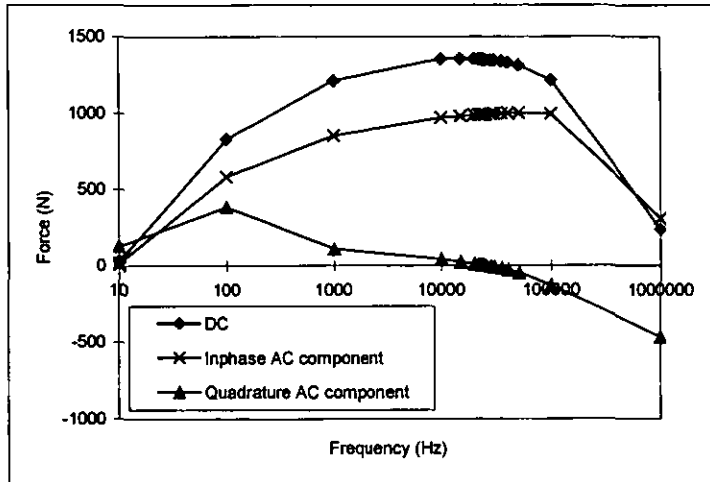


Figure 8.12 Effect of supply frequency on the components of force

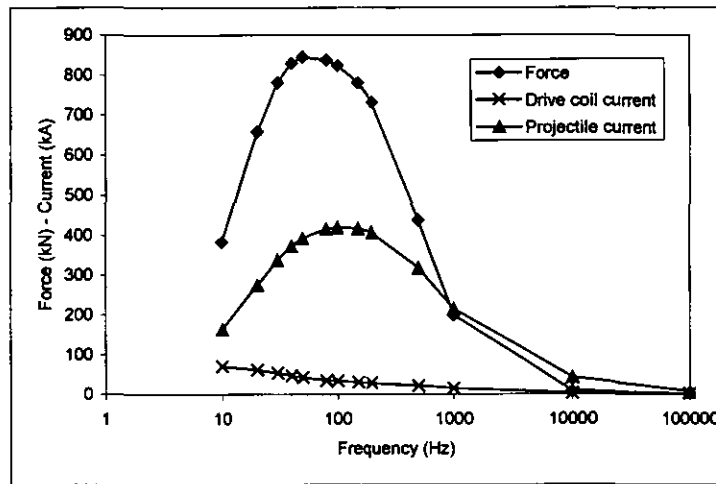


Figure 8.13 Effects of voltage source frequency on currents and maximum force

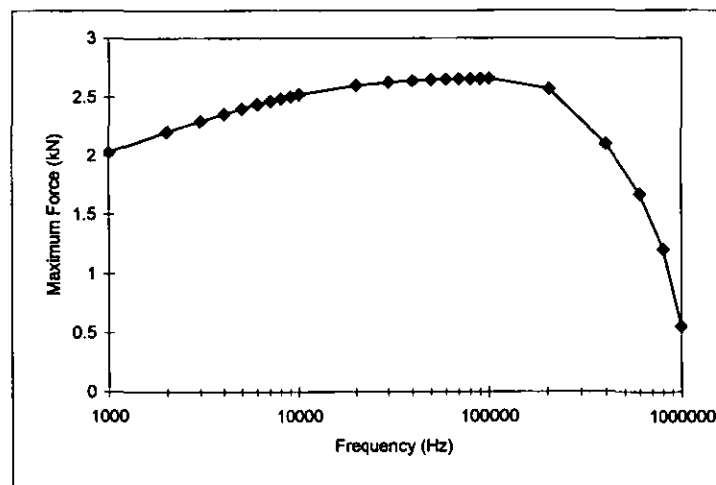


Figure 8.14 Effect of current source frequency on maximum force

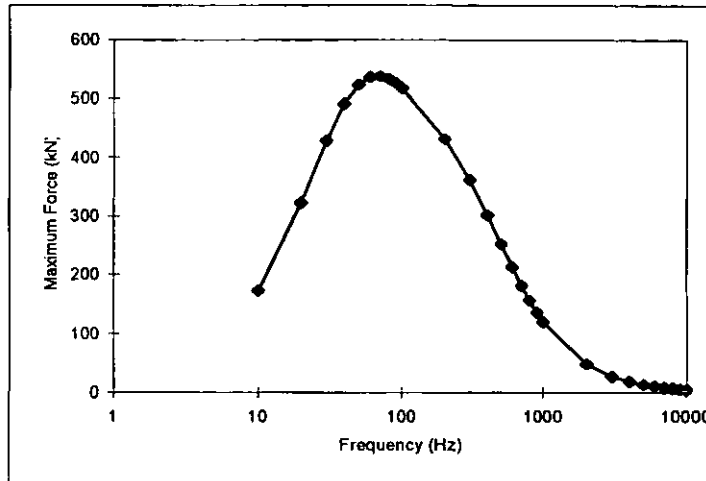


Figure 8.15 Effect of ideal voltage supply frequency on maximum force

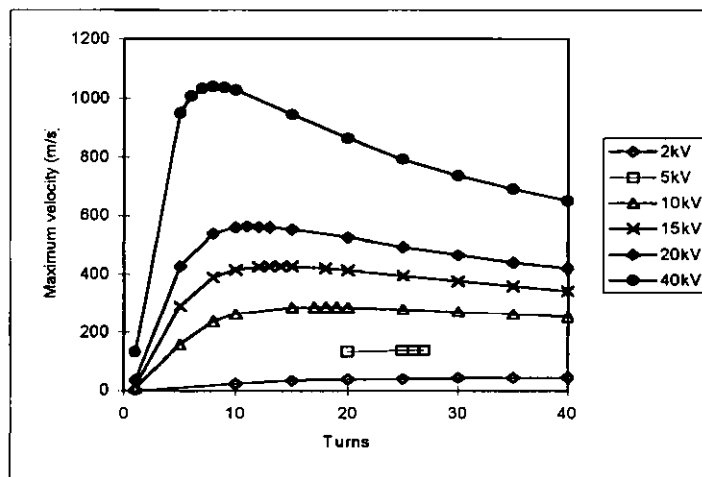


Figure 8.16 Effect of drive coil turns on maximum velocity

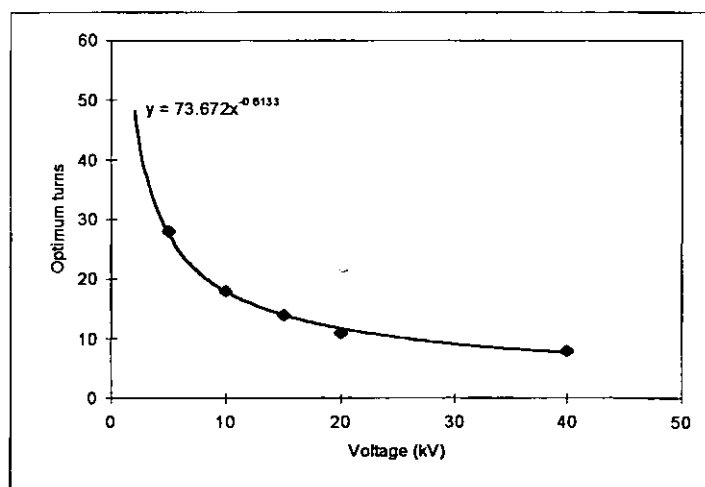


Figure 8.17 Optimum number of turns against initial capacitor voltage

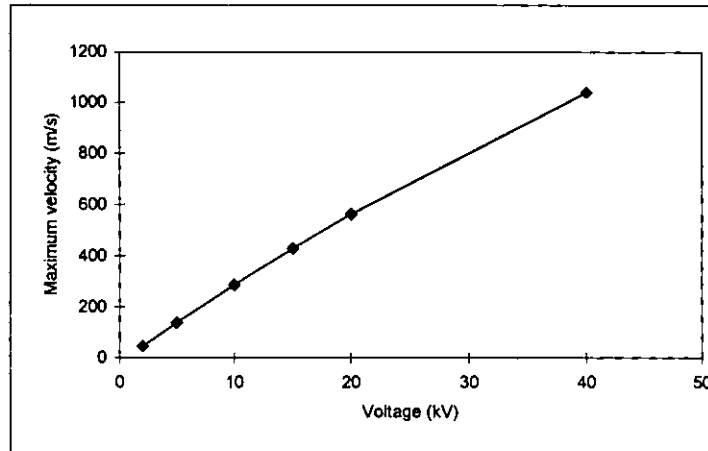


Figure 8.18 Maximum velocity against initial capacitor voltage

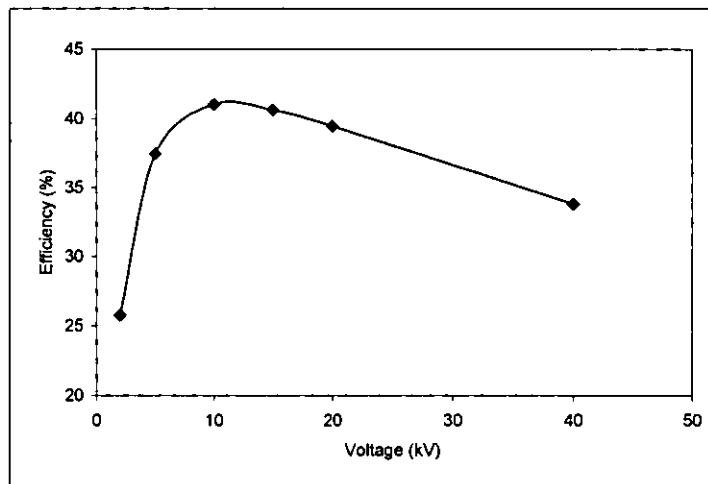


Figure 8.19 How launcher efficiency varies with capacitor voltage

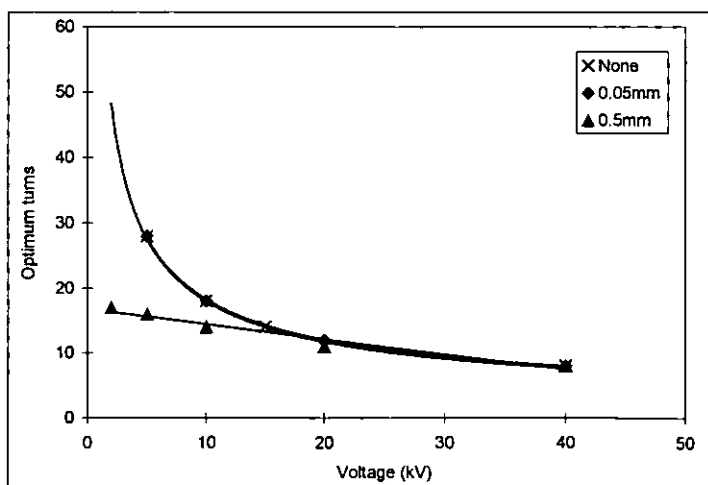


Figure 8.20 Optimum number of turns with different insulation thickness

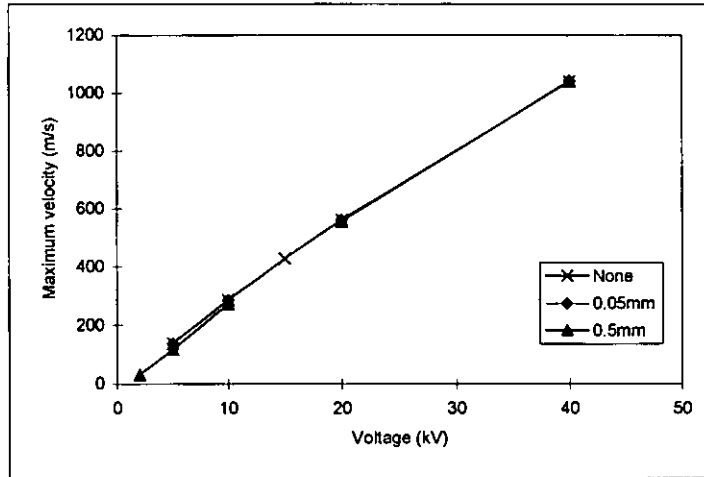


Figure 8.21 Maximum velocity with different insulation thickness

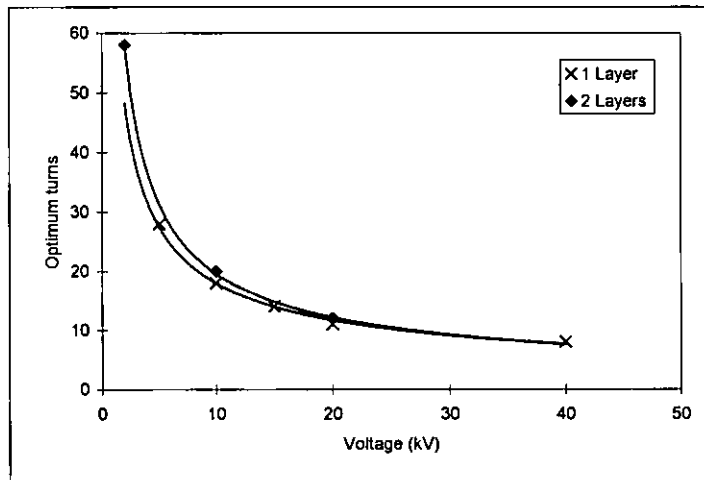


Figure 8.22 Optimum number of turns for two-layer coils

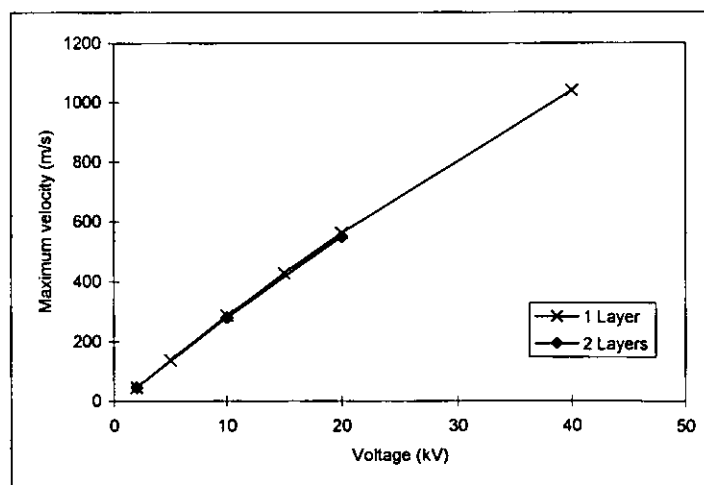


Figure 8.23 Comparison of maximum velocities with one and two layer drive coils

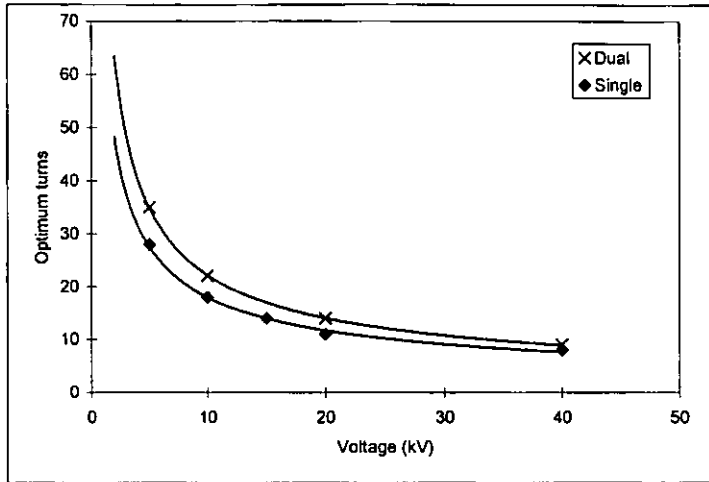


Figure 8.24 Optimum number of turns for dual projectile launchers

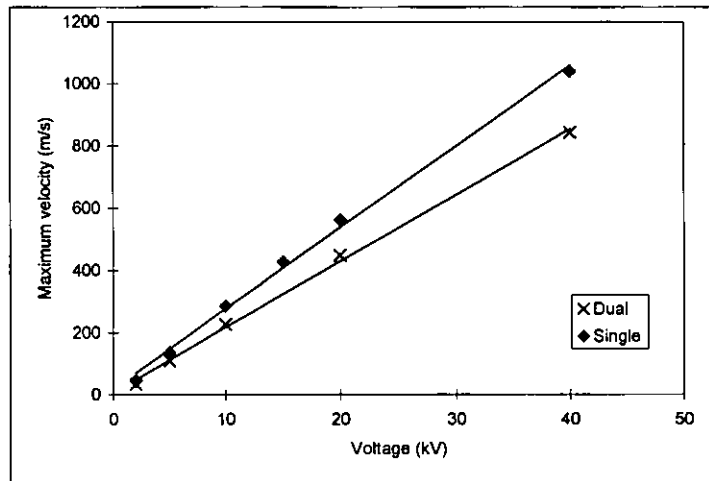


Figure 8.25 Maximum velocities for dual projectile launchers

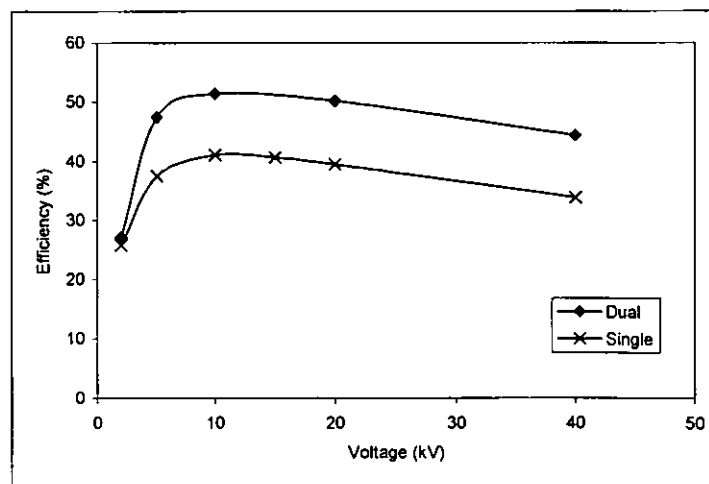


Figure 8.26 Effect of supply voltage on dual projectile launcher efficiency

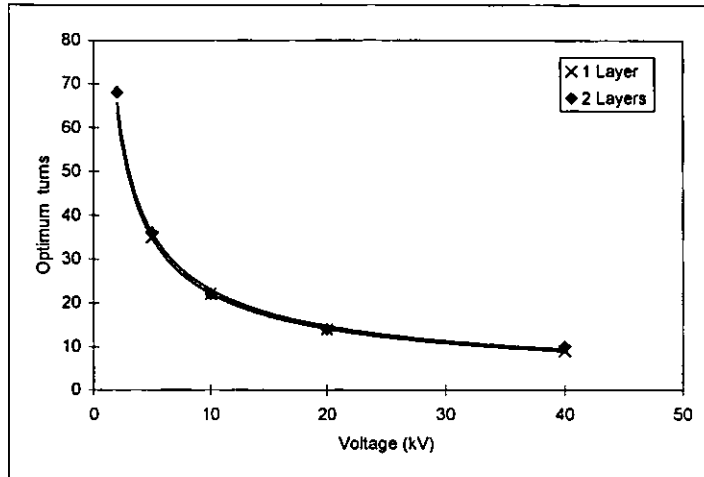


Figure 8.27 Optimum number of turn for a two-layer dual projectile launcher

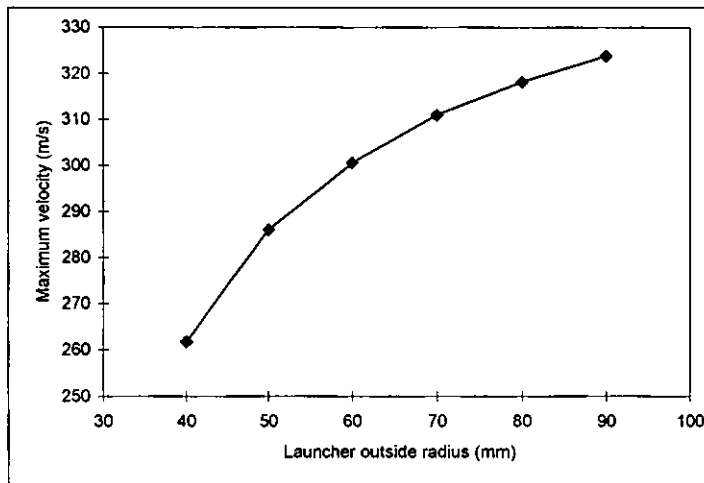


Figure 8.28 How maximum velocity varies with outside radius

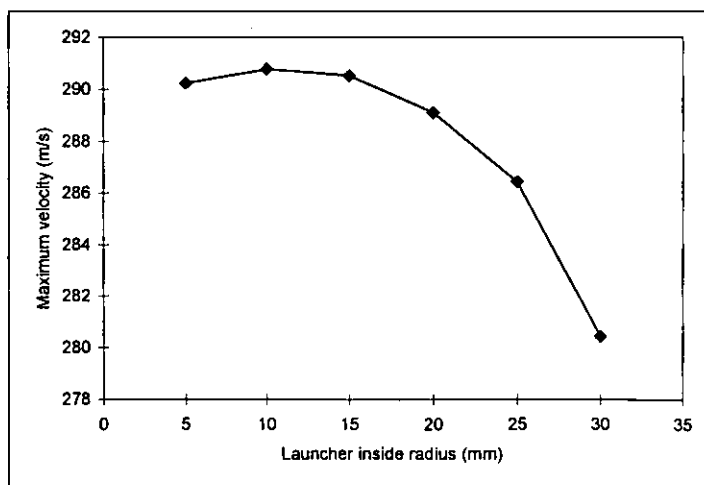


Figure 8.29 How maximum velocity varies with inside radius

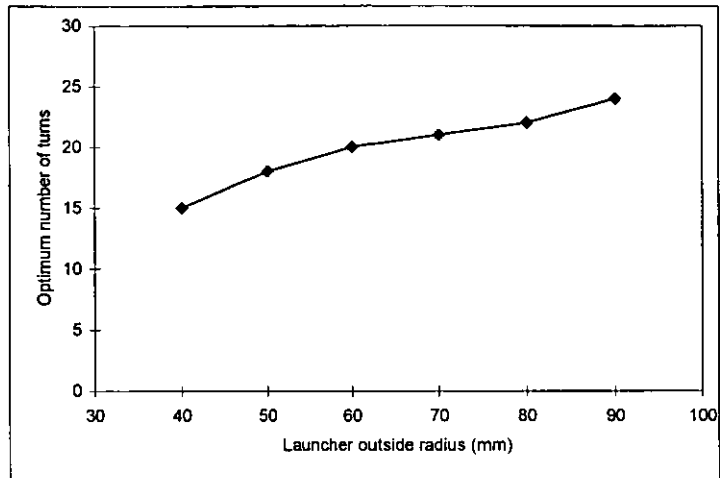


Figure 8.30 Optimum number of turns at various outside radius

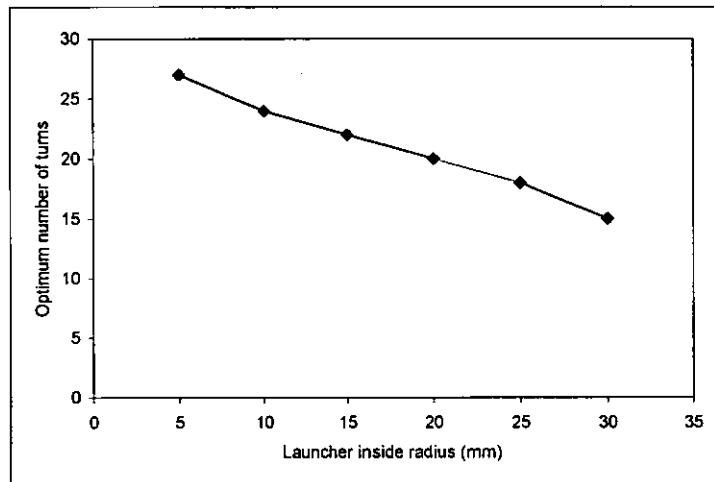


Figure 8.31 Optimum number of turns at various inside radius

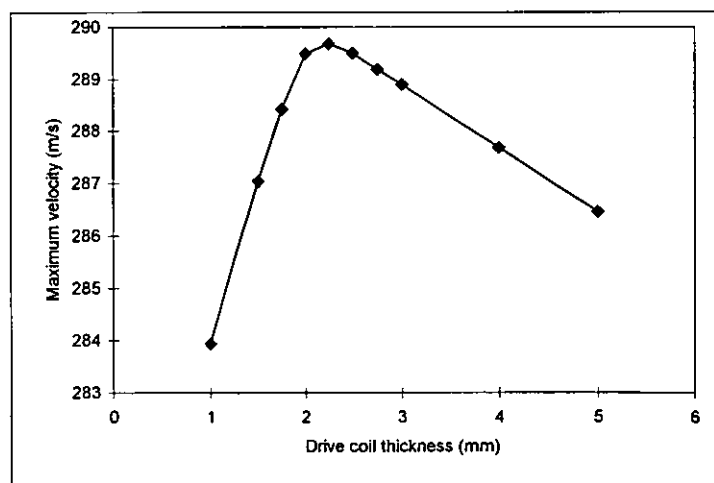


Figure 8.32 Optimum drive coil thickness

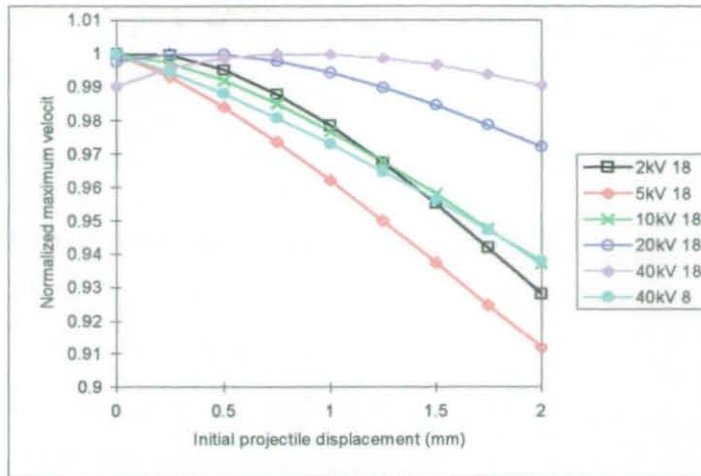


Figure 8.33 How maximum velocity varies with initial projectile displacement

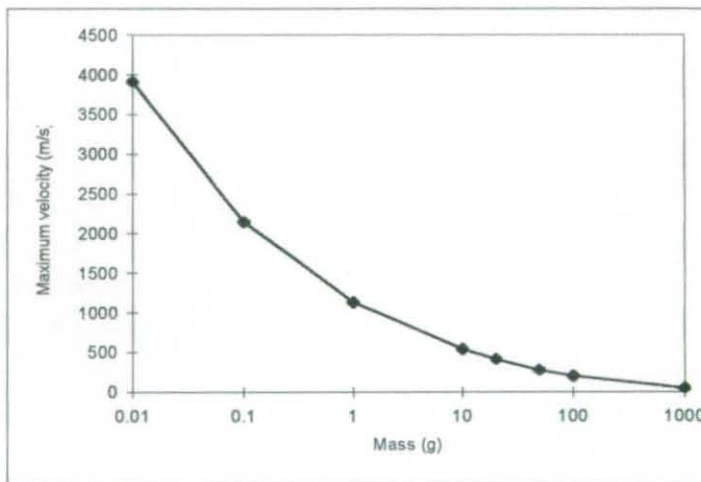


Figure 8.34 How maximum velocity varies with a wide range of projectile masses

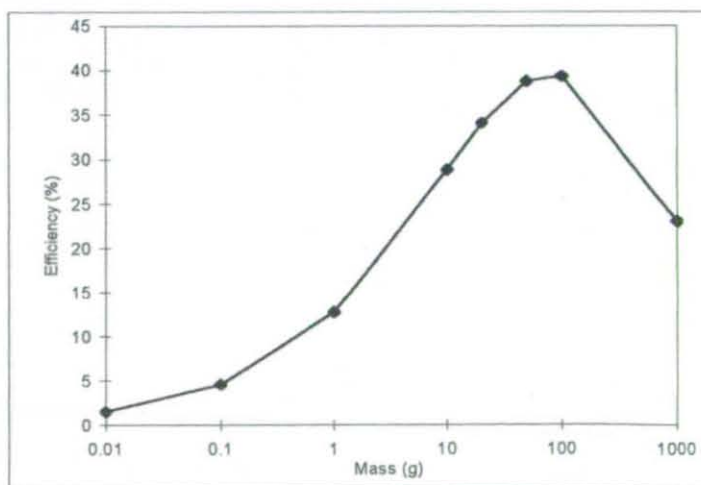


Figure 8.35 How projectile mass effects launcher efficiency



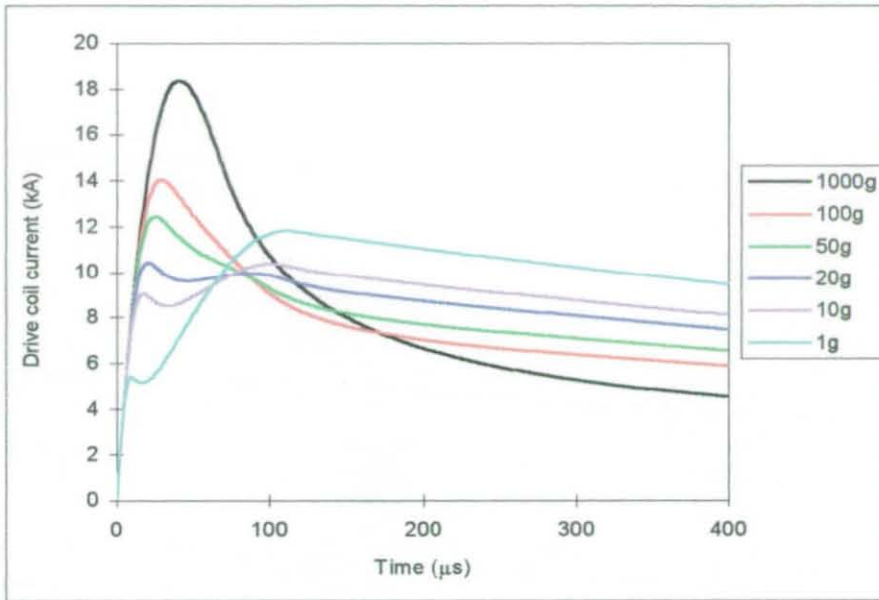


Figure 8.36 How projectile mass affects drive coil current

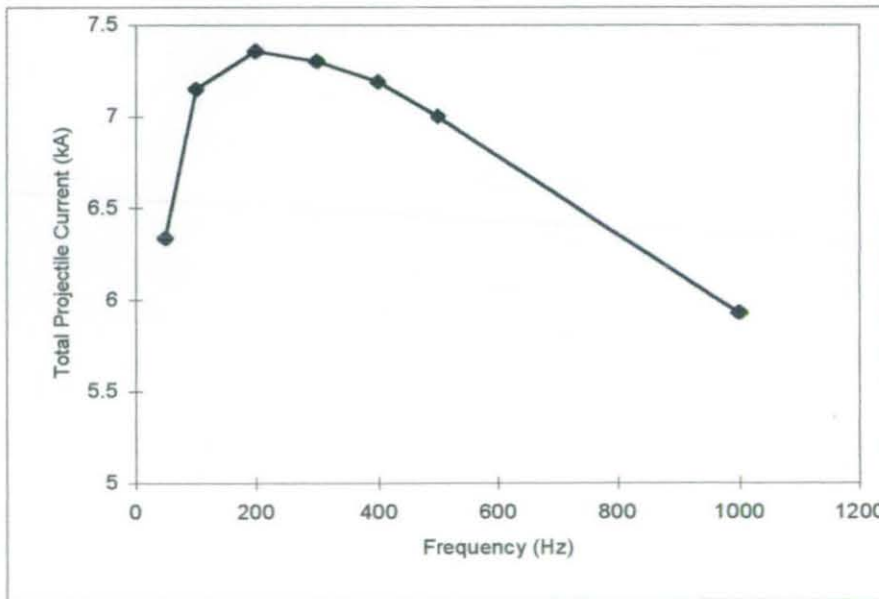


Figure 8.37 Effect of exciter supply frequency on total projectile current

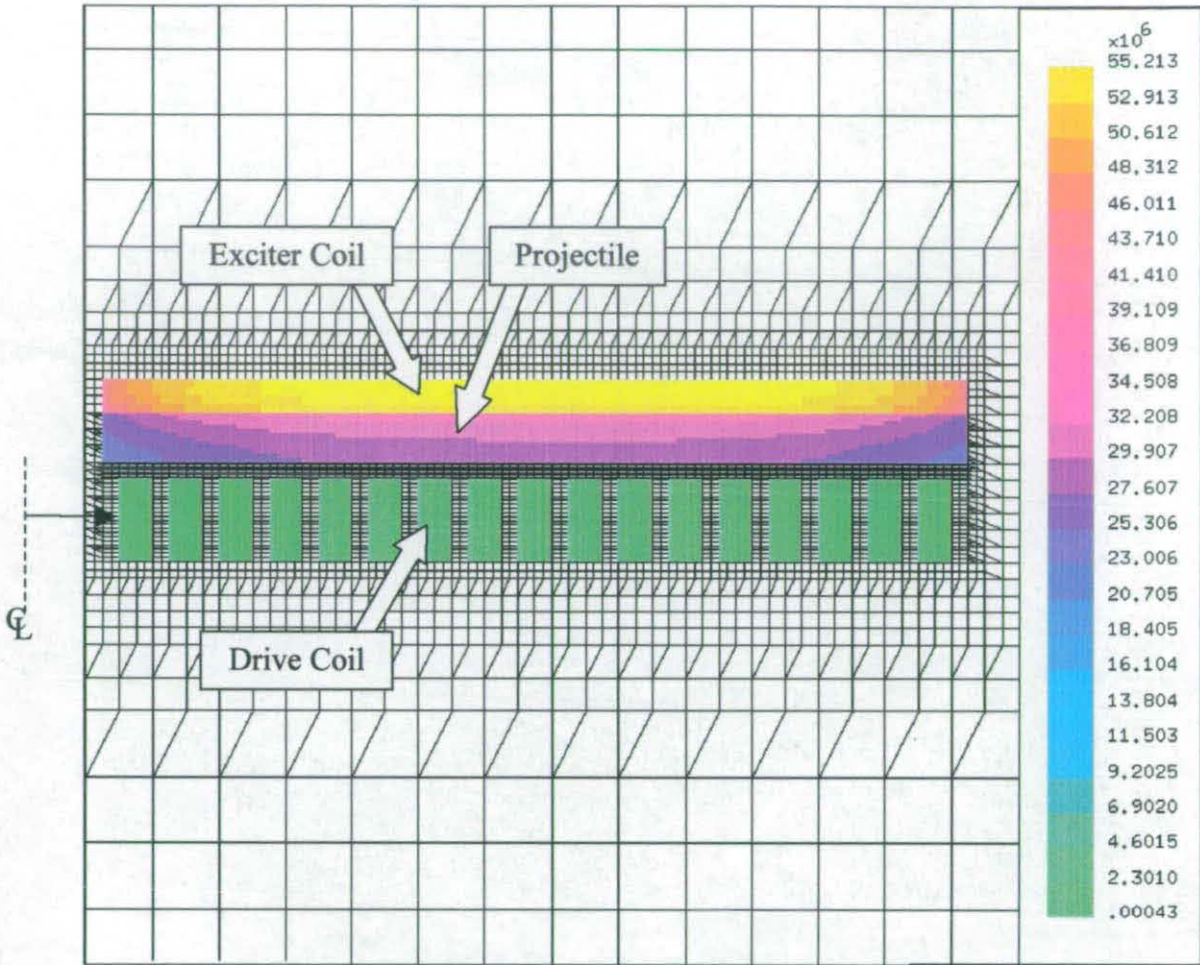


Figure 8.38 Pre-launch exciter and launch current distribution

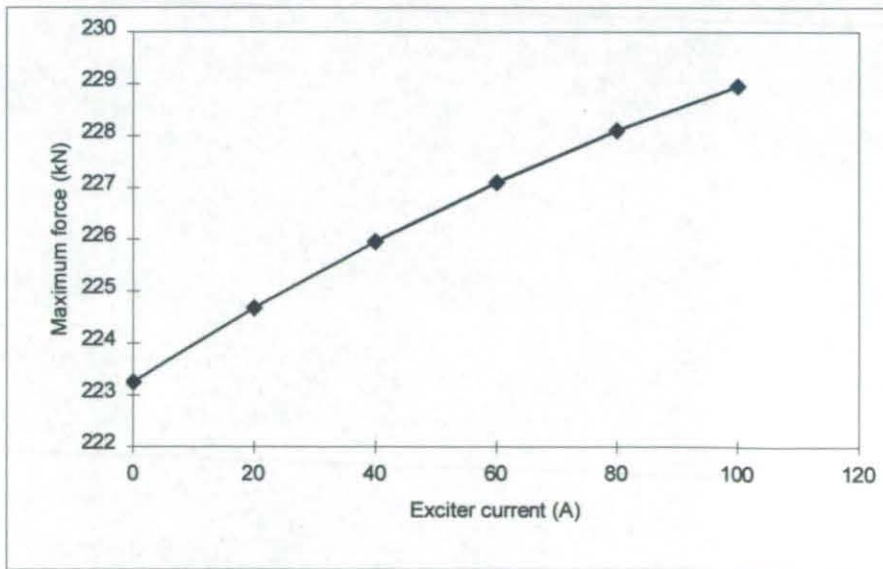


Figure 8.39 Effect of exciter current on maximum axial projectile force

## 9. EXPERIMENTAL EQUIPMENT

*This chapter discusses the development and construction of the launcher, power supply, test rig, and associated components. Also discussed are the methods of data collection and the instrumentation produced to support the experimental work carried out. The development of an improved speed measurement system led to the ability to measure the yaw of a projectile without effecting its flight. Comparisons between different methods of speed and yaw measurements are also described.*

### 9.1. THE TEST RIG

Previous launcher work by Williamson [129] used a horizontal launcher arrangement, with the launcher mounted several feet off the floor and a large sandbox was used as a reaction mass to absorb the recoil. However, when launchers were first studied at Loughborough [81] it was decided that a vertical launcher arrangement would enable the floor to be used as the reaction mass. During the initial investigations the speed sensors were mounted on the same frame as the launcher, but this caused problems as the launch energies were increased, and in later experiments the sensors were mounted on separate free standing frames. The sizes of the forces involved soon became clear, and it was possible that the sensors might be affected by recoil forces transmitted through the floor. To try to eliminate this problem and to allow easy construction of a dual projectile launcher, it was decided that the present launchers would be mounted horizontally.

The launcher structure developed is shown in Figure 9.1, and this allowed the experiments to be safely contained in a relatively small space. During single projectile launches a set of ballast bricks were used as a reaction mass, with the whole frame mounted on a rubber mat to allow slight horizontal movement, the sensors were mounted on separate stands. This meant that even if the recoil forces moved the launcher the sensors would accurately measure the projectile position relative to the initial position.

One problem with horizontal launchers is the question of how to hold the projectiles against a flat drive coil. Initially two strands of lightweight fishing line were used, but this took a long time to set-up for each shot. Another idea tested was to glue the projectile to the drive coil with a low strength adhesive, but experimental results indicated some deviation in the speeds that were measured. It was thought that this was probably due to variations in the cure time allowed between the application of the glue and the positioning of the projectile. With the cure time kept constant at two minutes, there was an improvement in the relative standard deviation of the measured speeds but this remained quite high, as Table 9.1 shows.

	Glued projectile	Glue with a fixed cure time	Retaining plate
Max (m/s)	14.025	14.471	13.661
Mean (m/s)	12.959	13.591	12.886
Min (m/s)	10.593	12.788	12.063
Standard deviation (m/s)	1.172	0.593	0.489
Relative standard deviation (%)	9.047	4.361	3.801

Table 9.1 Deviations in measured speed due to different projectile mounting methods.

This deviation was attributed to the build up of glue on both the projectile and drive coil surfaces. Although the glue could be removed, the time taken to remove the old glue, and re-glue the projectile would be comparable to the fishing line method. The effects of a plastic retaining plate bolted to the drive coil were also investigated. The retaining plate was a sheet PVC of approximately the same thickness as the projectile with a hole slightly bigger than the projectile in the centre. This reduced the relative standard deviation of the measured speeds even further, and since it was less messy, and much faster to use than the other methods, it was used for all future experiments.

## 9.2. VOLTAGE MEASUREMENT

Various different types of voltage measurement systems were considered, including the use of a Pockel cell, or an optical link system. However, since the maximum

voltage used would not exceed 10kV it was thought unnecessary to develop an optical system. A 1000:1 voltage divider was therefore constructed using a 200M $\Omega$  resistor in series with a 200k $\Omega$  adjustable resistor chain, across which the voltage was measured. Although this provided accurate readings when the voltage was constant or varying slowly, such as during charging, it was greatly affected by noise during a launch. A second 100M $\Omega$  resistor stack that had had been used in previous projects was also tested this was placed some distance from the power supply to reduce the effects of noise. Although the affects of noise were much reduced, it was unable to provide a clear transient voltage profile. In addition, the low resistance discharged the capacitor too rapidly to allow accurate firing of the supply. A third voltage divider was therefore constructed using a chain of resistors to produce a similar voltage divider to the first, with shielding provided by a grounded mu-metal box. A simple capacitive compensator was used to improve the transient response of the voltage divider, and a low voltage spark gap and a surge arrestor to protect the oscilloscope from possible fault conditions. Figure 9.2 shows a comparison between results from the three voltage dividers when measuring the same test discharge. This was generated by charging the power supply to 500V and discharging it through the drive coil without a projectile.

### 9.3. CURRENT MEASUREMENT

A Rogowski coil provides a simple yet effective method of measuring current, and it was decided to produce a set of coils and to calibrate these using a commercially available probe.

Several published papers were found on the subject [131], [132]. Using a construction method similar to that described in reference [133], a clean M3 nut was used to produce a helical groove in the inner insulation of a length of URM76 cable. A fine wire was then wound into the groove and the assembly was covered by heat shrink tubing for protection. A Rogowski coil produces a voltage that is proportional to the rate of change of current in the conductor passing through the coil. The voltage must therefore be integrated to obtain a current and the following methods were tested

- Passive Integrator
- Active Integrator
- Numerical Integrator

Figure 9.3 shows a passive integrator, which operates satisfactorily if  $V_{\text{out}}$  is connected to a very high resistance load and  $V_{\text{out}} \ll V_{\text{in}}$ , which was achieved by keeping the RC product large. A passive integrator was tested with limited success; the signal was integrated but was also distorted due to noise. An active integrator is a complex circuit, and to produce an accurate and reliable circuit could have been an expensive and time-consuming exercise. Numerical integration of the Rogowski coil output, when captured by a digital storage oscilloscope, was therefore thought to be the best option.

The stored signal can be easily integrated using a basic trapezoidal integration routine. Initial tests showed a large drift when comparing the commercial current probe signal to the signal integrated using the oscilloscope's onboard numerical integrator. It was thought that limiting the oscilloscope input bandwidth might reduce the drift, and some improvement can be seen when Figure 9.4 is compared with Figure 9.5. However, the majority of the error is caused by the zero offset, and any error in the zero offset is added incrementally to the integrated signal. Hence, even a small zero offset error can cause the large errors seen in Figure 9.4 and Figure 9.5. This error was removed by subtracting a linearly incremented amount from the numerically integrated signal. It can be seen from Figure 9.4, that the full bandwidth setting produces better results than the limited bandwidth setting when the zero offset error is removed. Figure 9.6 shows that all three Rogowski coils compare well with the commercial probe when calibrated.

#### 9.4. SPEED MEASUREMENT

Many different methods of projectile speed measurement have been developed and used in the study of electromagnetic launchers over recent years. Ideal measurement systems determine the speed of a projectile directly and do not interfere with its flight,

but in practice the speed is usually deduced from position and time measurements. The most commonly used position sensors are direct electrical contact, induced electrical and optical.

Direct electrical contact sensors rely on the projectile hitting a set of wires or conducting foils, and either breaking or making a circuit depending on the configuration. If the circuit is broken, the projectile interrupts the current in a circuit by cutting through a thin wire, but if the projectile is itself conductive, this may not occur until the whole of the projectile has cleared the wires. If a circuit is made, the projectile either pierces the insulation between two conductors or directly shorts the conductors. The advantage of this system is that it will detect the front of a projectile. However, if it is used with an induction launcher the very high magnetic fields generated during a launch can mask the real signal. Both systems have the additional drawback of making a direct contact with the projectile, if it is delicate then its flight might be affected. If the projectile is launched by an induction launcher large currents may be flowing in it, and hence safety precautions are required to prevent dangerously high voltages being applied to the monitoring equipment.

Inductive sensors can only work with conductive projectiles, but they are commercially available and have been widely used to detect bullets and arrows. They work by detecting the disruption caused to a magnetic field when a conductor passes through it. Although commercial sensors cost as little as £250 and can measure speeds of up to 3000 m/s, they are unsuitable for detecting projectiles launched by electromagnetic systems, since the pulsed magnetic fields generated by the launcher and the high projectile currents could damage or interfere with an inductive sensor.

Optical sensors are popular in the electromagnetic launcher community because of their inherent noise immunity and voltage isolation. Usually a laser is placed at one side of the anticipated flight path, illuminating an optical fibre or an electro-optical sensor on the other side. As the projectile passes through the laser beam, the drop in light is detected by the sensor.

Previous laser position sensing systems used at Loughborough had separate lasers for each beam, and were used in conjunction with a timer which was triggered when the power supply was discharged, to determine the time / position of the projectile. However this system is costly, and triggering the timer from the same trigger as the supply introduces inaccuracies. Later systems used a laser beam close to the drive coil to trigger the timer, but this was difficult to set up. The current system measures the time between the projectile braking two laser beams, and inherently assumes that the speed remains constant between the two sensors. Hence, the closer the beams are together, the more accurately the speed can be calculated. The system described here uses a single class 3a laser and two beam splitters to produce two pairs of lasers beams, as shown in Figure 9.7. Using these pairs of beams and two timers it was possible to calculate the projectile speed at two locations using only one laser. The beam splitters were thin pieces of Perspex set at  $45^\circ$  to the beam, with reflections off both surfaces providing a pair of beams that were perpendicular to the source beam. The beams provided adequate illumination of the optical sensors at a range of over half a meter. Using Figure 9.8 and equation 9.1, the distance between a pair of laser beams can be determined from the thickness of the Perspex sheet.

$$b = \sqrt{2} t \tan \alpha \quad \{9.1\}$$

The position sensing and speed calculation methods were calibrated over a wide range of speeds. The system was tested initially by dropping weights from a given height, with the mid-range speeds calibrated using a synchronous motor with a bar attached to its shaft. By locating the laser beams at various positions along the bar, a range of speeds were obtained. A high-speed camera was also used to validate the measured velocities during actual launches. Figure 9.9 shows a comparison between the speeds measured by the laser gates and that calculated from the high-speed camera images. During testing and calibration of the laser system, it was noticed that occasionally two pulses were produced by the photo-detectors, probably caused by light travelling through the hole in the centre of the projectile. If this were the case, it would suggest that the projectiles were yawing during flight, and this possibility was therefore investigated.



### 9.5. MEASUREMENT OF PROJECTILE YAW

The need to measure the yaw of a projectile is much less common than the need to measure its speed. The simplest method is from photographs taken in flight using a high-speed camera, but a much less costly method is by means of a witness plate. If the shape of the projectile is known, the imprint it leaves on the witness plate can be used to determine the angle of the projectile at the moment of impact. However, a witness plate usually disrupts the flight of the projectile, and prevents any useful measurements from being made further down range. In addition, the material used for the witness plate must be chosen carefully, to ensure that the yaw is not masked by the damage caused on impact with the witness plate.

The two pulses noticed during the speed calibration tests suggested that there might be a third method of determining projectile yaw. When launching annular plate projectiles, two possible situations arise depending on whether or not a gap is detected. The situation when a gap is detected can be considered as shown in Figure 9.10. Expressing the pulse and gap lengths by equations 9.2 and 9.4 respectively, enables the angle of yaw to be found from equation 9.4.

$$\text{Pulse length} = p = a \sin \theta + c \cos \theta \quad \{9.2\}$$

$$\text{Gap length} = g = b \sin \theta - c \cos \theta \quad \{9.3\}$$

$$\theta = \sin^{-1} \left( \frac{p + g}{a + b} \right) \quad \{9.4\}$$

If the projectile has not rotated sufficiently to produce a gap, its geometry can be considered as shown in Figure 9.11. From Figure 9.11 the pulse length can be expressed as

$$p = (2a + b) \sin \theta + c \cos \theta \quad \{9.5\}$$

or

$$p = A \sin (\theta + \alpha) \quad \{9.6\}$$

where

$$A = \sqrt{(2a + b)^2 + c^2} \quad \{9.7\}$$

and

$$\alpha = \tan^{-1}\left(\frac{c}{2a + b}\right) \quad \{9.8\}$$

The yaw is then found by substituting  $\beta = \theta + \alpha$  into equation 9.6.

A high-speed camera was used to validate the results obtained from the laser gates and witness plates. By setting the projectiles at a slight angle prior to launching, large yaw angles were achieved. The witness plates were made from heavy weight paper, and to ensure a clear mark was made on the witness plates the projectiles were painted with blue ink before launching. The yaw was calculated from the amount that the image on the witness plate deviated from the circular shape of the projectile. Figure 9.12 compares the results from the camera images and witness plates for test three shots. The camera images of shot three can be seen in Figure 9.13 and the resultant witness plate in Figure 9.14. The results for this series of tests demonstrate that witness plates can be used to measure the yaw of a projectile. However, they also highlight the limitation of the witness plates being able to determine the yaw of a projectile at only one point.

Initially setting the projectile at a slight angle enabled the high-speed camera to be used to validate the results from the laser gates. Figure 9.15 compares the yaw calculated from the laser gate signals with the angles measured from the camera images. The yaw angle of a projectile was determined from the camera images in two ways, by either measuring it directly from an image or from the relative displacements of the top and bottom of the projectile in the image. Figure 9.16 and Figure 9.17 show the signals from the first and second pair of laser gates. Figure 9.17 shows clearly the two pulses that were seen initially in the early laser calibration test. The results in Figure 9.15 and Figure 9.16 confirm that the yaw of a projectile can be determined even when there is no gap in the signals.

## 9.6. POWER SUPPLY

Although various power supplies and switching techniques were used, the basic circuit of Figure 9.18 remained the same throughout. The capacitor was charged via the current limiting resistor to the required voltage. The capacitor then discharged through the drive coil, when the main switch was closed. When the voltage across the crowbar switch reversed, it became forward biased and started to conduct. The crowbar protects the capacitor from the large reverse voltage that it would otherwise experience due to the ringing nature of the main circuit. After each launch, the dump switch was closed to ensure that no energy remained in the capacitor, and the wand resistor was used to ensure that no energy remained in any other part of the circuit. In addition, a shorting link was placed across the capacitor terminals after it had been discharged, to ensure that no residual charge built up on the capacitor.

The supply was remotely controlled via an optical fibre and protected signal cables. The control unit was protected from possibly lethal fault conditions by low voltage spark gaps, and surge arrestors. A standard CCD camera and monitor were used to monitor the status of the launcher and supply without entering the test chamber.

## 9.7. DETERMINATION OF POWER SUPPLY PARAMETERS

To enable accurate models of the test launchers to be compiled, the power supply parameters must be determined. Some of these were found from manufacturer's data sheets, but since many are affected by the construction and layout of the power supply, it was decided that most of these needed to be measured.

The power supply was first tested with a short circuit at the load end and the crowbar diodes were removed to allow the system to ring. The supply was charged to a few hundred volts and discharged into the short, producing the current waveform shown in Figure 9.19. Simple calculations enabled the total resistance and inductance of the main switch circuit to be determined [134].

The crowbar diodes were replaced, and the test repeated. Figure 9.20 compares the discharge current with that predicted using parameters determined above. Figure 9.21 shows a similar comparison between measured and predicted capacitor voltages. The effect of the crowbar switch can be seen clearly, with the negative voltage that remains on the capacitor being caused by the forward conduction drop of the crowbar.

Since the leads were made from parallel coaxial cables, their inductance could be accurately calculated. Using this value and the measured cable and short resistances, enabled the main switch parameters to be separated from the total circuit parameters. The electrical time constant of the crowbar circuit was found from the decay of the current once the main switch had stopped conducting. Although the  $L/R$  value of the crowbar circuit had been found, there is no easy method of measuring either the resistance or the inductance of the crowbar switch. It was therefore assumed that the crowbar diode resistance was the maximum figure quoted in the data sheets, with the corresponding inductance found from the circuit time constant. Similar techniques to those described here were used to determine the characteristics of all the supplies used during this project.

## 9.8. CONCLUSIONS

The launcher structure was designed to reduce the effects of launcher recoil on the position sensors, using past experience a horizontal launcher was chosen. After testing several methods of holding a projectile against the drive coil, a PVC retaining plate was chosen because it was quick, easy to use and produced the most consistent results.

Three possible voltage dividers were tested, with the arrangement finally chosen using a mu-metal box to shield the resistor chain from the effects of the power supply discharge. A set of Rogowski coils was used to measure the discharge current produced by the supply. Numerically integrating the signal from the Rogowski coils after the signal had been captured by a digital oscilloscope produced the most accurate results.

A laser beam position sensing system allowed the projectile speed to be accurately determined. The system was calibrated over a wide range of speeds, and the results were compared with measurements taken from a high-speed camera. The laser beam sensors could also be used to determine the yaw of a projectile, and results obtained were compared with results from both a high-speed camera and witness plates.

A power supply and control system were successfully developed and tested. A series of tests were also developed to characterise the power supply equivalent circuit parameters to enable the supply to be accurately modelled.

### 9.9. FIGURES

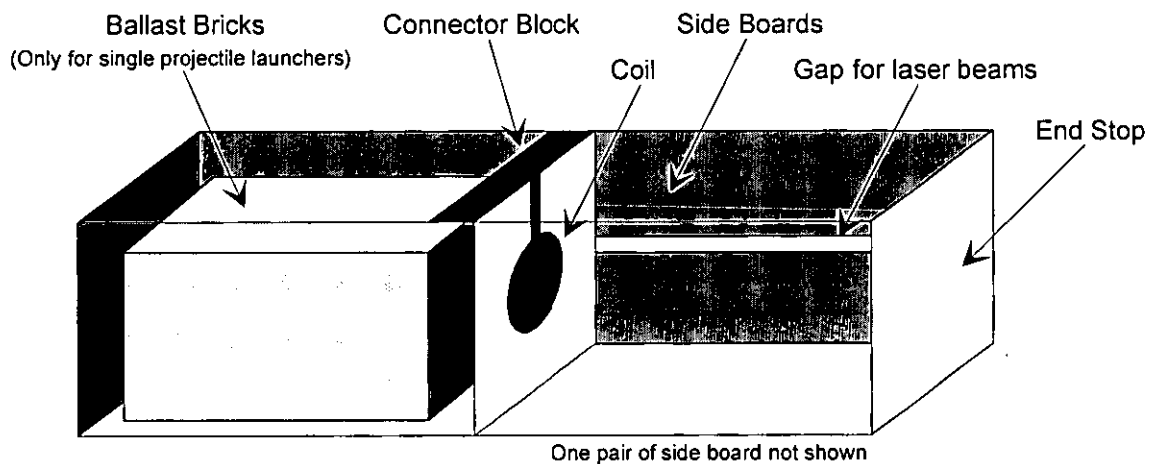


Figure 9.1 Rig frame set-up and arrangement

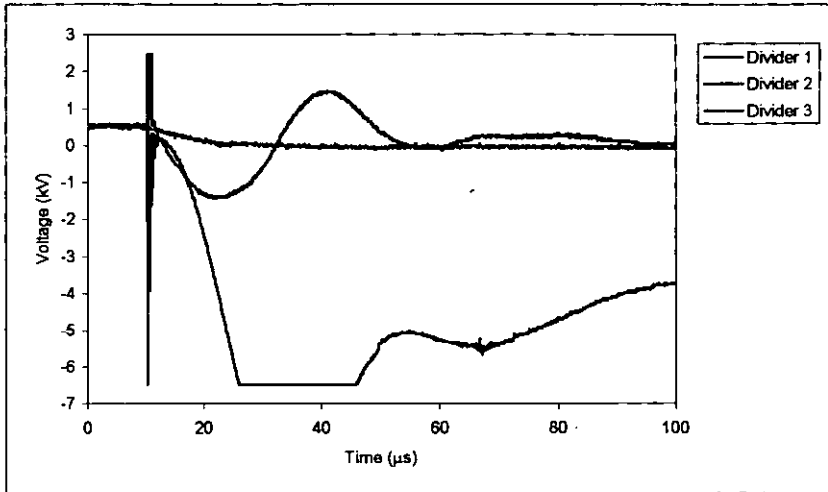


Figure 9.2 Comparison between voltage dividers

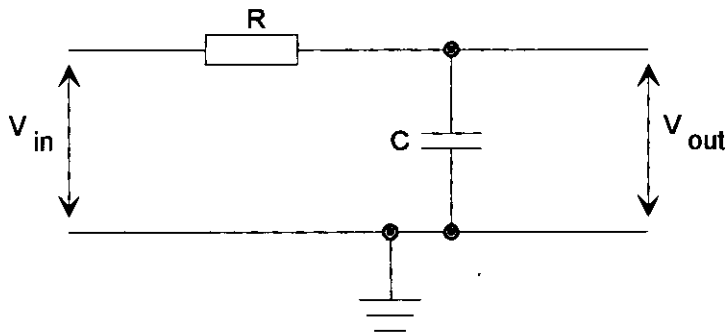


Figure 9.3 Passive integrator circuit

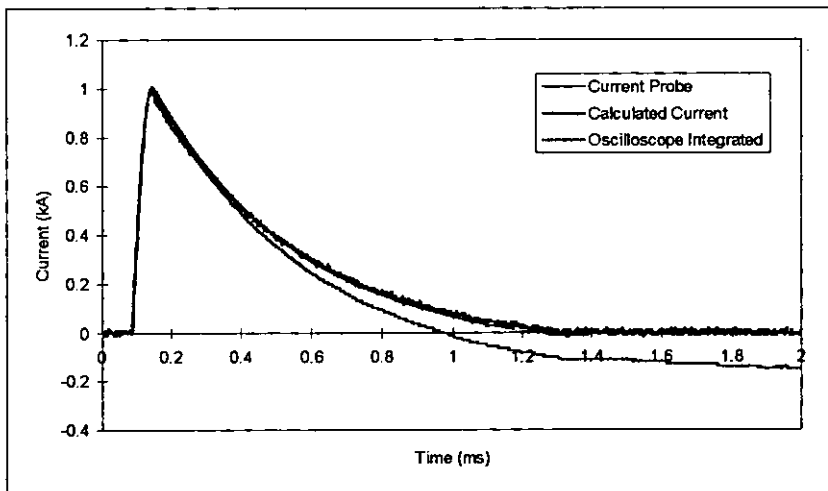


Figure 9.4 Full bandwidth current probe traces

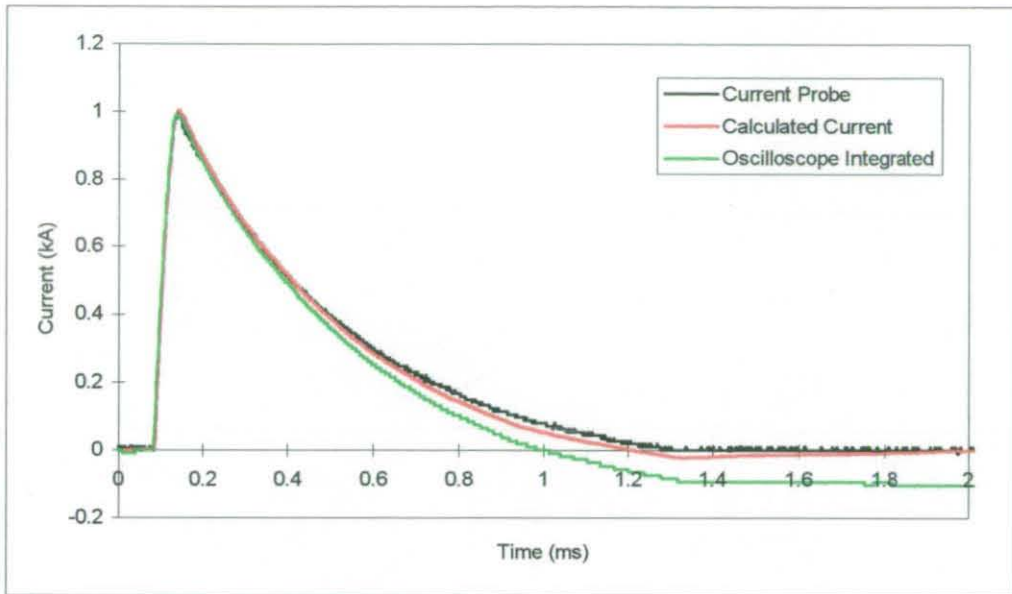


Figure 9.5 Limited bandwidth current probe traces

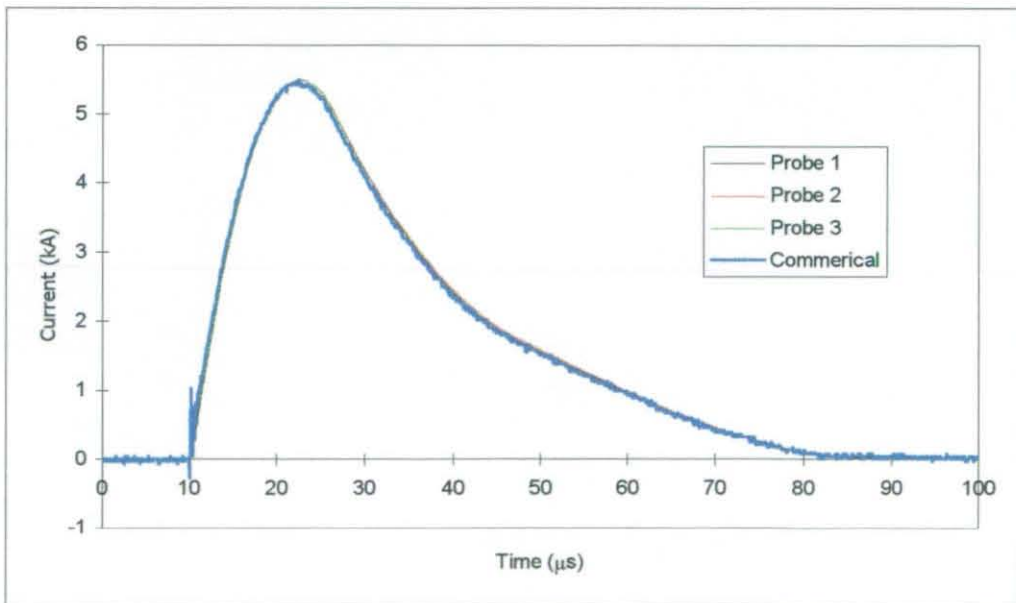


Figure 9.6 Current probe comparison and calibration traces

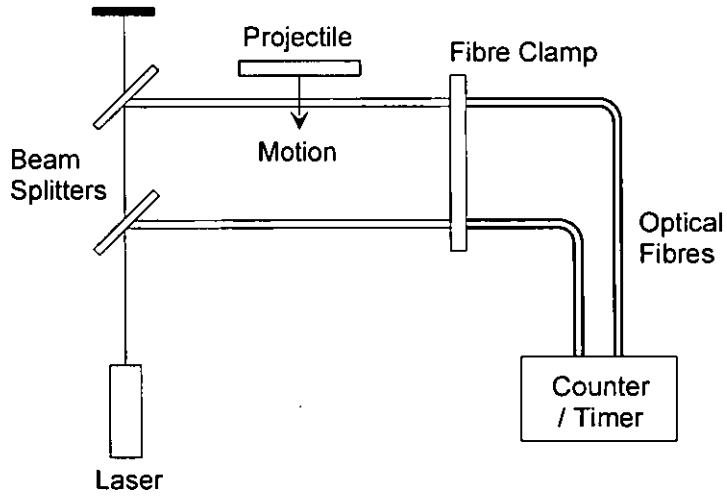


Figure 9.7 Laser position sensing system

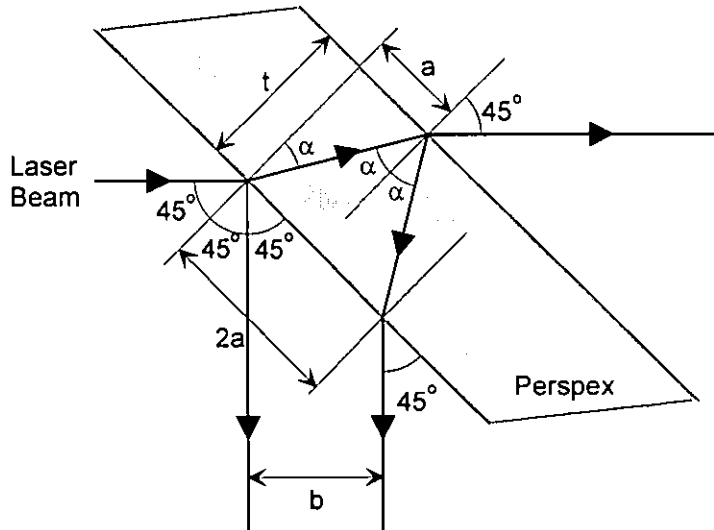


Figure 9.8 Beam splitter geometry



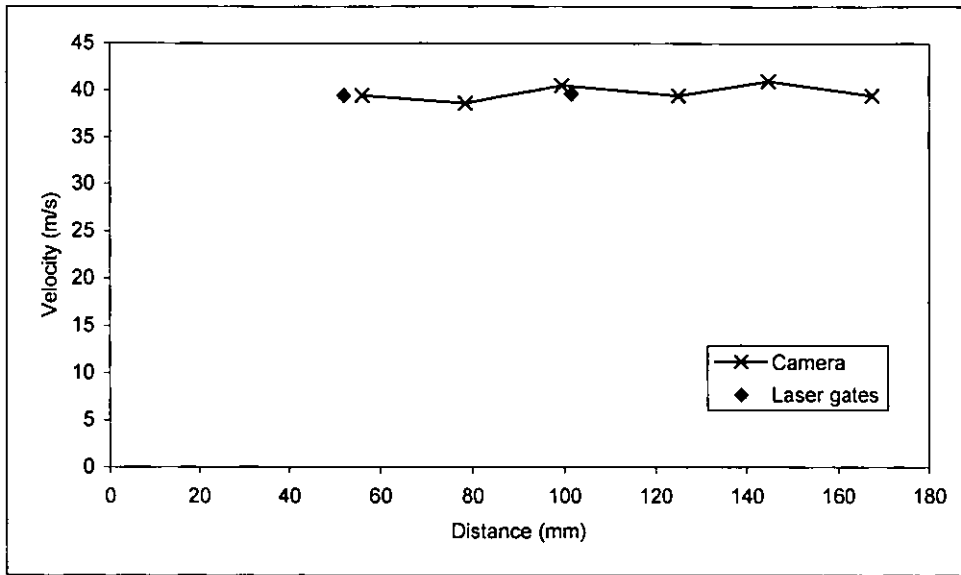


Figure 9.9 Results from speed measurement validation test

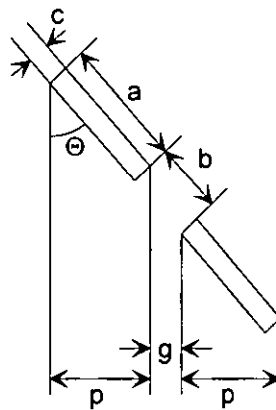


Figure 9.10 Position of projectile when a gap is detected

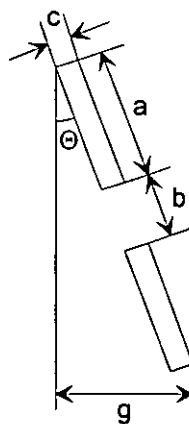


Figure 9.11 Position of projectile when no gap is detected

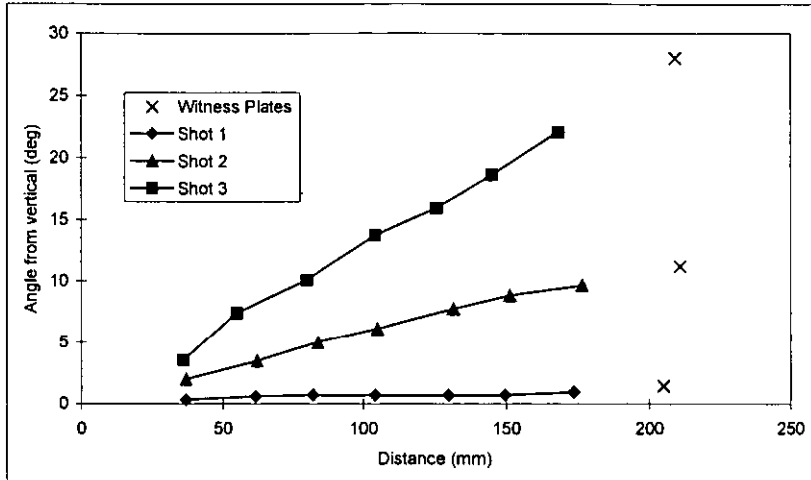
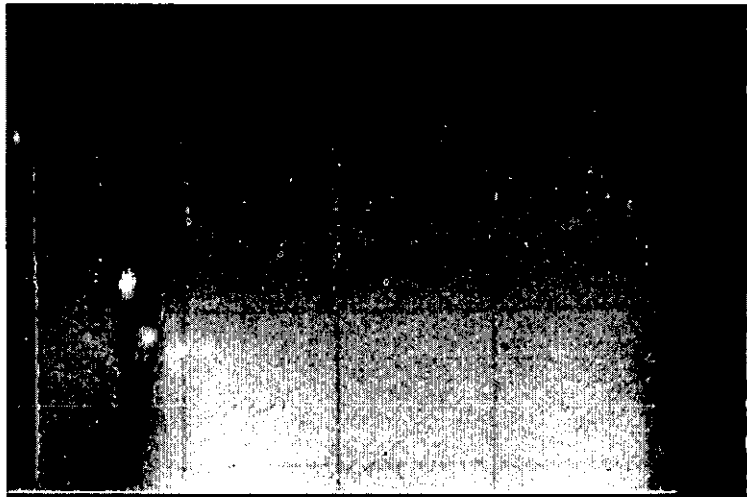
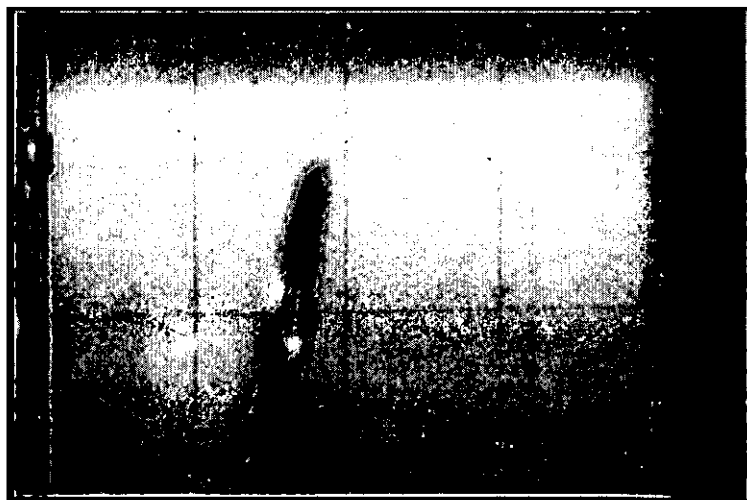


Figure 9.12 Projectile angles calculated from camera images and witness plates



Shot 3 at 1.2ms after launch



Shot 3 at 2.4ms after launch

Figure 9.13 Example of a projectile flying at an increasing angle



Shot 3 at 3.6ms after launch

Figure 9.13 Example of a projectile flying at an increasing angle (cont.)

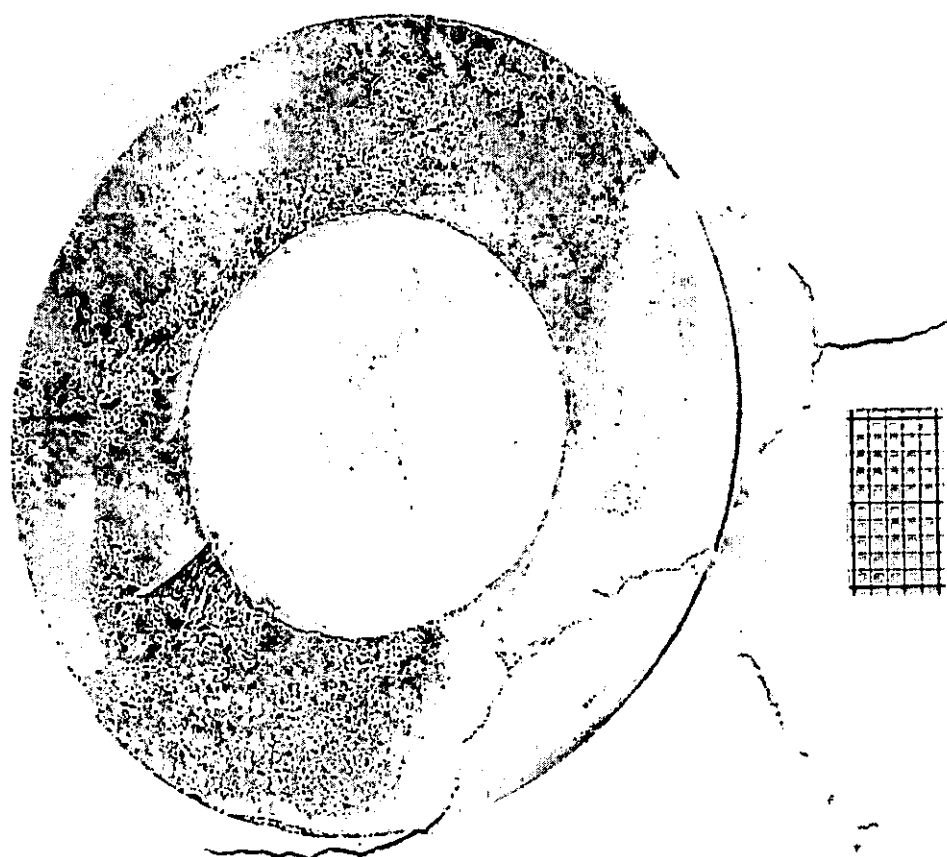


Figure 9.14 Picture of the witness plate from shot 3

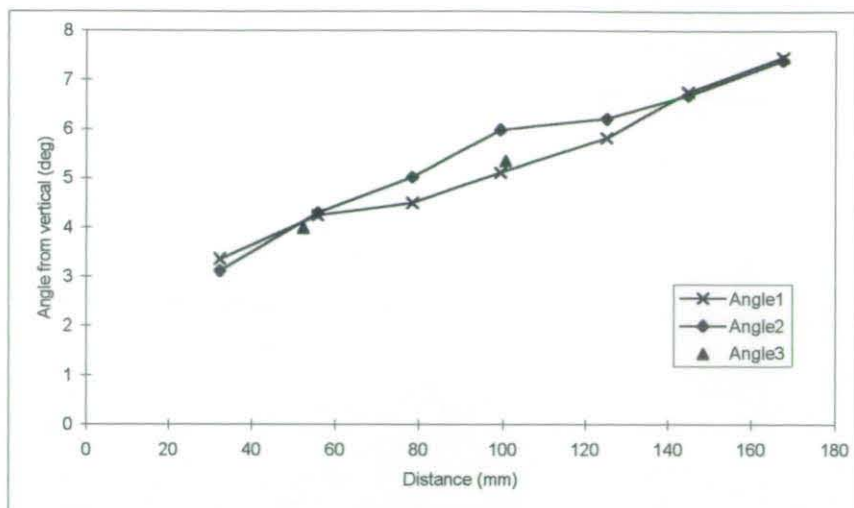


Figure 9.15 Projectile angle calculated from camera images and laser gates

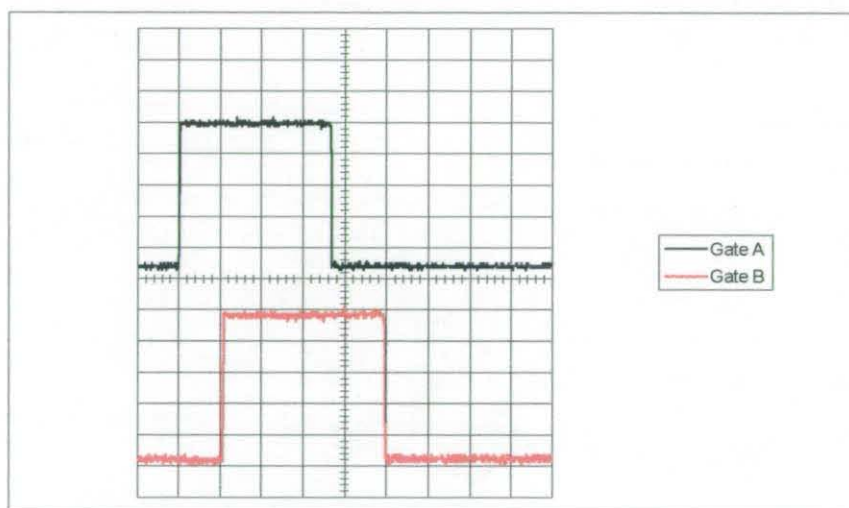


Figure 9.16 Signals from the first pair of laser gates

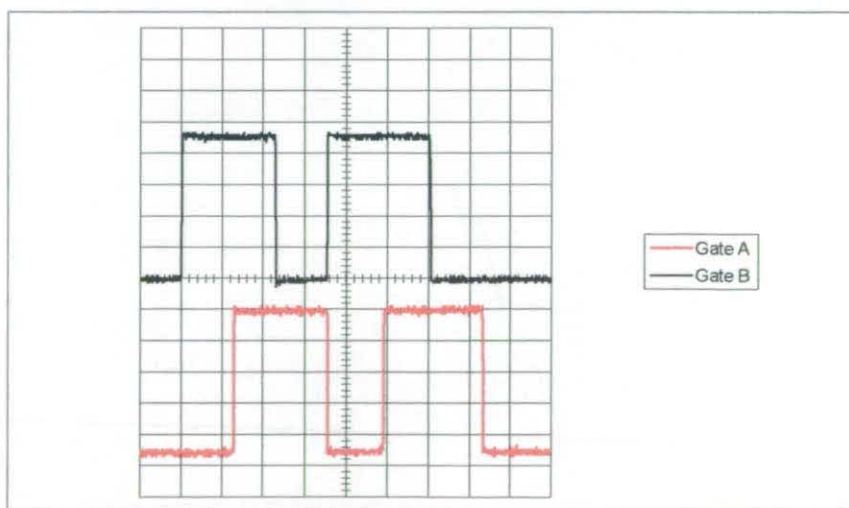


Figure 9.17 Signals from the second pair of laser gates

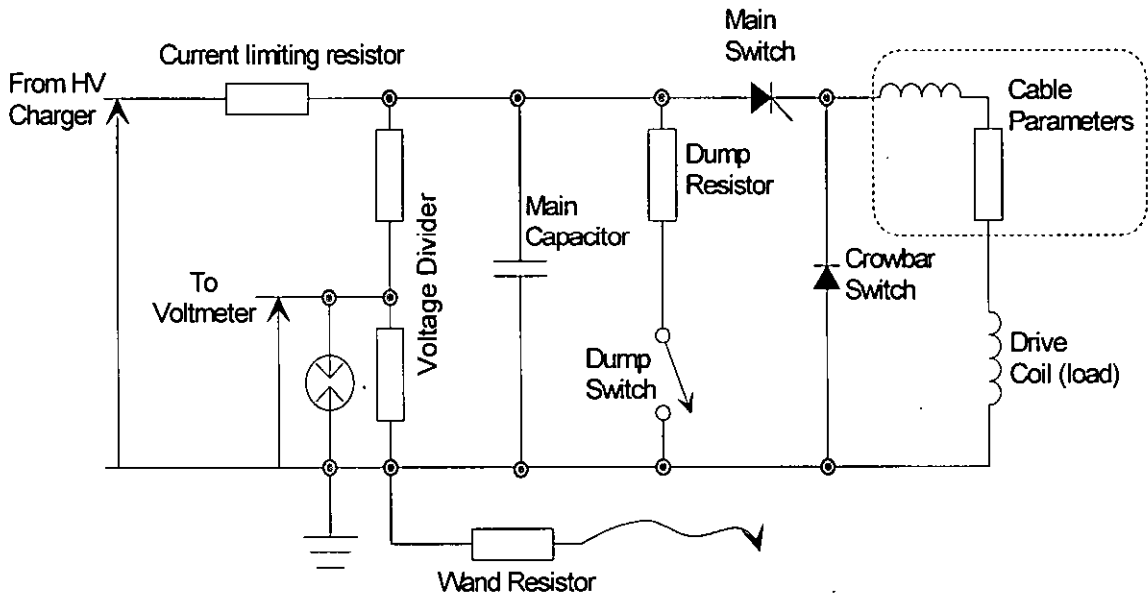


Figure 9.18 Basic power supply circuit

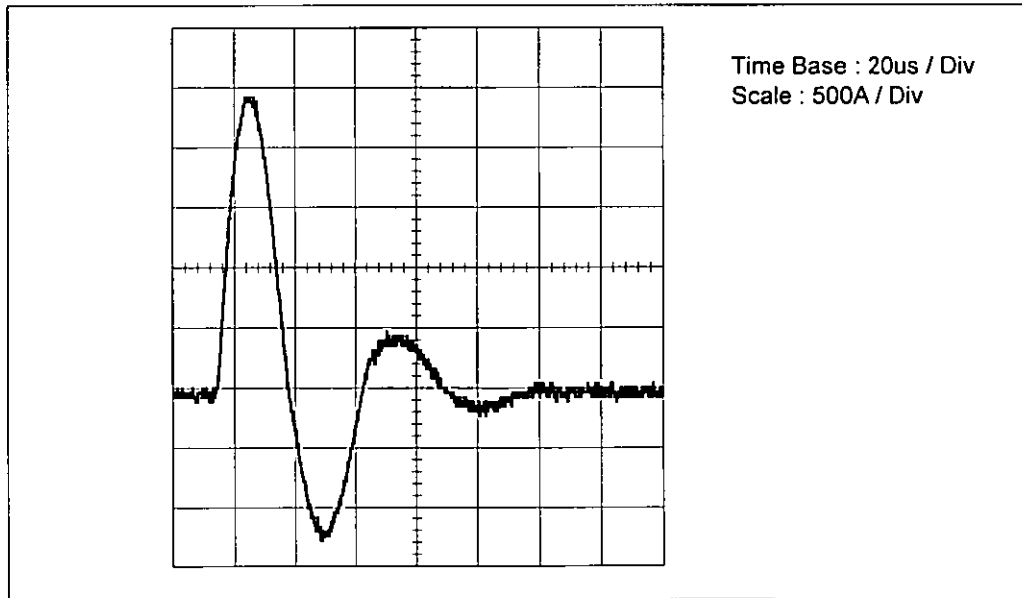


Figure 9.19 Typical current waveform from a ringing discharge test

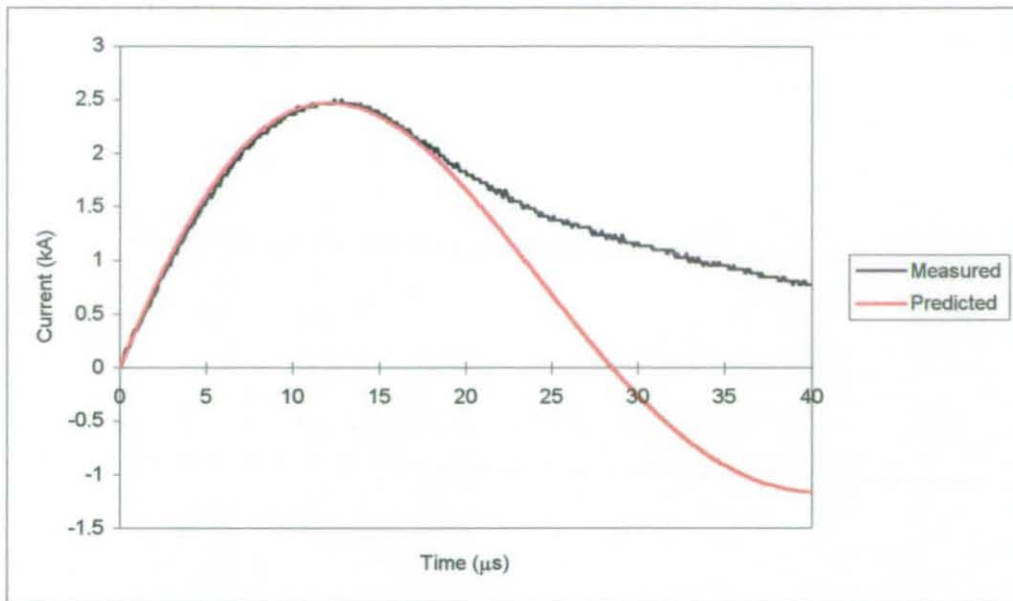


Figure 9.20 Comparison between measured and predicted current waveforms

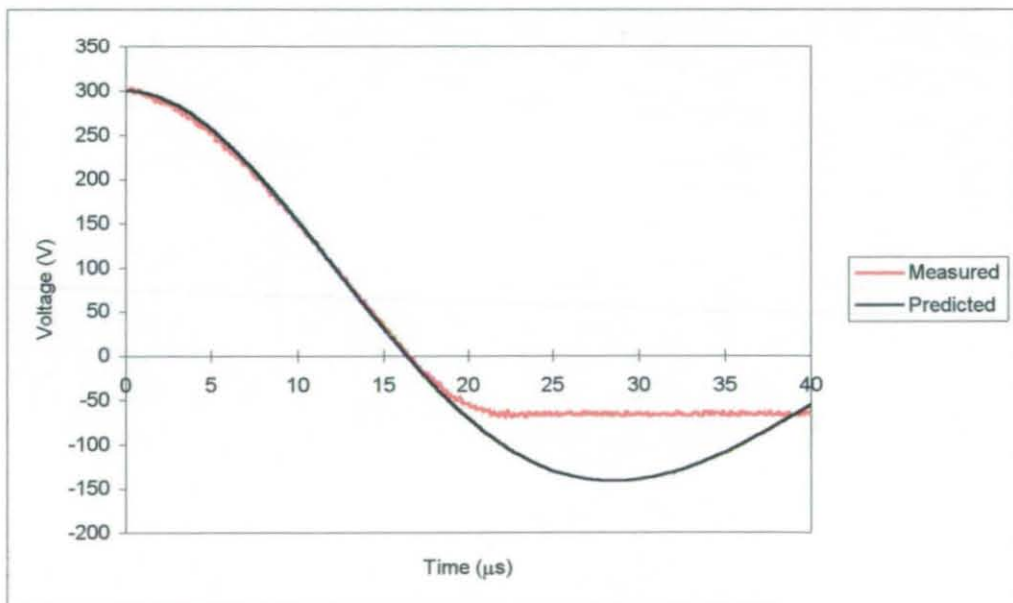


Figure 9.21 Comparison between measured and predicted voltage waveforms

# 10. EXPERIMENTAL WORK

*This chapter describes the construction of the launcher drive coils, and provides a chronological account of the experiment work undertaken.*

## 10.1. LAUNCHER CONSTRUCTION

The two main parts of any launcher are the drive and projectile coils, and due to the large stress exerted on the projectile it was impractical for this to be anything but a solid single-turn coil. The projectiles used for most experiments were cut from 3mm thick Aluminium plates, with the sizes of both the projectiles and drive coils chosen with the availability of materials in mind. Since the aim of the experimental launchers was to validate the model or sensory systems, the dimensions of the coils were not critical.

From early simulations, it was obvious that the drive coil had to be of a multi-turn construction to ensure the projectiles would reach a manageable velocity. The coil itself was hand wound onto a central disc and coated in epoxy adhesive. To support the coil while in use, a coil housing was made from two sheets of Tufnol, one supported the back of the drive coil and the other the outer edge. Once the drive coil had been mounted in its housing, it was held in place by an epoxy resin. The plastic retaining plate was mounted on the front and the whole assembly was then mounted on a thick plywood back plate. The connections of a single side drive coil protruded from the back of the drive coil and were fed by the supply cables behind the back plate, as shown in Figure 10.1.

The two-layer drive coils were constructed in a similar way to a single layered coil. Once the first layer had been wound, the lead from the centre of the coil was wound to produce the second layer, so that both of the coil leads came out of the side of the drive coil. For the dual projectile launcher, only the outer supporting Tufnol housing was used, together with two projectile retaining plates. The drive coil was again mounted on a plywood base plate, but with a hole in it to clear the second projectile, as shown in Figure 10.2.

## 10.2. INITIAL EXPERIMENTS

After the initial projectile tests the first drive coil, which had been made to test the coil manufacture techniques, was replaced by a new 25-turn rectangular cross-section coil. When the capacitor voltage was increased above 2kV the projectile was regularly being bent when it hit the end stop. To reduce the damage several methods of slowing the projectile more gently were tested. The simplest and most effective of these was to hang a thick paper pad immediately in front of the target. The additional air resistance and mass of the paper slowed the projectile down before it hit the end stop and, in addition, the paper helped to soften the impact.

A series of validation experiments were carried out with the second drive coil, although some damage to the drive coil and power supply was noticed. After repeated firings, one of the drive coil leads broke, as shown in Figure 10.3. This failure was attributed to the high levels of mechanical shock applied to the coil, and to prevent further failures, both coil leads were extended to allow for a slight movement. During the following tests one of the Tufnol rods used to clamp the diode / thyristor stack broke, after replacing the rods with insulated steel rods the supply was rebuilt.

To validate models of coils constructed from round cross-section wire a single-layer 12-turn drive coil was constructed. After re-characterising the supply, it was used to test the launcher at different capacitor voltages. However, while the supply was being charged up to 3kV it failed and no current or voltage measurements were captured. After dismantling the diode / thyristor stack, it became apparent that all the thyristors had failed to short-circuit. It was suggested that the insulation used on the steel rods had failed, causing too greater voltage to be applied to one of the thyristors. If one thyristor failed, while the others were not conducting, this would have led to all the devices being exposed to too high a voltage and would account for all the devices failing. To test the insulation of the steel tie rods, the stack was re-built with the thyristors replaced by an insulating block, and even when the capacitor bank was charged to 4.5kV no break down occurred. In the absence of the actual current and voltage waveforms, the round wire launcher was simulated and compared to the rectangular wire launcher, as shown in Figure 10.4 and Figure 10.5. Although,



it can be seen that the round wire coil drew a larger current it was still well within the thyristor capabilities, listed in Table 10.1.

	Device Limits	Rectangular Wire Coil Maximum	Round Wire Coil Maximum
$I_{TSM}$	8320 A	5490 A	6888 A
$di/dt$	1000 A/ $\mu$ s	650 A/ $\mu$ s	417 A/ $\mu$ s
$I^2t$	316 kA <sup>2</sup> s	2.453 kA <sup>2</sup> s	1.209 kA <sup>2</sup> s
$I^2\sqrt{t}$	3160 kA <sup>2</sup> $\sqrt{s}$	2770 kA <sup>2</sup> $\sqrt{s}$	2706 kA <sup>2</sup> $\sqrt{s}$

Table 10.1 Comparison between device parameters and predicted test conditions

It was decided that this thyristor failure was most likely caused by the age of the devices, although the previous failures might have contributed. All the thyristors had previously been extensively used in other pulsed power supplies, and had possibly reached the end of their normal working life.

After attempting to obtain direct replacement thyristors, it was apparent that this was not possible due to their high cost and long delivery times. Alternative thyristors were therefore used, with the number of thyristors required reduced from five to three due to the increased voltage stand-off capabilities of the new devices.

The high-speed camera provided clear results for both projectile yaw and deformation experiments. However, before the end of the projectile deformation tests the supply again failed, but fortunately both current and voltage traces of the failure were obtained, as shown in Figure 10.6. Again, all the thyristors in the stack were damaged, although they were used well within their working limits, shown in Table 10.2. Since they were also new, the failure could not be blamed on fatigue.

	Device Limit	Actual Maximum
$I_{TSM}$	9882 A	4550A
$di/dt$	1000 A/ $\mu$ s	304 A/ $\mu$ s
$I^2t$	430 kA <sup>2</sup> s	1.951 kA <sup>2</sup> s

Table 10.2 Comparison between device parameter and test conditions

The damage to the thyristors suggested that they had failed due to a voltage overload, but the supply failed when the voltage was only 3.2kV, well below the 4.8kV blocking voltage capability of the thyristor stack. This suggested that the capacitor voltage was not equally shared amongst the three thyristors, and since the supply voltage was being ramped up slowly when the breakdown occurred, it was unlikely that this was due to transient conditions. The most obvious cause of the thyristor failure is a failure of the voltage sharing resistors, but these were within their normal operating tolerances. Another possible cause was the failure of one of the leads that connected the diode / thyristor stack to the voltage sharing resistors. Figure 10.7 shows a simplified circuit diagram of the power supply, and with the circuit prior to the failure being regarded as quasi-steady-state, the different possible lead failures could be studied. Since the resistance of the drive coil was low in comparison with the voltage sharing resistors, a failure of leads five, six, or seven would not have caused the supply to fail during charging. The possible fault current paths, caused by the failure of one of the leads, are shown in Figure 10.8. It can be seen that if lead four had failed, only the bottom thyristor would have been damaged, as the other thyristors would have switched on normally due to the cascade nature of the firing circuit. If lead three had failed, the voltage across the bottom two devices might not have been evenly shared, due to manufacturing differences. However, the top thyristor would have turned on normally and would not have been damaged. If the second lead failed, the top two devices might have failed due to uneven voltage sharing. If the top two thyristors failed, the whole capacitor bank voltage would have been applied to the bottom device, which would have failed. If lead one had failed, the top device would have failed when the capacitor voltage exceeded 1.6kV. However, this would have meant the full capacitor bank voltage would have been shared between the bottom two thyristors, which would have failed when the bank voltage exceeded 3.2kV.

Unfortunately, any evidence of a broken lead or bad connection was destroyed when the stack was dismantled to test the thyristors. However, from the analysis above it seems most likely that the power supply failure was caused by the failure or bad connection of lead one. Although the previous power supply failure was attributed to

the age of the devices, it too could have been caused by poorly connected leads. Unfortunately, the project budget could not cover the costs of another set of thyristors, so a cheaper alternative switch had to be found.

The switch chosen was a nail switch, which is very simple and robust, and works by using a small nail to puncture the insulation between two conductors. The nail is forced through the top conductor and the insulation below causing a localised break down between the two conductors. To hit the nail, a weight was dropped down a guide tube on to the head of the nail. Initially, the weight was held up by a solenoid, which when energised released the weight.

Although the nail switch method had been used in previous pulse power supplies, it had been thought to be too inconsistent for use in model validation experiments. However, the results showed that the nail switch was surprisingly repeatable, and with the slightly modified power supply, the experimentation continued.

After completing a large number of medium voltage experiments the supply voltage was increased until the drive coil failed. Due to the 5kV limit of the first power supplies, a new power supply was required. A previously constructed supply capable of operating up to 20kV was used. This supply used ignitrons for the main and crowbar switches and, although these were known to have poor low voltage repeatability, they operated well at and above 3kV.

### 10.3. CONCLUSIONS

The drive coils used in this thesis were hand wound and set in Tufnol housing using epoxy adhesive. The first failure of the launcher was in the drive coil connection and was caused by mechanical shock; this was later overcome by increasing the length of the connecting leads. The next failure occurred when one of the Tufnol clamping rods in the diode / thyristor stack broke. The third failure occurred in the thyristor stack while the supply was being charged up and although the previous mechanical failure might have caused this fault, it was decided that the age of the components was the most likely cause. The thyristor stack was replaced with higher rated components to try and prevent any further problems, but during the projectile deformation

experiments the supply again failed. The voltage and current traces were captured and it was decided that the supply probably failed due to a loose connection. The thyristor stack was replaced by a nail switch, which was shown to be both simple and effective.

While the power supply developed during for this project was used for tests up to 4.5kV, a previously constructed ignitron supply was used to test the launcher at higher voltages.

#### 10.4. FIGURES

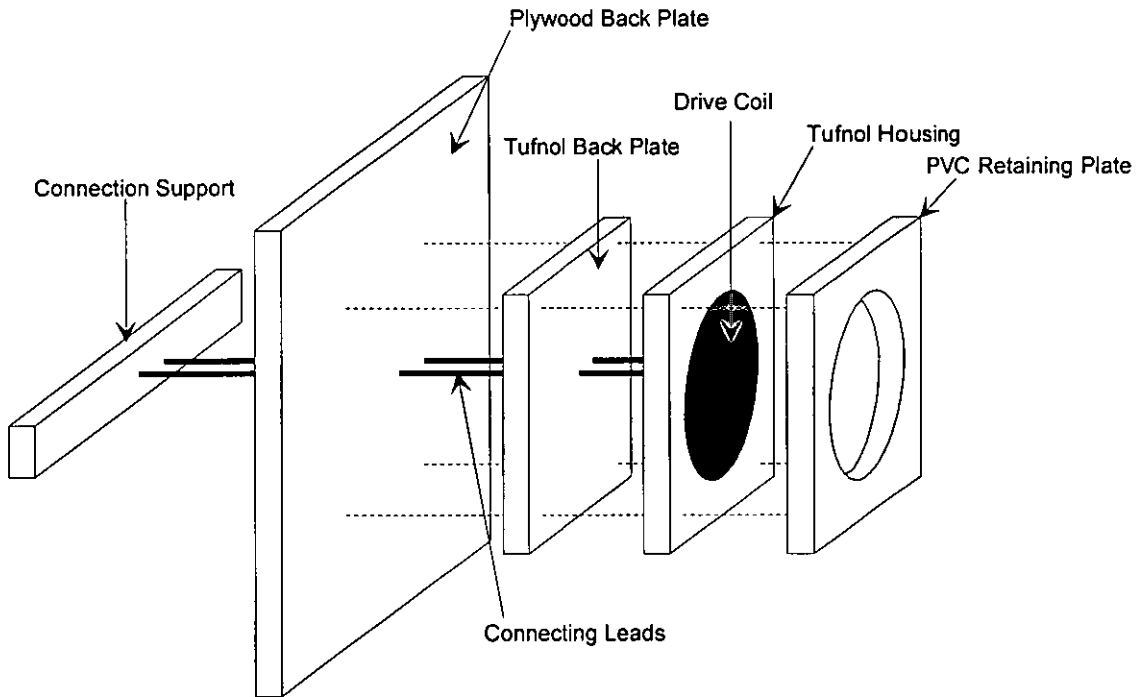


Figure 10.1 Exploded diagram of the single projectile launcher arrangement

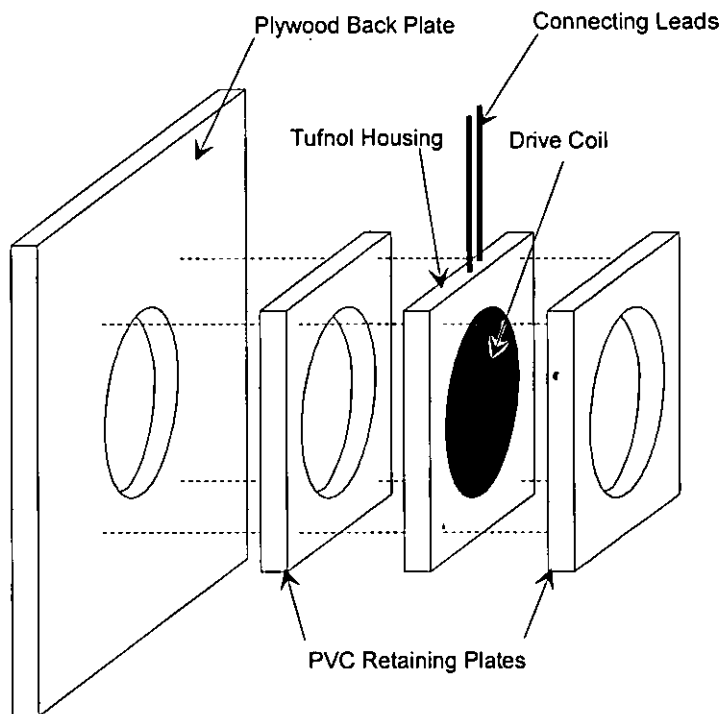


Figure 10.2 Exploded diagram of the dual projectile launcher arrangement

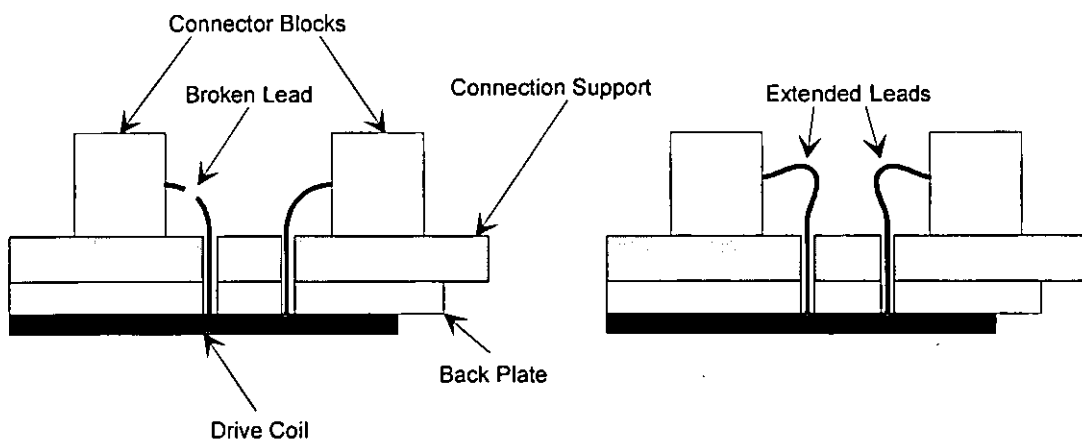


Figure 10.3 Location of the first coil failure

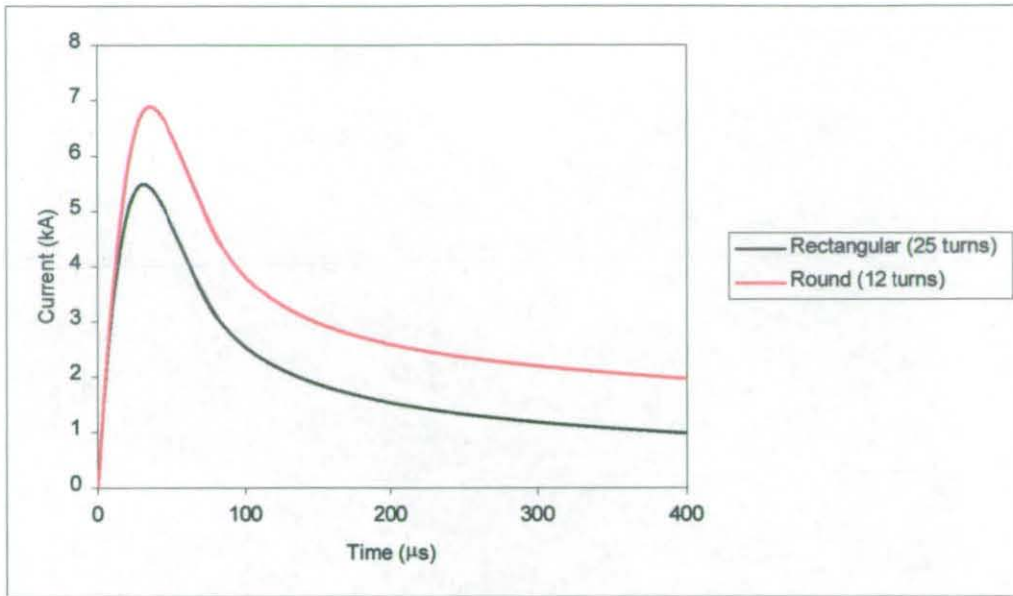


Figure 10.4 Drive coil currents for rectangular and round wire coils

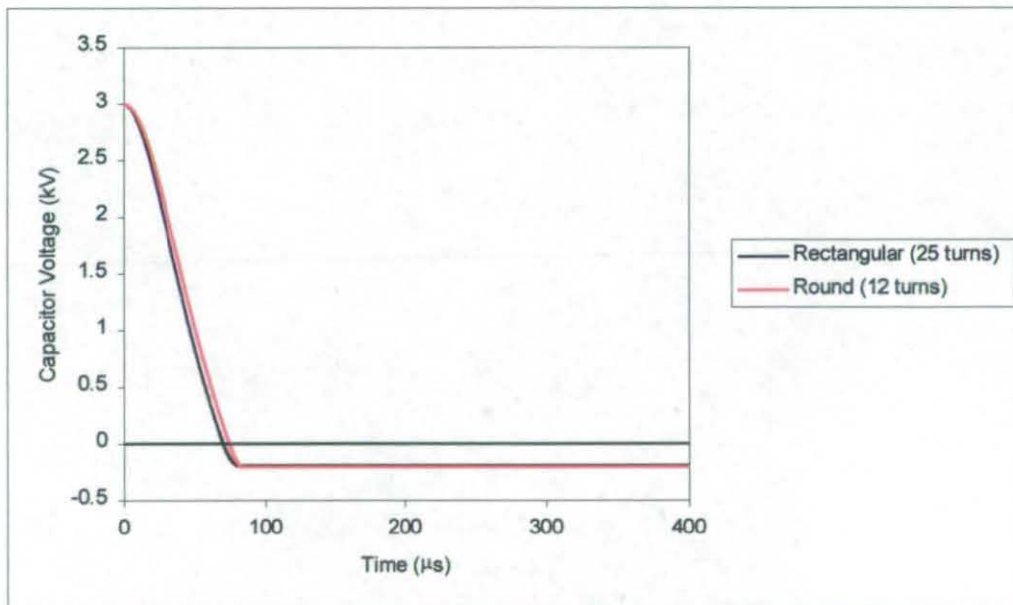


Figure 10.5 Capacitor voltages for rectangular and round wire coils

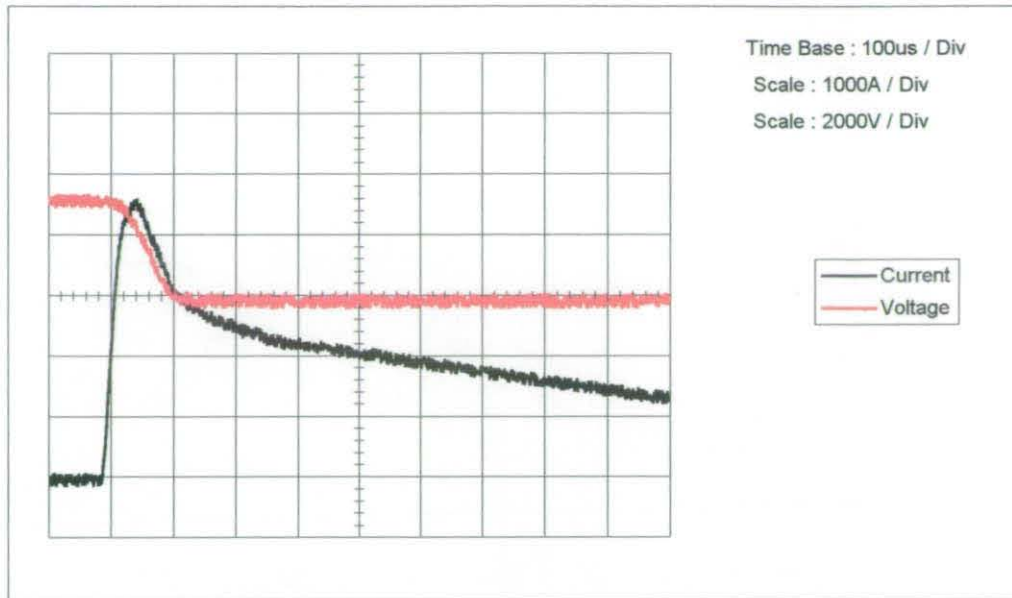


Figure 10.6 Current and voltage traces of supply failure

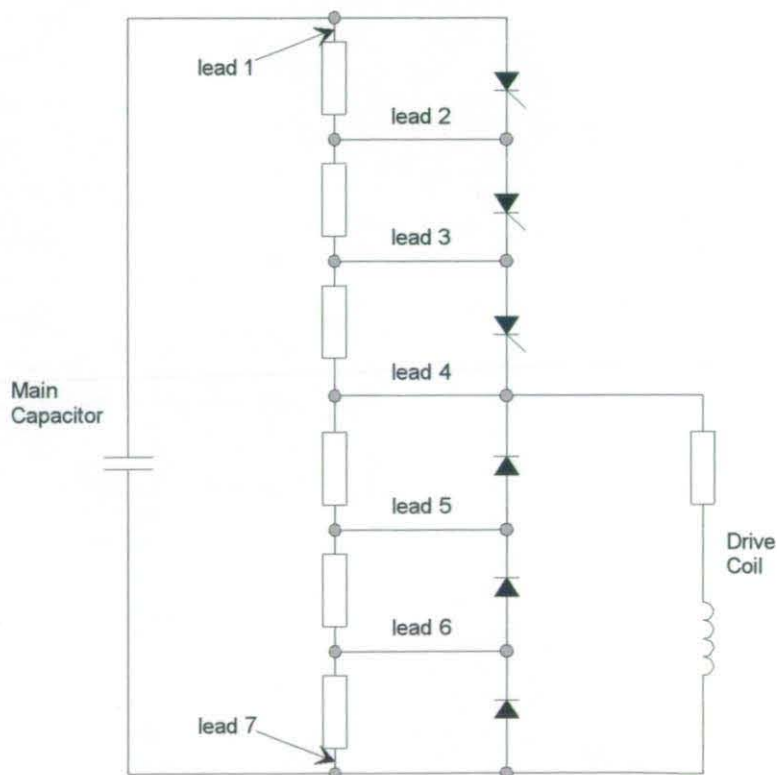


Figure 10.7 Simplified power supply circuit diagram

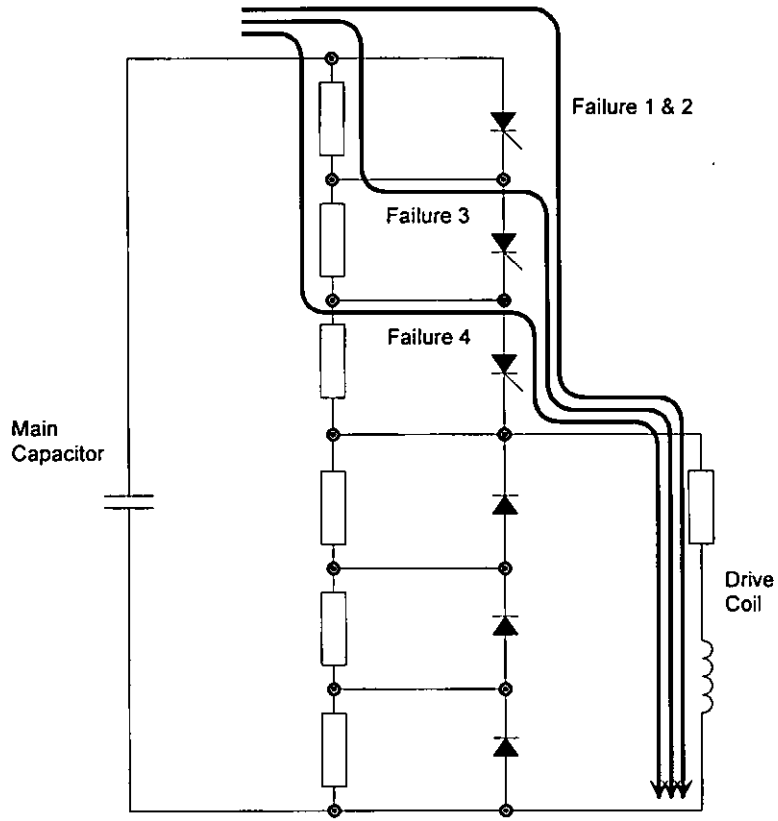


Figure 10.8 Possible fault current paths



# 11. RESULTS

*This chapter presents the experimental results that were obtained.*

## 11.1. MODEL VALIDATION

To validate the filamentary models developed in this thesis a series of experiments were carried out. These were split into three groups, with each group being intended to validate a particular part of the models. The first group was designed to validate the model of a single layer / single projectile launcher, in which the drive coil was wound from rectangular cross-section wire. The second set of tests highlighted the difference between round wire and equivalent area rectangular wire models. These tests helped to prove that the round wire model adequately represents drive coils wound from round wire. The third series of experiments was conducted as part of the two-layer / dual projectile launcher investigation.

### 11.1.1. RECTANGULAR WIRE MODEL

To test the validity of the rectangular wire model, a single layer 25 turn drive coil was constructed from rectangular enamelled copper strip of 5x0.9mm cross-section [Appendix C]. The launcher was fired ten times at each voltage using the standard aluminium projectile, and this sequence was repeated with the laser gate in three different positions. From initial experimental results there was no noticeable deceleration of the projectile, and to check this the laser gate locations were randomised. After a full series of test launches, it was apparent that the projectile velocity varied little from its maximum over the range of locations it was measured at. Figure 11.1 shows that the rectangular wire model accurately predicted the maximum velocity of the projectile. Figure 11.2 shows how the experimental and simulated launcher efficiencies vary with the supply voltage.

A second series of tests was carried out using the same coil, but with the higher energy ignitron power supply. Since the drive coil was not expected to survive many high-energy shots, only two firings were made at each voltage, with the laser gates in the same locations. Figure 11.3 shows that the experimental results closely follow the values predicted by the model. Figure 11.4 shows the calculated launcher efficiencies

for the high voltage tests and although there is some discrepancy between the predicted and experimental results, this is due to the highly sensitive nature of the efficiency calculations. Any errors in either the capacitor voltage or projectile speed measurement are squared, hence the resultant efficiency can be greatly affected by minor errors. In the comparison of current traces shown in Figure 11.5 it can be seen that the predicted current closely matches the measured current, with the secondary oscillations caused by the crowbar ignitron triggering. Some of this interference was picked up by the Rogowski coil although the majority was picked by the cable between the sensing coil and the oscilloscope.

Although the drive coil remained almost intact after the high-energy tests, the increase in the recoil forces caused significant damage to the back plate and terminal block, as shown in Figure 11.6. Although some of the damage can be attributed to the recoil forces, it is likely that the interaction between the currents flowing in the terminals and the magnetic field of the drive coil produced forces that increased the damage.

During the second 7kV firing a large flash was observed on the monitoring camera. The supply voltage was then increased to 8kV and the flash was captured by the high-speed camera. Figure 11.7 and Figure 11.8 show the breakdown at 3.01ms and 3.51ms after the launcher was fired. Previous frames were captured, but the intensity of the light overpowered the camera and the pictures were devoid of detail. The remains of an arc between the projectile and the drive coil can clearly be seen. On closer inspection of the drive coil, two breakdown sites were noticed. The breakdown on the left of Figure 11.9 was probably caused by an insulation breakdown between adjacent turns of the coil. The breakdown on the right of Figure 11.9 was the most likely site of a drive coil to projectile arc, which produced the damage to the projectile shown in Figure 11.10.

Additional insulating lacquer was added to the breakdown sites on the drive coil and a sheet of Melonex was placed between the projectile and drive coil. Once this had been done a second 8kV launch was made successfully, but when the voltage was increased to 9kV the whole drive coil housing failed and no further results were obtained. The damage to the drive coil can be seen in Figure 11.11.

### 11.1.2. ROUND WIRE MODEL

To test the validity of the round wire model a two-layer 24 turn drive coil was constructed from 2mm diameter enamelled copper wire [Appendix C]. The first layer was wound and set in adhesive and the lead from the centre of the first layer was wound to form the second layer. The layers of the drive coil were oriented to ensure that the current flowed in the same direction around the layers of the coil. The launcher was again fired ten times at each voltage, and this was repeated with the laser gates at three different positions. The results from the low voltage test shown in Figure 11.12 again demonstrate good agreement with the predicted results. Figure 11.13 shows a comparison between the experimental efficiencies and those found from the round wire model. To provide a comparison, the launcher was modelled again using the rectangular wire model. The models were set-up so that the centres of the conductors were in the same locations and they had the same cross-sectional area. Figure 11.14 shows a comparison between the predicted velocities of the two models when simulating the same system and Figure 11.15 gives a comparison between experimental and rectangular wire model results. Both Figure 11.14 and Figure 11.15 show that the rectangular wire model tends to predict low projectile velocities when modelling a round wire arrangement

Once the low voltage tests were completed, the power supply was replaced by the high voltage ignitron supply and the results shown in Figure 11.16 were obtained. It can be seen that there is a large difference between the predicted and measured velocities, which was attributed to the damaged condition of the launcher during these tests. During the low voltage tests, the drive coil had shown signs of damage and it was twice re-potted to help it survive. As the voltage was increased, the side of the drive coil closest to the projectile started to unravel. By the time the voltage reached 5kV the drive coil was so badly damaged that the projectile had to be held against the drive coil by sticky tape. Unexpectedly, the damaged drive coil seemed to perform better than expected, but this was probably due to small parts of the drive coil casing and potting been launched at high speed by the violent movement of the drive coil windings. However, the use of a badly damaged drive coil weakens any conclusions

that can be drawn from these results. Figure 11.17 shows the condition of the drive coil after a 6kV test.

Despite the damage, the predicted drive coil currents and voltages show good correlation with measured results. Figure 11.18 and Figure 11.19 show current traces from low and high voltage tests respectively, and these show that the low voltage supply does not interfere with the Rogowski coil as much as the ignitron supply. Figure 11.20 presents a comparison between the predicted and measured capacitor voltage for several example launches.

### 11.1.3. DUAL PROJECTILE MODEL VALIDATION

The dual projectile launcher used a two-layer drive coil to allow easier connection of the power supply leads. A 24 turn, round wire coil was constructed due to the availability of materials; it could have equally well been wound from rectangular cross-section wire [Appendix C].

To validate the dual projectile model, a series of test were undertaken in a similar manner to the two previous sets of experiments. Figure 11.21 and Figure 11.22 show that the model results agree very well with the measured results and it can be seen from Figure 11.22 that the launcher was tested up to 10kV. Whilst the ignitron supply was designed to operate at up to 20kV, it had not been recently tested and 10kV was thought to be a reasonable safety limit. As Figure 11.23 shows the damage to the drive coil was minimal, with the slight damage to the left-hand side of the coil probably due to unevenness in the coil construction. The additional insulation (black heat shrink tubing) was added because the enamel insulation had become damaged during construction. It would not be unreasonable to expect a similar coil to survive without any signs of damage if it was constructed more evenly.

Figure 11.24 and Figure 11.25 show the launcher efficiencies for the low voltage and high voltage test respectively. The results of the high voltage tests show a close agreement with predicted results, as do the high voltage current traces in Figure 11.26. The maximum efficiency calculated from practical results was 47% and since the

dimension and materials used for the practical launcher were arbitrarily chosen, this suggests that the maximum possible efficiency is likely to be greater than 50%.

## **11.2. STUDY OF PROJECTILE YAW**

To investigate the yaw of the projectiles detailed timing measurements were recorded during the first set of model validation experiments. The timing measurements were made by using the cursor feature on a pair of digital oscilloscopes connected to the outputs from the photo-detectors, enabling the yaw of the projectile to be calculated at two locations during each launch.

The calculated yaws of the projectiles are shown in Figure 11.27, where the calculated angle is that between the projectile and a plane parallel with the drive coil. Figure 11.27 shows that the yaw is not significantly affected by the launch energy. The projectiles were carefully placed flat against the drive coil, and the yaw appears to be random. However, it was noticed that if a projectile was not placed flat it would yaw in a particular direction, increasing the angle of the original misalignment.

## **11.3. STUDY OF PROJECTILE RIFLING**

After studying the yaw of a projectile during flight, consideration was given to the possibility of the projectile rotating or rifling during flight. Using the painted projectile, shown on the left in Figure 11.28, several launches were photographed. Figure 11.29 shows the images from one of the launches, and it can clearly be seen from Figure 11.29 that the projectile does not rotate in flight.

## **11.4. STUDY OF THE EFFECTS OF RE-USING A PROJECTILE**

Due to the large number of launches undertaken during the model validation experiments, it was not practical or economical to launch a projectile only once. A study was therefore undertaken to determine if flattening and re-using a projectile that had been damaged affected its performance. Figure 11.30 shows the average measured velocity of each launch in the first set of validation experiments. It can be seen that the number of times the projectile required flattening increased with the

capacitor voltage, and that the re-use of flattened projectiles had no noticeable effects on the average measured velocity.

### 11.5. PROJECTILE DEFORMATION

It had been noticed that during the high-energy experiments the projectiles were being deformed. In order to prove that this was due to the launch forces, and not caused by impact with the target, a study into projectile deformation was undertaken. Since only very slight deformation occurred during the highest energy test, it was obvious that thinner or softer projectiles should be used to study how the launch forces deform projectiles.

A series of experiments were undertaken using a variety of different materials, projectile thickness and shapes, over a range of voltages. Initially a batch of solid discs made from 0.25mm thick copper sheet, and were annealed and rolled flat before being used. A series of experiments was carried out over a range of supply voltages, deforming the projectiles as shown the Figure 11.31. It can be seen that the projectiles have been deformed into a bowl shape with the edge bent back and wrinkled, while the bowl part remained almost smooth. What was unexpected was that the bottom of the bowl was pointing towards the drive coil, as can be seen from the sequence of photographs in Figure 11.32. Figure 11.31 shows how the depth of the bowl that is formed increases with the supply voltage, suggesting that the projectiles were behaving in an almost fluid manner. The direction of the projectile motion shows that the bowl shape was not caused by air resistance. If the projectiles were considered to be in a soft plastic state, the bowl shape could have been caused by the inertia of the central region of the projectile.

Tests on un-annealed copper projectiles showed that these deformed in a very similar manner to annealed copper projectiles. However, 0.5mm thick aluminium projectiles were not so deformed and it could be seen that the wrinkles were evenly spaced around the edge. All deformed projectiles were measured using the heights of their centres above a flat surface, this measurement was then used as an indicator of the projectile deformation. Figure 11.33 shows a comparison of the projectile

deformations for different voltages and materials. It can be seen that annealing the copper projectile only slightly increased the resulting deformation. Although the aluminium projectiles provided some comparison between different materials, no direct comparison tests could be carried out due to a lack of 0.25mm thick aluminium sheet. However, thin aluminium projectiles manufactured from 0.1mm sheet were launched at 1kV and 3kV. Although those launched at 1kV suffered only minor deformation, those launched at 3kV were excessively deformed. Figure 11.34 and Figure 11.35 show a projectile from a 3kV test, and although this is deformed into a bowl shape, the centre is slightly domed forward. The small hole in the centre of the projectile was made during manufacture. It is thought that the centre of the projectile was domed forward due to the extreme deformation of the surround projectile and not by any special effect.

Since the projectiles used and modelled were normally annular rings, it was decided that a number of 0.25mm annular copper ring projectiles should be tested. The deformation of these was not as dramatic as the solid discs, but their deformation was measured in a similar way. The outside edges of the projectiles were bent back, as were the inside edges to a lesser extent, giving the projectiles an unevenly curved cross-section, as seen in Figure 11.36. Figure 11.37 shows that the projectile deformation varies almost linearly with the supply voltage.

Although both round disc and annular projectiles were made, even these shapes could become difficult to manufacture when using some materials. To investigate the effects of simpler projectile shapes a number of octagonal projectiles were manufactured from a combination of 0.25mm copper sheet and 0.5mm aluminium sheet. These deformed in a similar manner to the round disc projectile, as shown in Figure 11.38. However, the corners on the octagonal projectile seemed to increase the wrinkles both in the severity and in the distance that they penetrated into the projectile. The increase in the wrinkles slightly reduced the depth of the bowl, when compared with a round projectile launched at the same voltage and made from the same material.

A number of square projectiles were made from 0.25mm copper and 0.5mm aluminium sheet. Although, these were launched by the same drive coil as the round projectiles the results are clearly different. Figure 11.39 and Figure 11.40 show the deformation of square aluminium and copper projectiles respectively, in both figures the projectiles on the left were launched at 2kV and those on the right at 3kV. It can be seen that the corners fold back on the projectile while their tips remain pointing outwards. Figure 11.41 clearly shows the corners of a square projectile being bent backwards during its launch, and closer inspection reveals that the tips of the corners were pointing outward in the initial stages of the launch. This shows that the tips are not bent outwards due to impacting on the central section of the projectile. Considering the projectile as a plastic sheet that is hit with a ring shaped hammer, it would be expected that the tips would follow the corners and not be bent outwards. However, if the projectile is only in a plastic state for a short time, the tips might not have started to move before the rest of the projectile has become stiff again. Since little current would flow through the tips of the projectile, it is likely that little force would be applied to them.

The corners of a square copper projectile launched at 3kV must have been moving so fast that when they hit the centre of the projectile it was deformed by the impact, with impressions evident in Figure 11.42. What cannot be seen in Figure 11.42 are the impressions made by the corners of the projectile launched at 1kV. However, the corners were not in contact with the main body after the launch, this suggests that the corners rebounded or relaxed to the positions shown in Figure 11.40. Since the impact of the corners with the main projectile body was enough to deform the body, it suggests that the central part of the projectile was still reasonably soft, when the impact took place.

## 11.6. CONCLUSIONS

The results from the rectangular wire launcher clearly showed good collation between measured and predicted results, for both the low and high voltage tests. While the drive coil remained almost completely intact even during the high voltage test, significant damage occurred around the lead connections, probably caused by



launcher recoil and electromagnetic repulsive forces acting on the connectors. The use of the monitoring and high-speed cameras allowed insulation failures to be detected and repaired before the launcher was significantly damaged.

Results from the round wire launcher showed good correlation with the round wire model results, whilst highlighting the inaccuracy of using a rectangular wire model to simulate a round wire coil. However, the drive coil was seriously damaged during testing, even at low voltages. This was due to the recoil forces and the difficulty of gluing round conductors together. Although predicted and calculated low voltage launcher efficiencies again show a good correlation the damage caused to the drive coil invalidated any results that could have been drawn from the high voltage tests.

The reduction in recoil forces achieved in the dual projectile launcher was clearly demonstrated in the lack of damage to the drive coil, despite it being almost identical to the drive coil used in the round wire tests. The results from the dual projectile launcher confirm the accuracy of the model up to the safety limit of the power supplies. From the results of the high voltage test, a maximum efficiency of 47% was calculated, however this figure was obtained from only a single result.

A study of projectile yaw was undertaken using timing measurements taken during low voltage testing of the rectangular wire launcher. From this study, it was found that the yaw of the projectile was not related to the supply voltage. It was also found that projectile yaw increased steadily as the projectile travelled down range. From practical experience and the results of this study, it was concluded that the projectile yaw was determined by the accuracy of its location against the drive coil prior to launch.

The study of projectile rifling clearly showed that the projectile did not rifle during its flight, as expected. The study into the effects of re-using projectiles, showed that re-using a projectile that had been flattened, had little effect on its performance.

The projectile deformation tests demonstrated that a projectile could be significantly deformed by launch forces, and that not all previously noticed deformation could be explained by impact damage alone. The solid disc projectiles clearly showed that

projectile deformation is almost proportional to the supply voltage. The deformation test suggested that the projectile is in a plastic state during the early stages of the launch cycle. Since the projectile appears to become plastic very rapidly, it suggests this is due to the large forces present, and not due to the projectile heating. The octagonal and square projectiles showed that changing the projectile shape could significantly affect the manner and magnitude of the projectile deformation.

### 11.7. FIGURES

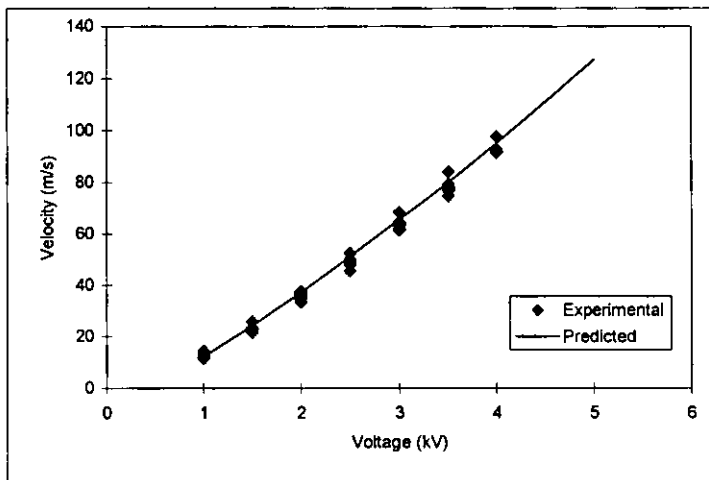


Figure 11.1 Low voltage rectangular wire launcher results.

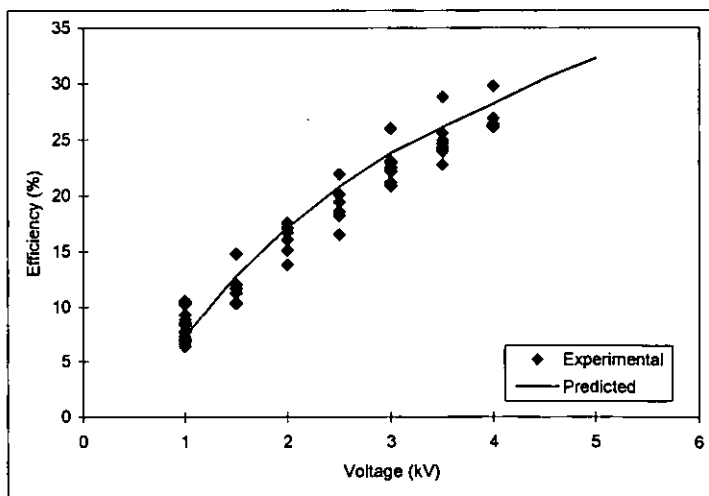


Figure 11.2 Low voltage rectangular wire launcher efficiencies

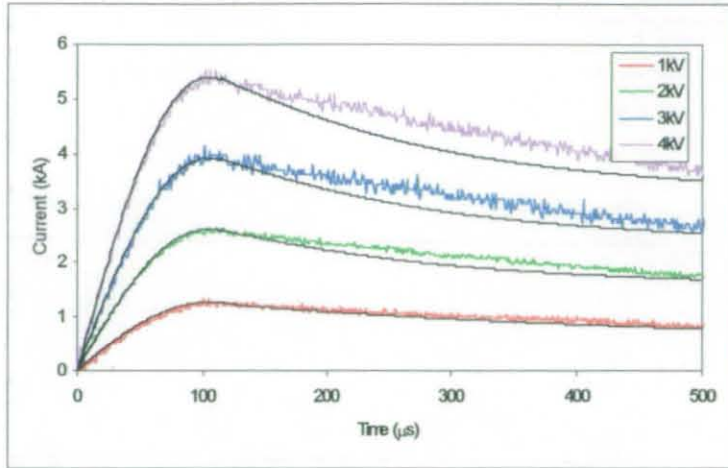


Figure 11.3 High voltage rectangular wire launcher results

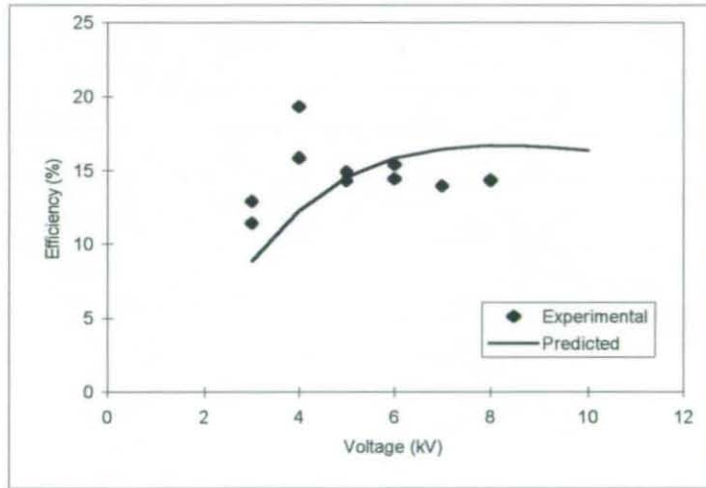


Figure 11.4 High voltage rectangular wire launcher efficiencies

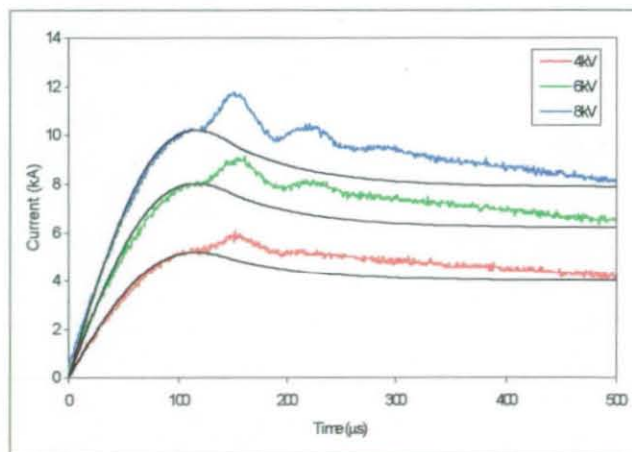


Figure 11.5 Rectangular wire drive coil currents

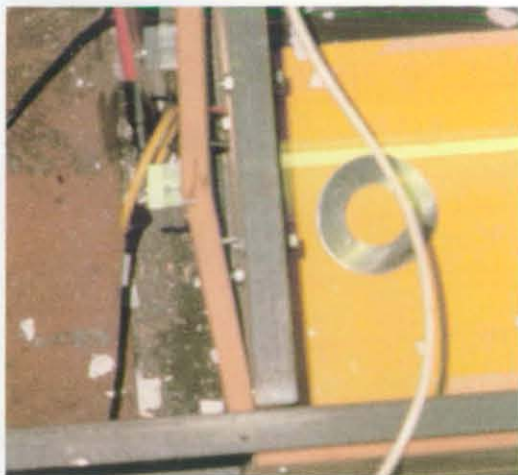


Figure 11.6 Photograph of damage to the drive terminal and support structure



Figure 11.7 Photograph of the drive coil break down after 3.01ms



Figure 11.8 Photograph of the drive coil break down after 3.51ms

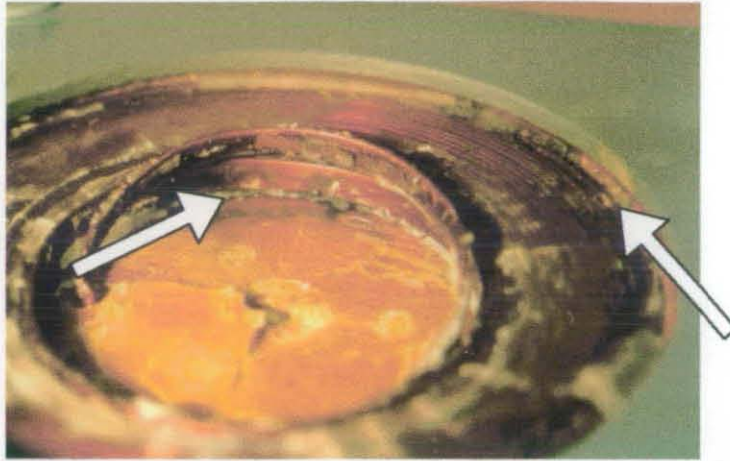


Figure 11.9 A close-up of the breakdown sites on the drive coil



Figure 11.10 A close-up of the damage to the projectile caused by an arc.

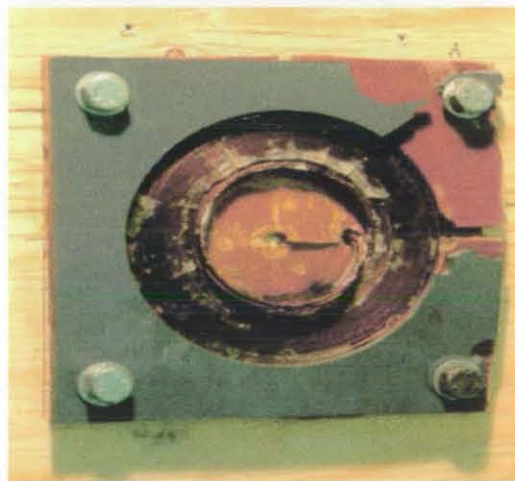


Figure 11.11 The final condition of the rectangular wire drive coil

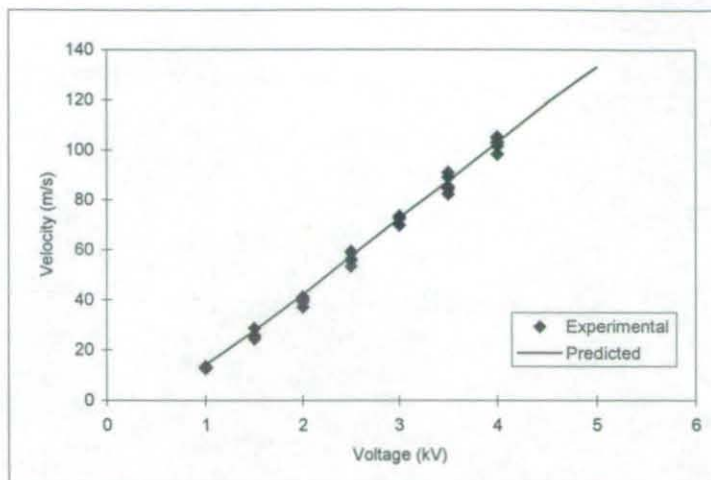


Figure 11.12 Results of low voltage round wire model validation tests

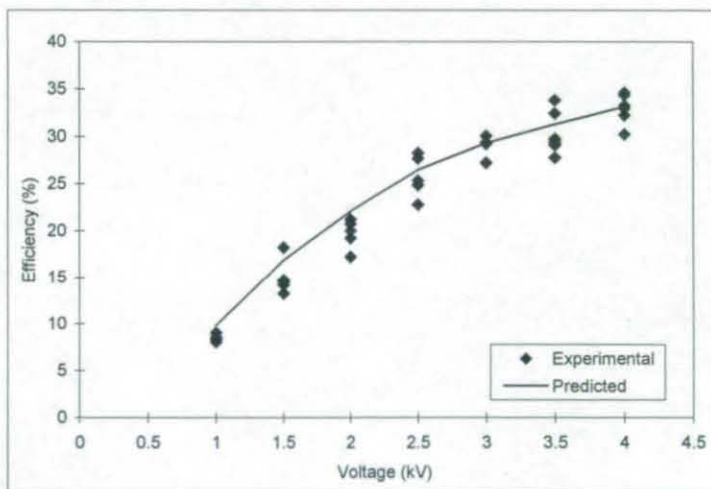


Figure 11.13 Efficiencies of the low voltage round wire drive coil tests

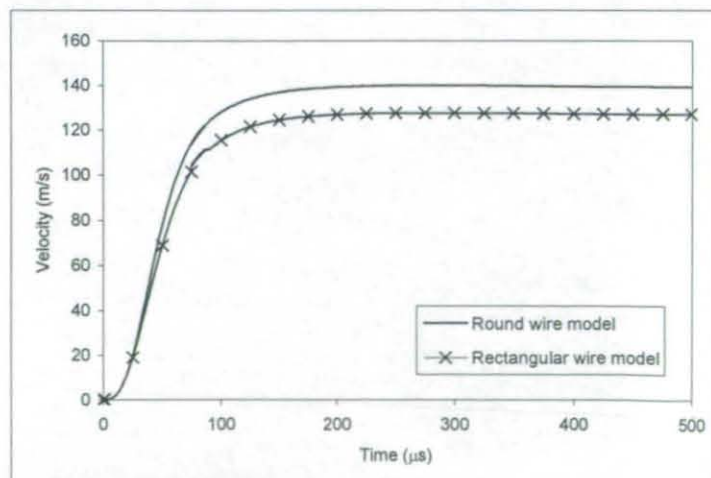


Figure 11.14 Comparison of round and rectangular wires model results.



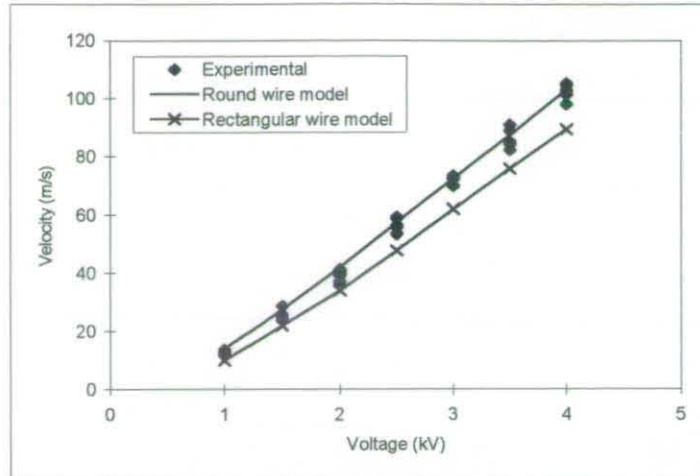


Figure 11.15 Comparison of rectangular wire model results and actual test results.

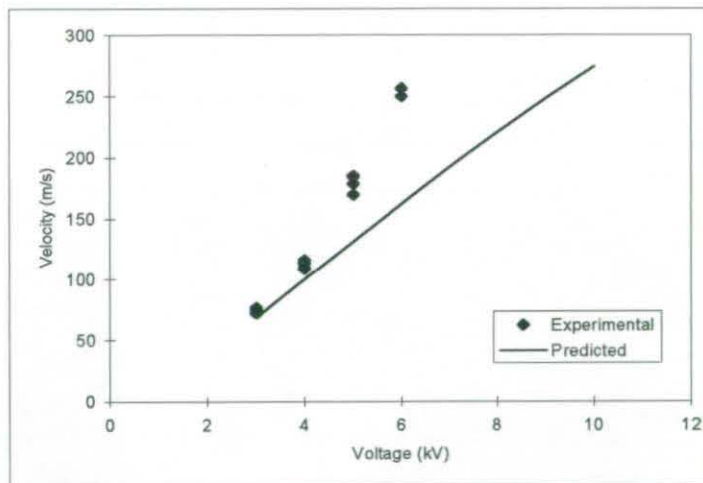


Figure 11.16 Results of high voltage round wire model validation tests

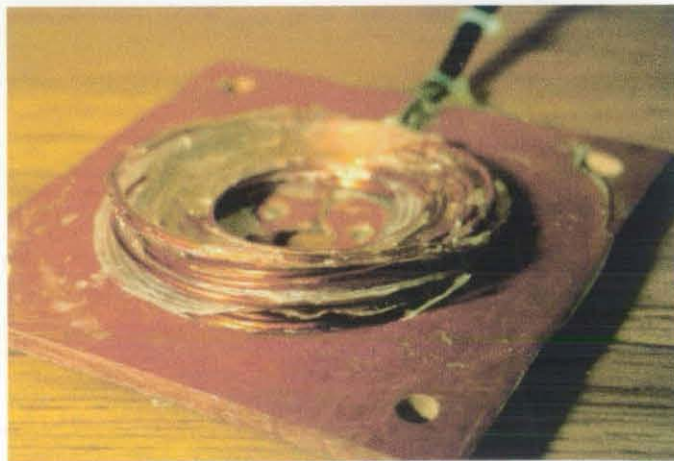


Figure 11.17 The final condition of the round wire drive coil

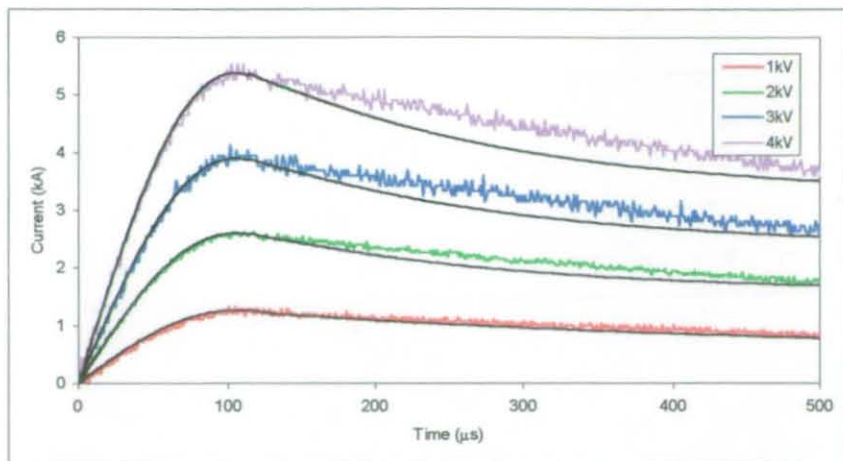


Figure 11.18 Low voltage round wire drive coil currents

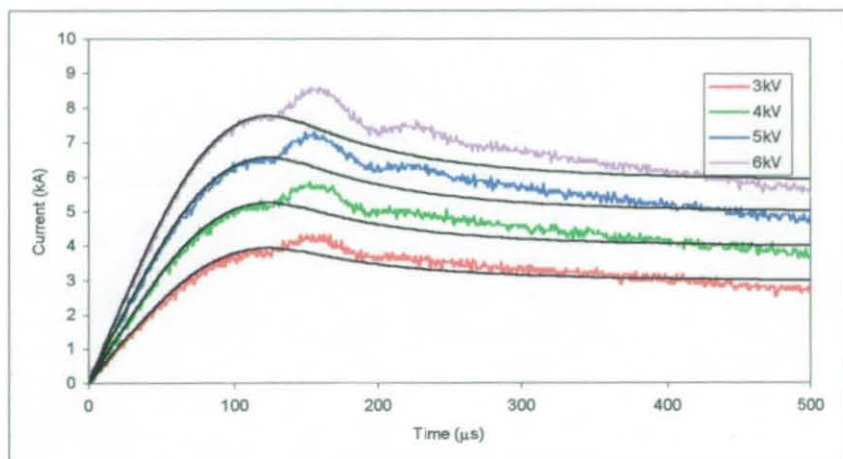


Figure 11.19 High voltage round wire drive coil currents

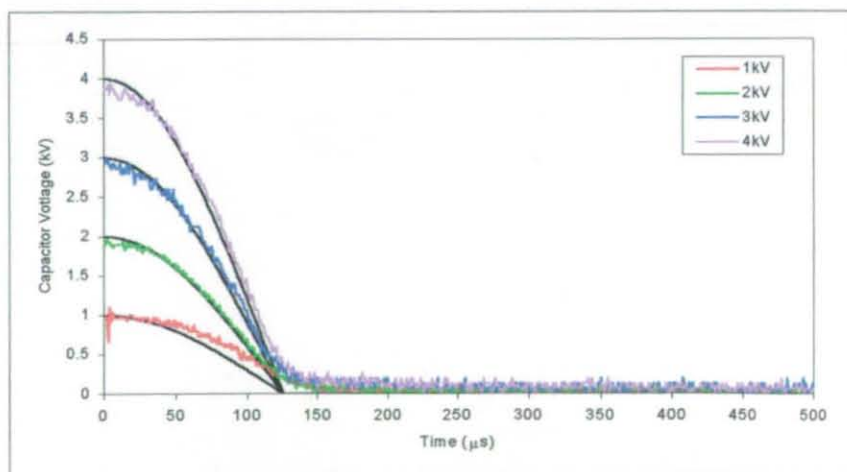


Figure 11.20 Low voltage round wire capacitor voltages



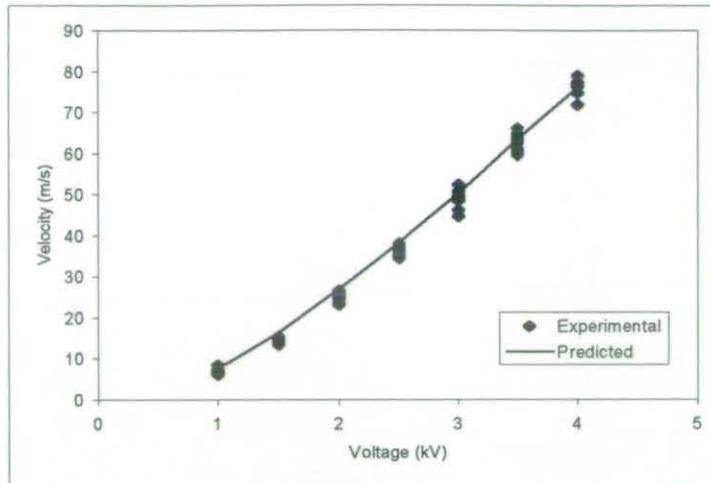


Figure 11.21 Results of low voltage dual projectile model validation tests

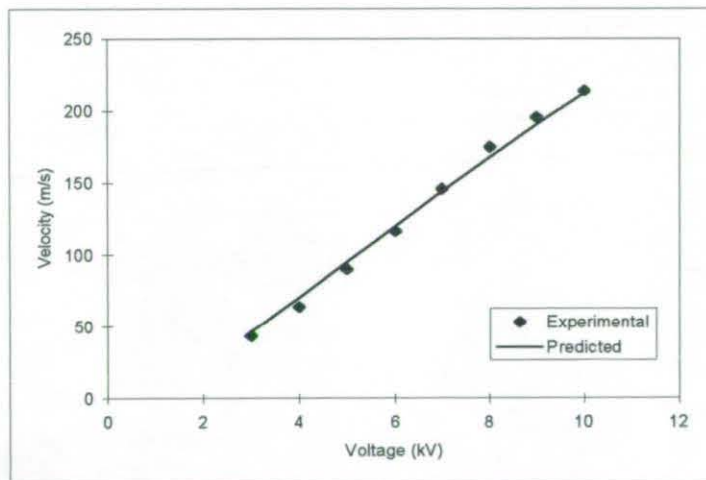


Figure 11.22 Results of high voltage dual projectile model validation tests

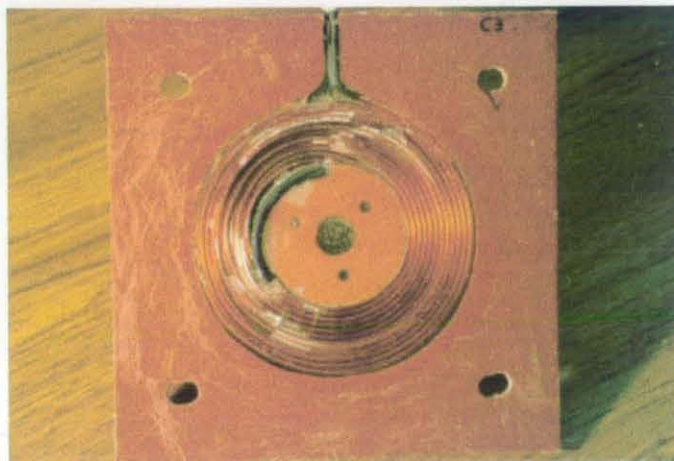


Figure 11.23 Photograph of damage to the dual projectile launcher drive coil.

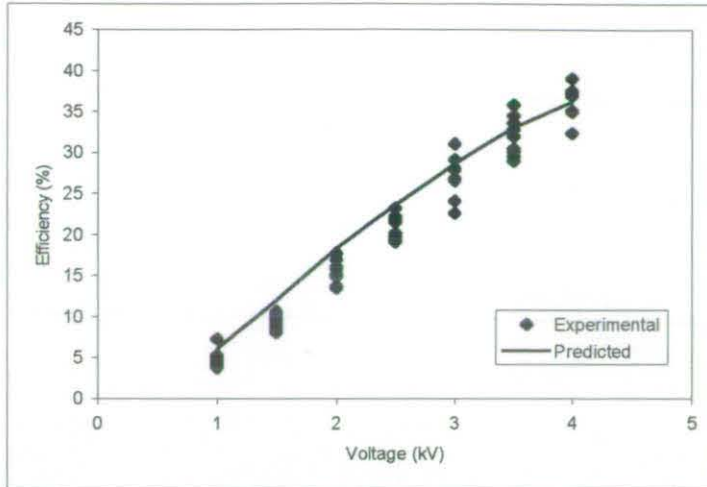


Figure 11.24 Low voltage efficiencies of dual projectile launcher

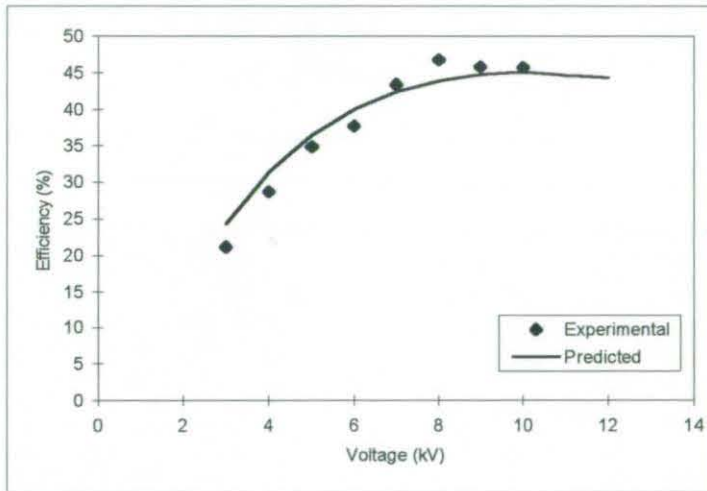


Figure 11.25 High voltage efficiencies of dual projectile launcher

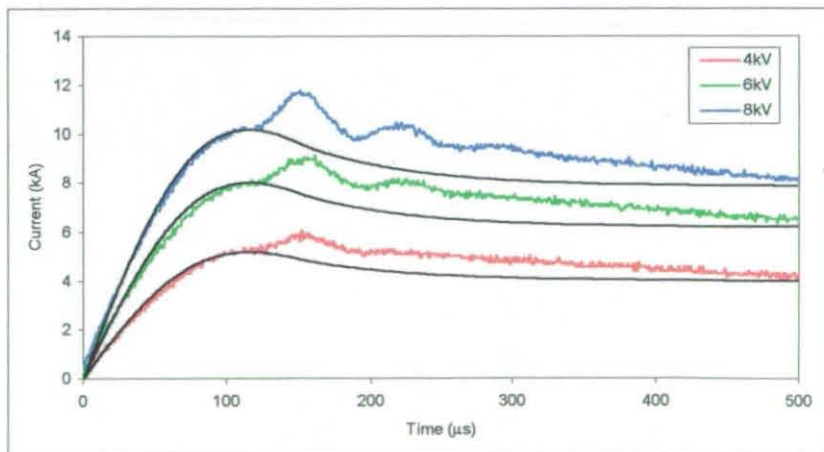


Figure 11.26 High voltage dual projectile drive coil current traces

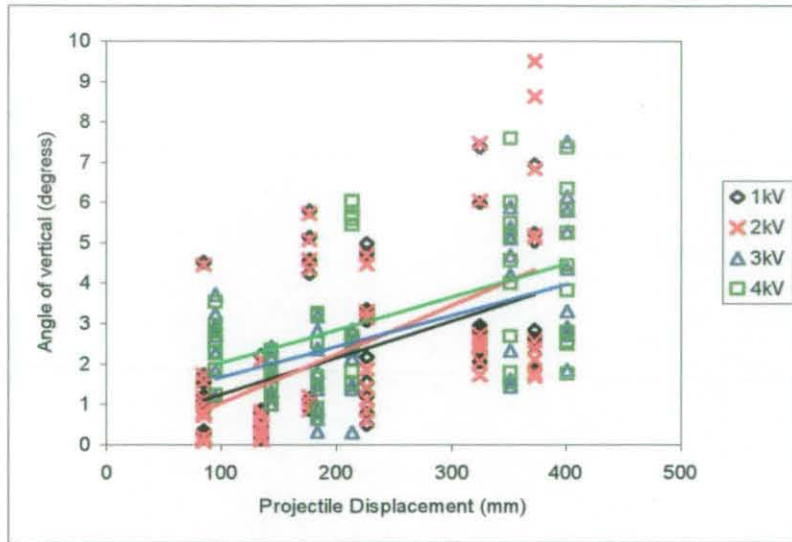


Figure 11.27 Calculated projectile trajectories

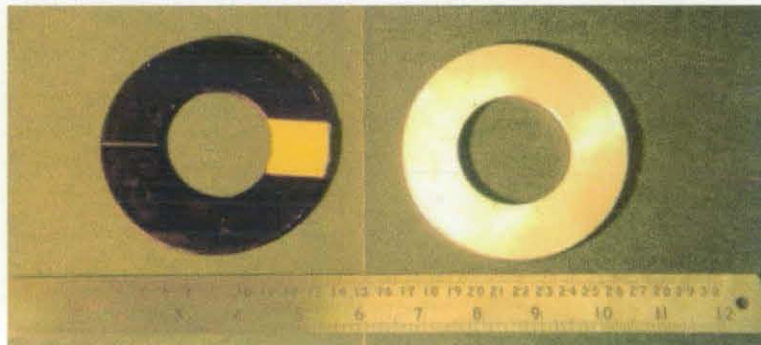
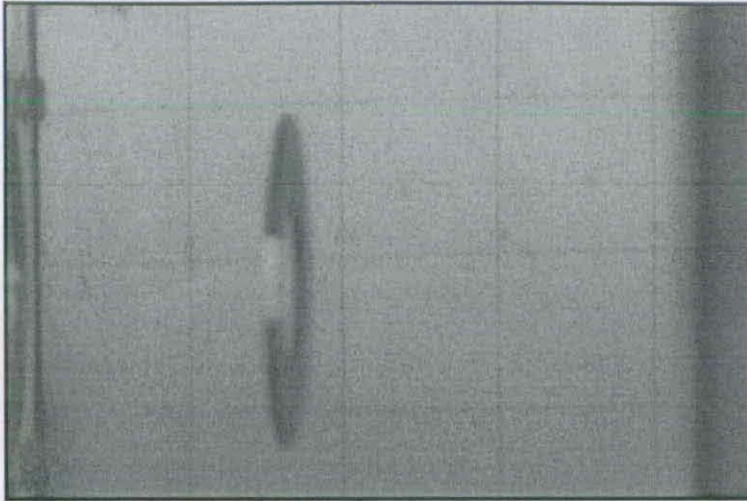
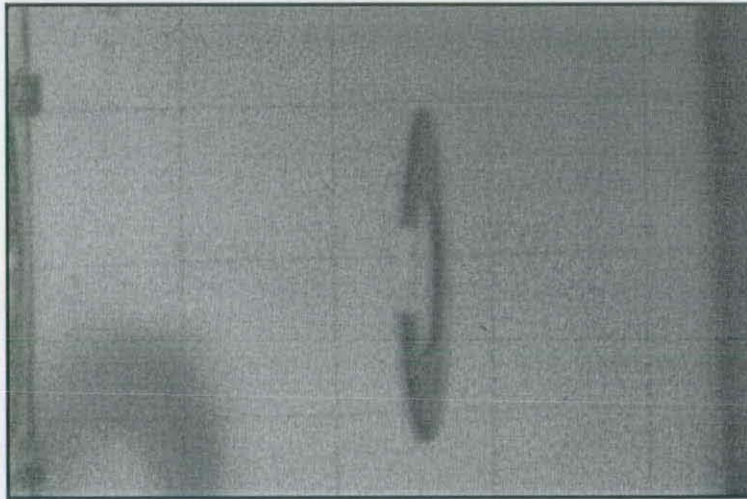


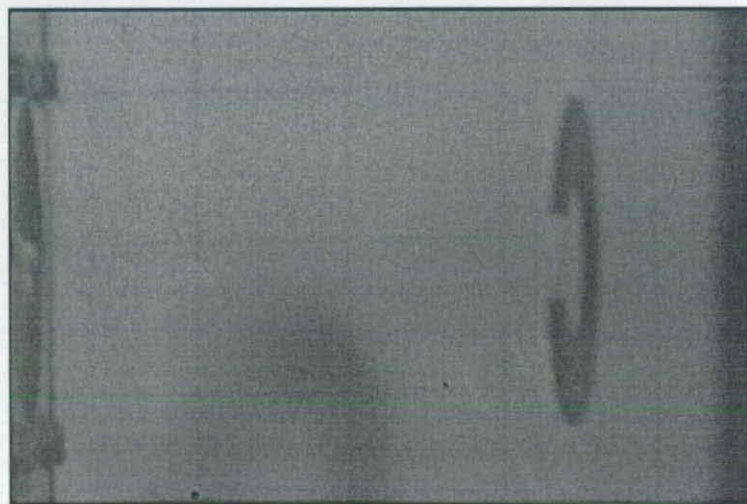
Figure 11.28 Normal and painted projectiles



After 1.2ms



After 1.7ms



After 2.2ms

Figure 11.29 High-speed photographs of painted projectile in flight



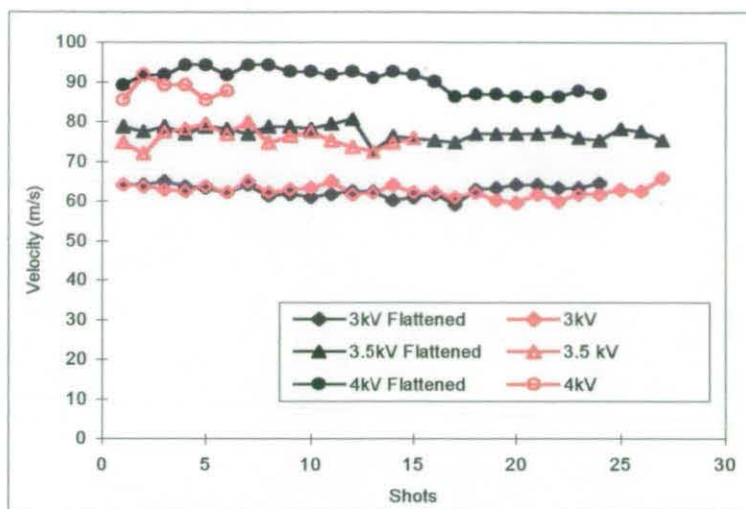


Figure 11.30 Effects of re-using flattened projectiles

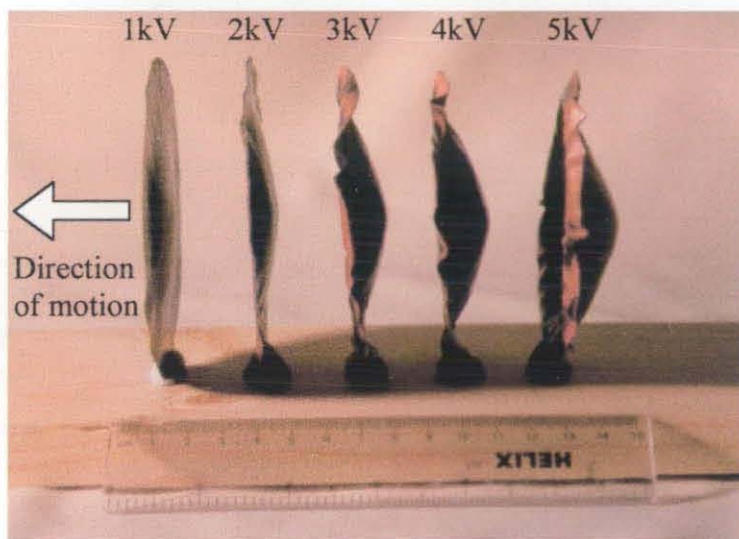
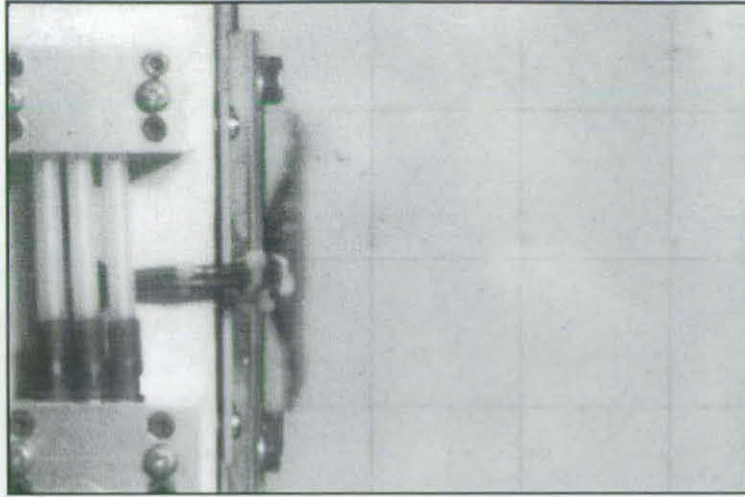
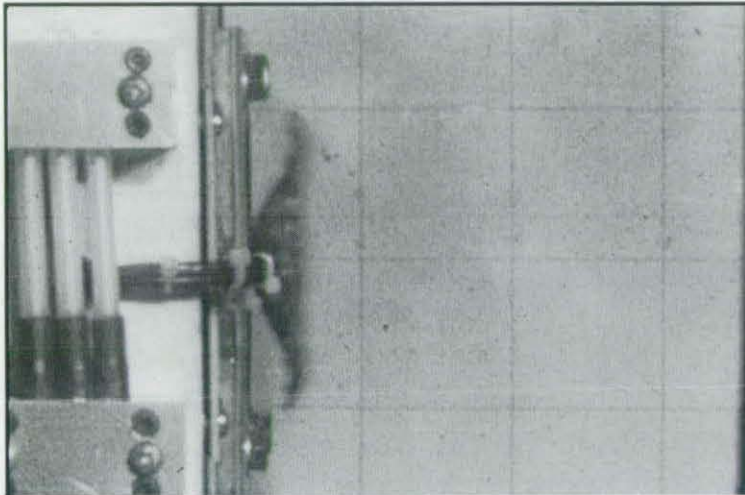


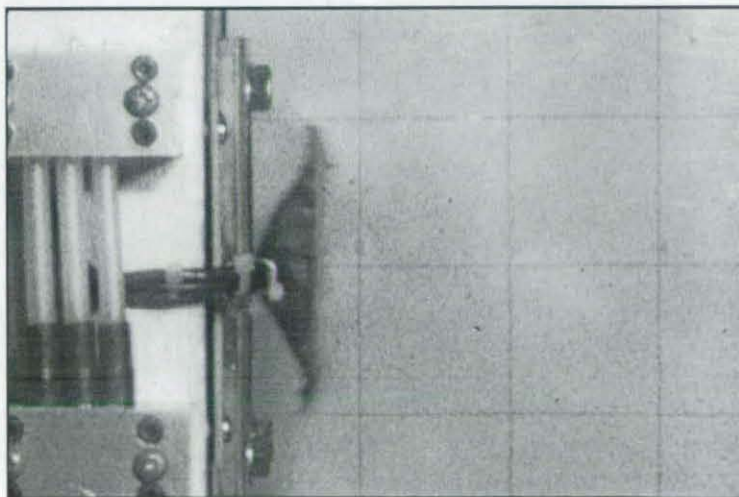
Figure 11.31 Annealed copper projectiles after launch



After 150 $\mu$ s



After 200 $\mu$ s



After 250 $\mu$ s

Figure 11.32 High-speed photographs of the example projectile



After 300 $\mu$ s

Figure 11.32 High-speed photographs of the example projectile (cont.)

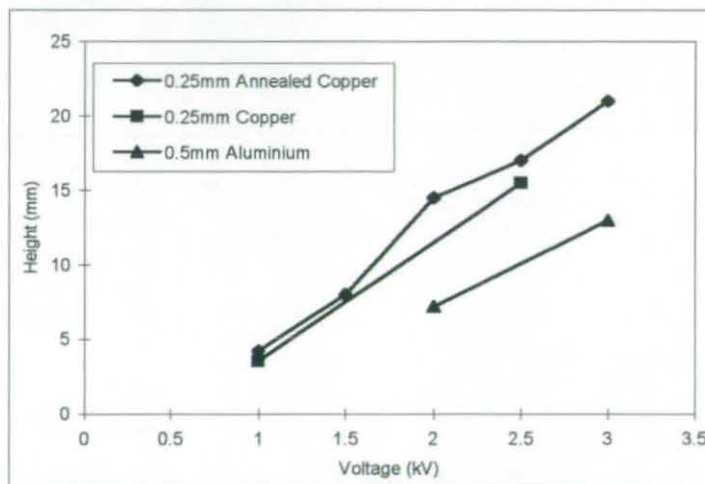


Figure 11.33 Disc projectile deformation against voltage



Figure 11.34 Front view of the thin aluminium projectile after a 3kV launch



Figure 11.35 Rear view of the thin aluminium projectile after a 3kV launch

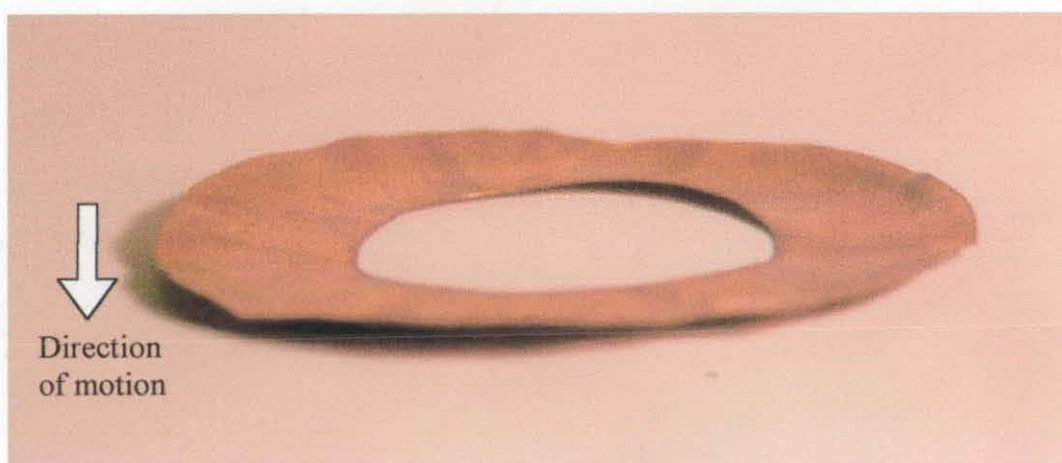


Figure 11.36 A deformed annular copper ring projectile

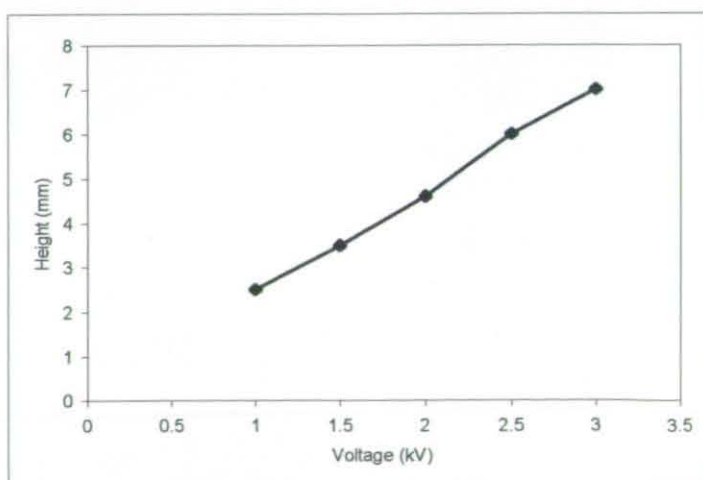


Figure 11.37 Ring projectile deformation against voltage





Figure 11.38 An octagonal projectile after launch

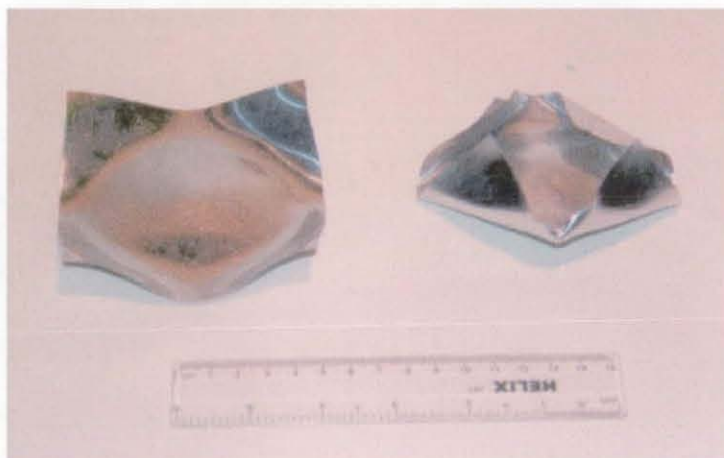
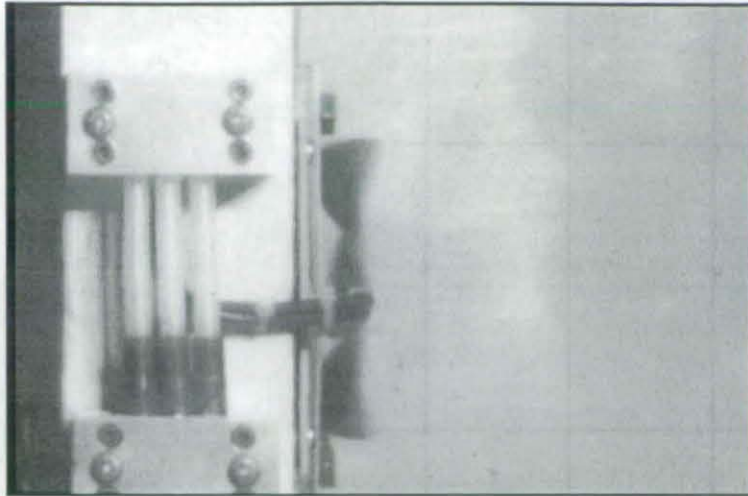


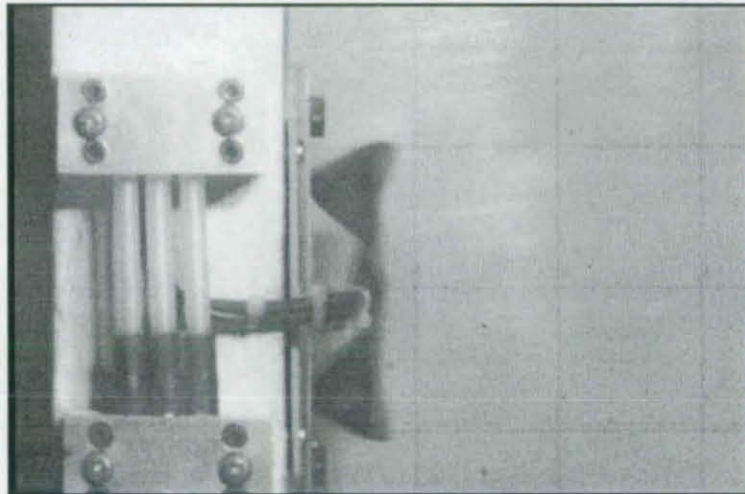
Figure 11.39 Square aluminium projectiles after launch



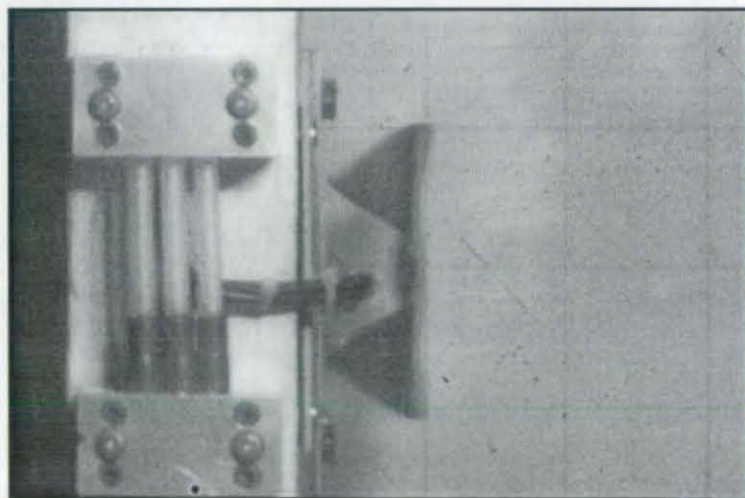
Figure 11.40 Square copper projectiles after launch



After 150 $\mu$ s



After 250 $\mu$ s



After 350 $\mu$ s

Figure 11.41 High-speed photographs of a square projectile during launch



Figure 11.42 Front view of square copper projectiles after launch

# 12. CONCLUSIONS AND FURTHER WORK

*This chapter presents the overall conclusions drawn from the work presented in this thesis and makes suggestions for its continuation.*

## 12.1. CONCLUSIONS

This thesis has described the development and testing of several different launchers, together with the numerical models required to accurately predict their performance. Filamentary analysis was chosen, as it provided a direct method for modelling the circular topology of a launcher, without the need to model the space around the launcher. Although a finite element model was used, this was limited to a low frequency and static formulation, which limited its use in modelling a transient and dynamic system.

The filamentary parameters were defined in a series of equations presented in Chapter 6. The filamentary inductances were formulated from the magnetic vector potential at a point some distance from a circular conductor. While the inductance equations had been formulated previously, some of them had not been used in earlier launcher models. These additional inductance calculations allowed the individual filamentary forces in both the radial and axial directions to be determined.

Filamentary resistance and thermal equations were developed, by using approximate functions to describe the material characteristics. These functions were derived from published experimental data, and were used to model successfully the material characteristics.

While the mechanical equation used was a simple force balance equation, it included the effects of aerodynamic resistance, which had not previously been included in models for this type of launcher. However, it was shown that the aerodynamic drag had little effect on the performance of a launcher, due to the very large electromagnetic forces.

To improve the performance of the modelling program a study of processor usage was undertaken. This led to several significant reductions in simulation run time and several approximations were tested to see how they would affect programme performance and accuracy. While all the approximations tested reduced the processing time, some of them produced unacceptably inaccurate solutions. In addition, a variable step-length model was implemented, which reduced the processing time for some simulations. Its greatest benefit was that it enabled simulations that had previously become unstable, to be modelled successfully.

The study of the effects of projectile mass on launcher performance showed that the projectile velocity increases as the mass is reduced. This study initially showed that the launcher efficiency also increases as the mass is reduced. However, expanding the range of the study showed that the launcher efficiency reached a maximum of 39%, with a mass of 100g, before rapidly decreasing. From the results obtained, it was concluded that the lighter projectiles were accelerated so fast that their movement induced large translational EMFs in the drive coil. These acted to oppose the supply current and hence impaired the launcher performance. The performance of the test launcher fell to 1.5% when the projectile mass was reduced to 0.01 gm.

In a study of the effects of the relative radii of the projectile and drive coil, it was shown that a slight projectile overhang was the optimum arrangement. However, the difference between the optimum arrangement and an arrangement with equal drive coil and projectile radii was so small that it was concluded that the radii should be the same. The effects of varying both the projectile and drive coil radii simultaneously showed that increasing the outside radius would improve the launcher performance and that the inside radius could be optimised for a given outside radius. During this study, the number of drive coil turns was optimised for each launcher arrangement, and the optimum number of turn increased slowly with launcher size. This suggested that scaling of the launcher could be used to design practical low voltage launchers with the optimum number of turns.

Several studies into the affects of varying the number of drive coil turns indicated that the optimum number of turns varied with the supply voltage. Also investigated was the effect of the inter-turn insulation thickness on the optimum turn / voltage relationship. While the insulation thickness did not effect the optimum at high supply voltages, it did at lower voltages. It was concluded that the lower voltage optima were affected most since they required a greater number of turns, and hence a greater amount of the available space was occupied by insulation. It was shown that the optimum number of turn only increased slightly when the drive coil was divided into two layers. This form of coil has the advantage that the connecting leads are on the outside edge, and it enabled more turns to be wound in a given coil size. This allows the optimum number of drive coil turns to be practical at lower supply voltages. Similar sets of simulations undertaken on a dual projectile launcher showed that the dual projectile launcher behaved in a similar manner to the single projectile launcher. Most interestingly, they also showed that a launcher could have an efficiency exceeding 50%.

Several novel launcher structures were tested to see if any improvement in launcher performance could be achieved by “magnetising” the projectile before it was launched. Although some improvements were possible, the complexity of the launcher was significantly increased. It was concluded that the most practical arrangement for pre-exciting the projectile was to place a low voltage disposable coil on the outside of the projectile. This would act as a current transformer, producing the required “magnetising” current in the projectile before launch.

To enable practical investigations to be undertaken, a range of sensing and control equipment were developed, including a laser beam position sensing and speed measuring system. It was shown that the laser beam sensing system could also be used to determine the yaw of a projectile in flight.

Predicted results show a good collation with the experimental results, for all the launchers tested. In addition, it was shown that the dual projectile launcher greatly reduces the recoil effects on the drive coil. The practical work also showed that the

yaw of a projectile does not depend on the supply voltage, but is determined by the initial positioning of the projectile with respect to the drive coil.

The study of projectile deformation shows clearly the extreme forces that acted on the projectile during a launch, with the projectile acted in a plastic manner due to the large forces present and not due to heating. It also showed that the projectile deformation was almost proportional to the supply voltage and that the projectile geometry could significantly effect the amount of deformation.

## **12.2. FURTHER WORK**

This thesis has described the development of several models, and has included results from several theoretical studies and practical experiments. There are however a number of areas that might warrant further investigation and areas that future investigations into flat electromagnetic launchers may wish to include are given below.

It was established that the launcher performance increased with an increase in the outside radius of the launcher. While this was true for the launchers studied, can this conclusion be generalised to cover any size of launcher? If so would including the associated increase in launcher mass limit the increase in performance? What effect does scaling have on the launcher performance and the optimum conditions studied in this thesis?

Studies of both single and dual projectile launchers showed that the introduction of a second layer in the drive coil allowed a greater number of turns, without greatly affecting the launcher performance. Could the introduction of a third layer in the drive coil produce a further improvement? In addition, could the same affect be achieved by increasing the supply inductance? If the optimum number of turns could be varied easily, without any noticeable degradation in the launcher performance, would this allow the launcher and power supply to be tuned to a practical optimum?

While the study of unusual launcher arrangements, predicted an improvement in launcher performance when the projectile was pre-excited, these were only theoretical, could a practical pre-excited test launcher be constructed, and would any increase in performance still be noticeable?

The methods and equations were developed to expand the filamentary model to include a flexible power supply configuration. While only single supply arrangements were considered it was suggested that an increase in the duration of the discharge pulse, by using multiple supplies, might improve the launcher performance. Would a study of multi-supply launcher predict any improvement in efficiency? Could the discharge times be controlled sufficiently accurately, or would practical limitations prevent the construction of a multi-supply launcher?

Other future work could include the implementation and validation of the projectile deformation model. In addition, a better method of describing and quantifying the amount of projectile deformation could be developed.



# References

- [1] Egeland A, "Birkeland's Electromagnetic Gun: A Historical Review", *IEEE Transactions on Plasma Science*, Vol. **17**, 1989, pp. 73-82
- [2] Harry DF, "Electromagnetic Propulsion : A New Initiative", *IEEE Transactions on Magnetics*, Vol. **18**, 1982, pp. 4-6
- [3] "1st Symposium on Electromagnetic Launch Technology", *IEEE Transactions on Magnetics*, Vol. **18**, 1982, pp. 1-213
- [4] "2nd Symposium on Electromagnetic Launch Technology", *IEEE Transactions on Magnetics*, Vol. **20**, 1984, pp. 197-411
- [5] Harry DF, "Introduction", *IEEE Transactions on Magnetics*, Vol. **22**, 1986, pp. 1379
- [6] "4th Symposium on Electromagnetic Launch Technology", *IEEE Transactions on Magnetics*, Vol. **25**, 1989, pp. 9-715
- [7] "5th Symposium on Electromagnetic Launch Technology", *IEEE Transactions on Magnetics*, Vol. **27**, 1991, pp. 1-660
- [8] Laithwaite ER, "The Way Ahead", *IEEE Transactions on Magnetics*, Vol. **27**, 1991, pp. 7-10
- [9] Atkinson SP; Ayleen R; Bloyce ARP; Haugh DC; Kirkpatrick DJ; Reip PW, "United Kingdom EM Gun Programme", *IEEE Transactions on Magnetics*, Vol. **25**, 1989, pp. 57-62
- [10] Haugh DC, "An Update on the UK Electric Gun Research Programme", *IEEE Transactions on Magnetics*, Vol. **33**, 1997, pp. 17-20
- [11] O'Callaghan D, "The UK Military Perception of Electromagnetic Technology", *IEEE Transactions on Magnetics*, Vol. **29**, 1993, pp. 354-355
- [12] Hammon HG; Dempsey J; Strachan D, "The Kirkcudbright Electromagnetic Launch Facility", *IEEE Transactions on Magnetics*, Vol. **29**, 1993, pp. 975-979
- [13] Powell JD; Batteh JH, "Arc Dynamics In The Rail Gun", *IEEE Transactions on Magnetics*, Vol. **18**, 1982, pp. 7-10
- [14] Young FJ; Hughes WF, "Rail and Armature Current Distributions in Electromagnetic Launchers", *IEEE Transactions on Magnetics*, Vol. **18**, 1982, pp. 33-41

- 
- [15] Marshall RA, "The TAERF Scientific Railgun Theoretical Performance", *IEEE Transactions on Magnetics*, Vol. **18**, 1982, pp. 11-15
- [16] Kotas JF; Guderjahn CA; Littman FD, "A Parametric Evaluation of Railgun Augmentation", *IEEE Transactions on Magnetics*, Vol. **22**, 1986, pp. 1573-1577
- [17] Hawke RS; Nellis WJ; Newman GH; Rego J; Susoeff AR, "Summary of EM Launcher Experiments Performed at LLNL", *IEEE Transactions on Magnetics*, Vol. **22**, 1986, pp. 1510-1515
- [18] Burton RL; Goldstein SA; Tidman DA; Wang SY; Winsor NK; Witherspoon FD, "EMET Technology for Rail Launchers", *IEEE Transactions on Magnetics*, Vol. **22**, 1986, pp. 1410-1415
- [19] Harding JT; Kaplan RB; Pierson HO; Tuffias RH; Upshaw JL, "Chemically Vapor Deposited Materials for Railguns", *IEEE Transactions on Magnetics*, Vol. **22**, 1986, pp. 1506-1509
- [20] Harry DF; Coose P; Meinel CP; Tidman DA, "Electromagnetic Earth-to-Space Launch", *IEEE Transactions on Magnetics*, Vol. **25**, 1989, pp. 9-16
- [21] Ribe FL; Barnes DC, "Review of Impact Fusion Concepts", *IEEE Transactions on Magnetics*, Vol. **25**, 1989, pp. 20-26
- [22] Beno JH; Weldon WF, "An Investigation into the Potential for Multiple Rail Railguns", *IEEE Transactions on Magnetics*, Vol. **25**, 1989, pp. 92-96
- [23] Igenbergs E, "A Symmetrical Rail Accelerator", *IEEE Transactions on Magnetics*, Vol. **27**, 1991, pp. 650-653
- [24] Burden RA; Gray JW; Oxley CM, "Explosive Foil Injection (EFI) Pre-Accelerator for Electromagnetic Launchers", *IEEE Transactions on Magnetics*, Vol. **25**, 1989, pp. 107-110
- [25] Parker JV, "Why Plasma Armature Railguns Don't Work (and what can be done about it)", *IEEE Transactions on Magnetics*, Vol. **25**, 1989, pp. 418-424
- [26] Parker JV, "The SRS Railgun : A New Approach to Restrike Control", *IEEE Transactions on Magnetics*, Vol. **25**, 1989, pp. 412-417
- [27] Rodger D; Leonard PJ; Eastham JF, "Modelling Electromagnetic Rail Launchers at Speed Using 3D Finite Elements", *IEEE Transactions on Magnetics*, Vol. **27**, 1991, pp. 314-317
- [28] "6th Symposium on Electromagnetic Launch Technology", *IEEE Transactions on Magnetics*, Vol. **29**, 1993, pp. 342-1224

- 
- [29] Murthy SK; Weldon WF, "Multiphase Railgun System : A New Concept", *IEEE Transactions on Magnetics*, Vol. 29, 1993, pp. 472-477
- [30] "8th Symposium on Electromagnetic Launch Technology", *IEEE Transactions on Magnetics*, Vol. 33, 1997, pp. 1-659
- [31] Kondrashov D; Keefer D, "A Maxwell's Equation Solver for 3D MHD Calculations", *IEEE Transactions on Magnetics*, Vol. 33, 1997, pp. 254-259
- [32] Hsieh KT; Kim BK, "International Railgun Modeling Effort", *IEEE Transactions on Magnetics*, Vol. 33, 1997, pp. 245-248
- [33] Cardelli E; Esposito N; Huerta MA, "Numerical Comparison Between a Differential and an Integral Approach in MHD Simulation of Electromagnetic Railgun Plasma Armatures", *IEEE Transactions on Magnetics*, Vol. 33, 1997, pp. 219-224
- [34] Bauer DP; Juston JM, "Rapid Testing for Multishot Railgun Bore Life", *IEEE Transactions on Magnetics*, Vol. 33, 1997, pp. 390-394
- [35] Mongeau P; Williams F, "Arc Commutated Launcher", *IEEE Transactions on Magnetics*, Vol. 18, 1982, pp. 42-45
- [36] Mongeau P; Williams F, "Helical Rail Glider Launcher", *IEEE Transactions on Magnetics*, Vol. 20, 1982, pp. 190-193
- [37] Mawardi OK, "Interior Ballistics of a Hybrid Electromagnetic Gun", *IEEE Transactions on Magnetics*, Vol. 18, 1982, pp. 60-63
- [38] Mongeau P, "Analysis of Helical Brush Commutation", *IEEE Transactions on Magnetics*, Vol. 20, 1984, pp. 231-234
- [39] Mongeau P, "Inductively Commutated Coilguns", *IEEE Transactions on Magnetics*, Vol. 27, 1991, pp. 568-572
- [40] Elliott DG, "Travelling Wave Synchronous Coil Gun", *IEEE Transactions on Magnetics*, Vol. 27, 1991, pp. 647-649
- [41] Snow WR; Willig RL, "Design Criteria for Brush Commutation in High Speed Travelling Wave Coilguns", *IEEE Transactions on Magnetics*, Vol. 27, 1991, pp. 654-659
- [42] Nalty KE; Driga MD, "Induction Generator Powered Coaxial Launchers", *IEEE Transactions on Magnetics*, Vol. 27, 1991, pp. 554-557
- [43] Ingram SK, "Theoretical Analysis of a Collapsing Field Accelerator", *IEEE Transactions on Magnetics*, Vol. 29, 1993, pp. 675-679

- [44] Bresie DA; Bacon JL; Ingram SW; Kennington KS; Weeks DA, "Spear Coilgun", *IEEE Transactions on Magnetics*, Vol. **31**, 1995, pp. 467-472
- [45] Onuki T; Laithwaite ER, "Optimised Design of Linear Induction Motor Accelerators", *IEE Proceedings*, Vol. **118**, 1971, pp. 349-355
- [46] Kolm H; Mongeau P, "Basic Principles of Coaxial Launch Technology", *IEEE Transactions on Magnetics*, Vol. **20**, 1984, pp. 227-230
- [47] Dirga MD; Weldon WF; Woodson HH, "Electromagnetic Induction Launchers", *IEEE Transactions on Magnetics*, Vol. **22**, 1986, pp. 1453-1458
- [48] Williamson S; Leonard PJ, "Analysis of Air-Cored Tubular Induction Motors", *IEE Proceedings*, Vol. **133**, 1986, pp. 285-290
- [49] Dirga MD; Weldon WF, "Induction Launcher Design Considerations", *IEEE Transactions on Magnetics*, Vol. **25**, 1989, pp. 153-158
- [50] Elliott DG, "Traveling Wave Induction Launcher", *IEEE Transactions on Magnetics*, Vol. **25**, 1989, pp. 159-163
- [51] Zabar Z; Naot Y; Birenbaum L; Levi E; Joshi PN, "Design and Power Conditioning for the Coil-gun", *IEEE Transactions on Magnetics*, Vol. **25**, 1989, pp. 627-631
- [52] He JL; Zabar Z; Levi E; Birenbaum L, "Transient Analysis of Multisection Induction Type Coil Launchers", *7th IEEE Pulse Power Conference*, 1989, pp. 140-143
- [53] He JL; Levi E; Birenbaum L; Naot Y, "Analysis of Induction-Type Coilgun Performance Based on Cylindrical Current Sheet Model", *IEEE Transactions on Magnetics*, Vol. **27**, 1991, pp. 579-584
- [54] He JL; Zabar Z; Levi E; Birenbaum L, "Transient Performance of Linear Induction Launchers Fed by Generators and Capacitor Banks", *IEEE Transactions on Magnetics*, Vol. **27**, 1991, pp. 585-590
- [55] Zabar Z; Lu XN; He JL, "Test Results For The Three Prototype Models of a Linear Induction", *IEEE Transactions on Magnetics*, Vol. **27**, 1991, pp. 558-562
- [56] Wu AY, "Parameter Studies for Traveling Wave Coaxial Launchers", *IEEE Transactions on Magnetics*, Vol. **27**, 1991, pp. 617-622
- [57] Weeks DA; Pratop SB, "Design of Rising Frequency Generator / Coaxial Accelerator", *IEEE Transactions on Magnetics*, Vol. **29**, 1993, pp. 716-721
- [58] Kim SW; Jung HK; Hahn SY, "An Optimal Design of Capacitor Driven Coilgun", *IEEE Transactions on Magnetics*, Vol. **30**, 1994, pp. 207-211

- [59] Kim K; Zabar Z; Levi E; Birenbaum L, "In Bore Projectile Dynamics in the Linear Induction Launcher (LIL) Part 1: Oscillation", *IEEE Transactions on Magnetics*, Vol. **31**, 1995, pp. 484-488
- [60] Kim K; Zabar Z; Levi E; Birenbaum L, "In Bore Projectile Dynamics in the Linear Induction Launcher (LIL) Part 2: Balloting, Spinning and Nutation", *IEEE Transactions on Magnetics*, Vol. **31**, 1995, pp. 489-492
- [61] Lu XN; Zabar Z; Levi E; Birenbaum L, "Transition Between Two Sections in a Linear Induction Launcher (LIL)", *IEEE Transactions on Magnetics*, Vol. **31**, 1995, pp. 493-498
- [62] Kim SW; Jung HK; Hahn SY, "Optimal Design of Multisage Coilgun", *IEEE Transactions on Magnetics*, Vol. **32**, 1996, pp. 505-508
- [63] Laio M; Zabar Z; Levi E; Birenbaum L, "Analysis of Generator Driven Linear Induction Launchers", *IEEE Transactions on Magnetics*, Vol. **33**, 1997, pp. 184-189
- [64] Burgess TJ; Cnare EC; Oberkampf WL; Beard S; Cowan M, "The Electromagnetic Q Gun and Tubular Projectiles", *IEEE Transactions on Magnetics*, Vol. **18**, 1982, pp. 46-55
- [65] Snow WR; Dunbar RS; Kubby JA; O'Neill GK, "Mass Driver Two : A Status Report", *IEEE Transactions on Magnetics*, Vol. **18**, 1982, pp. 127-134
- [66] Burgess TJ; Cowan M, "Multistage Induction Mass Accelerator", *IEEE Transactions on Magnetics*, Vol. **20**, 1984, pp. 235-238
- [67] McKinney K; Mongeau P, "Multiple Stage Pulsed Induction Acceleration", *IEEE Transactions on Magnetics*, Vol. **20**, 1984, pp. 239-242
- [68] Cowan M; Cnare EC; Dunggin BW; Kaye RJ; Tucker TJ, "The Reconnection Gun", *IEEE Transactions on Magnetics*, Vol. **22**, 1986, pp. 1429-1434
- [69] Bresie DA; Andrews JA; Ingram SW, "Parametric Approach to Linear Induction Accelerator Design.", *IEEE Transactions on Magnetics*, Vol. **27**, 1991, pp. 390-393
- [70] Cowan M; Widner MM; Cnare EC; Dunggin BW; Kaye RJ; Freeman JR, "Exploratory Development of the Reconnection Launcher 1986-1990", *IEEE Transactions on Magnetics*, Vol. **27**, 1991, pp. 563-567
- [71] Cnare EC; Widner MM; Dunggin BW, "A 10-stage Reconnection Demonstration Launcher", *IEEE Transactions on Magnetics*, Vol. **27**, 1991, pp. 644-646

- [72] Widner MM, "Warp-10: A Numerical Simulation Model for the Cylindrical Reconnection Launcher", *IEEE Transactions on Magnetics*, Vol. 27, 1991, pp. 634-638
- [73] Andrews JA; Devine JR, "Armature Design for Coaxial Induction Launchers", *IEEE Transactions on Magnetics*, Vol. 27, 1991, pp. 639-643
- [74] Bresie DA; Andrews JA, "Design of a Reluctance Accelerator", *IEEE Transactions on Magnetics*, Vol. 27, 1991, pp. 623-627
- [75] Bresie DA; Ingram SW, "Coilgun Technology at the Center for Electromechanics the University of Texas at Austin", *IEEE Transactions on Magnetics*, Vol. 29, 1993, pp. 649-654
- [76] Kaye RJ; Cnare EC; Cowan M; Dunggin BW, "Design and Performance of Sandia's Contactless Coilgun for 50mm", *IEEE Transactions on Magnetics*, Vol. 29, 1993, pp. 680-685
- [77] Williamson S; Horne CD, "Effects of Timing Errors on Coil-gun Performance", *IEEE International Pulse Power Conference*, 1993, pp. 564-567
- [78] Marder B, "A Coilgun Design Primer", *IEEE Transactions on Magnetics*, Vol. 29, 1993, pp. 701-705
- [79] Leonard PJ; Hainsworth G, "Analysis of the Performance of Tubular Pulsed Coil Induction", *IEEE Transactions on Magnetics*, Vol. 29, 1993, pp. 686-690
- [80] Hainsworth G; Rodger D, "Design Optimization of Coilguns", *IEEE Transactions on Magnetics*, Vol. 31, 1995, pp. 473-477
- [81] Gregory K; Smith IR; Vadher VV; Edwards MJ, "Experimental Validation of a Capacitor Discharge Induction Launcher Model", *IEEE Transactions on Magnetics*, Vol. 31, 1995, pp. 599-603
- [82] Nett J; Germandt L, "Inductive Acceleration of Moving Projectiles and Synchronization Between the Driving Field and the Projectile Motion", *IEEE Transactions on Magnetics*, Vol. 31, 1995, pp. 499-503
- [83] Hainsworth G; Rodger D, "Finite Element Modelling of Flux Concentrators for Coilguns", *IEEE Transactions on Magnetics*, Vol. 33, 1997, pp. 175-177
- [84] Laithwaite ER, "Induction Machines for Special Purposes", *George Newnes Ltd.*, 1966
- [85] Meagher TF, "The Conversion of Electromagnetic Energy into Shock Pulses", *ISA Transactions*, Vol. 3, 1964, pp. 313-321

- [86] Bondaletov VN; Goncharenko GM, "Acceleration of Conductors in a Pulsed Magnetic Field", *Soviet Physics - Technical Physics*, Vol. 15, 1971, pp. 1724-1729
- [87] Schmidt Harms CA, "A Compact Ignitor for Spectroscopic Arcs", *IEEE Transactions on Magnetics*, Vol. 18, 1985, pp. 705-707
- [88] Lell P; Igenbergs E; Kuczera H, "An Electromagnetic Accelerator", *Journal of Physics E: Scientific Instrumentation*, Vol. 16, 1983, pp. 325-330
- [89] Igenbergs E; Aigner S; Hùdepoh A, "The TUM/LRT Electromagnetic Launchers", *IEEE Transactions on Magnetics*, Vol. 22, 1986, pp. 1536-1541
- [90] Thornton E; Seddon N, "Compact Hypervelocity Induction Accelerator", *7th IEEE Pulse Power Conference*, 1989, pp. 144-146
- [91] Sadedin DR, "A Study of the Magnetic Induction-Repulsion Accelerator", *8th IEEE Pulse Power Conference*, 1991, pp. 68-72
- [92] Goldstein SA; Tidman DA; Sabdek F; Massey D; Vitkovitsky IM; Scherrer VE, "The MAID System - Data Base and Design Issues", *IEEE Transactions on Magnetics*, Vol. 18, 1982, pp. 105-114
- [93] Tidman DA; Goldstein SA, "Applications of Rep-Ratable Mass Accelerators (Such as MAID)", *IEEE Transactions on Magnetics*, Vol. 18, 1982, pp. 115
- [94] Spann ML; Pratop SB; Brinkman WG; Perkins D; Thelen RF, "A Rapid Fire Compulsator-Driven Railgun System", *IEEE Transactions on Magnetics*, Vol. 22, 1986, pp. 1753-1756
- [95] Werst MD; Brinkman WG; Spann ML, "Fabrication of a Compensated Pulsed Alternator for a Rapid Fire Railgun System", *IEEE Transactions on Magnetics*, Vol. 22, 1986, pp. 1812-1816
- [96] Burden RL; Faires KD; Reynolds AC, "Numerical Analysis", *Pringle, Weber & Schimdt*, 1997
- [97] Sarma MS; Yamamura A, "Nonlinear Analysis of Magnetic Bearings for Space Technology", *IEEE Transactions on Aerospace and Electronic Systems*, Vol. 15, 1979, pp. 134-140
- [98] Hrenikoff A, "Solutions of Problems in Elasticity by the Framework Method", *Journal of Applied Mechanics*, Vol. 8, 1941, pp. 169-175
- [99] McHenry D, "A Lattice Analogy for the Solution of Plane Stress Problems", *Journal of Applied Civil Engineering*, Vol. 21, 1943, pp. 59-82

- 
- [100] Turner MJ; Clough RW; Martin HC; Topp LJ, "Stiffness and Deflection Analysis of Complex Structures", *Journal of Aeronautical Sciences*, Vol. 23, 1956, pp. 805-823
- [101] Fraeijis de Veubeke B, "Displacement and Equilibrium Models in the Finite Element Method", *Wiley (New York)*, 1965
- [102] Pian THH, "Derivation of Element Stiffness Matrices by Assumed Stress Distribution", *AIAA Journal*, Vol. 2, 1964, pp. 1232-1336
- [103] Tanner RL; Andreassen MG, "Numerical Solution of Electromagnetic Problems", *IEEE Spectrum*, Vol. 4, 1967, pp. 53-61
- [104] Hainsworth G; Leonard PJ; Rodger D, "Finite Element Modelling of Magnetic Compression Using Coupled Electromagnetic - Structural Codes", *IEEE Transactions on Magnetics*, Vol. 32, 1996, pp. 1050-1053
- [105] Grover FW, "Inductance Calculations", *Dover Publications Inc (New York)*, 1946
- [106] Silvester PP, "Modern Electromagnetic Fields", *Prentice Hall (UK)*, 1968
- [107] Elliott DG, "Mesh-Matrix Analysis Method for Electromagnetic Launchers", *IEEE Transactions on Magnetics*, Vol. 25, 1989, pp. 164-169
- [108] Wu AY; Sun KS, "Formulation and Implementation of the Current filament method for the analysis of current diffusion and heating in conductors in railguns and homopolar generators", *IEEE Transactions on Magnetics*, Vol. 25, 1989, pp. 610-615
- [109] Hainsworth G; Leonard PJ; Rodger D; Lai HC, "A Comparison Between Finite Element and Mutual Inductance Models of Coilguns", *Proceedings of the 4th European Symposium on EML Technology*, 1993, pp. 1012
- [110] Kirchhoff G, "On the Solution of the Equations Obtained from the Investigation of the Linear Distribution of Galvanic Currents", *IRE Transactions on Circuit Theory*, Vol. 5, 1958, pp. 4-7
- [111] Le Corbeiller P, "Matrix Analysis of Electric Networks", *John Wiley & Sons*, 1950,
- [112] Maxwell JC, "A Treatise on Electricity and Magnetism", *Clarendon Press*, Vol. 1, 1904
- [113] Kron G, "Tensor Analysis of Networks", *Mac Donald (London)*, 1965
- [114] Happ HH, "The Structure of Orthogonal Electric Networks with Conventional Networks as Special Cases Part 1 : Orthogonal Z Network", *Matrix and Tensor Quarterly*, Vol. 15, 1965, pp. 99-108



- [115] Happ HH, "The Structure of Orthogonal Electric Networks with Conventional Networks as Special Cases Part 2 : Orthogonal Y Network", *Matrix and Tensor Quarterly*, Vol. 16, 1965, pp. 35-45
- [116] Happ HH, "The Structure of Orthogonal Electric Networks with Conventional Networks as Special Cases Part 3 : Conventional Networks as Special Cases of Orthogonal Networks", *Matrix and Tensor Quarterly*, Vol. 16, 1966, pp. 107-121
- [117] Gregory K, "The Rapid Numerical Solution of Transient Problems in Small-Scale Electrical Power Systems", *LUT Thesis*, 1994
- [118] Gerald CF; Wheatley PO, "Applied Numerical Analysis", *Addison-Wesley*, 1970
- [119] Lapidus L; Seinfeld JH, "Numerical Solution of Ordinary Differential Equations", *Academic Press (London & New York)*, Vol. 74, 1971
- [120] Ralston A; Herbert SW, "Mathematical Methods for Digital Computers", *John Wiley & Sons*, 1960
- [121] Graneau P, "A Re-examination of the Relationship between Self- and Mutual Inductance", *Journal of Electronics & Control*, Vol. 12, 1962, pp. 125-132
- [122] Garrett MW, "Calculation of Fields, Forces and Mutual Inductances of Current Systems by Elliptic Integrals", *Journal of Applied Physics*, Vol. 34, 1963, pp. 2567-2573
- [123] Lide DR, "CRC Handbook of Chemistry and Physics", *CRC Press*, 1997
- [124] Hoerner SF, "Aerodynamic Drag", *The Otterbein Press*, 1951
- [125] Brameller A; Allan RN; Hamam YM, "Sparsity", *Pitman*, 1976
- [126] Clifton S; Mongeau P, "Transient Response of Coaxial Pulse Coils", *IEEE Transactions on Magnetics*, Vol. 20, 1984, pp. 344-347
- [127] Hibbeler RC, "Mechanics of Materials", *Macmillan Publishing Company*, 1991, pp. 373-375
- [128] Young CW, "Roark's Formulas for Stress and Strain", *McGraw-Hill*, 1989, pp. 518-640
- [129] Williamson S; Horne CD; Haugh DC, "Design of Pulse Coil-guns", *IEEE Transactions on Magnetics*, Vol. 31, 1995, pp. 516-521
- [130] Novac BM; Smith IR; Senior P; Enache MC; Gregory K, "Can The Efficiency Of An Electrostatic To Kinetic Energy Conversion Process Exceed 50%", *11th IEEE Pulse Power Conference*, Vol. 2, 1997, pp. 1139-1143

- 
- [131] Nalty KE; Zowarka RC; Holland LD, "Instrumentation for EM launcher Systems", *IEEE Transactions on Magnetics*, Vol. 20, 1984, pp. 328-331
- [132] Stoll RL, "Method of Measuring Alternating Currents without Disturbing the Conducting Circuit", *IEE Proceedings*, Vol. 122, 1975, pp. 1166-1167
- [133] Murgatroyd PN; Chu AKY; Richardson GK; West D; Yearley GA; Spencer AJ, "Making Rogowski Coils", *Measurement & Science Technology*, 1991, pp. 1218-1219
- [134] Novac BM; Serban A; Smith IR; Stewardson HR, "Simple and Accurate Estimation of the Parameters of a Fast Discharge Circuit", *International Journal of Electrical Engineering Education*, Vol. 32, 1995, pp. 83-84
- [135] Thome RJ; Tarrh JM, "MHD and Fusion Magnetics", *John Wiley & Sons*, 1982

# A. CALCULATION OF COMPLETE ELLIPTIC INTEGRALS

The elliptic integral of the first and second kind are required for the definition of the filament self and mutual inductances, and their rates of change. The complete elliptic integrals of the first and second kind are defined as [A1].

$$K(k) = \int_0^{\pi/2} \frac{d\theta}{\sqrt{1 - k^2 \sin^2 \theta}} \quad \{A.1\}$$

$$E(k) = \int_0^{\pi/2} \sqrt{1 - k^2 \sin^2 \theta} \, d\theta \quad \{A.2\}$$

Exact solutions of elliptic integrals cannot be found, however there are many methods of approximation. The methods of approximation used in this thesis are fourth-order polynomial approximations [A2, A3]

$$K(k) = (a_0 + a_1 m_1 + a_2 m_1^2 + a_3 m_1^3 + a_4 m_1^4) + (b_0 + b_1 m_1 + b_2 m_1^2 + b_3 m_1^3 + b_4 m_1^4) \ln \frac{1}{m_1} \quad \{A.3\}$$

where	$a_0 = 1.38629436112$	$b_0 = 0.50000000000$
	$a_1 = 0.09666344259$	$b_1 = 0.12498593597$
	$a_2 = 0.03590092383$	$b_2 = 0.06880248576$
	$a_3 = 0.03742563713$	$b_3 = 0.03328355346$
	$a_4 = 0.01451196212$	$b_4 = 0.00441787012$

and  $m_1$  is the complementary parameter and is defined as  $m_1 = 1 - k^2$

where  $k$  is the modulus as defined in Chapter 6

$$E(k) = (1 + a_1 m_1 + a_2 m_1^2 + a_3 m_1^3 + a_4 m_1^4) + (b_1 m_1 + b_2 m_1^2 + b_3 m_1^3 + b_4 m_1^4) \ln \frac{1}{m_1} \quad \{A.4\}$$

where	$a_1 = 0.44325141463$	$b_1 = 0.24998368310$
	$a_2 = 0.06260601220$	$b_2 = 0.09200180037$
	$a_3 = 0.04757383546$	$b_3 = 0.04069697526$
	$a_4 = 0.01736506451$	$b_4 = 0.00526449639$

and  $m_1$  is defined as above.

### A.1. REFERENCES

- [A1] Korn, G.A. and Korn, T.M., *Mathematical handbook for scientists and engineers*, McGraw-Hill, 1961
- [A2] Hastings, C., *Approximations for digital computers*, Princeton University Press, 1955
- [A3] Abramowitz, M. and Stegun, I.A. (Eds.), *Handbook of mathematical functions with formulas, graphs and mathematical tables*, U.S. Dept. of commerce 1964

## B. MATERIAL CHARACTERISTICS

To correctly determine the temperature and resistance of each filament in a model, the material characteristics must be known. The thermal characteristics of four metals were determined and approximated to a series of functions. The functions were determined by fitting an approximate function to sets of experiment results available in several different sources [B1-B6]. The approximate functions are limited to the temperature ranges plotted below.

### B.1. COPPER

$$\rho_{Cu}(\phi) = -3.54 + 7.31 \times 10^{-2} \phi - 1.75 \times 10^{-5} \phi^2 + 1.48 \times 10^{-8} \phi^3 \times 10^{-9} \Omega m \quad \{B.1\}$$

$$c_{Cu}(\phi) = 170.9 + 4.923 \times 10^{-2} \phi' + 161.5 \left(1 - e^{-1.928 \times 10^{-2} \phi'}\right) + 66.54 \left(1 - e^{-4.67 \times 10^{-3} \phi'}\right) \text{ J/kg/K} \quad \{B.2\}$$

where  $\phi' = \phi - 70$

These functions are compared with measured data in Figure B.1 and Figure B.2

### B.2. ALUMINIUM

$$\rho_{Al}(\phi) = -6.89 + 0.12 \phi - 3.24 \times 10^{-5} \phi^2 + 3.66 \times 10^{-8} \phi^3 \times 10^{-9} \Omega m \quad \{B.3\}$$

$$c_{Al}(\phi) = 287.528 + 0.398 \phi' + 550.3 \left(1 - e^{-1.375 \times 10^{-2} \phi'}\right) \text{ J/kg/K} \quad \{B.4\}$$

where  $\phi' = \phi - 70$

These functions are compared with measured data in Figure B.3 and Figure B.4

**B.3. TUNGSTEN**

$$\rho_W(\phi) = -10 + 0.225\phi + 3 \times 10^{-5} \phi^2 \times 10^{-9} \Omega\text{m} \quad \{\text{B.5}\}$$

$$c_W(\phi) = -92.11 + 0.0251\phi + 217.7(1 - e^{-0.0165\phi}) \text{ J/kg/K} \quad \{\text{B.6}\}$$

These functions are compared with measured data in Figure B.5 and Figure B.6

**B.4. TITANIUM**

$$\rho_{\text{Ti}}(\phi) = 74.736 + 1.01\phi + 2.72 \times 10^{-3} \phi^2 - 3 \times 10^{-6} \phi^3 + 8 \times 10^{-10} \phi^4 \times 10^{-9} \Omega\text{m} \quad \{\text{B.7}\}$$

$$c_{\text{Ti}}(\phi) = -345.4 + 0.3014\phi + 787.12(1 - e^{-0.015\phi}) \text{ J/kg/K} \quad \{\text{B.8}\}$$

These functions are compared with measured data in Figure B.7 and Figure B.8

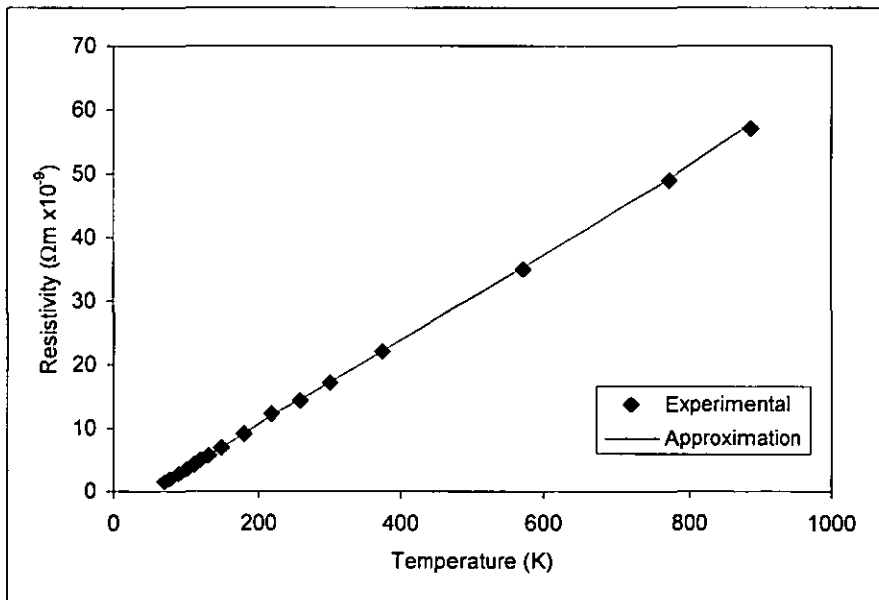
**B.5. FIGURES**

Figure B.1 Resistivity of copper

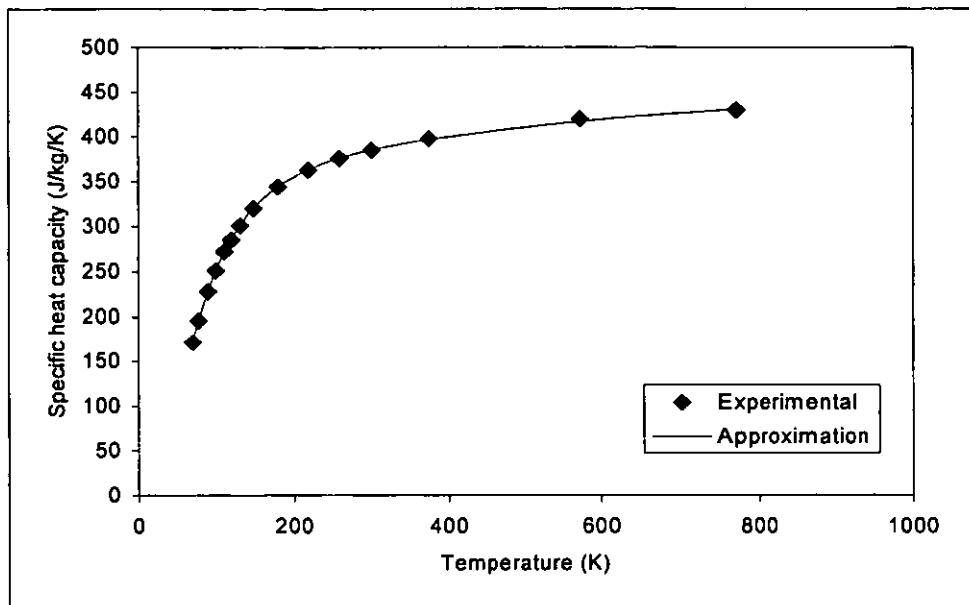


Figure B.2 Specific heat capacity of copper

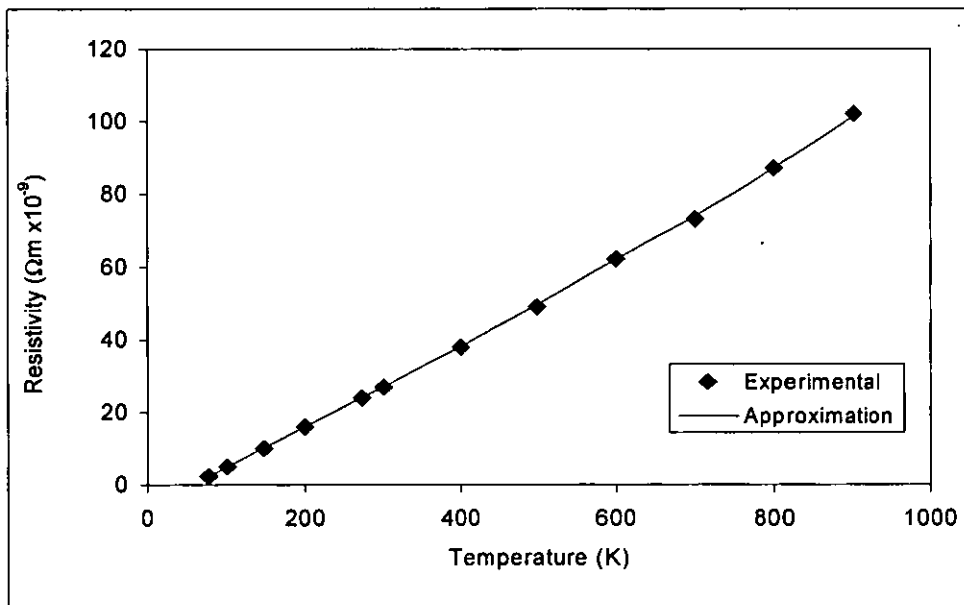


Figure B.3 Resistivity of aluminium

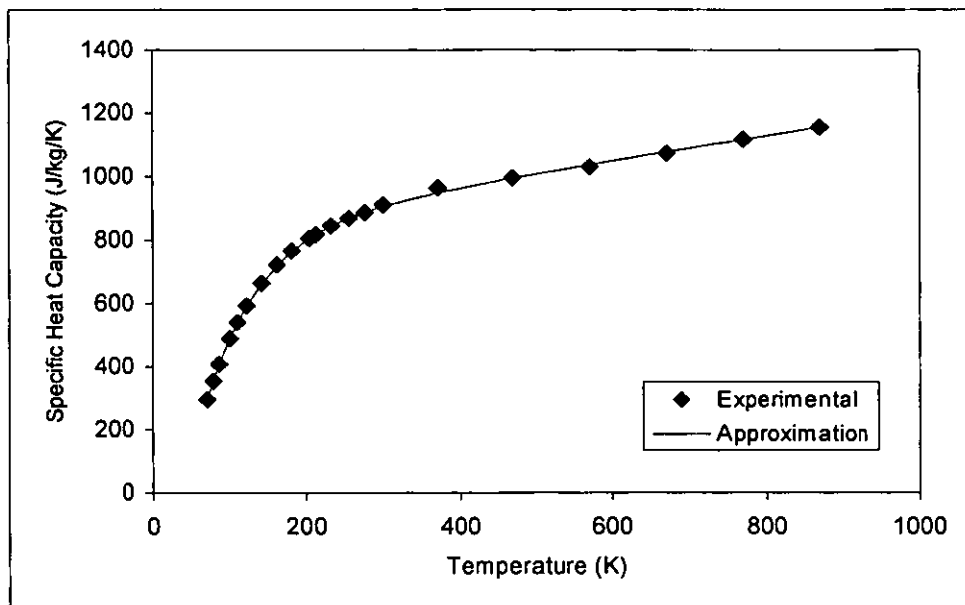


Figure B.4 Specific heat capacity of aluminium

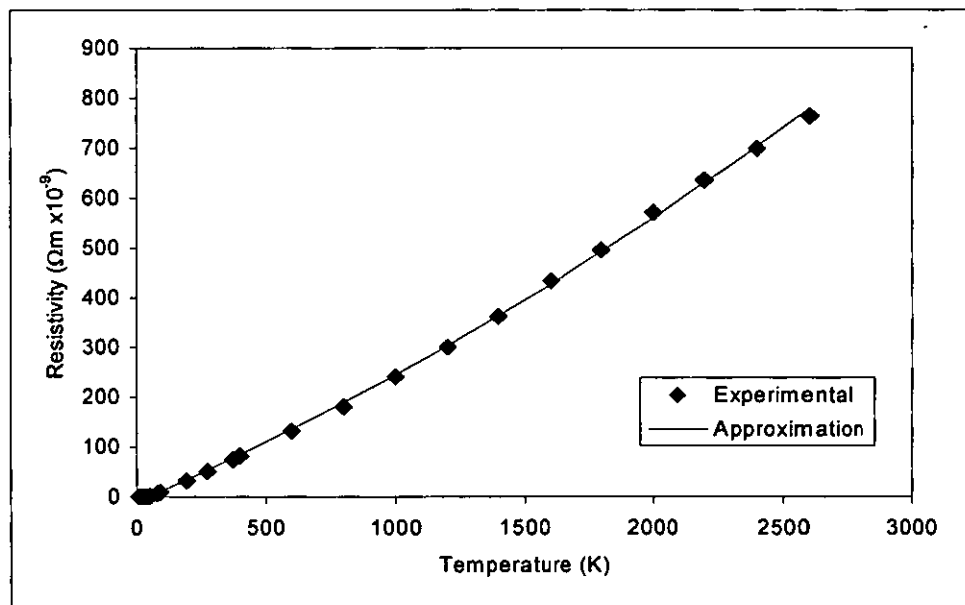


Figure B.5 Resistivity of tungsten



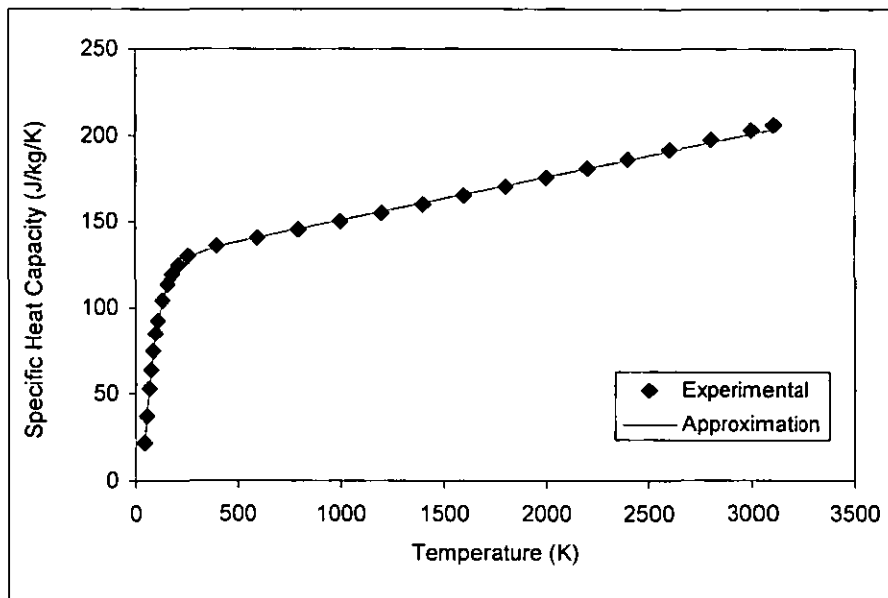


Figure B.6 Specific heat capacity of tungsten

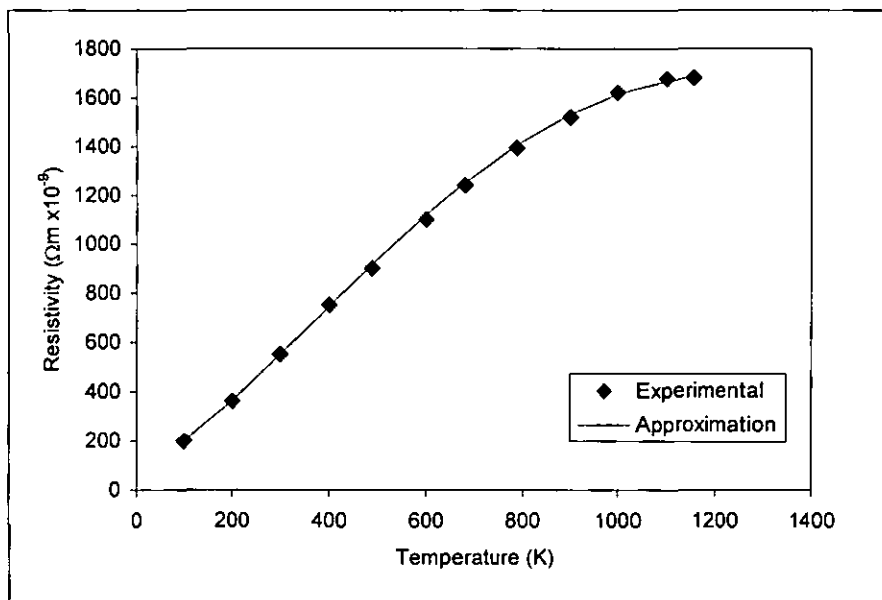


Figure B.7 Resistivity of titanium

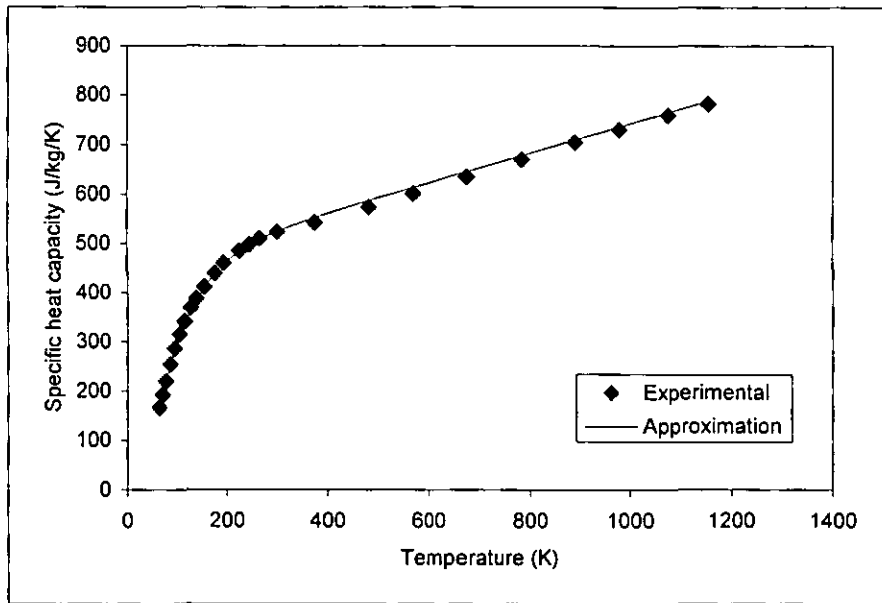


Figure B.8 Specific heat capacity of titanium

## B.6. REFERENCES

- [B1] *The Metals Handbook*, ASM International, Vol. 2, 1990
- [B2] *CRC Handbook of Chemistry and Physics*, CRC Press, 1974
- [B3] Goldsmith, A., Waterman, T.E. and Hirschhorn, H.J., *Handbook of Thermophysical Properties of Solid Materials*, Macmillan, Vol. 1, 1961
- [B4] Touloukian, Y.S. and Buyco, E.H., "Specific Heat: Metallic Elements & Alloys", *Thermophysical Properties of Matter*, IFI / Plenum, Vol. 4, 1970
- [B5] Cox, M., "Thermal and Electrical Conductivities of Tungsten and Tantalum", *Physical Review*, Vol. 64, 1943, pp. 245
- [B6] Wyatt, J.L., "Electrical Resistance of Titanium Metal", *Journal of Metals*, Vol. 5, part 2, July 1953, pp. 903-905

## C. LAUNCHER DIMENSIONAL DATA

The launcher used in the initial model validation test had the following dimensions.

### Projectile :

Material	Aluminium
Inside radius	24.5mm
Outside radius	50.5mm
Thickness	1.5mm
Vertical offset	0.5mm

### Drive Coil :

Material	Copper
Inside radius	25mm
Turns	17
Turn Height	2.5mm
Turn Width	1mm
Inter-turn space	0.5mm
Vertical offset	-2.5mm

The following launcher and simulation details were used during the model speed comparison tests and as the basis for all the later launcher design studies.

### General Details:

Large step length	1e-6 seconds
Small step length	1e-7 seconds
Simulation run length	0.0004 seconds
Constant retarding force	0 N
Drag coefficient	0
Total projectile mass	0.05 kg
Drive coil temperature	20 C
Projectile temperature	20 C

### Power Supply Details:

Main branch resistance	0.012 ohms
Main branch inductance	3.8e-7 H
Main branch capacitance	0.0001 F
Main forward voltage drop	10 V
Crowbar branch resistance	0.00255 ohms
Crowbar branch inductance	2.8e-8 H
Crowbar forward voltage drop	10 V
Cable resistance	0.018 ohms
Cable inductance	4.2e-7 H
Initial capacitor voltage	2000 V

### Drive Coil Details:

Number of turns	1
Number of layers per turn	25
Material	copper
Inside radius [y0]	25 mm
Vertical displacement [z0]	-5 mm
Conductor width [y1]	1 mm
Conductor height [z1]	5 mm
Horizontal conductor separation [y2]	0 mm
Vertical conductor separation [z2]	0 mm
Number of horizontal filaments	1
Number of vertical filaments	5

## Projectile Details:

Number of turns 1  
 Number of layers per turn 1  
 Material aluminium  
 Inside radius [y0] 25 mm  
 Vertical displacement [z0] 1 mm  
 Conductor width [y1] 25 mm  
 Conductor height [z1] 3 mm  
 Horizontal conductor separation [y2] 0 mm  
 Vertical conductor separation [z2] 0 mm  
 Number of horizontal filaments 25  
 Number of vertical filaments 3

The dimensions referred to in the square brackets are shown in Figure C.1.

The following table shows the approximate dimensions of the experiment launchers used in this thesis.

	Rectangular wire launcher	First round wire launcher	Second round wire launcher	Dual projectile launcher
Material	Copper strip	Copper wire	Copper wire	Copper wire
Wire dimensions	5 x 0.9mm	2mm diameter	2mm diameter	2mm diameter
Inside radius	25mm	25mm	25mm	25mm
Outside radius	50mm	50mm	50mm	50mm
Layers	1	1	2	2
Turns	25	12	24	24

The projectile used in all but the deformation test had the following dimensions.

Material Aluminium  
 Inside radius 25mm  
 Outside radius 50mm  
 Thickness 3mm

C.1. FIGURE

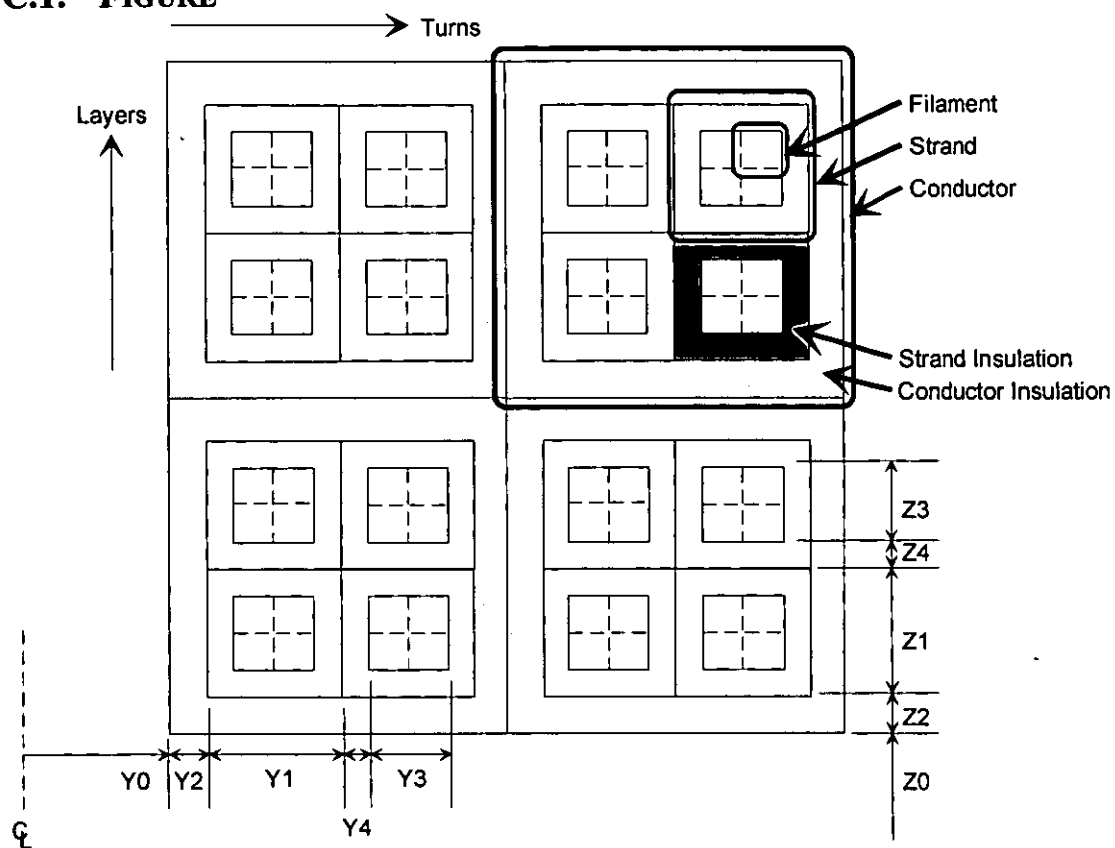


Figure C.1 Definition of rectangular coil dimensions



